

MỤC LỤC

HUMANITIES AND SOCIAL SCIENCES

- Factors Influencing Cross-culture Internship Acceptance:
A Case study of Collaboration between two Universities
in Vietnam and Thailand
Các nhân tố ảnh hưởng đến độ chấp thuận tham gia
chương trình thực tập xuyên quốc gia: nghiên cứu chương trình
hợp tác giữa hai đại học Việt Nam và Thái Lan
Nhu - Hang Ha 3
Anh - Phuong Bui
- Another View of the “Closed-door policy” of the Nguyen Dynasty
with Western countries (1802 - 1858)
Một góc nhìn khác về chính sách “đóng cửa” của triều Nguyễn
với các nước phương Tây (1802-1858)
Tran Dinh Hung 12
Tran Xuan Hiep

NATURAL SCIENCES

- Density Functional Theory studies of Hg and Pb ions Binding
with Chitin and Chitosan
Nghiên cứu sự liên kết của Chitin và Chitosan với ion Hg và Pb
bằng phương pháp phiếm hàm mật độ
Thi Hai Anh Mai 18
Thi Chinh Ngo
Duy Quang Dao
- Evaluation of the SRAC model for analyzing
the control rod worths of the DNRR
Đánh giá mô hình tính toán SRAC trong phân tích
giá trị thanh điều khiển lò phản ứng hạt nhân Đà Lạt
Phan Thi Thuy Giang 25
Do Quang Binh
Tran Hoai Nam
- A Liouville-type theorem for a parabolic system
Định lý kiểu Liouville cho hệ phương trình parabolic
Phan Quoc Hung 30
Nguyen Thai An
Nguyen Trung Hieu
Nguyen Thi Quynh
- Software Architecture and Design for Testability
Thiết kế và kiến trúc phần mềm cho khả năng kiểm thử hệ thống
Duc-Man Nguyen 35
Anh-Dao Nguyen
Bao-Trang Nguyen
- A Simulation Model of the Dalat Nuclear Research Reactor using SRAC code
Mô phỏng lò phản ứng hạt nhân Đà Lạt sử dụng chương trình SRAC
Tran Hoai Nam 45
Phan Thi Thuy Giang
Nguyen Kien Cuong
Tran Viet Phu
- Evolution of bubble structure in ^{34}Si nucleus at finite temperature
Sự tiến hóa của cấu trúc "bubble" trong hạt nhân ^{34}Si tại nhiệt độ hữu hạn
L.Tan Phuc 49
N.Quang Hung
- Thermoluminescence Property of Eu^{3+} doped $\text{Sr}_3\text{B}_2\text{O}_6$ Phosphors Prepare
by Combustion Method
Tính chất nhiệt phát quang của $\text{Sr}_3\text{B}_2\text{O}_6$ pha tạp Eu^{3+} chế tạo
bằng phương pháp nổ
Ho Van Tuyen 59
Nguyen Thi Thai An
Le Van Khoa Bao
Nguyen Ha Vi

An experiment on using agar layer as the confining medium for the laser-induced shock process Thí nghiệm sử dụng agar làm môi trường giới hạn trong quá trình shock gây nên bởi tia laser	Nguyen Thi Phuong Thao	63
--	------------------------	----

SCIENCES AND TECHNOLOGY

Soil Slope Stability Evaluation Using a Fuzzy Instance-Based Classifier with Flower Pollination Algorithm Đánh giá sự ổn định của mái dốc bằng phương pháp phân loại mờ và thuật toán tối ưu hóa	Hoang Nhat Duc Tran Xuan Linh	67
Introduction to Differential Privacy and Its Applications Giới thiệu Differential Privacy và ứng dụng	Nguyen Huu Hiep	77
A Passivity Approach to Proportional Controller Design for dynamic systems Thiết kế bộ điều khiển tỉ lệ dựa trên thụ động cho hệ thống động	Hoang Ngoc Ha Le Phuong Quyen	86
A Computational Study of Antioxidant Potential of Diterpenoid Amides in the Extract of the Leaves of <i>Erythrophleum fordii</i> Nghiên cứu tiềm năng chống oxy hóa của các hợp chất Diterpenoid Amides trong chiết xuất từ lá của cây Lim xanh bằng phương pháp Hóa tính toán	Truc Xuyen Nguyen Phan Thi Hau Nguyen Mai Thi Hai Anh Thi Chinh Ngo Duy Quang Dao	93
Physical Layer Secrecy of 5G Non-Orthogonal Multiple Access in Uplink Networks Bảo mật lớp vật lý trong mạng 5G sử dụng cơ chế đa truy cập phi trực giao NOMA ở đường truyền lên	Nguyen Van Long Ha Duc Binh Tran Duc Dung	98
An Investigation of Space Vector Modulation Methods for Matrix Converters Khảo Sát Phương Pháp Điều Chế Vector Không Gian Cho Bộ Biến Tần Ma Trận	Nguyen Huu Nhan	105

Factors Influencing Cross-culture Internship Acceptance: A Case study of Collaboration between two Universities in Vietnam and Thailand

Các nhân tố ảnh hưởng đến độ chấp thuận tham gia chương trình thực tập xuyên quốc gia: nghiên cứu chương trình hợp tác giữa hai đại học Việt Nam và Thái Lan

Nhu-Hang Ha^a, Anh-Phuong Bui^b

^a Graduate School, Duy Tan University, Danang, Vietnam

^b Faculty of Hospitality and Tourism, Duy Tan University, Danang, Vietnam

(Ngày nhận bài: 27/01/2018, ngày phản biện xong: 28/03/2018, ngày chấp nhận đăng: 29/03/2018)

Abstract

Participating in a cross-culture internship is a way to receive practical international experiences. However, the number of students joining this program is limited. This study examines the influencing factors on internship acceptance by using the concept of Technology Acceptance Model. Data was collected from a program between two universities in Vietnam and Thailand. The results show significant positive relationship between individual characteristics, internship program characteristics, culture and social norms with perceived usefulness of the internship (PU) while working conditions has impact on perceived ease of fulfilling the internship (PEF). The academia and industry could all benefits from this study.

Keywords: cross-culture internship, internship acceptance model, individual characteristics, internship characteristics, culture and social norms, workplace conditions

Tóm tắt

Tham gia chương trình thực tập xuyên quốc gia trở thành một nội dung quan trọng để có được kinh nghiệm thực tế quốc tế tốt nhất. Tuy nhiên, số lượng sinh viên sẵn sàng tham gia chương trình như vậy hiện nay vẫn còn rất hạn chế. Nghiên cứu này xem xét các yếu tố ảnh hưởng đến sự chấp nhận tham gia chương trình thực tập xuyên quốc gia bằng cách sử dụng mô hình chấp nhận công nghệ (TAM). Số liệu thu thập từ một chương trình hợp tác giữa trường đại học Việt Nam và Thái Lan. Kết quả cho thấy sự khác biệt của cá nhân, đặc điểm của chương trình thực tập, văn hóa và quan điểm xã hội có tác động tích cực đến nhận thức tính hữu ích của chương trình thực tập. trong khi điều kiện làm việc có ảnh hưởng đến nhận thức chương trình dễ dàng thực hiện được. Nghiên cứu về chương trình thực tập như thế này mang lại lợi ích cho cả giới nghiên cứu và các nhà quản lý.

Từ khóa: chương trình thực tập xuyên quốc gia, mô hình chấp nhận thực tập, khác biệt của cá nhân, đặc điểm của chương trình thực tập, văn hóa và quan điểm xã hội, điều kiện làm việc.

I. Introduction

Higher education for internationalized talents with intercultural competence is a new concept aiming to take students out of their colleges

and universities and to push them to become active interns in other foreign countries in order to obtain life-changing experiences (Xiaochi, 2012). Traditionally, universities focus more on

teaching theoretical knowledge than on practical skills, such as those that are required by employers (Chen, et al., 2011). Due to this disparity, internship programs are a way of improving this situation (Coco, 2000). Universities, therefore, have incorporated internship programs to let students apply theoretical learning in practice before they graduate (Santiago, 2009).

By the end of 2015, the ASEAN Economic Community (AEC) had officially taken effect and ASEAN countries had begun implementing the ASEAN Mutual Recognition Arrangement on Tourism Professions (MRA-TP), bringing both opportunities and challenges to the tourism industry of South East Asia. The MRA-TP is designed to recognize the skills and qualifications of working tourism professionals from different ASEAN countries and to enable the mobility of employment for this labor force among members (Thirumaran and Arumynathan, 2016). Some tourism and hospitality businesses are prepared to employ people with tourism education and training certificates from different countries. However, it has been established that some of these businesses are reluctant to accept student trainees for internship and further employment. Consequently, international internship programs have become one of the effective training models. Joining cross-cultural internship programs is a step for a student which creates much needed preparation for those who intend to work in regional areas. This is because the major purpose of such cross-cultural internship programs is to develop and strengthen student's skills and to prepare them for the profession (Parveen and Mirza, 2012).

This type of internship is an open architecture endeavor and is available to all programs to adapt to their specific needs. However, the use of the cross-cultural internship in University A, Vietnam is still at an initial stage and needs practical verification. The number of students who can attend this program is limited. Therefore,

this paper aims to clarify the influencing factors on internship acceptance to make necessary corrections by examining a case study of a cross-cultural internship program, which is conducted by Vietnamese and Thai universities. This cross-cultural internship program will continue for years to come and the findings of this paper could also serve as lessons-learned for the management and academia interested in cross-cultural internship.

In order to reach the research purpose, we use the Technology Acceptance Model (TAM) as the roadmap for all our explanations. Following their ideas, this study constructed another artifact, a theoretical framework as an extension of TAM, to explain the interns' behavior regarding the internship arrangement. The theoretical framework shows four different types of determinants of "perceived usefulness of the internship" and "perceived ease of fulfilling the internship". They are: *individual characteristics*, *internship characteristics*, *social norms*, and *workplace conditions*. These influence the decision-making process from "Behavior intention" to "Acceptance behavior". The paper first presents the context study by describing the cross-cultural internship program; and introduces the theoretical framework. Then we discuss the methodology, followed by a detailed analysis of the empirical data. It concludes with recommendations, limitations and suggestions for future research.

II. The Case of the Cross-Cultural Internship Program

The first and largest private university in Central Vietnam, University A was established in 1994. They are considered the biggest private university in the central region of Vietnam. A majority of the students are from the surrounding provinces and 80% of those choose a workplace in Central provinces. University A has built up a good relation with over 50 universities worldwide, in countries like USA, Canada, Australia, Singapore, New Zealand, India, Thailand, etc. This helps create

an international atmosphere. By conducting the cross-cultural internship program, University A can provide students with specialized knowledge and experiences to meet the needs of economic and social development. The case project consists of three parties, University A, University B in Thailand, and Resort C in Danang, Vietnam - the partner of University A.

University B is one of the most prestigious educational institutions in northern Thailand, was founded in 1924. It offers bachelor, master, and doctoral degree programs in education, humanities and social sciences, business management, science and technology, as well as agricultural technology. They realize the rapid and ever-changing development in societies; therefore, they are continually developing new curricula and focusing positive community development.

Resort C is a luxury five-star beach resort nestled in the heart of Son Tra Peninsula Nature Reserve, overlooking a private bay. Delve into the soul of Vietnamese culture and heritage with the nearby cultural and natural sites including the UNESCO World Heritage Sites Hoi An Ancient Town and Hue Imperial City, they offers the most impressive event facilities and services in the region. Being an intern here, students have a chance to work in a professional environment.

In this study we focus on the specific program in Tourism and Hospitality Management which is operated by the Faculty of Hospitality and Tourism in University A. The primary purpose of the program is to exchange spiritual values between young people of different countries. Under this program, international senior students can legally enter Vietnam for 3 months during their final academic year and work for Resort C. The program candidates must have a colloquial level of English and will be considered as full-time students of university. After finishing a three-month resident internship at Resort C they are awarded an internship certificate. The

application procedure is shown in Figure 1. In this case, University A takes responsibility for providing free accommodations and for arranging the internship sites (hotels, resorts, or tourism companies) for students coming from Thailand. University B in Thailand is in charge of recruiting students for this program and conducting primary selection activities. Resort C provides supervised practical training for students within three months.

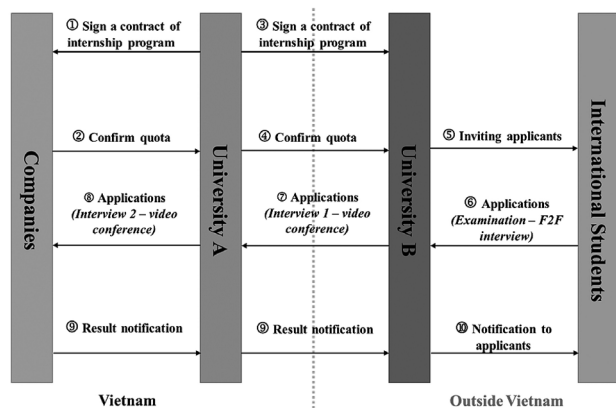


Figure 1. Application procedure

We divide cross-cultural internship program into three stages: In the *selecting stage*, intern candidates take written and oral examinations testing professional skills and English skills which are conducted by University B. Then, they meet Resort C prior to selection. Due to the distance, telephone conferencing or other technical exchanges (such as interactive video) are used. These meetings include an interview to determine the intern-sponsor “fit.” The interview was run professionally and openly. It was a difficult time for the interviewers to choose the best candidates for the internship. This stage supports Resort C to determine a candidate’s motivation and preparation for a specific international position and allow them to evaluate a candidate’s interactional communication competence and functional expertise.

In the *training stage*, students are required to take professional training courses at a work

place. The purposes of these courses are to equip students with: (1) intercultural communicative skills; (2) intercultural work experience; and (3) intercultural understanding. In addition, every week they will have two days for studying Vietnamese and cuisine classes that will help them understand Vietnamese culture and integrate into the community without obstacles. During this time, University A also holds different culture exchange activities to let their students and international interns have a chance to gain knowledge of foreign cultures and strengthen international relationships.

In the *monitoring stage*, advisors from the universities and supervisors from the work sites closely monitor the interns' progress. Two tools are needed to effectively carry out this task: First, the students should make daily reports and send them to their assigned advisors in University A and she/he will transfer them to the advisor in University B. The second tool is the informal progress evaluation to be completed by the intern's supervisor and sent directly to the faculty advisor. The advisor and supervisor can help an intern prevent a premature ending to her or his assignment by holding regular meetings that provide supportive feedback. This close personal assistance also helps prevent major problems associated with culture shock. Monitoring and supporting will provide much of the needed information to complete the internship.

All students receive a scholarship that includes a waiver of tuition, free accommodation, and free meals during work shifts. The sites for internship training are within a 30 to 45-minute drive from the University A campus. During the three months, students go to Resort C for practical training for five days per week. The supervisor at this location serves as their mentor. The other two days, interns take Vietnamese and cuisine classes at the Faculty of Hospitality and Tourism in University A. Interns are expected to enhance the required competences before receiving certificates from the employers.

The case project officially started in January 2016 and ended in April 2016.

III. Theoretical Background and Research Framework

1. Internship

Various research views internship programs from different perspectives. Students see internships as valuable learning experiences for which they should receive academic credit, financial compensation and earn a grade. From the employer's perspective, it is a "golden opportunity to try before buying" students they might wish to recruit after graduation (Abdullah, et. al., 2015). As a result of that, universities and colleges places strong emphasis on acquiring internship positions. In this study, internship is a kind of experiential learning where students take the opportunity to apply learned theories from schools in real world situations. It provides an opportunity for students to integrate and consolidate thinking and action.

2. Potential Benefits and Costs for Each Stakeholder

For students, internships frequently enhance their prospects of receiving job offers before graduation (Feldman and Bolino, 2000). In addition, they have opportunities to develop social and relational skills as well as applying communication and problem-solving skills in the work place. The internships also offer students the chance to train using the latest technology. In some cases, they can get the financial benefits of paid employment (Beard, 1998, Deasy et.al., 2011, Fall 2006, Feldman et. al., 1998). However, the interns also face some problems such as employers and interns often do not have consistent or shared expectations regarding the internship. Sometimes, unchallenging, scattered, routine, or career-irrelevant "busy work" tasks may be assigned. They also can get little support from the internship supervisors/mentors, from the top management,

or from faculty sponsors. These pitfalls can significantly reduce internship satisfaction.

For universities, by conducting internship programs they can create some benefits including: business support for an internship course, feedback concerning the curriculum, extended learning style options for students, real-world insight to the faculty supervisor, along with other ancillary benefits. Internships can also facilitate better relationships between schools and potential employers of their graduates (Beard, 1988; Berger, 1991). Thus, the school plays an important role as a bridge between students and enterprises in an internship program. By contract, the school needs to spend the cost for recruiting staff to obtain, publicity, and monitoring academic internships for course credit. More challenging is the fact that faculty have to be recruited to supervise internships when they have many other duties that pay off in more immediate and tangible ways, such as scholarly publication. This can be a major challenge, particularly because these faculty efforts are often seen as under-appreciated and under-compensated.

For employers, numerous articles address the potential benefits and costs for employers who utilize interns. Beard (1998) lists various benefits to the business deriving from internships, such as more effective recruitment and selection of future employees, being provided with needed part-time and special project employees, enhanced corporate image in the community, reduced training costs, and injection of new ideas into the organization; internships can lead to improved retention. Since internships do not require long-term employment commitments on the employers' part, they are an excellent "try-before-you-buy" method of staffing. Thus, internship is a relatively safe and low-risk approach for the business to attract and select potential employees (Williamson, Cable and Aldrich, 2002). However, there are some factors leading to the underutilization of interns.

The employers also need to provide mentoring and assistance, ensure the safety of the internship workplace, and proper arrangements with internship work and time.

3. The Research Framework

The TAM builds on the theory of reasoned action (TRA) which has its roots in social psychology and attempts to explain why individuals engage in consciously intended behaviors. In TAM, a user's motivation to adopt a new technology can be explained by three constructs: (1) perceived ease-of-use, (2) perceived usefulness, and (3) intention to use. Perceived usefulness is defined by Fred Davis as "the degree to which a person believes that using a particular system would enhance his or her job performance". Perceived ease-of-use is defined this as "the degree to which a person believes that using a particular system would be free from effort" (Davis, 1989). The TAM has been continuously studied and expanded-the two major upgrades being the TAM 2 (Venkatesh and Davis 2000 and Venkatesh, 2000) and the Unified Theory of Acceptance and Use of Technology (or UTAUT, Venkatesh et al. 2003). A TAM 3 has also been proposed in the context of e-commerce with an inclusion of the effects of trust and perceived risk on system use (Venkatesh and Bala, 2008).

For the purposes of this study, usefulness is defined as the perception formed by the students' belief that attending the cross-cultural internship enhances their performance. Meanwhile, the ease of fulfilling is defined as completing the cross-cultural internship easily without much effort. The framework assumes that students are likely to join this program to the extent that they believe it would help them to improve performance and to the degree to which an individual believes that joining this program would be free of cognitive effort ease of fulfilling its requirements. The theoretical framework shows four different types of determinants of perceived usefulness of the

internship and perceived ease of fulfilling the internship (Figure 2):

- Individual characteristics including personality and English language proficiency that can potentially influence individuals' perceptions of usefulness and ease.
- Internship characteristics such as the salient features of the internship arrangement (working schedule, task description, payment scheme for interns, supervisor support) that can help individuals develop favorable (or unfavorable) perceptions regarding the usefulness or ease.
- Cultural and social norms which capture various social processes and mechanisms that guide individuals to formulate perceptions of various aspects of the internship arrangement.
- Workplace conditions which represent organizational support that facilitate the fulfillment of the internship.

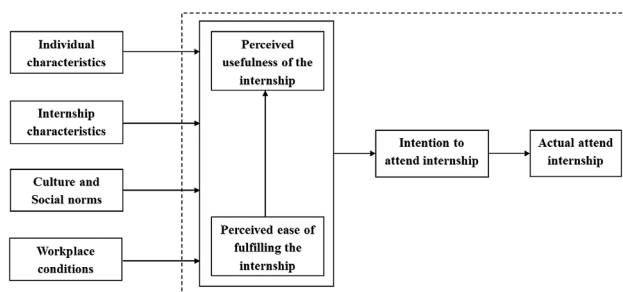


Figure 2. Theoretical framework for internship acceptance

IV. Data Collection and Analysis

We conducted semi-structured interviews with three Thai students who joined this internship collaboration between University A and University B, in order to create the workplace diversity industry and take part in the integration of the ASEAN Economic Community in 2015 (AEC) for the students to understand the acceptance behavior. There were two male students who had majored in Tourism Management (Student 1 - SDT 1), Hotel Management (Student 3 - STD 3), and one female student who was also

studying Tourism Management (Student 2 - SDT 2). Each interview lasted about 30–45 minutes. The interview questions (based on the constructs of framework for internship acceptance) were sent to the interviewees in advance to allow them to become familiar with the topic. Each interview was recorded and transcribed. The representatives of university A and resorts in Vietnam were also interviewed to confirm the results which we received from the students. We also observed these students at work to validate the results of the interviews.

For students, we focused on their perception of the cross-cultural internship program. Basing on the level of satisfaction (high, medium, low) we dig into the influencing factors (perceived usefulness of internship and perceived ease of fulfilling the internship). Later, we figure the factors impact on their perception (Individual characteristics, Internship characteristics, Culture and social norm, Workplace conditions).

Table 1. Interview question guide

Question type	Question
Opening	• Where are you from and what's your name?
Introduction	• Describe the cross-cultural internship program
Transition	• Do you feel satisfy with the arrangement of this program (accommodation, travel, advisor, supervisor, training courses)
Key	<ul style="list-style-type: none"> • Do you think this program is useful? Which factors make you feel like that and why? (based on the following factors: Individual differences, Internship characteristics, Culture and social norm, Workplace conditions) • Do you think this program's requirements are easy to fulfill? Which factors make you feel like that and why? (based on the following factors: Individual differences include, Internship characteristics, Culture and social norm, Workplace conditions)
Ending	<ul style="list-style-type: none"> • Do you have any remarks, suggestions, and additions? • Can you give us some advice on how to improve this program

The procedures of content analysis were divided into two stages. The first stage dealt with single interview transcripts. The second stage of content analysis dealt with cross interview transcripts, and aimed at the integration of all the individual factors, variables and links from all interviews, in order to develop a comprehensive model. Through this work, an in-depth case history of the project was completed.

V. Findings and discussion

Using the proposed theoretical framework in the context of this case project, the resident interns' perception and acceptance of the internship can be

clearly explained in terms of the four determinants. In terms of *individual differences*, each resident intern's tolerance toward the difficulty of a task assignment may be different. Those with low tolerance could have negative perceptions regarding the ease of fulfilling the internship. On the other hand, students with working experience absorb the value of this type of internship. They have a chance to do real work as official employees, and work with foreign supervisors and serve international customers.

STD 3: When I was a junior student, I worked part-time for a cafeteria; I became familiar with dealing with customers. When I came here, I felt comfortable.

STD 2: My major is Tourism Management. I have no experience in working at a restaurant. I feel like everything is so new, I need to study a lot of things.

Moreover, language barriers may also cause misunderstanding between supervisors and resident interns. English is not the mother tongue of the interns, supervisors or advisors. In some cases, the advisors are unable to transfer the spirit of this program to interns to let them understand the work-site regulations before they start to work. Supervisors, of course, encounter obstacles when they try to explain the contents of practical training to interns.

STD 1: I work as a waiter in restaurant, however, some of my supervisors are not good at English, and it is difficult for me to understand their instructions. I don't know how to handle my tasks.

We found that the most significant element of individual characteristics which impacts the perception of interns is *self-interest*. Based their own purpose, the interns had various reactions on the internship program.

STD 1: I love to travel, and I know Vietnam is so beautiful, so I decided to come here!

STD 2: I would like to work for a good resort

in Thailand; therefore, I really want to learn more about hotels and restaurants. However, it is difficult for me to get a position in a good hotel to practice in Thailand. When I learned about this opportunity, I was willing to join since this program is useful.

STD 3: I would like to learn more about new cultures and to get more experiences in foreign countries. I found that this program was interesting, so I came here.

The hospitality industry has some special features related to *internship characteristics*. Those who work in this industry need to adapt with requirements related to multiple skills and flexible work schedules. It takes time for interns to get familiar with the working environment. We found that the location of work-sites had considerable impact on the interns' decision.

STD 1: Vietnam is so close to Thailand, I think there is no problem for me to join.

STD 2: I work in a restaurant; I need to get up very early (around 4:00 am) to get there because it takes 1 hour from the school's campus to there. Sometimes, I feel very tired!

STD 3: I work for a French restaurant, they don't allow me to use my phone and I need to remember everything by memory instead of taking pictures... it's tough!

For those students who come from ASEAN countries, there is not much difference in culture and social norms, but they also can have difficulties with living conditions (eg. food, weather, and thinking).

STD 1: I got sick many times and sometimes I needed to go to the hospital and stay there for 2 days due to the weather.

STD 2: The food here is delicious, but we still miss Thai food. However, we have no time to cook here. In addition, we also have no kitchen to prepare our food.

In general, we found that the factors that had an impact on perceived ease of fulfilling the internship included individual differences, internship characteristics, culture and social norms, and those affecting perceived usefulness are individual differences, internship characteristics and workplace conditions. The interns felt satisfied with the program and earn value from this.

STD 1: The program is conducted so professionally. We have everything!

STD 3: We understand more about Vietnamese culture; support us for future jobs in this field. The content of the internship is the same as what we were training, it is not really a problem for us to fulfill all the requirements.

Moreover, from the information collected from students' ideas also shows that *perceived enjoyment* of the internship may also be considered another influencing factor on the acceptance behavior. Students have right to terminate this program in case they feel it does not fit their learning purpose. However, after one week arriving and working at Resort C, they feel very exciting. They had chances to do “real things” there. The chef taught them how to prepare the foods, and they get into the restaurant to serve customers as an official employee. In addition, the advisors took them to visit many attractions in Danang to let them have more opportunities to explore people and culture here.

STD 2: Our internships have been unforgettable. At first, everything was unfamiliar but, with the support of advisor, supervisor, and friend, we have easily adapted to the new environment and overcome some challenges. We have gained useful practical skills and hope to be able to come back soon.

STD 2: The internship gave us many precious chances in developing personal and working skills. We were not only trained communication skills in working, but we also learned the way

how to connect with colleagues and interact with customers effectively. In addition, I took part in many interesting activities with students. The unforgettable experience in this internship helped us broaden useful knowledge of culture and people in Danang as well as in Vietnam.”

Unfortunately, in this study the proposed framework was not proved quantitatively due to the small size of sample. Therefore, we revise the proposed framework for validation in further studies as follows (Figure 3):

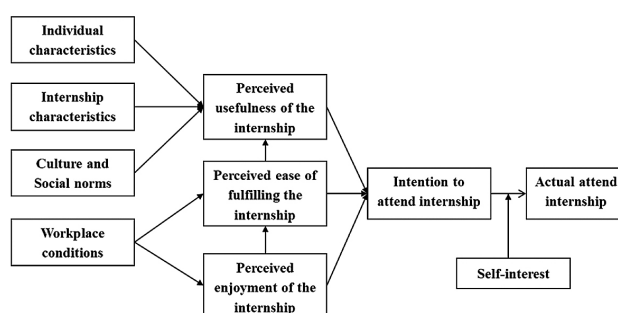


Figure 3. The revised research framework of acceptance behavior

Even the Resort C management is willing to recruit those students officially. However, to make the most of the internships, students are also encouraged to follow the advice below. First, they need to be prepared before the internship. Students need to have the basic knowledge of the field to support themselves and create better opportunities to apply theories into practice. They should have positive attitude about the internship because the supervisor will treat them like real staff and put them into real situations. .

VI. Conclusion

This study proposed a theoretical framework for predicting the acceptance behavior of internship training. The results show significant positive relationship between individual characteristics, internship program characteristics, culture and social norms with perceived usefulness of the internship (PU) while working conditions has impact on perceived ease of fulfilling the internship

(PEF). In addition, we also found that the intention to attend the internship is also get influence of perceived enjoyment of the internship. However, it has only been validated with a single case project. More case study research may be needed to establish their generality in the future. By applying the theoretical framework to understand how and why trainees make a decision about accepting and fulfilling the internship training, top management can make decisions about interventions that can lead to greater acceptance and effective implementation. Universities can also revise curriculum and training programs to fit with exchange programs; and enhance relationship with local partners to create more opportunities for their students. Moreover, all partners need to focus on the environment of internship to make students feel enjoyable and be willing to attend. This program brings benefits to the interns in term of enhancing the skills to work in an international environment and also provides value to advisors and local students in Vietnam in terms of studying new language and culture.

References

1. Abdullah, R., Zahari, H., Mat, N. A. N., Zain, R. A., and Derani, N. (2015). Hospitality internships: an employment advantage or perilous experience. *Journal of Basic and Applied Scientific Research*, 5(8), 34-38.
2. Beard, D. F. (1998). The status of internships/cooperative education experiences in accounting education. *Journal of Accounting Education*, 16(3), 507-516.
3. Berger, J. (1991). Making an internship work. *Public Relations Journal*, 47(4), 30.
4. Chen, C. T., Hu, J. L., Wang, C. C., and Chen, C. F. (2011). A study of the effects of internship experiences on the behavioural intentions of college students majoring in leisure management in Taiwan. *Journal of Hospitality Leisure Sport and Tourism Education*, 10(2), 61-73.
5. Coco, M. (2000). Internships: A try before you buy arrangement. *SAM Advanced Management Journal*, 65(2), 41.
6. Deasy, C., Doody, O., and Tuohy, D. (2011). An exploratory study of role transition from student to registered nurse (general, mental health and intellectual disability) in Ireland. *Nurse Education in Practice*, 11(2), 109-113.
7. Fall, L. (2006). Value of engagement: Factors influencing how students perceive their community contribution to public relations internships. *Public Relations Review*, 32(4), 407-415.
8. Feldman, D. C., and Bolino, M. C. (2000). Skill utilization of overseas interns: antecedents and consequences. *Journal of International Management*, 6(1), 29-47.
9. Feldman, D. C., Folks, W. R., and Turnley, W. H. (1998). The socialization of expatriate interns. *Journal of Managerial Issues*, 403-418.
10. P. Maertz Jr, C., A. Stoeberl, P., and Marks, J. (2014). Building successful internships: Lessons from the research for interns, schools, and employers. *Career Development International*, 19(1), 123-142.
11. Parveen, S., and Mirza, N. (2012). Internship program in education: effectiveness, problems and prospects. *International Journal of Learning and Development*, 2(1), 487-498..
12. Parveen, S., and Mirza, N. (2012). Internship program in education: effectiveness, problems and prospects. *International Journal of Learning and Development*, 2(1), 487-498.
13. Santiago, A. (2009). Impact of sandwich course design on first job experience. *The Asia-Pacific Education Researcher*, 18(2), 205-217.
14. Thirumaran, K., and Arumynathan, P. (2016). Destination ASEAN, Beyond 2015. In *Development of Tourism and the Hospitality Industry in Southeast Asia* (pp. 1-11). Springer Singapore.
15. Thirumaran, K., and Arumynathan, P. (2016). Destination ASEAN, Beyond 2015. In *Development of Tourism and the Hospitality Industry in Southeast Asia* (pp. 1-11). Springer Singapore.
16. Venkatesh, V., and Bala, H. (2008). Technology acceptance model 3 and a research agenda on interventions. *Decision sciences*, 39(2), 273-315.-315.
17. Venkatesh, V., and Davis, F. D. (2000). A theoretical extension of the technology acceptance model: Four longitudinal field studies. *Management science*, 46(2), 186-204.
18. Xiaochi, Z. (2012). Discussion on international internship and intercultural competence from a perspective of higher educational internationalization-A case study of the program work and travel USA. *Cross-Cultural Communication*, 8(5), 62.
19. Williamson, I. O., Cable, D. M., and Aldrich, H. E. (2002). Smaller but not necessarily weaker: How small businesses can overcome barriers to recruitment. In *Managing People in Entrepreneurial Organizations* (pp. 83-106). Emerald Group Publishing Limited.

Another View of the “Closed-door policy” of the Nguyen Dynasty with Western countries (1802 - 1858)

Một góc nhìn khác về chính sách “đóng cửa” của triều Nguyễn với các nước phương Tây (1802-1858)

Tran Dinh Hung^a, Tran Xuan Hiep^b

^a*Faculty of Histor - Hue University's College of Education, Vietnam
Khoa Lịch sử, Đại học Sư phạm Huế, Việt Nam*

^b*Faculty of Social Sciences and Humanities - Duy Tan University, Vietnam
Khoa Khoa học và Xã hội nhân văn, Đại học Duy Tân, Việt Nam*

(Ngày nhận bài: 08/02/2018, ngày phản biện xong: 15/03/2018, ngày chấp nhận đăng: 20/03/2018)

Abstract

Diplomatic relations of the Nguyen Dynasty took place in a very complex period. Foreign policy and behavioral culture with Western countries, especially France, was a difficult problem for the Nguyen Kings. In terms of policy, there was a lack of clarity and duality in diplomatic relations with France and the West. The consequences of these policies have been debated by historians throughout history. This article will present another perspective of the Nguyen Dynasty in its relations with Western countries during its independence and self-control (1802-1858). Accordingly, the author investigates foreign policy of Nguyen Dynasty and The West based on Limited Access Policy (under King Gia long and King Minh Mang Rule) to Anti Access policy (under Reign of King Thieu Tri and King Tu Duc).

Keywords: Nguyen Dynasty, Limited access, Anti-access, “Closed-door”, 1802-1858

Tóm tắt

Quan hệ đối ngoại của triều Nguyễn diễn ra trong bối cảnh lịch sử phức tạp. Thái độ ứng xử và chính sách ngoại giao như thế nào với các nước đến từ phương Tây, đặc biệt Pháp, là một “vấn đề khó” cho các vị vua nhà Nguyễn. Chính sách được xem như “thiếu rõ ràng” và “mang tính hai mặt” của triều đình Nguyễn với Pháp, các nước phương Tây và hệ quả của nó đã được các nhà nghiên cứu lịch sử tranh luận từ lâu. Bài báo này sẽ trình bày một cách nhìn khác về cách tiếp cận của triều Nguyễn trong mối quan hệ với các nước phương Tây trong giai đoạn độc lập, tự chủ (1802-1858). Theo đó, tác giả nhìn chính sách đối ngoại của triều Nguyễn với phương Tây dựa trên quan điểm phát triển, với cách tiếp cận là: Từ chính sách Tiếp cận hạn chế (dưới thời vua Gia Long và Minh Mạng) đến chính sách Chống tiếp cận (dưới thời vua Thiệu Trị và Tự Đức).

Từ khóa: Triều Nguyễn, Tiếp cận hạn chế, Chống tiếp cận, “đóng cửa”, 1802-1858

1. Introduction

Foreign policy between the Nguyen Dynasty and the West (1802-1858) has been researched by many scholars in Vietnam and abroad. Before 2000, scholars tended to have similar views about

the issue as follows: (1) It was a “closed-door and rebuffed policy” against the West; (2) Kings of Nguyen Dynasty “prohibited and murdered Christians” and discriminated Westerners; (3) Nguyen Dynasty’s kings had political views which were “short-sighted” and “blind.”

However, from 2000 to the present, many new publications have been published and nearly twenty scientific workshops related to the Nguyen Dynasty have been organized. Most notably the book “The History of Nguyen Dynasty - A new approach” (2005) has collected many articles from many scholars who studied the Nguyen Dynasty, as well as the conference on “Nguyen Lords and Nguyen Dynasty in the history of Vietnam from the sixteenth to the late nineteenth century”, Thanh Hoa, Vietnam (18-19 October 2008).

In general, almost all research agreed with some new and different views on the Nguyen dynasty’s foreign policy with Western countries such as: (1) Put that policy into the context of complicated history at that time to “understand” and “sympathy” for the closure of the Nguyen dynasty, not a radical critique; (2) Nguyen dynasty not completely “closed” country; (3) foreign policy was not entirely wrong, sometimes soft, subtle; (4) it was a “duality” “policy and the conflict between “closed-door” and “open-door” policies...

This paper does not intend to judge the above views. Instead, it aims to provide a different vision of the approach of the Nguyen Dynasty in its relations with Western countries during the independence and autonomy period (1802-1858). In other words, that is from the “Limited access” policy to “Anti-access” policy.

2. From “limited access” policy under reign of King Gia Long (1802-1819) and King Minh Mang (1820-1840)...

“Limited access” is a new term which the author gives and uses in this article to refer to the foreign policy of the Nguyen Dynasty with Western countries. The term “limited access” is understood in the sense that King Gia Long and King Minh Mang maintained relations with the Western countries. However, there were clear limits and frameworks in place to control and restrict their penetration and influence within the territory of Vietnam.

July 1802, Nguyen Anh (King Gia Long) came to the throne, ushering in period of Nguyen dynasty domination in Vietnam (1802-1945). Foreign policy with the West has been shaped under this king.

For France, King Gia Long had a special and favorable relationship with the French before 1802, so when he became King, he continued to bestow favor on France, especially during the reception ceremony [1, 7-9], [10, 181]. However, the king usually warned his courtiers about threats to national security from trade and missionaries of France. When the Western countries, including France, showed desire to establish commercial firms in the ports of Vietnam, he adamantly refused: “The port is extremely important place, completely impossible for the office of foreigners placed there” [23, 515].

Moreover, Gia Long almost exclusively conducted relations with France in the field of trade. Some French merchants in Bordeaux as Baguerie, Stuttenberg, Philippon sent trading ships to Vietnam in the years 1817- 1819 and they were treated kindly and provided duty-free importation of goods [30, 413]. The French officials in Gia Long dynasty as Chaigneau repeatedly attempted to persuade the King to set up official diplomatic and trade relations with France but failed [32, 43-49], [16, 20].

The Restrictive policy of Gia Long is also reflected in the rules, principles, and frameworks in dealing with France and the West.

After ascending the throne in 1802, King Gia Long chose Da Nang port as a place to welcome foreigners on behalf of diplomatic envoys or merchants. Since then, Da Nang became the only official port to welcome guests from the West. The Nguyen Dynasty only welcomed Westerners on condition that they must have credentials. If they have the credentials, then the two sides must work together closely and follow procedure. Normally, foreign embassies in Da Nang port,

after confirming their credentials and donating gifts to the King, will have their boats docked after careful examination. Afterwards, they are allowed to send people to the shore, under supervision of the local soldiers, to purchase the essential supplies such as food, drinks, and charcoal. Everyone must stay on ships waiting for local officials to write a report and consult the King. The King's directives often arrive 10 to 15 days after a ship has docked. In urgent cases, the response can take three days.

Protocol before the 17th year of Gia Long (1817), instructed that foreign ships arriving in the port of Da Nang will be greeted by the "flag and firing 21 shots of cannon." But later, the King only allowed 3 to 6 shots as a welcome. The official reception of the host country may take place in Hue court if the King agrees, but usually it was held in Da Nang by the representative of the court, or officials of Thuong Bac Affairs in coordination with local officials and soldiers.

For the other Western countries, the relationship also stops at welcoming ceremonies and regular trade. In 1804, the King of England sent an ambassador named John W. Roberts with gifts and credentials because they desired to open commercial trade in Tra Son, Quang Nam, but King Gia Long rejected [6, 184-185]. Afterwards, they continued to send credentials two or three more times but failed [10, 181]. King Gia Long repelled diplomatic relations with the British because: "the British is cunning, deceitful, not our race, their heart certainly different from us, not to stay" [23, 552].

This policy of Gia Long showed clear intentions: did not allow the West the opportunity to penetrate or establish bases (including commercial bases on the Vietnam territory). He said that it would jeopardize the national security. The speech also showed his contempt attitude with Westerners.

In 1803, a US merchant ship called "Fame" brought Captain Jeremiah Briggs to Cochinchina

(Vietnam) in an effort to find new sources of sugar and coffee. They were allowed trafficking by Gia Long in Vietnam [17, 3-4]. The second and third visits of Americans in 1819 were also welcomed thoughtfully. However, these trades did not obtain any significant results [17, 7-10].

A modern Vietnamese researcher, Cao Huy Thuan, in commenting upon the policy of King Gia Long with the West, assumed that: Although the Gia Long's policy with the West was cold, he still preserved it. However, he did not allow to establish official contacts as well as the political commitment to the Western governments, because he was afraid of power of the Westerners [31, 49-50]. Another scholar, Hal Dareff, confirmed that Gia Long "close the border" to "prevent the entry of foreigners with their strange way of life ", but" ... unfortunately, the country has already existed foreigners - the missionaries" [3, 28]. Indeed, Christianity is a difficult and complex issue in external relations with the West of Gia Long and succeeding kings (this issue will be addressed in another paper).

Before his death, King Gia Long chose Prince Dam (King Minh Mang, 1820-1840) as successor with the intent: that man not only inherited the throne, but also inherited his will. In fact, King Minh Mang "is only the implementation of the basic ways of Gia Long" [20, 339].

Minh Mang expressed his cold attitude clearly to the French. He refused all requests for the establishment of formal diplomatic relations, or signing a trade agreement between the two countries. He only welcomed ambassadors and normal trade as a way to maintain relationships. Foreigners were forced to comply with the same strict regulations that had existed before. In 1821, 1822, 1824, France sent warships constantly to Vietnam to negotiate formal treaty but all were rejected [22, 124-125], [25, 1755].

For Americans, in 1832 and 1836, Edmund Roberts, special envoy of US President, made two trips to Vietnam with the aim of "signing the trade

agreement in favor of the US trade” [9, 53] and Nguyen Dynasty was welcome [25, 1772-1773]. However, these trips were not successful. The cause was attributed to both parties deeply conflicted about diplomatic etiquette [27, 5-6], [28, 357-364], [19, 4-5]. While Roberts and some scholars believed that the conflict of protocol was the cause of the failure, but I think it is just an excuse for Nguyen government’s refusal of the American proposals. The root cause was that Minh Mang did not want to make any relations with the West. This is a consistent policy that has been exercised before. Even if there was not a cultural collision between two nations, the US mission would still find it difficult to achieve their purpose.

For England, in 1821, John Crawfurd led a mission to Vietnam for the only trafficking desire like other countries. In his diary, Crawfurd ‘discovered’ that the Vietnamese people were extremely sticklers for ceremony and had a very pretentious character. His mission was treated with perfect respect, but they were also tightly controlled as prisoners. Crawfurd was denied a meeting with Emperor Minh Mang with reason “this man is just one officer dispatched by a Governor, not by a monarch’s orders” [25, 1749]. However, Crawfurd was announced that the British could trade in the Central of Vietnam [2, 99-103]. Later, the British ships were docked in Vietnam several times, but also failed to achieve their desired purpose.

It can be seen, Minh Mang still continued the policy of Gia Long. Of course, the Westerners did not just want a relationship at that level, since it is inconsistent with Western-style diplomacy. The two sides have different approaches on this matter, so negotiations were often stalled without reaching any results.

To 1939, the Opium War broke out in China, which made King Minh Mang aware of the risk that Vietnam faced in continuing a “closed-door” policy. In 1840, he hastily appointed a

delegation to Penang, Calcutta, Djakarta to probe the situation [4, 37-44]. Particularly, Minh Mang sent an envoy led by Ton That Tuong to France to offer a commercial agreement with Vietnam, in exchange for a commitment to protect Vietnam in case of Vietnam was attacked [7, 43]. This trip was the first time “active” negotiation of Nguyen Dynasty conducted a state-level diplomacy with Western countries. It was a shift in foreign policy with the West of Minh Mang. If Minh Mang had not suddenly died, then the situation could be different movements! Unfortunately, this groundbreaking was not continued by the two successors - Thieu Tri and Tu Duc.

3. To “Anti-access” policy under the reign of King Thieu Tri (1841-1848) and King Tu Duc (1848-1858)

“Anti-access” is also a new term in use to talk about the foreign policy of the Nguyen Dynasty with the West under the reign of King Thieu Tri and King Tu Duc. Anti-access policy is to deny or refuse any contact, diplomatic or trade relationship (including normal trade), with Western countries. It seeks to “close” the country completely with foreigners and does not give them the opportunity to access to the territory of Vietnam.

Step into the reign of King Thieu Tri (1841-1847) and especially King Tu Duc (1848-1883), the diplomatic door of the Nguyen Dynasty completely “shut down” to the West. In the 1843, 1845, 1847, respectively the French and American warships docked in Da Nang and made pressure of Hue court to force itself to release the French clergy being held in Hue, as well as religious freedom [29, 214], [33, 493-494], [34]. King Thieu Tri did not allow for any direct contacts between the two sides. Even in 1847, the French and Vietnamese navies fought fiercely with each other in Da Nang. “Failure of the Nguyen’s fleet made Thieu Tri was furious, ordered to kill all the Westerners staying at Vietnam” [29, 216]. He also ordered to smash

all objects bought from the West and made effigies of Western soldiers to shoot. Obviously the reaction was very “childish,” and showed the deadlock and inability of the head of State of Vietnam during this time. After these events, the banning of Christians and the closed-door policy of the King were pushed to the highest levels.

To the British, knowing that the Nguyen Dynasty conflicted with the French, John F. Davis carried Queen Victoria’s credentials to Vietnam’s emperor to discuss the signing of a trade treaty and establish formal diplomatic relations. Gutzlaff, who accompanied Davis to Vietnam in May 3/1847, recorded that: He ashore twice to move the Queen’s letter to Emperor Vietnam but no one received the message. They were also not allowed to go to the Hue capital to express their aspirations [15, 113], [14, 24-25].

November 1847, Thieu Tri died. Tu Duc came to the throne at a time when the relationship between the Hue court and the West, particularly France, was worsening. Major issues in foreign policy of the Tu Duc dynasty with France and the West was centered on the issue of Christianity. The banning of Christians from Minh Mang until Tu Duc at beginning were not very effective. While he has not found a more effective solution yet, he decided to increase the “intensity” of the religious ban with a more stringent edict [8, 297].

Under these circumstances, the French emperor decided to send Ambassador Extraordinary and Plenipotentiary Charles de Montigny to Vietnam to negotiate. While Montigny was staying in Siam and Cambodia, William de Ville-sur-Lelieur Arc commanded Catinat warship to Da Nang dated 16/09/1856 to send Montigny’s letter to King Tu Duc, but the local officials were ordered not to receive the letter from France. Lelieur sailed to Thuan An sea port to deliver, but Vietnam officials there did not recognize it either. Lelieur had to leave the letter on the coast and headed back to Da Nang. Here, the warship of Lelieur fired on Da

Nang and sent an army on ashore to lock the 60 cannons and poured large gunpowder amounts of Hue imperial army into the sea [29, 218].

Montigny arrived in Da Nang on January 23, 1857. In the context of negotiation, Montigny wanted to sign a trade treaty between both nations, established a French consulate in the Hue capital, open Da Nang’s sea port, and free Christian missionaries. In response, similar to previous times, the Hue royal court rejected all requests. Montigny was very angry and indicated his proposals were civilized diplomatic procedures which were admitted by many countries, while the treatment of the Nguyen Dynasty was a humiliation for France. The only way to get results was through the use of force.

This was the last attempt of the French diplomacy lead by professional diplomatic envoys, but still not achieve desired results. Meanwhile, in France, many officials and clergies continued to promote the use of force to invade Vietnam. In 1858, the French expeditionary army attacked Da Nang port. Therefrom, a new chapter in the relationship between Vietnam and France opened, which in tandem with the losing national territory and sovereignty in the hands of the French, the autonomy and self-determination in relation to the French in particular and the West in general has gradually slipped from the hands of the Nguyen dynasty.

4. Conclusion

In the context of complex history in the first half of the 19th century, in which the penetration of Western elements was considered a great threat to national security and traditional culture of the nation, the Hue court has developed a prudent and highly defensive foreign policy towards the adverse effects of the West. The “limited access” policy was shaped by King Gia Long with the policy of “limiting” contact and access from the West through a system of mandatory principles and rituals, and

rejection of any proposal to sign a trade or diplomatic agreement with Westerners. The “Gia Long style” diplomacy was followed by Minh Mang. However, during the reign of King Thieu Tri and King Tu Duc, this diplomatic door was increasingly closed and eventually completely closed to the Western world. In other words, it is a shift from the limited access policy to anti-access policy. This foreign policy is clearly not a wise foreign policy because it led to detrimental consequences for the Nguyen dynasty and the country.

References

- [1] Binh Ton That (1995). *Storytelling Nguyen’s kings*. Thuan Hoa publisher. Hue
- [2] Crawfurd, John (1830). *Journal of an Embassy from the Governor-General of India to the Courts of Siam and Cochinchina; Exhibiting a View of the Actual State of Those Kingdoms*. London: Colburn and Bentley.
- [3] Dareff , Hal (1971). *The Story of Vietnam, a background book on the war in Southeast Asia*. Parents’ Magazine Press. New York.
- [4] Duyet Dinh Thi (2012). The change in foreign policy with the West of King Minh Mang, “*Journal of Southeast Asian Studies*”, No3 (144). p.37-44.
- [5] Giau Tran Van (2001). *Anti-invasion: History of Vietnam from 1858 to 1898*. Ho Chi Minh city publisher. Ho Chi Minh.
- [6] Fry, Howard T. (2013). *Alexander Dalrymple and the Expansion of British Trade*. Routledge
- [7] Honey, P.J. (1968). *Genesis of a Tragedy: The Historical Background to the Vietnam War*. Benn.
- [8] Huon Phan Phat (1958). *Vietnam Catholic history*. Vol. 1. Sai Gon.
- [9] James, D. Richardson (1896). *A Compilation of the Messages and Papers of the Presidents, 1789-1897*. Washington D.C.: Government Printing Office.
- [10] Kim Tran Trong (1971). *A brief history of Viet Nam*. Sai Gon.
- [11] Kiem Nguyen Van (1999). *Policies towards Catholics under Thieu Tri, Old and Now Magazine*, No 64B (6).
- [12] Lam Dinh Xuan, Khanh Nguyen Van, Le Nguyen Dinh (2001). *History of Vietnam*. Vol. 2 Education Publisher. Hanoi.
- [13] Lan Hoang Van, Chinh Ngo Thi (1974). *History of Vietnam (1858 – the late of 19th century)*. Vol.3, Part 1. Education Publisher, Hanoi.
- [14] Leigh R. Wrigh (1970). *The Origins of British Borneo*. Hong Kong University Press.
- [15] Lutz, J. Gregory (2008). *Opening China: Karl F.A. Gtzlaff and Sino-Western Relations, 1827-1852*. Wm. B. Eerdmans Publishing, Michigan.
- [16] McLeod, Mark W. (1991). *The Vietnamese response to French intervention, 1862–1874*. Praeger.
- [17] Miller, Robert Hopkins (1990). *The United States and Vietnam, 1787-1941*. DIANE Publishing.
- [18] Ngoc Nguyen Quang (2003). *The process of the history of Vietnam*, Education Publisher. Hanoi.
- [19] Pan, Stephen & Lyons, Dennis (1966). *Vietnam Crisis, The East Asian Research Institute*, Riverside. New York.
- [20] Quang Nguyen Phan & Dan Vo Xuan (2000). *Vietnam’s history from the origins to 1884*. Ho Chi Minh city publisher.
- [21] Quoc Su quan trieu Nguyen (2001). *Dai Nam thuc luc*. Vol.1. Education Publisher. Hanoi.
- [22] Quoc Su quan trieu Nguyen (The Nguyen Dynasty’s Institute for National History) (2001). *Dai Nam thuc luc*. Vol.2. Education Publisher. Hanoi.
- [23] Quoc Su quan trieu Nguyen (2001). *Dai Nam thuc luc*. Vol.3. Education Publisher. Hanoi.
- [24] Quoc Su quan trieu Nguyen (2001). *Dai Nam thuc luc*. Vol.4. Education Publisher. Hanoi.
- [25] Quoc Su quan trieu Nguyen (2010). *Minh Mang chinh yeu*. Thuan Hoa Publisher. Hue.
- [26] Quynh Truong Huu, Doan Phan Dai, Minh Nguyen Canh (2000). *The outline of History of Vietnam*. Vol. 1. Education Publisher. Hanoi.
- [27] Roberts, Edmund (1837). *Embassy to the Eastern Courts of Cochinchina, Siam, and Muscat, in the U.S. Sloop-of-War Peacock, David Geisinger, Commander, During the Years 1832-3-4*. New York: Harper & Brothers.
- [28] Ruschenberger, W.S.W. (1838). *A Voyage Round the World; Including An Embassy to Muscat and Siam, in 1835, 1836, and 1837*. Philadelphia: Carey, Lea, & Blanchard.
- [29] Shreiner, Alfred (1905). *A brief of Dai Nam*. Sai Gon.
- [30] Son Pham Van (1983). *Complete history of Vietnamese*. Japan.
- [31] Thuan Cao Huy (1988). *Catholicism and colonialism in Vietnam*. Paris university.
- [32] Wynn Wilcox (2010). *Vietnam and the West: New Approaches*. SEAP Publications
- [33] Xuan Nguyen Dac (2008). *Constitution of the United States vessel opening French colonial war to conquer Vietnam Nguyen Dynasty*. Hà Nội.
- [34] *The Colonial Moment The Making of French Indochina, 1958-1897*, available at <http://www.ucpress.edu/content/chapters/10448.ch01.pdf>

Density Functional Theory studies of Hg and Pb ions Binding with Chitin and Chitosan

Nghiên cứu sự liên kết của Chitin và Chitosan với ion Hg và Pb bằng phương pháp phiếm hàm mật độ

Thi Hai Anh Mai,^a Thi Chinh Ngo,^b Duy Quang Dao,^{b*}

^aFaculty of Agriculture and Forestry, Tay Nguyen University, Vietnam

Khoa Nông Lâm nghiệp, Đại học Tây Nguyên, Việt Nam

^bInstitute of Research and Development, Duy Tan University, Vietnam

Viện Nghiên cứu và Phát triển, Trường Đại học Duy Tân, Việt Nam

(Ngày nhận bài: 30/01/2018, ngày phản biện xong: 22/03/2018, ngày chấp nhận đăng: 28/03/2018)

Abstract

Density functional theory (DFT) studies contributed to analyzing the interaction between chitin and chitosan with Hg(I), Hg(II) and Pb(I), Pb(II) ions. All DFT calculations were performed at M06-2X/LanL2DZ level of theory using N-acetylglucosamine and glucosamine monomers as models of chitin and chitosan, respectively. Geometries of all complexes were optimized, as well as the enthalpies and the Gibbs free energies of interactions were calculated. The obtained results suggest that Hg(I) and Pb(I) cations tend to bind to glucosamine at O4/N5 positions with the best stability, while these cations prefer the O3/O4 positions in the case of binding to N-acetylglucosamine. The most stable binding positions of these two molecules with Hg(II) and Pb(II) cations are all at O3/O4 molecules. Moreover, the Pb(I) complexes are more stable than the Hg(I) ones, whereas the Pb(II) complexes are less stable than the Hg(II) ones. These results are in good agreement with reported experimental data.

Keywords: Glucosamine; N-acetylglucosamine; interaction; DFT; mercury, lead.

Tóm tắt

Tương tác của chitin và chitosan với các ion Hg(I), Hg(II) và Pb(I), Pb(II) được nghiên cứu bằng lý thuyết phiếm hàm mật độ (DFT). Tất cả các tính toán DFT được thực hiện ở mức lý thuyết M06-2X/LanL2DZ sử dụng cấu trúc monomer N-acetylglucosamine và glucosamine như là mô hình của chitin và chitosan. Cấu trúc hình học của các phức tạo thành được tối ưu, cũng như năng lượng Gibbs tự do và enthalpy tương tác cũng được tính toán. Kết quả thu được dự đoán rằng các cation Hg(I) và Pb(I) có xu hướng kết nối với glucosamine tại vị trí O4/N5 với độ ổn định cao nhất, trong khi các cations này ưu tiên kết hợp với N-acetylglucosamine ở vị trí O3/O4. Cả hai hợp chất này đều kết hợp với cation Hg(II) và Pb(II) ở vị trí O3/O4. Ngoài ra, các phức Pb(I) thì ổn định hơn các phức Hg(I), trong khi các phức Pb(II) thì kém ổn định hơn các phức Hg(II). Kết quả tính toán này hoàn toàn tương thích với các kết quả thu được từ thực nghiệm.

Từ khóa: Glucosamine; N-acetylglucosamine; tương tác; DFT; chì, thủy ngân

1. Introduction

Nowadays, a huge amount of heavy metals in untreated wastewater is generally derived

from a variety of industrial activities such as mining, power plants, plating facilities, electrical equipment manufacturing, etc. This

* Corresponding author: daoduyquang@gmail.com

emission into our nature contributes to one of main environmental concerns.[1] Among the treatment approaches, chitin and chitosan have been widely studied and applied as effective low-cost biosorbents. Chitin consists in a high molecular weight linear polymer of 2-acetamido-2-deoxy-D-glucopyranose units linked together by 1,4-glycosidic bonds, while chitosan is the N-deacetylated product of chitin.[2] Chitosan and chitin are able to form stable complexes with a wide range of metal ions such as Ni(II), Cu(II), Cr(III), Cd(II), Hg(II), Pb(I), due to the presence of amino and hydroxyl groups on their structure which can act as chelation sites. Moreover, the formation of metal-chitosan/chitin complexes may involve in different mechanisms (chelation versus electrostatic attraction), depending on solution composition, pH and speciation of the metal ions.[3]

Several derivatives of chitosan have been experimentally studied as potential adsorbents of Hg(II) and Pb(II) ions in the removal of the metal ions from industrial effluents.[3, 4] For example, Hg(II) ions could be selectively separated from Cu(II), Pb(II), Cd(II), Zn(II), Ca(II) and Mg(II) by using modified magnetic chitosan with Schiff's base cross-linker.[5] A maximum Hg(II) adsorption capacity of 1127.1 (mg Hg(II)/g chitosan) is recorded using chitosan particles. [1] Chitosan-coated cotton fiber via a Schiff-base bond and a C–N single bond can selectively adsorb Hg(II) from binary ion systems in the presence of the coexistent ions Pb(II), Cu(II), Ni(II), Cd(II), Zn(II), Co(II), Mn(II) and Ag(I).[6] Chitosan functionalized by generation 1.0–3.0 of amino-terminated hyperbranched polyamidoamine polymers is also used to removal Hg(II).[7]

Moreover, Rangel-Mendez *et al* report that the selectivity of chitosan for cadmium, copper, and lead in both reactive and clarified water is sorted as follows: Cu(II) > Cd(II) > Pb(II). [8] The adsorption capacities of Pb(II) ions

from aqueous solution onto chitosan, chitosan-glutaraldehyde and chitosan-alginate beads are 34.98, 14.24 and 60.27 mg/g, respectively.[9] Citralidene chitosan, prepared by condensation of citral and chitosan, is also used to remove Hg(II) and Pb(II) contained in water. As a result, maximum sorption capacity was found to be 250 mg g⁻¹ for Pb(II) and 333.33 mg/g for Hg(II).[10] This means that the adsorption of Hg(II) is better than the one of Pb(II).

It can be seen that despite the importance of interaction of metal ions with chitosan and its derivatives, only a few computational studies dealing with the binding of metal ions (*i.e.* mercury and lead cations) with chitosan are found in the literature. Density functional theory (DFT) at B3LYP/LanL2DZ level of theory have been showed as a helpful method to investigate the interaction between chitosan and its derivatives with Pb(II) cation.[11] It is found that the most stable complex is obtained at O3/O4 position (Figure 1).

Thus, the goal of this work is to give more insight into the mechanism of Pb/Hg-chitosan/chitin monomer interactions. All possible binding configurations between Hg(I)/Hg(II) and Pb(I)/Pb(II) cations with glucosamine and N-acetylglucosamine were evaluated in detail (Figure 1). Geometries of complexes were optimized at DFT/M06-2X/LanL2DZ level of theory, as well as enthalpies and Gibbs energies were also calculated.

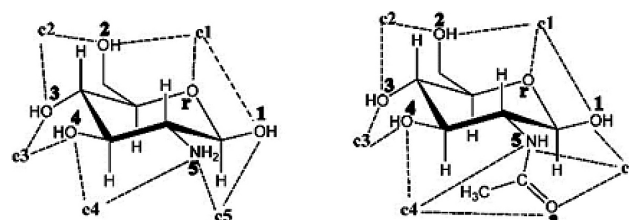


Fig. 1: Labelling scheme for different configurations studied for the complexes between Hg and Pb cations with glucosamine (left) or N-acetylglucosamine (right)

2. Theoretical and computational methods

All computations were performed using the Gaussian 09 Rev E.01 program.[12] Geometry optimizations and vibrational frequency calculations were conducted using M06-2X method [13] coupled with LanL2DZ basis set.

The interaction enthalpies (H_{int}) and Gibbs free energies (G_{int}) at 298.15K for the complexes between the metal ions and the glucosamine or the N-acetylglucosamine compounds were obtained as follows:

$$H_{\text{int}} = H_{M^{n+}\text{-compound}} - H_{M^{n+}} - H_{\text{compound}} \quad (1)$$

$$G_{\text{int}} = G_{M^{n+}\text{-compound}} - G_{M^{n+}} - G_{\text{compound}} \quad (2)$$

where $H_{M^{n+}\text{-compound}}$, $G_{M^{n+}\text{-compound}}$ are respectively the enthalpy and Gibbs energy at $T = 298.15$ K for the complex between a metal ion ($M = \text{Hg}$ or Pb , and $n = 1$ or 2) and glucosamine or N-acetylglucosamine, and $H_{M^{n+}}$, H_{compound} , and $G_{M^{n+}}$, G_{compound} are the total enthalpies and Gibbs energy at $T = 298.15$ K for the separated fragments.

3. Results and discussion

3.1. Optimized structure of glucosamine and N-acetylglucosamine

Figure 2 shows the views of geometrical structures of glucosamine and N-acetylglucosamine optimized at M06-2X/LanL2DZ level of theory in the gas phase.

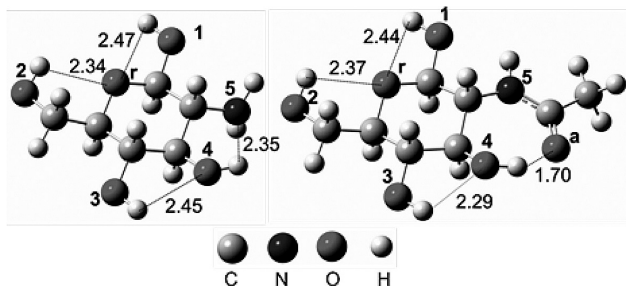


Fig. 2: Optimized structures of glucosamine (left) and N-acetylglucosamine (right) calculated at M06-2X/LanL2DZ, (distances in unit)

Generally, some intramolecular hydrogen bonds could be established in the structures of the studied monomers. In principle, a hydrogen bond

consists in an attractive force arising between a *donor* covalent pair $X-H$ in which H atom is bound to a more electronegative atom X, with neighboring electronegative ion or molecule, A, which must possess a lone pair of electron in order to form a hydrogen bond.[14]

In the studied structures, the hydrogen bonds could be formed between H atoms of hydroxyl groups $-OH$ with the O atoms of the another ones, or with N atom of the amine group $-NH_2$. As can be observed in **Figure 2**, The distances between $O-H \cdots O-H$ of N-acetylglucosamine and glucosamine are about 2.29 and 2.47 Å, the one of $O-H \cdots O$ is about 2.34 to 2.47 Å. The existence of several intramolecular hydrogen bonds allows to stabilize the molecular structures of the monomers.

Table 1: Natural bond orbital (NBO) analysis of some selected interactions for glucosamine and N-acetylglucosamine

Donor NBO (i)	Acceptor NBO (j)	E(2), kcal/mol
<i>Glucosamine</i>		
LP(1) N5	$\sigma^*(1)$ O4-H	2.6
<i>N-acetylglucosamine</i>		
LP(1) Oa	$\sigma^*(1)$ O4-H	8.04
LP(2) Oa	$\sigma^*(1)$ O4-H	18.57

In order to confirm the evidence for hydrogen bonds, natural bond orbital (NBO) analysis has been investigated at the same level of theory. For glucosamine molecule, electron densities donation from the first lone pair of electron on N5 atom, LP(1) N5, to unoccupied σ orbital on O4-H bond, $\sigma^*(1)$ O4-H, is observed at stabilization energy of 2.6 kcal/mol. Bond length of $N5 \cdots H-O4$ is equal to 2.35 Å. Moreover, transfer of electron densities from the first and the second lone pairs of electron on Oa atom, LP(1) Oa and LP(2) Oa, to unoccupied σ orbital on O4-H bond, $\sigma^*(1)$ O4-H, is also stabilized at energy of 8.04 and 18.57 kcal/mol, respectively. The bond distance of $Oa \cdots H-O4$ is of 1.70 Å (**Figure 1**).

These results allow confirming the existence of hydrogen bonds $N5 \cdots H-O4$ and $Oa \cdots H-O4$ in the structure of glucosamine and N-acetylglucosamine, respectively.

3.2. Optimized geometries of complexes

As mentioned in **Figure 1**, the metal ions can bind to glucosamine and N-acetylglucosamine by 5 interaction configurations, namely from c1 to c5, in which the metal cation binds to O and N atoms.

For each of five interaction configurations, **Tables 2** and **3** show selected geometric parameters between these two chitosan monomers and metal ions Hg(I)/Pb(I) and Hg(II)/Pb(II) respectively and bound hetero-atoms (i.e. O and N atoms). **Tables 4** and **5** present the respective enthalpies and Gibbs free energies at $T = 298.15K$ of all stable complexes. Moreover, **Figures 2** and **3** display the structure of the most stable complexes

of mono- and divalent cations with glucosamine and N-acetylglucosamine, respectively.

As shown on **Table 2**, monovalent Hg(I) cation interacts with glucosamine monomer with distances varied from 2.42 to 2.55 Å, while Pb(I) cation interacts with the monomer with distances from 2.35 to 2.47 Å. Similarly, Hg(I) cation binds with N-acetylglucosamine with distances from 2.32 to 2.52 Å, while the distances of Pb(I) ion with the binding sites alter from 2.09 to 2.45 Å.

Furthermore, the lengths between Hg(II) cations and the binding sites of glucosamine fluctuate between 2.15 and 2.30 Å, while the ones in case of N-acetylglucosamine are 2.11–2.37 Å. And Pb(II) cations bind to the interacting sites of glucosamine by distances changing from 2.14 to 2.37 Å, and to the ones of N-acetylglucosamine from 1.99 to 2.31 Å.

Table 2: Atomic distances (Å) for complexes between Hg(I) and Pb(I), and glucosamine or N-acetylglucosamine molecules

Complex	Ion	Glucosamine				N-acetylglucosamine			
		Atom	Distance	Atom	Distance	Atom	Distance	Atom	Distance
c1	Hg	r	2.44	2	2.55	r	2.47	2	2.52
	Pb	r	2.38	2	2.47	r	2.39	2	2.45
c2	Hg	2	2.46	3	2.45	2	2.46	3	2.43
	Pb	2	2.35	3	2.40	2	2.37	3	2.37
c3	Hg	3	2.43	4	2.42	3	2.44	4	2.37
	Pb	3	2.37	4	2.37	3	2.38	4	2.30
c4	Hg	4	2.46	5	2.51	4	2.47	a	2.32
	Pb	4	2.39	5	2.46	4	2.31	a	2.09
c5	Hg	1	2.53	5	2.48	1	2.52	a	2.32
	Pb	1	2.43	5	2.43	1	2.44	a	2.22

Table 3: Atomic distances (Å) for complexes between Hg(II) and Pb(II), and glucosamine or N-acetylglucosamine molecules

Complex	Ion	Glucosamine				N-acetylglucosamine			
		Atom	Distance	Atom	Distance	Atom	Distance	Atom	Distance
c1	Hg	r	2.29	2	2.27	r	2.33	2	2.23
	Pb	r	2.21	2	2.33	r	2.23	2	2.31
c2	Hg	2	2.26	3	2.22	2	2.30	3	2.11
	Pb	2	2.24	3	2.14	2	2.31	3	1.99
c3	Hg	3	2.30	4	2.15	3	2.24	4	2.16
	Pb	3	2.16	4	2.22	3	2.21	4	2.10
c4	Hg	4	2.24	5	2.30	4	2.24	a	2.37
	Pb	4	2.19	5	2.37	4	2.21	a	2.34
c5	Hg	1	2.29	5	2.26	1	2.26	a	2.14
	Pb	1	2.24	5	2.33	1	2.25	a	2.03

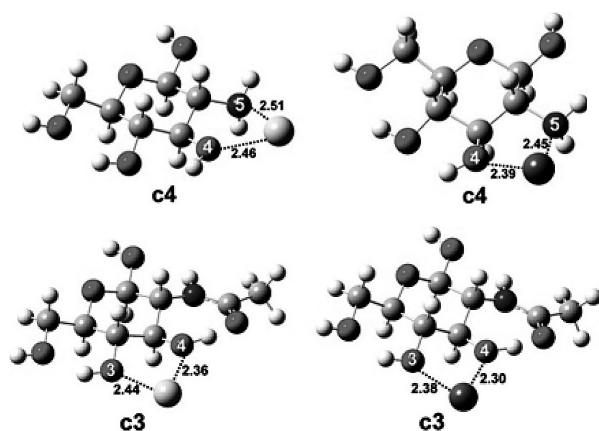


Fig. 3: The most stable configurations optimized for the interaction of Hg(I), left, and Pb(I), right, cations with glucosamine (A) or with N-acetylglucosamine (B). Bond distances are shown in angstroms (Å), 1 Å = 0.1 nm.

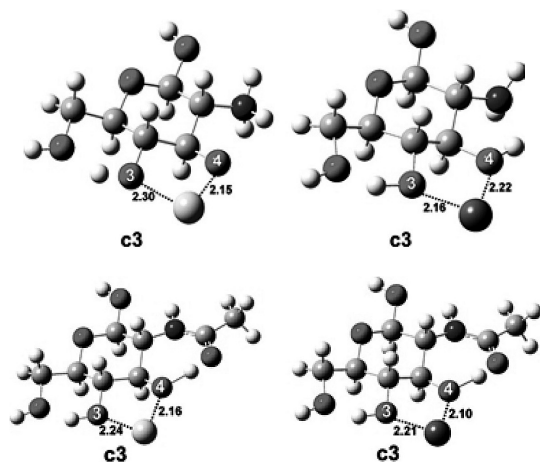


Fig. 4: The most stable configurations optimized for the interaction of Hg(II), left, and Pb(II), right, cations with glucosamine (A) or with N-acetylglucosamine (B). Bond distances are shown in angstroms (Å), 1 Å = 0.1 nm.

Table 4 exhibits the enthalpies and the Gibbs free energies of interaction between the monovalent cations with glucosamine and N-acetylglucosamine.

Generally, the formation of all complexes should be favored in terms of thermodynamic, and their formation reactions are all exergonic. Indeed, the interaction enthalpies (H_{int}) of Hg(I)-glucosamine complexes are from -242.0 to -283.1 kJ·mol⁻¹, and the ones of Hg(I)-N-acetylglucosamine complexes are from -241.6 to -304.2 kJ·mol⁻¹. Besides, the H_{int} values of Pb(I)-glucosamine vary from -275.5 to -315.2 kJ·mol⁻¹, and the ones of Pb(I)-N-acetylglucosamine are from -240.6 to -342.0 kJ·mol⁻¹. Similarly, the interaction Gibbs energies (G_{int}) of Hg(I)-glucosamine complexes change from -207.6 to -247.5 kJ·mol⁻¹, and the ones of Hg(I)-N-acetylglucosamine are about -205.9 and -265.7 kJ·mol⁻¹. While the G_{int} values of Pb(I)-glucosamine complexes are about -239.8 to -278.3 kJ·mol⁻¹, the ones of Pb(I)-N-acetylglucosamine complexes vary from -199.3 to -303.0 kJ·mol⁻¹.

The obtained results resumed on Table 4 show that the most stable monovalent complexes with glucosamine are established at c4 interaction configuration, while the most

stable ones with N-acetylglucosamine are given at **c3** configuration. Moreover, it can be deduced from the H_{int} and G_{int} values that the monovalent

complexes with Pb(I) are more stable than the ones with Hg(I) cation.

Table 4: Enthalpies and Gibbs free energies of interaction (kJ mol^{-1}) for Hg(I) and Pb(I) in complexes with glucosamine or N-acetylglucosamine. Bold is used to denote the most stable configurations.

Complex	Metal	Glucosamine		N-acetylglucosamine	
		$H_{int}/\text{kJ} \cdot \text{mol}^{-1}$	$G_{int}/\text{kJ} \cdot \text{mol}^{-1}$	$H_{int}/\text{kJ} \cdot \text{mol}^{-1}$	$G_{int}/\text{kJ} \cdot \text{mol}^{-1}$
c1	Hg	-269.6	-237.2	-241.6	-208.5
	Pb	-305.9	-271.9	-277.0	-243.3
c2	Hg	-242.0	-207.6	-241.3	-205.9
	Pb	-275.5	-239.8	-276.0	-238.6
c3	Hg	-282.6	-246.7	-304.2	-265.7
	Pb	-312.9	-276.4	-342.0	-303.0
c4	Hg	-283.1	-247.5	-272.2	-240.4
	Pb	-315.2	-278.3	-240.6	-199.3
c5	Hg	-268.8	-235.1	-264.5	-230.7
	Pb	-297.1	-262.4	-305.9	-270.2

Table 5: Enthalpies and Gibbs free energies of interaction (kJ mol^{-1}) for Hg(II) and Pb(II) in complexes with glucosamine or N-acetylglucosamine. Bold is used to denote the most stable configurations.

Complex	Metal	Glucosamine		N-acetylglucosamine	
		$H_{int}/\text{kJ} \cdot \text{mol}^{-1}$	$G_{int}/\text{kJ} \cdot \text{mol}^{-1}$	$H_{int}/\text{kJ} \cdot \text{mol}^{-1}$	$G_{int}/\text{kJ} \cdot \text{mol}^{-1}$
c1	Hg	-807.4	-768.2	-811.9	-770.4
	Pb	-699.8	-661.2	-657.4	-619.8
c2	Hg	-708.4	-670.8	-851.9	-812.9
	Pb	-625.1	-588.1	-784.8	-743.5
c3	Hg	-863.8	-823.8	-873.4	-828.6
	Pb	-706.6	-664.3	-806.1	-761.0
c4	Hg	-784.3	-745.0	-763.6	-722.3
	Pb	-664.7	-625.7	-654.8	-614.4
c5	Hg	-752.7	-715.0	-779.7	-744.9
	Pb	-627.6	-589.3	-718.2	-678.4

The same results are acquired in cases of the divalent complexes, i.e. Hg(II) and Pb(II) cations, and glucosamine or N-acetylglucosamine (**Table 5**). However, it can be seen from **Table 5** that the most stable complexes with both of the compounds are obtained at **c3** position. Also comparing the H_{int} and G_{int} values reveals that the interaction of Hg(II) cation with the compounds is stronger than the one of Pb(II) cation. These

results are in good agreement with the one obtained by experiments.[10]

In fact, the enthalpies of interaction at **c3** positions of Hg(II)-glucosamine and Hg(II)-N-acetylglucosamine are -863.8 and -873.4 $\text{kJ} \cdot \text{mol}^{-1}$, respectively. And the Gibbs energies of the same complexes are -823.8 and -828.6 $\text{kJ} \cdot \text{mol}^{-1}$, respectively. Similarly, the H_{int} of interaction for Pb(II)-glucosamine and Pb(II)-

N-acetylglucosamine for **c3** configuration are equal to -706.6 and -806.1 kJ·mol⁻¹, respectively, and the G_{int} of interaction of the same complexes are -664.3 and -761.0 kJ·mol⁻¹, respectively. The structure of the most stable complexes for Hg(I)/Pb(I) and Hg(II)/Pb(II) cations with glucosamine and N-acetylglucosamine, respectively are depicted in **Figures 3 and 4**.

4. Conclusions

The interactions of Hg(I)/Hg(II) and Pb(I)/Pb(II) cations with glucosamine and N-acetylglucosamine were studied using density functional theory approaches. The optimized geometries, interaction enthalpies and Gibbs energies of interaction of all possible complexes were calculated by employing M06-2X/LanL2DZ level of theory. It is found that (i) the most stable complexes of Hg(I) and Pb(I) with glucosamine are obtained with **c4** interaction configuration (i.e. O4/N5 binding sites), whereas the ones with N-acetylglucosamine are found at **c3** configurations (i.e. O3/O4); (ii) the most stable complexes of Hg(II) and Pb(II) with glucosamine and with N-acetylglucosamine are all found at **c3** (O3/O4) configuration; (iii) finally, the formation of the complexes with Pb(I) are more favorable than the ones with Hg(I), but conversely, the complexes with Hg(II) are more stable than the ones with Pb(II), this observation agrees with the experimental data.

Acknowledgements

This research is funded by Vietnam National Foundation for Science and Technology Development (NAFOSTED) under grant number 104.06-2015.09.

References

- [1]. Shafaei, A., F.Z. Ashtiani, and T. Kaghazchi, *Equilibrium studies of the sorption of Hg(II) ions onto chitosan*. Chemical Engineering Journal, 2007. **133**(1-3): p. 311-316.
- [2]. Varma, A.J., S.V. Deshpande, and J.F. Kennedy, *Metal complexation by chitosan and its derivatives: A review*. Carbohydrate Polymers, 2004. **55**: p. 77-93.
- [3]. Vieira, R.S. and M.M. Beppu, *Dynamic and static adsorption and desorption of Hg(II) ions on chitosan membranes and spheres*. Water Res, 2006. **40**(8): p. 1726-34.
- [4]. Miretzky, P. and A.F. Cirelli, *Hg(II) removal from water by chitosan and chitosan derivatives: a review*. J Hazard Mater, 2009. **167**(1-3): p. 10-23.
- [5]. Donia, A.M., A.A. Atia, and K.Z. Elwakeel, *Selective separation of mercury(II) using magnetic chitosan resin modified with Schiff's base derived from thiourea and glutaraldehyde*. J Hazard Mater, 2008. **151**(2-3): p. 372-9.
- [6]. Qu, R., et al., *Removal and recovery of Hg(II) from aqueous solution using chitosan-coated cotton fibers*. J Hazard Mater, 2009. **167**(1-3): p. 717-27.
- [7]. Ma, F., et al., *Adsorption behaviors of Hg(II) on chitosan functionalized by amino-terminated hyperbranched polyamidoamine polymers*. J Hazard Mater, 2009. **172**(2-3): p. 792-801.
- [8]. Rangel-Mendez, J.R., et al., *Chitosan selectivity for removing cadmium (II), copper (II), and lead (II) from aqueous phase: pH and organic matter effect*. J Hazard Mater, 2009. **162**(1): p. 503-11.
- [9]. Ngah, W.S.W. and S. Fatinathan, *Pb(II) biosorption using chitosan and chitosan derivatives beads: Equilibrium, ion exchange and mechanism studies*. Journal of Environmental Sciences, 2010. **22**(3): p. 338-346.
- [10]. Alikutty, P., et al., *Studies on the sorption capacity for Pb(II) and Hg(II) of citralidene chitosan*. Polymer Bulletin, 2014. **71**(8): p. 1919-1932.
- [11]. Hassan, B., K. Muraleedharan, and V.M. Abdul Mujeeb, *Density functional theory studies of Pb (II) interaction with chitosan and its derivatives*. Int J Biol Macromol, 2015. **74**: p. 483-8.
- [12]. Frisch, M.J., et al., *Gaussian 09 E.01*. 2015, Gaussian, Inc. Wallingford, CT, USA.
- [13]. Zhao, Y. and D.G. Truhlar, *The M06 suite of density functionals for main group thermochemistry, thermochemical kinetics, noncovalent interactions, excited states, and transition elements: Two new functionals and systematic testing of four M06-class functionals and 12 other function*. Theoretical Chemistry Accounts, 2008. **120**: p. 215-241.
- [14]. George A., J. and S. Wolfram, *Hydrogen Bonding in Biological Structure*. 1 ed. 1991: Springer-Verlag Berlin Heidelberg. 569.

Evaluation of the SRAC model for analyzing the control rod worths of the DNRR

Đánh giá mô hình tính toán SRAC trong phân tích
giá trị thanh điều khiển lò phản ứng hạt nhân Đà Lạt

Phan Thi Thuy Giang^{a,b,*}, Do Quang Binh^c, Tran Hoai Nam^a

^a*Institute of Fundamental and Applied Sciences, Duy Tan University, Da Nang*

^b*Department of Nuclear Physics, Faculty of Physics and Engineering Physics, VNUHCM-University of Science, HCMC*

^c*Ho Chi Minh City University of Technology and Education, HCMC*

(Ngày nhận bài: 07/11/2017, ngày phản biện xong: 29/12/2017, ngày chấp nhận đăng: 20/03/2018)

Abstract

The Dalat Nuclear Research Reactor (DNRR) is a 500 kW pool-type research reactor located in Dalat, Vietnam. It was upgraded from a 250 kW TRIGA MARK II reactor in 1960s. The first criticality was achieved on Nov 1st, 1983. The DNRR operates about 1300 hours per year for the radioisotope production, neutron activation and research goals. This study deals with the evaluation of the control rod worths of the DNRR using SRAC code system and the ENDF/B-VII.0 nuclear data library. The results are compared with the experimental data. A good agreement is found with the maximum deviation of the control rod worths about 14%. This indicates the accuracy of the analysis model and possible application for further neutronics analysis of the DNRR.

Keywords: DNRR, VVR-M2, SRAC, control rod worth.

Tóm tắt

Lò phản ứng hạt nhân nghiên cứu Đà Lạt (DNRR) công suất 500 kW đặt ở thành phố Đà Lạt, Việt Nam. Lò được nâng cấp từ lò TRIGA MARK II công suất 250 kW được xây dựng vào những năm 1960, đạt tới hạn lần đầu ngày 01/11/1983. Hiện nay lò DNRR hoạt động mỗi năm khoảng 1300 giờ với mục đích chính: sản xuất đồng vị, kích hoạt neutron và nghiên cứu. Bài báo này trình bày các đánh giá về giá trị thanh điều khiển của lò Đà Lạt sử dụng chương trình SRAC và thư viện số liệu hạt nhân ENDF/B-VII.0. Kết quả được so sánh với số liệu thực nghiệm cho thấy sự phù hợp tốt với sai khác lớn nhất khoảng 14%. Điều này khẳng định tính chính xác của các mô hình tính toán và khả năng áp dụng cho các phân tích neutronic xa hơn cho lò Đà Lạt.

Từ khóa: Lò phản ứng hạt nhân nghiên cứu Đà Lạt, VVR-M2, SRAC, giá trị thanh điều khiển.

1. Introduction

Controlling system is one of the key components of a nuclear reactor since it is mainly responsible for the reactor safety. The control rods (CRs) are inserted into the core to maintain

the power level at desired states. They are made by materials such as boron, hafnium, cadmium, indium, silver, etc. That have a large thermal neutron absorption cross-section. When the CRs are inserted into or withdrawn from the core lead to the decrease or increase of the reactivity.

Studying on the control rod worth under different operation conditions and core configurations is a challenge in developing neutronics analysis methods. Because of the strong thermal neutron absorption characteristic of the control rods' material, the thermal neutron flux varies rapidly with the control rods' positions. It needs special methods to treat the diffusion theory in the thermal research reactor such as the Monte Carlo or the approximation methods. The SRAC code system, an open code on the approximation method that can solve a doubly heterogeneous system by cell calculations [1] with much less calculation time in comparison with the Monte Carlo method is currently chosen.

This study presents the calculation results of the control rod worths of the DNRR reactor using the SRAC code system and the ENDF/B-VII.0 nuclear data library [2]. The calculations were performed to evaluate these parameters at the startup conditions [3]. This work was done to set a benchmark model for the burn-up and fuel management analysis of the DNRR.

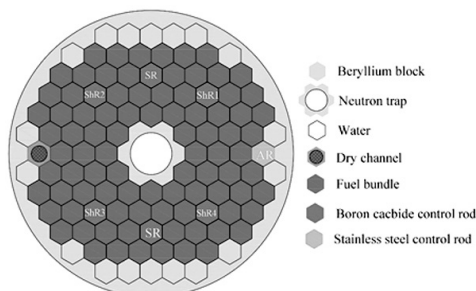


Figure. 1 Configuration of the DNRR core with 88 fuel assemblies.

2. Description of the DNRR

The DNRR was reconstructed and upgraded to 500 kW in 1980s. The reactor is loaded with the Russian VVR-M2 fuel type. Table 1 shows the detail characteristics of the DNRR, control rods and fuel bundles. The reactor core has a radius of 442 mm and height of 600 mm surrounded by the graphite reflector thickness of 305 mm.

Table 1. Specification of the DNRR

Reactor type	Pool type
Nominal thermal power (kW)	500
Coolant and moderator	Light water
Core cooling mechanism	Natural convection
Reflector	Graphite, Beryllium
Horizontal beam-ports	4 (1 tangential, 3 radials)
Active core height (mm)	600
Core equivalent diameter (mm)	442
Graphite reflector height (mm)	560
Graphite reflector thickness (mm)	30.5
Number of control rods	7 (2 SR, 4 ShR, 1 AR)
Material of SR, ShR	B ₄ C
Material of AR	Stainless steel
Fuel type	VVR-M2
Fuel meat	U-Al alloy
Uranium enrichment (wt%)	36
Average ²³⁵ U (g)	40.2
Fuel pitch (mm)	35
Fuel thickness (mm)	0.7
Aluminum cladding (mm)	0.9
Tube gap (mm)	2.5-3

In the present work, the core is loaded with 121 hexagonal cells including 88 fuel bundles, 18 beryllium blocks, 7 control rods, 1 dry channel and 7 cells of neutron trap. The VVR-M2 fuel bundle is the highly enriched uranium type, ²³⁵U enrichment of 36 wt%, made of aluminum-uranium alloy cladded in aluminum. The only automatic regulating rod (AR) is made of stainless steel. The safety rods and shim rods (SRs and ShRs) are made of boron carbide (B₄C). All the control rods are 650 mm in length. The neutron trap is a water cylinder with 65 mm in diameter surrounded by six beryllium blocks (Fig. 1).

3. Measurement of the control rod worth

The calculated cases simulating explicitly the experiment data of the AR control rod worth

were carried out by the positive period method in 1984 [3]. In this method, the criticality of the DNRR was established with the full insertion of the AR at a very low power to exclude the effects of temperature, power and xenon poisoning. Then the AR was withdrawn from the bottom to a new position to increase the reactivity and power level. Doubling times measurement were carried out in conjunction with the inhour equation [4] to obtain the corresponding positive reactivity as follows:

$$\rho(\$) = \frac{1}{\beta_{eff}} \left[\frac{l}{l+T} + \frac{T}{l+T} \sum_{i=1}^6 \frac{\beta_i}{1+T \cdot \lambda_i} \right] \quad (1)$$

where, l is the prompt neutron generation time and T is the reactor period. λ_i and β_i are the decay constant and the fraction of the delayed neutrons of the i^{th} group, respectively. β_{eff} is the effective delayed neutrons fraction (the β_{eff} of the DNRR is 0.0081 [5]).

The criticality of the initial power level was restored for the next step by setting the new ShR positions when the AR position was preserved in the core. Iterating this process for each of the AR withdrawal positions, the integral reactivity was then obtained. These experiments showed the results within 7% of uncertainty.

Table 2. Comparison between the SRAC calculated control rod worth and the experimental data.

(a) ShR2=ShR3=65											
ShR1=ShR4	AR	$\Delta\rho_{CAL}$	$\Delta\rho_{EXP}$	ShR1, ShR4	AR	$\Delta\rho_{CAL}$	$\Delta\rho_{EXP}$	ShR1, ShR4	AR	$\Delta\rho_{CAL}$	$\Delta\rho_{EXP}$
36.8	65	0.522	0.593	36	65	0.511	0.529	35.8	65	0.507	0.555
37.5	40	0.32	0.414	36.8	40	0.315	0.361	36.7	40	0.312	0.397
39.2	25	0.127	0.169	38.1, 37.5	30	0.182	0.203	36.7	30	0.179	0.235
39.2	0	0	0	38.7	20	0.077	0.084	38.5, 38.3	20	0.077	0.112
				38.8	0	0	0	38.5, 38.3	0	0	0
(b) ShR1=ShR4=65											
ShR2=ShR3	AR	$\Delta\rho_{CAL}$	$\Delta\rho_{EXP}$	ShR2=ShR3	AR	$\Delta\rho_{CAL}$	$\Delta\rho_{EXP}$	ShR2, ShR3	AR	$\Delta\rho_{CAL}$	$\Delta\rho_{EXP}$
37.5	65	0.409	0.439	36.3	65	0.398	0.461	36.3	65	0.364	0.379
38	40	0.274	0.329	37	40	0.267	0.349	37.2	40	0.233	0.279
39.5	20	0.074	0.085	38.5	20	0.073	0.098	37.7	30	0.126	0.18
39.5	0	0	0	38.5	0	0	0	38.0, 39.0	20	0.073	0.082
								38.2, 39.5	0	0	0
(c) ShR1=ShR2=ShR3=ShR4											
ShR1234	AR	$\Delta\rho_{CAL}$	$\Delta\rho_{EXP}$	ShR1234	AR	$\Delta\rho_{CAL}$	$\Delta\rho_{EXP}$				
45	65	0.493	0.489	45	65	0.46	0.474				
45.7	40	0.319	0.322	45	40	0.288	0.326				
46.7	20	0.094	0.104	45	30	0.168	0.204				
47.2	0	0	0	45	20	0.074	0.092				
				45	0	0	0				

4. Calculation model

The SRAC code system is a neutronics code developed by Japan Atomic Energy Agency (JAEA). Two codes of the SRAC system have

been used in this work. The PIJ code is the collision probability method code used for the lattice calculations to prepare the macroscopic cross-sections of fuel cell, control rods and other

lattice cells. The cross-sections in the output files are collected into 7 energy groups (4 fast groups, 3 thermal groups). The CITATION code is a multi-dimensional diffusion code chosen for the full core calculations. The core of the DNRR is described as the hexagonal grids with each of which has a 35 mm of the minimal diameter. The whole core calculation of X-Y-Z system is composed by array of 37x37 cells of the X-Y dimensions. The Z dimension is split into a number of layers depending on material components.

5. Results and discussions

The k_{eff} was calculated by simulating the critical reactor with the accurate AR, ShRs, SRs positions in the experiment. When the AR was withdrawn at a certain position, the new k_{eff} was calculated. As a result, the differential and integral control rod worth ρ_i and ρ , respectively, are determined by:

$$\rho_i = \rho_0 - \rho_1 = \left(1 - \frac{1}{k_{eff0}}\right) - \left(1 - \frac{1}{k_{eff1}}\right) = \frac{1}{k_{eff1}} - \frac{1}{k_{eff0}} \tag{2}$$

$$\rho = \sum_i \rho_i \tag{3}$$

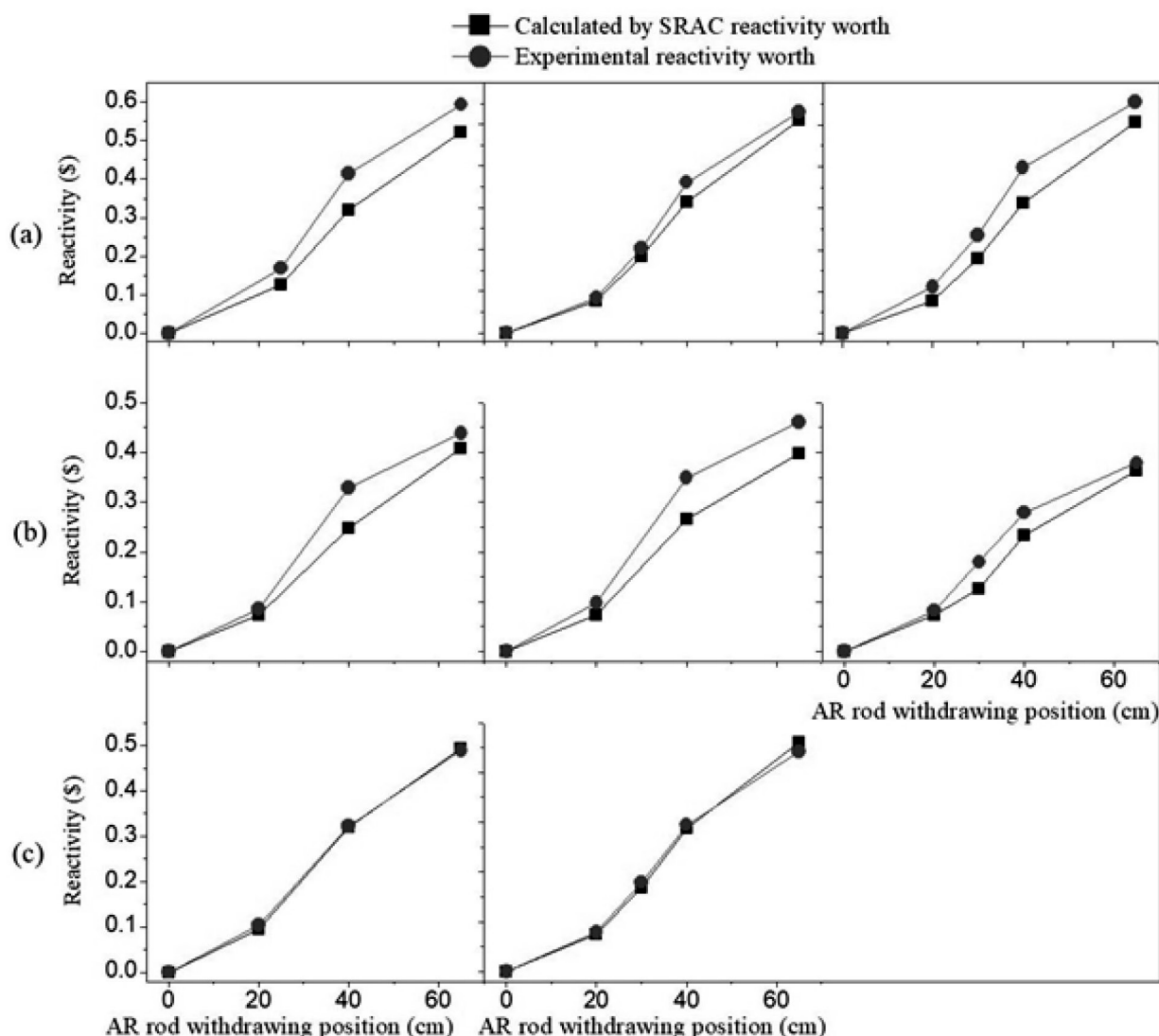


Figure. 2 SRAC calculations and experimental integral control rod worth for AR.

The values of the integral reactivities against the AR withdrawal position is shown in Fig. 2. It can be seen that, the integral control rod worth of the AR is about 0.5 \$. This value is rather small in comparison with the ShR or SR values. It's because the AR is made of stainless steel, which has smaller thermal neutron absorption cross-section than the ShR, SR made of boron carbide . The highest value is in the group (a) and the lowest one is in the group (b). That indicates explicitly the effect of the ShR1 and ShR4 on the AR integral characteristics. These ShRs were closer to the AR position than the rest of the control rods. Consequently, they absorbed thermal neutrons more than other control rods and caused a considerable reduction of the integral reactivity in the case (b) with the complete insertion of the ShR1,4.

The experimental values are used to determine the error of the calculation values. Most of the calculation results are slightly smaller than the experiment data. The maximum deviation of the integral reactivities is 14% in the case with the insertions of ShR1, 4 = 65 cm and ShR2, 3 from 36.3 cm to 38.5 cm. In particular, there is a small difference between the calculation and experimental values in the group (c). The points coincide together with less than 4% of uncertainty as shown in Fig. 2. These results demonstrate a good agreement of the analysis models in comparison with the experimental data.

6. Conclusions

The analysis model was suitable for the core configuration of 88 fuel bundles. The control rod

worth of the AR was about 0.5 \$. This value was approximately a quarter of the control rod worth of the ShR because of the disparate material components. The maximum deviation of the calculations was 14% in comparison with the experimental values. In the cases of all the ShRs at the same position in the reactor core, the values showed a good match with the measured data. The results showed that the calculation model was reliable and could be applied for further neutronics analysis of the DNRR.

Acknowledgements

This work was funded by National Foundation for Science and Technology Development (NAFOSTED), Vietnam under grant 103.04-2016.30.

References

- [1] K. Okumura, T. Kugo, K. Kaneko, K. Tsuchihashi, SRAC2006: A Comprehensive Neutronics Calculation Code System, 2006.
- [2] M. Chadwick, P. Obložinský, M. Herman, N. Greene, R. McKnight, D. Smith, P. Young, et al., Endf/b-vii.0: Next generation evaluated nuclear data library for nuclear science and technology, Nuclear Data Sheets 107, 2006, pp. 2931–3060.
- [3] D. H. Pham, Q. H. Ngo, H. L. Vu, K. M. Tran, Report startup of nuclear research reactor: Part 2-Physics startup for core configuration with a neutron trap, Technical Report, Nuclear Research Institute, 1984.
- [4] Z. Akcasu, G. S. Lellouche, L. M. Shotkin, Chapter 2 - point kinetic equations, in: *Mathematical Methods in Nuclear Reactor Dynamics*, Academic Press, 1971, pp. 48–87.
- [5] Safety Analysis Report for the Dalat Nuclear Research Reactor, Technical Report, Nuclear Research Institute, 2009.

A Liouville-type theorem for a parabolic system

Định lí kiểu Liouville cho hệ phương trình parabolic

Phan Quoc Hung^a, Nguyen Thai An^a, Nguyen Trung Hieu^a, Nguyen Thi Quynh^b

^a*Institute for Research and Development, Duy Tan University*

Viện Nghiên cứu và Phát triển Công nghệ cao, Trường Đại học Duy Tân

^b*Faculty of Fundamental Science, Hanoi University of Industry*

Khoa Khoa học Cơ bản, Trường Đại học Công nghiệp Hà Nội

(Received: 13 December 2017, Revised: 10 January 2018, Accepted: 20 March 2018)

Abstract

We study Liouville-type theorem for semilinear parabolic system of the form $u_t - \Delta u = u^p + \beta u^r v^{r+1}$, $v_t - \Delta v = v^p + \beta u^{r+1} v^r$ where $p = 2r + 1$, $r > 0$, $\beta > 0$. Very recently, Quittner [17] has established the optimal result in dimension $N \leq 2$, and partial results in higher dimensions under the range $p < N/(N - 2)$. Using the techniques of Gidas-Spruck and Bidaut-Véron, we partially improve the results of Quittner in dimensions $N \geq 3$.

Keywords: Liouville-type theorem, Parabolic system.

Tóm tắt

Chúng tôi chứng minh định lí kiểu Liouville cho hệ parabolic nửa tuyến tính $u_t - \Delta u = u^p + \beta u^r v^{r+1}$, $v_t - \Delta v = v^p + \beta u^{r+1} v^r$ trong đó $p = 2r + 1$, $r > 0$, $\beta > 0$. Gần đây, Quittner [17] đã thiết lập kết quả tối ưu cho trường hợp số chiều $N \leq 2$, và kết quả cho số chiều cao hơn với điều kiện $p \leq N/(N - 2)$. Sử dụng kĩ thuật của Gidas-Spruck và Bidaut-Véron, chúng tôi cải tiến kết quả của Quittner trong trường hợp số chiều $N \geq 3$.

Từ khóa: Định lí kiểu Liouville, Hệ parabolic.

1. Introduction

In this article, we study the semilinear parabolic system of the following form

$$\begin{cases} u_t - \Delta u = u^p + \beta u^r v^{r+1}, & (x, t) \in \Omega \times I \\ v_t - \Delta v = v^p + \beta u^{r+1} v^r, & (x, t) \in \Omega \times I, \end{cases} \quad (1)$$

where $p = 2r + 1$, $r > 0$, $\beta > 0$, Ω is a domain of \mathbb{R}^N , and I is an interval of \mathbb{R} .

This type of system can be used to describe heat propagations in a two-component combustible mixture [3, 9], in this case u and v represent the temperatures of the interacting components. In dynamics of biological groups

[6, 13], the system (1) models the interaction of two biological groups without self-limiting, where the diffusion terms reflect that the speed of the diffusion is slow. In addition, it can also be used to describe some models such as Bose-Einstein condensation [7], or chemical processes [11].

System (1) has been recently studied in various mathematical directions, such as the local and global existence [1, 14], the Hölder regularity [7], the symmetry property [16, 10], and the Liouville-type theorems [15, 17].

We recall that Liouville-type theorem is the nonexistence of solution of problem (1) in the entire space $\mathbb{R}^N \times \mathbb{R}$. In recent years, the Liouville property has been refined

considerably and emerged as one of the most powerful tools in the study of initial and boundary value problems for nonlinear PDEs, see the monograph [18].

The aim of this paper is to prove the Liouville property of the problem (1). Before the statement of main result, let us recall the following exponents:

$$p_S := \begin{cases} \frac{N+2}{N-2} & \text{if } N \geq 3, \\ \infty & \text{if } N = 1, 2, \end{cases} \quad (2)$$

$$p_B := \begin{cases} \frac{N(N+2)}{(N-1)^2} & \text{if } N \geq 2, \\ \infty & \text{if } N = 1. \end{cases} \quad (3)$$

We first recall its elliptic counterpart

$$\begin{cases} -\Delta u = u^p + \beta u^r v^{r+1}, & x \in \mathbb{R}^N \\ -\Delta v = v^p + \beta u^{r+1} v^r, & x \in \mathbb{R}^N. \end{cases} \quad (4)$$

System (4) arises in mathematical models for various phenomena in physics, such as nonlinear optics and Bose-Einstein condensation (see e.g. [2, 8, 20]). It is well known that the Liouville-type result for (4) plays an important role in the study of both elliptic and parabolic problems. The optimal Liouville-type theorem for (4) was completely proved in [19] (see also [12]) via moving plane techniques, under the optimal range $p < p_S$.

For the corresponding parabolic problem (1), the Liouville property is less understood. By adding up the two equations and using Young's inequality, one can easily reduce to a scalar parabolic inequality and deduce the Fujita-type result of problem (1), namely there is no positive solution in $\mathbb{R}^N \times \mathbb{R}_+$ if $1 < p \leq 1 + \frac{2}{N}$. Recently, the Liouville type theorem for (1) has been proved in [15] in dimension $N = 1$ and for radial solutions in any dimension, under additional assumption $\beta > -\frac{r}{3r+2}$. More recently, Quittner [17] has proved the optimal Liouville type theorem for (1) in dimensions $N \leq 2$ under optimal assumption $\beta > -1$. In dimension $N \geq 3$, Quittner [17] has also established Liouville type theorems under the condition $p < \frac{N}{N-2}$. The main tools in [17] are scaling and energy estimates. In this paper, we use a different approach to establish a Liouville-type theorem for problem (4) in a larger range of p . Our result is as follows.

Theorem 1.1. *Assume that $p < p_B$ and $\beta > 0$. Then the system (1) does not possess any nontrivial nonnegative classical solution in $\mathbb{R}^N \times \mathbb{R}$.*

Our tool for proof of Theorem 1.1 is based on Gidas-Spruck technique developed by Bidaut-Véron [4] (see also [5] for elliptic system), which consists of nonlinear integral estimates and the Bochner formula. This technique is completely different from that of [17]. We stress that $\frac{N}{N-2} < p_B$ when $N \geq 3$, and our result is a partial improvement of Quittner [17] in higher dimensions. Besides, our result can be seen as an application of the Gidas-Spruck technique to a parabolic system.

The rest of this paper is devoted to the proof of Theorem 1.1

2. Liouville-type theorems

We denote by \int the integral $\int_{B_1 \times (-1, 1)} dxdt$.

Lemma 2.1. *Assume that $p < p_B$ and $\beta > 0$. Let $0 \leq \varphi \in \mathcal{D}(B_1 \times (-1, 1))$ and (u, v) be positive solution of (1) in $B_1 \times (-1, 1)$. Denote*

$$\begin{aligned} I_1 &= \int \varphi u^{-2} |\nabla u|^4, \quad I_2 = \int \varphi v^{-2} |\nabla v|^4, \quad I = I_1 + I_2, \\ L_1 &= \int \varphi (u^p + \beta u^r v^{r+1})^2, \quad L_2 = \int \varphi (v^p + \beta u^{r+1} v^r)^2, \\ L &= L_1 + L_2. \end{aligned}$$

Then there holds

$$\begin{aligned} I + L &\leq C \int \varphi (|u_t| u^{-1} |\nabla u|^2 + |v_t| v^{-1} |\nabla v|^2 + u_t^2 + v_t^2) \\ &+ C \int |\nabla \varphi \cdot \nabla u| (u^p + u^r v^{r+1} + |u_t| + u^{-1} |\nabla u|^2) \\ &+ C \int |\nabla \varphi \cdot \nabla v| (v^p + u^{r+1} v^r + |v_t| + v^{-1} |\nabla v|^2) \\ &+ C \int |\Delta \varphi| (|\nabla u|^2 + |\nabla v|^2) + C \int |\varphi_t| (u^{p+1} + v^{p+1}), \quad (5) \end{aligned}$$

where $C = C(N, p, \beta)$.

Proof. Denoting

$$\begin{aligned} J_1 &= \int \varphi u^{-1} |\nabla u|^2 \Delta u, \quad J_2 = \int \varphi v^{-1} |\nabla v|^2 \Delta v, \quad J = J_1 + J_2, \\ K_1 &= \int \varphi (\Delta u)^2, \quad K_2 = \int \varphi (\Delta v)^2, \quad K = K_1 + K_2. \end{aligned}$$

Applying [18, Lemma 8.9] with $q = 0, -1 \neq k < 0$

$$\begin{aligned} &-\left(\frac{N-1}{N}k+1\right)kI_1 + \frac{N+2}{N}kJ_1 - \frac{N-1}{N}K_1 \\ &\leq \frac{1}{2} \int |\nabla u|^2 \Delta \varphi + \int (\Delta u - ku^{-1} |\nabla u|^2) \nabla u \cdot \nabla \varphi. \end{aligned}$$

Therefore,

$$\begin{aligned} &-\left(\frac{N-1}{N}k+1\right)kI + \frac{N+2}{N}kJ - \frac{N-1}{N}K \\ &\leq \frac{1}{2} \int (|\nabla u|^2 + |\nabla v|^2) \Delta \varphi + \int (\Delta u - ku^{-1} |\nabla u|^2) \nabla u \cdot \nabla \varphi \\ &\quad + \int (\Delta v - kv^{-1} |\nabla v|^2) \nabla v \cdot \nabla \varphi. \quad (6) \end{aligned}$$

We next estimate J . First, using the integration by parts, we have

$$\begin{aligned} \int \varphi |\nabla u|^2 u^{r-1} v^{r+1} &= \int \varphi v^{r+1} \nabla u \cdot \nabla \left(\frac{u^r}{r} \right) \\ &= -\frac{1}{r} \int \varphi u^r v^{r+1} \Delta u - \frac{r+1}{r} \int \varphi u^r v^r \nabla u \cdot \nabla v \\ &\quad - \frac{1}{r} \int u^r v^{r+1} \nabla \varphi \cdot \nabla u, \end{aligned} \tag{7}$$

$$\begin{aligned} \int \varphi |\nabla v|^2 u^{r+1} v^{r-1} &= \int \varphi u^{r+1} \nabla v \cdot \nabla \left(\frac{v^r}{r} \right) \\ &= -\frac{1}{r} \int \varphi u^{r+1} v^r \Delta v - \frac{r+1}{r} \int \varphi u^r v^r \nabla u \cdot \nabla v \\ &\quad - \frac{1}{r} \int u^{r+1} v^r \nabla \varphi \cdot \nabla v. \end{aligned} \tag{8}$$

Adding up (7)-(8) and using the Young inequality $2u^r v^r \nabla u \cdot \nabla v \leq |\nabla u|^2 u^{r-1} v^{r+1} + |\nabla v|^2 u^{r+1} v^{r-1}$, we obtain

$$\begin{aligned} \int \varphi (|\nabla u|^2 u^{r-1} v^{r+1} + |\nabla v|^2 u^{r+1} v^{r-1}) &\geq -\frac{1}{p} \int \varphi u^r v^{r+1} \Delta u \\ &\quad - \frac{1}{p} \int \varphi u^{r+1} v^r \Delta v - \frac{1}{p} \int (u^r v^{r+1} \nabla \varphi \cdot \nabla u + u^{r+1} v^r \nabla \varphi \cdot \nabla v). \end{aligned} \tag{9}$$

Next, integrating by parts, we have

$$\begin{aligned} \int \varphi u^{p-1} |\nabla u|^2 &= \int \varphi \nabla u \cdot \nabla \left(\frac{u^p}{p} \right) \\ &= -\frac{1}{p} \int (\varphi u^p \Delta u + u^p \nabla \varphi \cdot \nabla u), \end{aligned} \tag{10}$$

$$\begin{aligned} \int \varphi v^{p-1} |\nabla v|^2 &= \int v \nabla \varphi \cdot \nabla \left(\frac{v^p}{p} \right) \\ &= -\frac{1}{p} \int (\varphi v^p \Delta v + v^p \nabla \varphi \cdot \nabla v). \end{aligned} \tag{11}$$

Hence, it follows from (9)-(11) that,

$$\begin{aligned} -J &= \int \varphi u^{-1} |\nabla u|^2 (u^p + \beta u^r v^{r+1} - u_t) \\ &\quad + \int \varphi v^{-1} |\nabla v|^2 (v^p + \beta u^{r+1} v^r - v_t) \\ &\geq \frac{1}{p} \int \varphi ((u^p + \beta u^r v^{r+1})(-\Delta u) + (v^p + \beta u^{r+1} v^r)(-\Delta v)) \\ &\quad - C \int (\varphi |u_t| u^{-1} |\nabla u|^2 + \varphi |v_t| v^{-1} |\nabla v|^2) \\ &\quad - C \int ((u^p + u^r v^{r+1}) |\nabla \varphi \cdot \nabla u| + (v^p + u^{r+1} v^r) |\nabla \varphi \cdot \nabla v|). \end{aligned} \tag{12}$$

Substituting $-\Delta u = u^p + \beta u^r v^{r+1} - u_t$, $-\Delta v = v^p + \beta u^{r+1} v^r - v_t$ and integrating by parts in t , we have

$$\begin{aligned} -J &\geq \frac{1}{p} \int \varphi (u^p + \beta u^r v^{r+1})^2 + \frac{1}{p} \int \varphi (v^p + \beta u^{r+1} v^r)^2 \\ &\quad - C \int (\varphi |u_t| u^{-1} |\nabla u|^2 + \varphi |v_t| v^{-1} |\nabla v|^2) \\ &\quad - C \int ((u^p + u^r v^{r+1}) |\nabla \varphi \cdot \nabla u| + (v^p + u^{r+1} v^r) |\nabla \varphi \cdot \nabla v|) \\ &\quad - C \int |\varphi_t| (u^{p+1} + v^{p+1}). \end{aligned}$$

Therefore, for any $-1 \neq k < 0$, we have

$$\begin{aligned} \frac{N+2}{N} kJ - \frac{N-1}{N} K &\geq \left(-\frac{N+2}{pN} k - \frac{N-1}{N} \right) \times \\ &\int \varphi ((u^p + \beta u^r v^{r+1})^2 + (v^p + \beta u^{r+1} v^r)^2) \\ &\quad - C \int (\varphi |u_t| u^{-1} |\nabla u|^2 + \varphi |v_t| v^{-1} |\nabla v|^2) \\ &\quad - C \int ((u^p + u^r v^{r+1}) |\nabla \varphi \cdot \nabla u| + (v^p + u^{r+1} v^r) |\nabla \varphi \cdot \nabla v|) \\ &\quad - C \int |\varphi_t| (u^{p+1} + v^{p+1} + u^{r+1} v^{r+1}) - C \int \varphi (u_t^2 + v_t^2). \end{aligned} \tag{13}$$

Since $p < p_B$, we can take $k > -N/(N-1)$ close to $-N/(N-1)$ such that

$$\left(\frac{N-1}{N} k + 1 \right) (-k) > 0 \quad \text{and} \quad \frac{N+2}{pN} (-k) - \frac{N-1}{N} > 0.$$

Lemma follows from (6) and (13). \square

Lemma 2.2. Assume that $p < p_B$ and $\beta > 0$. Let (u, v) be positive solution of (1) in $B_1 \times (-1, 1)$, then

$$\int_{B_{1/2}} \int_{-1/2}^{1/2} (u^{2p} + v^{2p}) dx dt \leq C(N, p, \beta). \tag{14}$$

Proof. We follow the argument as in proof of [18, Proposition 21.5]. One can choose the test-function φ such that $\varphi = 1$ in $B_{1/2} \times (-1/2, 1/2)$, $0 \leq \varphi \leq 1$ and

$$|\nabla \varphi| \leq C\varphi^{(3p+1)/4p}, |\Delta \varphi| \leq C\varphi^{(p+1)/2p}, |\varphi_t| \leq C\varphi^{(p+1)/2p}.$$

The same argument as in proof of [18, Proposition 21.5] yields

$$\begin{aligned} & \int |\nabla u|^2 (|\Delta \varphi| + \varphi^{-1} |\nabla \varphi|^2 + |\varphi_t|) \leq \varepsilon(I + L) + C(\varepsilon), \\ & \int |\nabla v|^2 (|\Delta \varphi| + \varphi^{-1} |\nabla \varphi|^2 + |\varphi_t|) \leq \varepsilon(I + L) + C(\varepsilon), \\ & \int (\varphi |u_t| u^{-1} |\nabla u|^2 + (u^p + u^r v^{r+1} + |u_t|) |\nabla u \cdot \nabla \varphi| \\ & + \int u^{-1} |\nabla u|^2 |\nabla u \cdot \nabla \varphi| + \int (|\Delta \varphi| |\nabla u|^2 + u^{p+1} |\varphi_t|) \\ & \leq \varepsilon(I + L) + C(\varepsilon) \left(1 + \int \varphi |u_t|^2\right), \\ & \int (\varphi |v_t| v^{-1} |\nabla v|^2 + (v^p + u^{r+1} v^r + |v_t| + v^{-1} |\nabla v|^2) |\nabla v \cdot \nabla \varphi|) \\ & + \int (|\Delta \varphi| |\nabla v|^2 + v^{p+1} |\varphi_t|) \\ & \leq \varepsilon(I + L) + C(\varepsilon) \left(1 + \int \varphi |u_v|^2\right). \end{aligned}$$

On the other hand,

$$\begin{aligned} & \int \varphi (|u_t|^2 + |v_t|^2) = \int \varphi u_t (\Delta u + u^p + \beta u^r v^{r+1}) \\ & + \int \varphi v_t (\Delta v + v^p + \beta u^{r+1} v^r) \\ & = \int \varphi \partial_t \left(\frac{u^{p+1} + v^{p+1}}{p+1} - \frac{|\nabla u|^2 + |\nabla v|^2}{2} + \frac{\beta u^{r+1} v^{r+1}}{r+1} \right) \\ & - \int (u_t \nabla \varphi \cdot \nabla u + v_t \nabla \varphi \cdot \nabla v) \\ & = \int \varphi_t \left(- \frac{u^{p+1} + v^{p+1}}{p+1} + \frac{|\nabla u|^2 + |\nabla v|^2}{2} - \frac{\beta u^{r+1} v^{r+1}}{r+1} \right) \\ & - \int (u_t \nabla \varphi \cdot \nabla u + v_t \nabla \varphi \cdot \nabla v) \\ & \leq C \int |\varphi_t| (u^{p+1} + v^{p+1} + |\nabla u|^2 + |\nabla v|^2) \\ & + \frac{1}{2} \int \varphi (|u_t|^2 + |v_t|^2) + \frac{1}{2} \int \varphi^{-1} |\nabla \varphi|^2 (|\nabla u|^2 + |\nabla v|^2). \end{aligned}$$

Hence,

$$\begin{aligned} \int \varphi (|u_t|^2 + |v_t|^2) & \leq C \int |\varphi_t| (u^{p+1} + v^{p+1} + |\nabla u|^2 + |\nabla v|^2) \\ & + \frac{1}{2} \int \varphi^{-1} |\nabla \varphi|^2 (|\nabla u|^2 + |\nabla v|^2). \end{aligned}$$

The same argument as in proof of [18, Proposition 21.5] then gives

$$\int \varphi (|u_t|^2 + |v_t|^2) \leq 2\varepsilon(I + L) + C(\varepsilon).$$

Therefore,

$$I + L \leq C(\varepsilon) + C(N, p, \beta)\varepsilon(I + L).$$

By choosing ε sufficiently small, we obtain $I, L \leq C$. \square

Proof of Theorem 1.1. Let (u, v) be a nontrivial non-negative solution of (1) in $\mathbb{R}^N \times \mathbb{R}$. Then (u, v) is positive due to the strong maximum principle. For any $R > 0$, we rescale

$$u_R(x, t) = R^{2/(p-1)} u(Rx, R^2 t), v_R(x, t) = R^{2/(p-1)} v(Rx, R^2 t).$$

Then (u_R, v_R) is also solution. By Lemma 2.2, we have

$$\begin{aligned} & \int_{|y| < R/2} \int_{|s| < R^2/2} (u^{2p} + v^{2p})(y, s) dy ds \\ & = R^{N+2-4p/(p-1)} \int_{|x| < 1/2} \int_{|t| < 1/2} (u_R^{2p} + v_R^{2p})(x, t) dx dt \\ & \leq C R^{N+2-4p/(p-1)}. \end{aligned}$$

Letting $R \rightarrow \infty$ then $u \equiv v \equiv 0$. This is a contradiction. \square

References

- [1] Herbert Amann. Global existence for semilinear parabolic systems. *J. Reine Angew. Math.*, 360:47–83, 1985.
- [2] Thomas Bartsch, Norman Dancer, and Zhi-Qiang Wang. A Liouville theorem, a-priori bounds, and bifurcating branches of positive solutions for a nonlinear elliptic system. *Calc. Var. Partial Differential Equations*, 37(3-4):345–361, 2010.
- [3] Jerrold Bebernes and David Eberly. *Mathematical problems from combustion theory*, volume 83 of *Applied Mathematical Sciences*. Springer-Verlag, New York, 1989.
- [4] Marie-Françoise Bidaut-Véron. Initial blow-up for the solutions of a semilinear parabolic equation with source term. In *Équations aux dérivées partielles et applications*, pages 189–198. Gauthier-Villars, Éd. Sci. Méd. Elsevier, Paris, 1998.
- [5] Marie-Françoise Bidaut-Véron and Thierry Raoux. Asymptotics of solutions of some nonlinear elliptic systems. *Comm. Partial Differential Equations*, 21(7-8):1035–1086, 1996.
- [6] Robert Stephen Cantrell, Chris Cosner, and Vivian Hutson. Permanence in ecological systems with spatial heterogeneity. *Proc. Roy. Soc. Edinburgh Sect. A*, 123(3):533–559, 1993.
- [7] E. N. Dancer, Kelei Wang, and Zhitao Zhang. Uniform Hölder estimate for singularly perturbed parabolic systems of Bose-Einstein condensates and competing species. *J. Differential Equations*, 251(10):2737–2769, 2011.
- [8] E. Norman Dancer, Juncheng Wei, and Tobias Weth. A priori bounds versus multiple existence of positive solutions for a nonlinear Schrödinger system. *Ann. Inst. H. Poincaré Anal. Non Linéaire*, 27(3):953–969, 2010.
- [9] M. Escobedo and M. A. Herrero. Boundedness and blow up for a semilinear reaction-diffusion system. *J. Differential Equations*, 89(1):176–202, 1991.

- [10] J. Földes and P. Poláčik. On cooperative parabolic systems: Harnack inequalities and asymptotic symmetry. *Discrete Contin. Dyn. Syst.*, 25(1):133–157, 2009.
- [11] P Glandsdorf and I Prigogine. Thermodynamic theory of structure, stability and fluctuations, 1971.
- [12] Yuxia Guo and Jiaquan Liu. Liouville type theorems for positive solutions of elliptic system in \mathbb{R}^N . *Comm. Partial Differential Equations*, 33(1-3):263–284, 2008.
- [13] Hans Meinhardt. *Models of biological pattern formation*, volume 6. Academic Press London, 1982.
- [14] Jeff Morgan. Global existence for semilinear parabolic systems. *SIAM J. Math. Anal.*, 20(5):1128–1144, 1989.
- [15] Quoc Hung Phan. Optimal Liouville-type theorems for a parabolic system. *Discrete Contin. Dyn. Syst.*, 35(1):399–409, 2015.
- [16] P. Poláčik. Symmetry properties of positive solutions of parabolic equations: a survey. In *Recent progress on reaction-diffusion systems and viscosity solutions*, pages 170–208. World Sci. Publ., Hackensack, NJ, 2009.
- [17] Pavol Quittner. Liouville theorems for scaling invariant superlinear parabolic problems with gradient structure. *Math. Ann.*, 364(1-2):269–292, 2016.
- [18] Pavol Quittner and Philippe Souplet. *Superlinear parabolic problems*. Birkhäuser Advanced Texts: Basler Lehrbücher. [Birkhäuser Advanced Texts: Basel Textbooks]. Birkhäuser Verlag, Basel, 2007. Blow-up, global existence and steady states.
- [19] Wolfgang Reichel and Henghui Zou. Non-existence results for semilinear cooperative elliptic systems via moving spheres. *J. Differential Equations*, 161(1):219–243, 2000.
- [20] Juncheng Wei and Tobias Weth. Radial solutions and phase separation in a system of two coupled Schrödinger equations. *Arch. Ration. Mech. Anal.*, 190(1):83–106, 2008.

Software Architecture and Design for Testability

Thiết kế và Kiến trúc Phần mềm cho Khả năng kiểm thử hệ thống

Duc-Man Nguyen, Anh-Dao Nguyen, Bao-Trang Nguyen

International School, Duy Tan University, Danang 550000, Vietnam

Khoa Đào tạo quốc tế, Đại học Duy Tân, Việt Nam

(Ngày nhận bài: 27/02/2018, ngày phản biện xong: 26/03/2018, ngày chấp nhận đăng: 29/03/2018)

Abstract

Developing reliable software is becoming more and more critical considering that software applications are becoming pervasive in our daily lives. The need for more reliable software requires that, amongst others, it is adequately tested to provide further confidence in its ability to perform as expected. However, testing software becomes a boring task as the size and complexity of software increases. Therefore, the next logical step is to make the task of testing easier and more efficient. It means that the software system must have a testability attribute. Testability is a crucial software quality attribute that is ineffective if it is not available at an early stage in the development life-cycle. Though many researchers and quality controllers have proved its importance, still the research has not gained much momentum in emphasizing the need of making testability analysis necessary in all software development phases. In this paper, we investigate the factors, issues, and methods of testability estimation of a software system in various stages of development life cycle. The result of paper may help software designers to understand the importance of the design for testability and apply in reality.

Keywords: Software Architecture, Software Testing, Testability, Software Design, Reliable Software, software quality attribute.

Tóm tắt

Việc phát triển phần mềm đáng tin cậy ngày càng trở nên quan trọng khi cho rằng các ứng dụng phần mềm đang ngày càng trở nên phổ biến trong cuộc sống của chúng ta. Nhu cầu về phần mềm có độ tin cậy cao đòi hỏi phải được thử nghiệm một cách đầy đủ để đảm bảo sự ổn định và hơn nữa là sự tin tưởng khả năng của phần mềm thực hiện như những gì được mong đợi. Tuy nhiên, kiểm thử phần mềm trở thành một nhiệm vụ nhàm chán khi kích thước và sự phức tạp của phần mềm ngày càng tăng lên. Do đó, vấn đề hiện nay là làm sao cho công việc thử nghiệm trở nên dễ dàng và hiệu quả hơn. Điều này đồng nghĩa hệ thống phần mềm phải có thuộc tính testability (có khả năng kiểm thử). Khả năng kiểm thử là một thuộc tính chất lượng phần mềm quan trọng mà nó sẽ không hiệu quả nếu không được đưa vào giai đoạn đầu của vòng đời phát triển phần mềm. Mặc dù nhiều nhà nghiên cứu và các nhà kiểm soát chất lượng đã chứng minh được tầm quan trọng của nó, nhưng nghiên cứu vẫn chưa đạt được nhiều thành công trong việc nhấn mạnh sự cần thiết phải phân tích khả năng kiểm thử trong tất cả các giai đoạn phát triển phần mềm. Trong nghiên cứu này, chúng tôi nghiên cứu các yếu tố, các vấn đề và phương pháp đánh giá khả năng kiểm thử của một hệ thống phần mềm trong các giai đoạn khác nhau của vòng đời phát triển. Kết quả của bài báo có thể giúp các nhà thiết kế phần mềm hiểu được tầm quan trọng của việc thiết kế phần mềm đảm bảo khả năng kiểm thử và áp dụng vào thực tế.

Từ khóa: Kiến trúc phần mềm, Thiết kế phần mềm, Kiểm thử phần mềm, khả năng kiểm thử, độ tin cậy phần mềm, thuộc tính chất lượng

1. INTRODUCTION

Quality has become more important with the increasing dependence on software. In the

last decades, the demand for quality of software products has been increasingly emphasized. The software industry has been delivering exponential

improvement in cost and performance. The problems of software are not declining, because of late delivery, behind the scheduled, beyond the budgeted and is full of residual faults. Around 31% of projects got canceled before completion, 53% over-run their cost, and estimated by an average of 189% in which for every 100 projects there were 94 projects restarted [7]. A key problem of the software industry is its lack of ability to develop bug-free software. If software engineers are asked to state that the developed software is bug-free officially, no software would have ever been released. The goal of software engineering is to create high-quality software on time and within budget. If a product meets its requirements, we may say it is a superior quality product. The whole thing is measured with respect to requirements, and if it matches, it is a quality product.

The research on software testability primarily started in 1975s. It was accepted in McCall and Boehm software quality model, which built the foundation of ISO 9126 software quality model. Since the 1990s, the software engineering society began to initiate quantitative research on software testability. Formally, software testability has been defined and described in literature from the different point of views. The definitions of testability [8]:

(1) Defines it as the degree to which a software artifact supports testing in a given test context. If the software testability artifact is high, then finding faults in the system by means of testing is easier.

(2) Defines it as attributes of software that bear on the effort needed to validate a software product.

These two standard definitions aim to different targets and both are qualitative without any operational guidelines. The testability has become a quality factor contributing to system maintainability as ISO standards measurements and can be used to predict the amount of effort required for testing and help to manage the required resources effectively.

So, the study of testability actually helps in finalizing software design and coding changes for friendly testing, reducing the cost of system test as well as improving the quality of software. Through the test effort reduction using these new researches, not only the software design and code are improved, but also the new levels of software reliability and credibility can be reached. All this leads to the desire of designing and developing of highly testable systems. But the desire does not end here; there is a need to measure and verify the testability, quality, and reliability of the system which is where the challenges are faced.

As the software grows more complex and gradually replace human decision-makers in every facet of our society, the software quality and reliability require careful attention. Moreover, when the life of human beings and huge fortunes are dependent on automated systems, software quality assurance can no longer be treated lightly. The study shows many software can be unreliable when human beings are employed for decision making because there is always a possibility of subtle errors or drifts that may culminate into a disaster. It is well understood that delivering quality software is no longer an advantage but a necessary factor.

However, most of the industries not only fail to deliver a good quality product to their customers but also do not understand the relevant quality attributes. Building reliable and quality end software is becoming more and more critical because of the continuously growing complexity and criticality of software. The advancement in the software development process has been accelerated drastically in recent decades. The complexity of applications and development environments has been substantially increased, and schedules have been pinched. So in this case, software quality tends to suffer; ensuring the desired level of quality and dependability became more crucial, complicated and expensive [8].

Software testing is one of the most important

ways to assure the quality of software systems. The effectiveness of testing decides the quality of software products. However, testing has now become a tedious task and an expensive activity because the size and complexity of software are growing rapidly. A recent survey reveals that the cost incurred in testing often range from 40% to 80% of the entire cost involved in development [9]. Software testing is an economic problem closely intertwined with nearly all major technical issues in Software Engineering [6]. Testability is a quality factor; its measurement or evaluation can be used to predict the amount of effort required for testing and help to allocate required resources. Most of the studies measure testability or precisely the attributes that have an impact on testability at the source code level [10]. Estimating testability at a later stage leads to the late arrival of desired information, leading to late decisions about changes in design. This increases cost and rework.

Therefore, early evaluation of testability in the development process may enhance the quality and reduce testing efforts and costs. One proactive strategy that organizations can adapt is to design their software products with testability as one of the key design criteria [3].

Most importantly, the architecture, design (and requirements) of the system should be made explicitly testable. An architect should not only start out with the basics of good design as well as be able to separate concerns & to code, run, test, or debug objects in isolation but also design for:

- **Controllability:** The degree to which it is possible to control the state of the component(s) under test before/after a test is run. Most importantly, a tester or automated software test must be able to roll back changes in state, so that the test can be repeated (regression testing). This may involve designing a system that provides additional transactions for tests, rollback scripts, new API methods or GUI controls to modify the

system just for test purposes..

- **Observability:** The degree to which it is possible to observe test results. Most importantly, a tester or automated software test must be able to inspect all relevant attributes in the system to evaluate if the test succeeded or not. This may involve designing a system with extra API methods or GUI controls just for being able to read or display state.

- **Isolateability:** The degree to which the component under test can be tested in isolation.

- **Separation of concerns:** The degree to which the component under test has a single, well defined responsibility.

- **Understandability:** The degree to which the component under test is documented or self-explaining.

- **Automatability:** The degree to which it is possible to automate testing of the component under test. Making sure a system is both controllable and observable usually goes a long way in enabling automate testing.

The testability of software components can be improved by:

- Test-driven development
- Design for testability

Software testability is an external software attribute that evaluates the complexity and the effort required for software testing. For any system which needs to be made test friendly, the testability measures need to be applied itself from the beginning during the designing phase to further coding and testing phase. So, it is better to keep test-driven development (TDD) approach where the tests come first and largely determine the API design of the system, forcing it to be something that the tests can work with. The same is often stated as Design For Testability (DFT), which means building a system that keeps testability measures in line at designing as well as

coding phase so that tracing errors is easier along with reduced testing effort [6]. It is basically a systematic way of development which maximizes the effective testing efforts. With the course of time, a lot of research has been done on testability issues during the designing and coding phase.

2. LITERATURE REVIEW

Testability is not an intrinsic property of a software artifact and cannot be measured directly as other software attributes. Instead testability is an extrinsic property which results from interdependency of the software to be tested and the test goals, test methods used, and test resources [6]. A lower degree of testability results in increased test effort and high development cost. In extreme cases a lack of testability may prevent testing parts of the software or software requirements a tall. Measuring testability is a challenging and most crucial task towards estimating testing efforts. Several approaches like model based testability measurement, program based testability and dependability testability assessment has been proposed. Also a number of metrics on testability measurement have been proposed, some at design and analysis phase or some at source code level.

Software design may result in a model of the domain problem by formally capturing and representing the user's requirements and hence paving the way for a conceptual relation. It may serve well as a communication medium between designer and the user on one end, and act as a basis for implementation on the other end. It is the key to the successful development of quality software. It is also the step that will determine the overall structure, nature, and approach of the resulting software. This is evident that the software design is an important stage spanning the whole software lifecycle, not only for software development but also for re-developing legacy systems.

Quality of software design heavily affects

the quality of the final products because design is the backbone of any software system. A defective backbone may not allow harmonious growth and cannot easily accommodate changes without cumbersome prosthesis with possibly introducing various kinds of side effects. Due to the fact that, most of the time requirement analysis is incomplete, software designs should be built in such a way so as to make them easily understandable, testable, alterable, and preferably stable. If software design fails to accurately cover requirement specification, it may result in a failure of the project. On the other hand if it is made too complicated, it may cause unnecessary problems during and after the implementation that may result in shooting up the cost of a project. Researchers and practitioners recommend that flaws are best found by pondering design issues that go far beyond code. So, controlling and improving software design quality has been one of the important issues in Software Engineering.

The testable design is more specific than a good design as it is explicitly intended to match a particular test context. Improving software testability is an important objective to reduce the number of defects that result from poorly designed software [2][1]. Any technique that enhances a software design at an early stage can have a highly beneficial impact on the final testing cost and its efficiency. Although software testability is most obviously relevant during testing, paying attention to testability early in the development process can potentially enhance testing and significantly improve testing phase effectiveness. Indeed, what makes a design testable is the easiness to test the components in the design. Therefore, one proactive strategy that organizations can adapt is to design their software products with testability as a key design criterion [3]. It is suggested by a renowned expert that testers must realize that testability requires them to understand the software design, which may provide the basis for suggestions and facilitate concrete discussions.

The insight provided by software testability is valuable during designing, coding, testing, and quality assurance. However, testability is an elusive concept and a difficult exercise for its correct measurement or evaluation. Furthermore, it is difficult to get a clear view of all the potential factors that can affect testability and the dominant degree of these factors under different testing contexts [5]. The mechanisms available for testability estimation of object-oriented software may typically be used in later phases of software development lifecycle and depend on information extracted from the operationalization of software. Such methods provide an indication of testability, but too late to improve the product, before its completion. The characteristics of testable software like adequate complexity, low coupling and good separation of concerns make it easier for reviewers to understand the software artifacts under review. Lots of works have been carried out in describing the need and importance of incorporating software testability since the early 90s. Many methods of measuring testability have been proposed. But, the significant achievements made by the researchers in the area have not been widely accepted and are not adopted in practice by industry [5][3]. Following briefly presents some relevant efforts made by researchers in the direction of finding testability factors:

Robert Binder, testability Guru, in [6] did a novel work in finding out the need and significance of considering testability while developing the software system. He introduces controllability and observability as two main facets of testability. He considered six factors of software testability including representation characteristics, implementation characteristics, built-in-test capabilities, test suite, test support environment, development process. The factors are described at a high level of abstraction, which leads to no clear relationship with the metrics that are based on design artifacts and the implementation. It seems that there is no

empirical evidence of the correlation between the suggested metrics and testability. The limitation of the study is all factors are related to higher level of abstraction having not in-depth relation with object-oriented design constructs. Also, all suggested metrics are not empirically proved.

Bruce and Haifeng Shi [11] examined the factors that affect software testability in object-oriented software and proposed a preliminary framework for the evaluation of software testability metrics. They also formulated a set of guidelines in object-oriented design to improve software quality by increasing their testability. Characteristics of object-oriented software systems contributing to software testability were categorized into three groups namely: structure factors, communication factors, and inheritance factors. James Bach in 1999 defined testability as anything that makes software easier to test by making it easier to design and executes tests. Bach presented heuristics of software testability. He described testability and stability. He strongly believed that these are the characteristics of the program leading to testable software.

Jungmayr in [12,15] identified testability as a major factor determining time and effort needed to test a software system. He strongly recommended deploying testability into the system continually right from the beginning, especially at the design phase. Large numbers of software related factors that affect testability during design were identified. He grouped them into nine main testability factors namely complexity, separation of concerns, coupling, fault locality, controllability, observability, automatability, built-in-test capability, and diagnostic capability. The limitation of the study is more tests are required to exercise their interfaces. Other important factors such as observability and controllability except dependencies are overlooked in the research.

Y. Wang in [3] demonstrated that software

testability at class and system levels could be quantitatively modeled and analyzed. He defined testability as a product of test controllability and observability. A set of fundamental built-in-test capability mechanism oriented to the basic control structures of code was developed to improve the testability of software in terms of controllability, visibility, operability, simplicity, understandability, suitability.

In [3] Bruntink and van Deursen identified the factors, which are related to testability of object-oriented software and relate testability to the number of test cases needed to test a system and to the effort required to develop each test case. They define and evaluate a set of metrics for assessing the testability of classes of a Java system. The approach characterizes software testability for object-oriented systems using source code metrics. They categorize the source code factors as the: factors that influence the number of test cases required to test the system, and factors that affect the effort required to develop each test case. They establish a correlation between class level metrics, test level metrics, and the number of lines of code per test class. But inheritance-related metrics and the proposed testability metrics are not correlated.

Samar Moucha Wrab et al. [10] recommended that testability analysis can yield the highest payoff if focused during analysis and design stages of the development cycle. A decision to change the design to improve testability after coding may be costly and error-prone. The authors investigated on how to measure testability based on design artifacts and proposed a framework that may help to assess testability of design that is particularly modeled with the UML. Many hypotheses are proposed for each attribute to explain its expected relationship with testability, but these hypotheses are not empirically validated.

Jerry Gao, and Ming-Chih Shih [14], presented a model that is based on Gao's pentagram model and

analytical approach for testability measurement of components. The testability review process at design and analysis phase was performed keeping five significant testability characteristics, which were used in testability metrics calculation and obtaining five testing points to draw the final pentagram. Furthermore, testability is considered as one of the characteristics of the architecture, design, and implementation. Using this model of testability, it is possible to discuss in detail and analyze testability more explicitly. They advocate that testing of product lines can be made more efficient and effective by considering testability already during architectural design. The limitation of the study was validated on large-scale industrial software's. Though it was validated well on few case studies, still model did not gain much popularity due to complex notations.

Emmanuel Mulo presented a report strengthening the integration of testability throughout development process [8]. He considers testability from two main viewpoints; as an inherent property in the systems under consideration or as a strategy in the development process to make testing easier. As an inherent property, testability is defined by the terms observability and controllability. He strongly recommended applying certain tactics in practice that improve on a tester's ability to better manipulate the software and to better observe and interpret the results from the execution of tests.

3. HEURISTICS AND TACTICS OF SOFTWARE TESTABILITY

According to James Bach [19], the practical testability of a product is how easy it is to test by a particular tester and test process, in a given context. Practical testability is a function of five other testabilities: project-related testability, value-related testability, subjective testability, intrinsic testability, and epistemic testability. They can be shown in Figure 1 below.

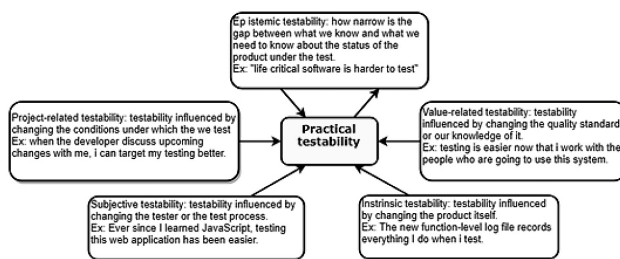


Figure 1- Heuristics of Software testability [19]

Epistemic Testability:

Prior Knowledge of Quality: If we already know a lot about a product, we don't need to do as much testing.

Tolerance for Failure: The less quality required, or the more risk that can be taken, the less testing is needed

Project-Related Testability:

Change Control: frequent and disruptive change requires retesting and invalidates our existing product knowledge. Careful change control helps the product to evolve in testable stages.

Information Availability: we get all information we want or need to test well.

Tool Availability: We are provided all tools we want or need to test well.

Test Item Availability: We can access and interact with all relevant versions of the product.

Sandboxing: We are free to do any testing worth doing (perhaps including mutation or destructive testing), without fear of disrupting users, other testers, or the development process.

Environmental Controllability: We can control all potentially relevant experimental variables in the environment surrounding our tests.

Time: Having too little time destroys testability. We require time to think, prepare, and cope with surprises.

Value-Related Testability:

Oracle Availability: We need ways to detect each kind of problem that is worth looking for. A well-written specification is one example of such an oracle, but there are lots of other kinds of

oracles (including people and tools) that may help.

Oracle Authority: We benefit from oracles that identify problems that will be considered important.

Oracle Reliability: We benefit from oracles that can be trusted to work overtime and in many conditions.

Oracle Precision: We benefit from oracles that facilitate identification of specific problems.

Oracle Inexpensiveness: We benefit from oracles that don't require much cost or effort to acquire or operate.

User Stability & Unity: The less users change and the less variety and discord among users, the easier the testing.

User Familiarity: The more we understand and identify with users, the easier it is to test for them.

User Availability: The more we can talk to and observe users, the easier it is to test for them.

User Data Availability: The more access we have to natural data, the easier it is to test.

User Environment Availability: Access to natural usage environments improves testing.

User Environment Stability & Unity: The fewer user environments and platforms change and the fewer of them there are, the easier it is to test.

Subjective Testability:

Product Knowledge: Knowing a lot about the product, including how it works internally, profoundly improves our ability to test it. If we don't know about the product, testing with an exploratory approach helps us to learn rapidly.

Technical Knowledge: Ability to program, knowledge of underlying technology and applicable tools, and an understanding of the dynamics of software development generally, though not in every sense, makes testing easier for us.

Domain Knowledge: The more we know about the users and their problems, the better we can test.

Testing Skill: Our ability to test in general obviously makes testing easier. Relevant aspects of testing skill include experiment design, modeling, product element factoring, critical thinking, and test framing.

Engagement: Testing is easier when a tester is closer to the development process, communicating and collaborating well with the rest of the team. When testers are held away from development, test efficiency suffers terribly.

Helpers: Testing is easier when we have help. A helper is anyone who does not consider himself responsible for testing the product, and yet does testing or performs some useful service for the responsible testers.

Test Strategy: A well-designed test strategy may profoundly reduce the cost and effort of testing.

Intrinsic Testability:

Observability: To test, we must be able to see the product. Ideally we want a completely transparent product, where every fact about its states and behavior, including the history of those facts is readily available to us.

Controllability: To test, we must be able to visit the behavior of the product. Ideally, we can provide any possible input and invoke any possible state, a combination of states, or sequence of states on demand, easily and immediately.

Algorithmic Simplicity: To test, we must be able to visit and assess the relationships between inputs and outputs. The more complex and sensitive the behavior of the product, the more we will need to look at.

Unbugginess: Bugs slow down testing because we must stop and report them, or work around them, or in the case of blocking bugs, wait until they get fixed. It's easiest to test when there are no bugs.

Smallness: The less there is of a product, the less we have to look at and the less chance of bugs due to interactions among product components.

Decomposability: When different parts of a product can be separated from each other, we have an easier time focusing our testing, investigating

bugs, and retesting after changes.

Similarity (to known and trusted technology): The more a product is like other products we already know the easier it is to test it. If the product shares substantial code with a trusted product or is based on a trusted framework, that's especially good.

Testability tactics:

Tactics of testability allow for easier testing when an increment of software development is completed. Architectural techniques for enhancing the software testability have not received as much attention as more mature fields such as modifiability, performance, and availability, but, since the testing is costly when developing the software system, anything architect can do to reduce the cost will gain the benefit. Executing the test procedures requires some software to provide input to the software being tested and to capture the output. The design and generation of the test harness in some systems will take substantial time and expense. There are two categories of tactics for testing: providing input and capturing output, and internal monitoring.

Three tactics for managing input and output are: (1) Record/playback refers to both capturing information crossing an interface and using it as input into the test harness. The information crossing an interface during normal operation is saved in some repository and represents output from one component and input to another. Recording this information allows test input for one of the components to be generated and test output for later comparison to be saved. (2) Separating the interface from the implementation allows substitution of implementations for various testing purposes. Stubbing implementations allows the remainder of the system to be tested in the absence of the component being stubbed. Substituting a specialized component allows the component being replaced to act as a test harness for the remainder of the system. (3) Having specialized testing interfaces allows the capturing or specification of variable values

for a component through a test harness as well as independently from its normal execution. Specialized access routes and interfaces should be kept separate from the access routes and interfaces for required functionality. Having a hierarchy of test interfaces in the architecture means that test cases can be applied at any level in the architecture and that the testing functionality is in place to observe the response[5].

The tactics based on internal monitoring will support the testing process. The built-in monitors can maintain state, performance load, capacity, security, or other information accessible through an interface. This interface can be a permanent interface of the component or it can be introduced temporarily via an instrumentation technique such as aspect-oriented programming or preprocessor macros. A common technique is to record events when monitoring states have been activated. Monitoring states can actually increase the testing effort since tests may have to be repeated with the monitoring turned off. Increased visibility into the activities of the component usually more than outweigh the cost of the additional testing[16].

Figure 3 provides a summary of the tactics used for testability.

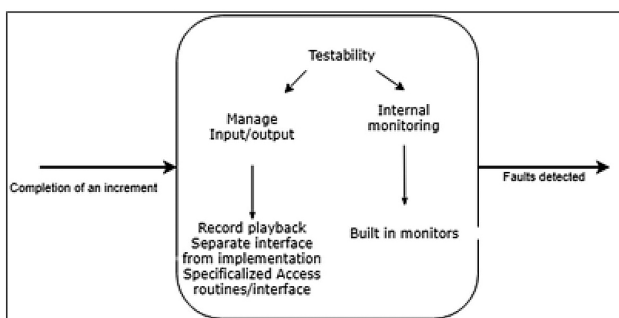


Figure 2 Testability tactics [16]

4. IMPROVING TESTABILITY AT DESIGN PHASE

Testability assessment at the source code level is a good indicator of effort estimation; it leads to the late appearance of information in the software development process. Despite the fact that estimating testability near the beginning of

the development process significantly reduces the overall cost and rework. Early estimation of testability mainly at design phase form a roadmap to industry persons and researchers to review, and preferably, measure and improve software testability at the design phase. So reducing effort and improving software testability is a key objective to reduce the number of defects that result from defectively designed software.

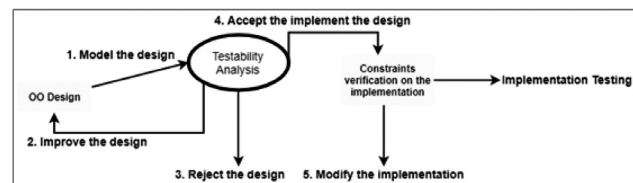


Figure 3 - Process of testability analysis at design phase [18]

Architecture support for testing is including:

- (i) Architecture-based analysis: Use an architecture or architectural model to make predictions about a system, generally absent any implementation. In architecture-based testing, we concentrate on Architecture analysis that can be used to improve testing outcomes in some way, for example, reducing the cost of testing.
- (ii) Generation of code-targeted test artifacts: Use architecture to produce artifacts (e.g., test cases, test plans, coverage measures) useful in testing an implementation of a system.
- (iii) Designing for testability: Techniques for designing a system so that it is more testable – that is, more likely to reveal a fault when tested.
- (iv) Testing conformance of implementation to architecture: Compare an implementation to the architecture that it is supposed to follow, to see if it complies.

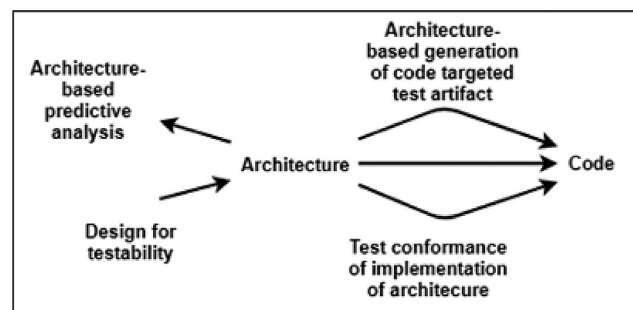


Figure 4-Architecture support for testing(Clements, 2011)

5. CONCLUSION

Many approaches have been presented in the literature for improving and measuring software testability. The studies give many proofs that as late as testability measurement be put in the software development lifecycle phase, as hard as work has to be done. Updating the design of system to recover testability after coding has started may cause of extremely costly and errors. It means estimating testability as soon as first phases of development system bring remarkable decrease cost, effort, time to test or rework. Spending time in estimating testability at design phase of software development will earn more value at the rest because of the fully given evidence for testability. In conclusion, testability is a quality attributes that show and help to compute how much time and how hard to implement in software testing phase. After all analysis and study process found that to make sure delivering high-quality software within time and budget, improving software testability in early stages like architecture and design and decreasing effort in running test measurement are significant factors

REFERENCES

- [1]. M. A. Khanum and A. M. Tripathi, "An-Empirical-Study-on-Testability-Measurement-of-Object-Oriented-Software.doc," vol. 6, no. 5, pp. 1285–1290, 2015.
- [2] G. Asproni, "Design For Testability," 2015.
- [3] Y. Wang, "Design for Test and Software Testability", University of Calgary, 2003. <http://www.ucalgary.ca/~ageras/wshop/abstracts/2003/design-for-estability.htm>
- [4]. J. Voas and Miller , "Improving the software development process using testability research" , Proceedings of the 3rd international symposium on software Reliability Engineering , p. 114--121, October, 1992, RTP, NC, Publisher: IEEE Computer Society.
- [5] L. Zhao, "A new approach for software testability analysis", International Conference on Software Engineering, Proceeding of the 28th international conference on Software Engineering , Shanghai, 2006, pp. 985–988.
- [6] R. V. Binder, 1994, "Design for Testability in Object Oriented Systems," communication of the ACM , vol. 37 (9), pp. 87-101
- [7] K.K. Aggarwal, Yogesh Singh. New Age International, Jan 1, 2005 - Software engineering.
- [8] Mulo, E. "Design for Testability in Software Systems." Master's Thesis (2007).
- [9] Andy Zaidman, Bart Van Rompaey, Serge Demeyer, and Arie van Deursen. On how developers test open source software systems. Technical Report TUD-SERG-2007-012, Delft University of Technology, Software Engineering Research Group, 2007.
- [10] S. Mouchawrab et al, "A measurement framework for object-oriented software testability," Carleton University, Technical Report, SCE-05-05, year 2005
- [11] B. W. N. Lo and H. Shi, "A preliminary testability model for object-oriented software," In Proc. Int. Conf. on Software Engineering, Education, Practice, pages 330- 337. IEEE. 1998
- [12] S. Jungmayr, "Testability during design", Software technik-Trends, Proceedings of the GI Working Group Test, Analysis and Verification of Software, Potsdam, 2002, pp. 10 -11.
- [13] M. Bruntink and A. V. Deursen, "Predicting class testability using object -oriented metrics," in Proc. IEEE International Workshop on Source Code Analysis and Manipulation, 2004, pp. 136- 145
- [14] J. Gao and M. C. Shih, "A component testability model for verification and measurement", In Proceedings of the 29th Annual International Computer Software and Applications Conference (COMPSAC '05), pages 211–218. IEEE Computer Society, 2005.
- [15] S. Jungmayr, "Reviewing Software Artifacts for Testability," 2002.
- [16] P. Clements and R. Kazman, Software Architecture in Practice. Addison-Wesley, 2013
- [17] Jianping, Fu, Liu Bin, and Lu Minyan."Present and future of software testability analysis." Computer Application and System Modeling (ICCSM), 2010 International Conference on. Vol. 15. IEEE, 2010
- [18] Malla, Prakash, and Bhupendra Gurung. "Adaptation of Software Testability Concept for Test Suite Generation: A systematic review." (2012).
- [19] J. Bach, "Heuristics of Software Testability," 2015.
- [20] P. Clements, "Architecture Support for Testing," Slides, no. March, 2011.

A simulation model of the Dalat nuclear research reactor using SRAC code

Mô phỏng lò phản ứng hạt nhân Đà Lạt sử dụng chương trình SRAC

Trần Hoài Nam^{a,*}, Phan Thị Thùy Giang^{a,b}, Nguyễn Kiên Cường^c, Trần Việt Phú^d

^aInstitute of Fundamental and Applied Sciences, Duy Tan University, Da Nang

^bDepartment of Nuclear Physics, Faculty of Physics and Engineering Physics, VNUHCM-University of Science, HCMC

^cNuclear Research Institute, Dalat

^dInstitute for Nuclear Science and Technology, VINATOM, Hanoi

(Ngày nhận bài: 03/11/2017, ngày phản biện xong: 17/01/2018, ngày chấp nhận đăng: 20/03/2018)

Abstract

A simulation model of the Dalat Nuclear Research Reactor (DNRR) has been developed using the SRAC code. Numerical calculations of the DNRR core were performed for analyzing the effective multiplication factors, k_{eff} , of the core in two cases corresponding to the complete withdrawal and the full insertion of control rods. Power distribution has also been investigated in comparison with MCNP5 calculations. The difference in the k_{eff} values is within 271 pcm compared to that obtained with MCNP5 calculations. The deviation of the relative power densities is within 4% for most of the fuel bundles in the middle core, while the maximum deviation is about 7% appearing at some peripheral bundles.

Keywords: Neutronics analysis, HEU, DNRR.

Tóm tắt

Mô hình mô phỏng lò phản ứng hạt nhân Đà Lạt sử dụng chương trình SRAC đã được xây dựng. Các tính toán chi tiết cho vùng hoạt lò phản ứng được thực hiện nhằm phân tích hệ số nhân neutron hiệu dụng, k_{eff} , trong hai trường hợp tương ứng với việc rút hết thanh điều khiển và đưa toàn bộ thanh điều khiển vào vùng hoạt lò phản ứng. Phân bố công suất cũng được khảo sát và so sánh với các kết quả tính toán sử dụng chương trình MCNP5. Kết quả cho thấy sự khác nhau về giá trị k_{eff} vào khoảng 271 pcm so với kết quả thu được từ các tính toán MCNP5. So sánh phân bố công suất giữa 2 chương trình cho thấy sai khác nằm trong khoảng 4% ở giữa vùng hoạt và sai số lớn nhất là 7% xảy ra tại thanh nhiên liệu ở biên vùng hoạt.

Từ khóa: Phân tích neutronics, HEU, lò phản ứng hạt nhân Đà Lạt.

1. Introduction

The Dalat Nuclear Research Reactor (DNRR) is operated by Dalat Nuclear Research Institute and is the unique reactor of the country. The first criticality of the DNRR was achieved on November 1st, 1983 and the operation with full power was achieved in March 1984. During the

period from 1984 to 2007, the core was loaded with highly enriched uranium (HEU) fuel with ²³⁵U enrichment of 36% [1, 2]. Then, the DNRR core was partly converted to low enriched uranium (LEU) fuel with ²³⁵U enrichment of 19.75% in 2007. The full core conversion to LEU fuel was completed in January 2012 [1].

The DNRR consists of many components such as a neutron trap, water gaps, irradiation channels, horizontal beam ports, beryllium blocks, control rods, rotary specimen rack and graphite reflector, which make the core geometry become complicated. Even in Monte Carlo simulation, possible modifications are usually made to simplify the core geometry. Alternatively, a deterministic simulation model of the DNRR core is useful taking into account of the advantage in computational time.

In the present work, analysis models of the DNRR reactor have been developed using the SRAC deterministic code system [3]. Numerical calculations have been conducted based on the core configuration loaded with HEU fuel bundles. The effective multiplication factors and power distribution were analyzed in comparison with that obtained from MCNP5 calculations [4].

2. The DNRR

Fig. 1 shows the horizontal cross section view of the DNRR reactor [2]. The core consists of 121 hexagonal cells including fuel bundles, control rods, irradiation channels and beryllium blocks. The VVR-M2 fuel bundle is made of aluminum-uranium alloy clad in aluminum. The outer tube has a hexagonal sharp, and the two inner tubes are cylindrical. The reactor core is controlled by seven control rods: two safety rods (SR), four shim rods (ShR) and one automatic regulating rod (AR). The safety and shim rods are made of boron carbide (B_4C), while the automatic regulating rod is made of stainless steel. The neutron trap at the center of the core is a water cylinder surrounded by six beryllium blocks. The beryllium block has the same outer shape and dimension as the fuel bundle. A beryllium ring of serrated beryllium blocks is located between the active core and the graphite reflector and serves as an additional reflector. The core and the graphite reflector are placed in the reactor pool.

In the present work, neutronics calculations have been performed based on the core configuration of 88 HEU fuel bundles.

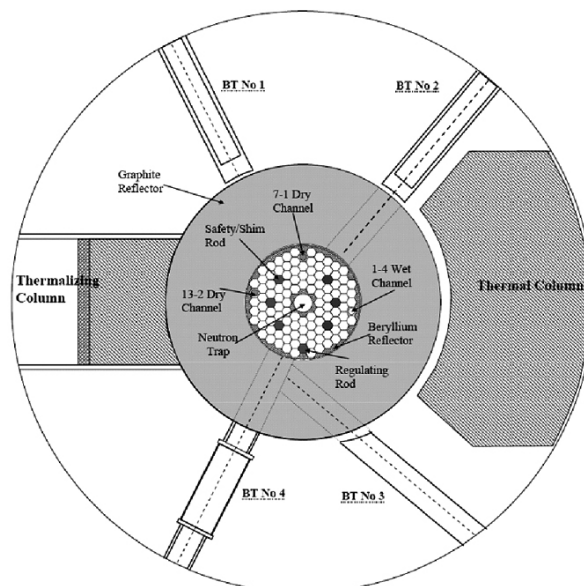


Figure. 1 Horizontal cross section view of the DNRR.

3. SRAC model

SRAC is a deterministic code system developed by Japan Atomic Energy Agency for neutronics calculation of both lattice physics and core physics of various reactor types [2]. The macroscopic cross sections of fuel cell, neutron trap, control rods and other non-fuel lattice cells were prepared via lattice cell calculations using the PIJ code and ENDF/B-VII.0 data library [5]. For fuel cell, the hexagonal fuel bundle was modeled with a small geometrical modification of the outer hexagonal fuel tube of the VVR-M2 fuel bundle. In the lattice calculations using the PIJ code, the model of 107 energy groups was used. Then, the cross sections were collapsed into seven-energy group data model (4 fast groups and 3 thermal groups) for full core calculations. The COREBN of the SRAC code system was used for the full core calculation with hexagonal lattice cells. The full core model was described by hexagonal grids of 37x37 in the X-Y plane as shown in Fig. 2.

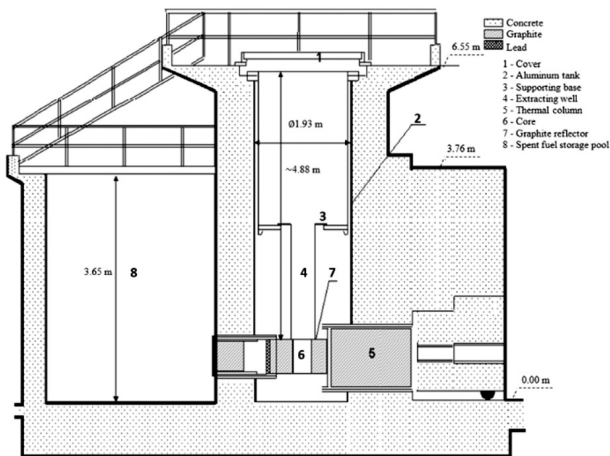


Figure. 2 Vertical cross section view of the DNRR.

4. Results and discussions

4.1. Multiplication factor

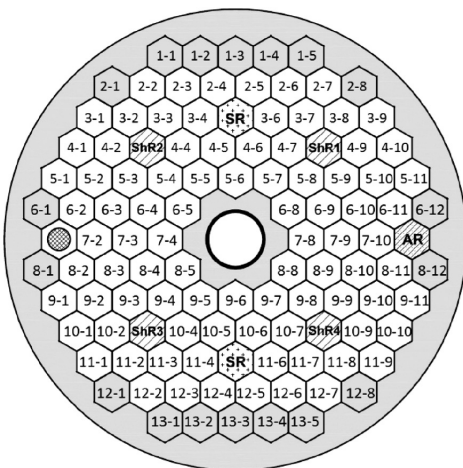


Figure. 3 The DNRR core configuration.

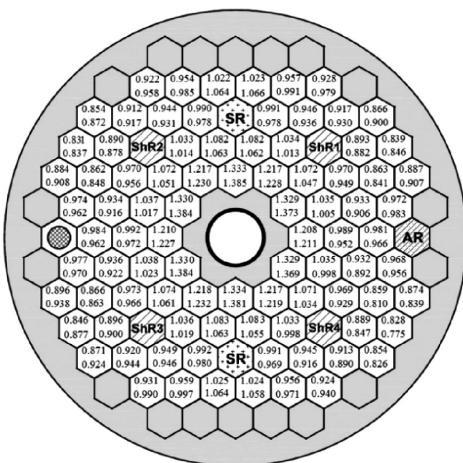


Figure. 4 Relative power distribution in the core at the initial critical condition (ShR = 45.7 cm. and AR = 40 cm).

The multiplication factors k_{eff} of the DNRR in two cases corresponding to the complete withdrawal and full insertion of the control rods have been analyzed. The k_{eff} values have been compared to the MCNP5 calculations as shown in Table 1. It can be seen that in the case (A) of control rod withdrawal, the k_{eff} values obtained from the two codes are well consistent. In the case (B) of fully insertion of the four shim rods and the automatic regulating rod, the difference is about 242 pcm which is considerably good agreement. This agreement between the SRAC and MCNP5 calculations gives a certain confidence for further analysis of the DNRR core.

Table 1. The k_{eff} is calculated by SRAC and MCNP5

Code	SRAC	MCNP5
All control rods are completely withdrawn (A)	1.08633	1.08632 ± 0.00006
Four shim rods and automatic regulating rod are fully inserted (B)	0.98029	0.97787 ± 0.00005

4.2. Power distribution

Power distributions of the DNRR core have been analyzed in detail for the case corresponding to the partial insertion of the control rods (ShR = 45.7 cm, AR = 40 cm) in comparison with MCNP5 calculations. Fig. 4 shows the radial relative power distribution at the initial critical condition. The radial power peaking factor is 1.445 which appears at the fuel bundle 9-6. This value is 1.481 obtained in the MCNP5 calculation. Comparing the relative power distributions obtained with the two code, the deviation of the relative power densities is within 4% at most of fuel bundles, except some bundles located at periphery where the maximum deviation is about 7%.

Fig. 5 depicts the axial power distributions at the fuel cells 9-6 and 7-10 in the cases of control rods insertion. The fuel cell 9-6 corresponds to the

highest power rating. The fuel cell 7-10 is located next to the AR. One can see that when the control rod is partially inserted, the power profile is shifted to the lower half of the core, and the power peaking factor increases. The axial power peaking factor is about 1.710 in the case of control rods out, while it is about 1.823 in the case of control rods insertion. Comparing between the two codes, the axial power profiles are well agreed. The larger difference is found at the boundary interfaces between the active fuel and the upper and lower reflectors.

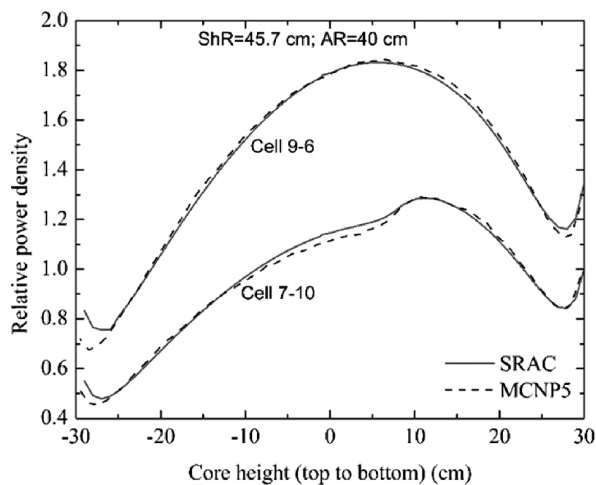


Figure. 5 Axial power distribution in the core.

5. Conclusions

A simulation model of the DNRR using the SRAC code system has been developed using the SRAC code system. Preliminary calculations were performed for analyzing the effective multiplication factors and power distribution in the core in comparison with MCNP5 calculations. The results show that the difference of the k_{eff} values between the two codes is within 271 pcm. The deviation of the relative power distributions

between the two codes is within 4% for most of the fuel bundles in the middle core, while the maximum deviation is about 7% which appears at peripheral bundles.

Acknowledgements

This work was funded by National Foundation for Science and Technology Development (NAFOSTED), Vietnam under grant 103.04-2017.20.

References

- [1] N. N. Dien, L. B. Vien, L. V. Vinh, D. V. Dong, N. X. Hai, P. N. Son, C. D. Vu, Results of operation and utilization of the dalat nuclear research reactor, Nuclear Science and Technology 4 (2014) 1–9.
- [2] SAR Report, Safety analysis report for The Dalat Nuclear Research Reactor, Technical Report, Nuclear Research Institute, Dalat, Vietnam, 2009.
- [3] K. Okumura, T. Kugo, K. Kaneko, K. Tsuchihashi, SRAC2006: A Comprehensive Neutronics Calculation Code System, Technical Report, JAEA-Data/Code 2007-004, 2006.
- [4] X-5 Monte Carlo Team, MCNP - A General Monte Carlo N-Particle Transport Code. Version 5, Technical Report, LA-UR-03-1987, April 24, 2003 (revised October 3rd, 2005), 2005.
- [5] M. Chadwick, P. Obložinský, M. Herman, N. Greene, R. McKnight, D. Smith, P. Young, et al., Endf/b-vii.0: Next generation evaluated nuclear data library for nuclear science and technology, Nuclear Data Sheets 107, 2006, pp. 2931–3060.
- [6] D. Q. Binh, N. Q. Huy, N. P. Lan, H. V. Thong, A method for determining the fuel burn-up distribution of nuclear research reactors by measurements at subcritical states, Annals of Nuclear Energy 24 (1997), pp. 1233–1240.
- [7] T. B. Fowler, D. R. Vondy, F. B. Kemshell, Nuclear reactor core analysis code: CITATION, Technical Report, ORNL-TM-2496, RSICC, 1971.

Evolution of bubble structure in ^{34}Si nucleus at finite temperature

Sự tiến hóa của cấu trúc “bubble” trong hạt nhân ^{34}Si tại nhiệt độ hữu hạn

L. Tan Phuc^a, N. Quang Hung^a

^a*Institute of Fundamental and Applied Sciences, Duy Tan University, Vietnam*

Viện nghiên cứu Khoa học Cơ bản và Ứng dụng, Đại học Duy Tân, Việt Nam

(Ngày nhận bài: 08/01/2018, ngày phản biện xong: 26/02/2018, ngày chấp nhận đăng: 20/03/2018)

Abstract

A special structure of the nucleon density, which is characterized by the depletion of the central density, is called nuclear bubble structure. It is well known that the formation of bubble structure is caused by the very low occupancy of s -orbitals, whose radial wave functions have the maximum peak in the interior of the nucleus. Three microscopic models are employed in the present work for investigating the evolution of bubble structure in ^{34}Si nucleus, namely the finite temperature Skyrme-Hartree-Fock (FTHF), the Hartree-Fock plus finite temperature Bardeen-Cooper-Schrieffer theory (FTBCS) and the Hartree-Fock plus exact pairing at finite temperature (FTEP). The Skyrme interaction MSk3, which well reproduces the binding and two-proton (neutron) separation energies, is used for our numerical calculations. The analysis of the numerical calculations for ^{34}Si nucleus shows that the bubble structure in the proton density distribution of this nucleus, which dominates at zero temperature, becomes less pronounced as temperature is increased and completely disappears when temperature reaches a critical value T_F , above which the depletion factor measuring the depletion of the central density vanishes. It is also found that due to the different behavior of pairing gaps, the values of T_F obtained within the FTEP is found equal to 4 MeV, which is smaller than that obtained within the FTBCS (4.5 MeV).

Keywords: nuclear bubble structure, non-relativistic mean field, nuclear density, pairing correlation, finite temperature.

Tóm tắt

Cấu trúc “bubble” trong hạt nhân nguyên tử được đặc trưng bởi sự sụt giảm của mật độ hạt nhân tại tâm. Nguyên nhân gây ra sự sụt giảm này là do giá trị rất nhỏ của số lượng tử chiếm đóng trên quỹ đạo s - nơi có hàm sóng phụ thuộc vào bán kính luôn có đỉnh cực đại tại tâm hạt nhân. Trong công trình này, chúng tôi sử dụng ba phương pháp vi mô để mô tả sự tiến hóa của cấu trúc “bubble” trong hạt nhân nguyên tử ^{34}Si tại nhiệt độ hữu hạn. Cụ thể là: phương pháp trường trung bình Hartree-Fock với lực Skyrme tại nhiệt độ hữu hạn (FTHF), phương pháp Hartree-Fock kết hợp với lý thuyết Bardeen-Cooper-Schrieffer tại nhiệt độ hữu hạn (FTBCS) và phương pháp Hartree-Fock với lời giải chính xác bài toán kết cặp tại nhiệt độ hữu hạn (FTEP). Nhiều phiên bản của tương tác dạng Skyrme đã được sử dụng và lực MSk3 đã được chọn bởi vì các giá trị của năng lượng liên kết và năng lượng tách hai proton thu được từ phương pháp FTEP tại nhiệt độ $T = 0$ trùng khớp với giá trị thực nghiệm. Phân tích kết quả tính toán cho hạt nhân ^{34}Si cho thấy sự tồn tại của cấu trúc “bubble” trong phân bố mật độ proton của hạt nhân này tại $T = 0$, sau đó giảm dần theo sự gia tăng nhiệt độ và hoàn toàn biến mất khi nhiệt độ lớn hơn hoặc bằng nhiệt độ giới hạn T_F . Tại $T \geq T_F$, hệ số đo độ sụt giảm mật độ hạt nhân tại tâm bị triệt tiêu hoàn toàn. Do sự khác nhau của khe năng lượng kết cặp, các giá trị T_F thu được trong tính toán FTEP (4 MeV) thấp hơn so với trong FTBCS (4.5 MeV).

Từ khóa: cấu trúc “bubble” hạt nhân, trường trung bình phi tương đối tính, mật độ hạt nhân, sự kết cặp, nhiệt độ hữu hạn.

1. Introduction

The depletion of the central nucleon density in the interior of an atomic nucleus, which is called the bubble structure, was discussed in many decades ago. The first prediction was proposed by Wilson in 1946 [1] when he employed the classical oscillation of bubble structure to describe the low-lying states of spherical nuclei. Until the 1970s, the first microscopic calculations for bubble structure were undertaken by Campi and Sprung [2]. Many works were presented by other authors ever since [3–7]. In recent years, bubble structure has been also investigated in superheavy and hyperheavy nuclei [8–11].

The depletion of central nuclear density is caused by the absence of s -orbital wave, whose function is characterized by a maximum peak at the interior of nucleus. Therefore, the s -orbital wave functions are expected to significantly contribute to the central density distribution and the absence of these waves leads to the depletion in the nucleon density at its center. The contribution of s -orbitals wave functions was investigated in Refs. [12, 13] indicating that the main contribution of the central density comes from the s -orbitals. Thus, the conditions of a possible bubble nucleus are the vacancy of s -orbitals, weak pairing correlations, and small fluctuations to ensure the very low s -orbitals occupancy [14].

For the reasons above, the candidates of possible bubble nuclei are those with spherical shape having zero or very low occupancy on the s -orbitals. Two of them are ^{22}O and ^{34}Si nuclei. ^{22}O has 14 neutrons in its shells. Thus, the $2s_{1/2}$ orbital is not occupied by the outermost neutrons whereas the proton shell is a magic shell with 8 protons. This makes it become a good candidate of bubble nucleus with the depletion factor of neutron density to be about $24 \sim 28\%$ [5]. The latter is defined as the measure of the

depletion magnitude of the nucleon density. The neighboring isotope, ^{24}O , has two neutrons filling the $2s_{1/2}$ -orbital, which is empty in ^{22}O . Therefore, ^{24}O , which is expected to have no bubble structure in its neutron density, is perceived to be an adjoint candidate of ^{22}O to investigate its bubble structure. With the same structure, an excellent candidate of proton bubble is ^{34}Si ($Z=14$, $N=20$) nucleus, which has the vacancy of $2s_{1/2}$ orbital in the proton shells and the rigid spherical neutron shells prevent any coupling and correlations. Similar with ^{24}O , ^{36}S , which has a full filling $2s_{1/2}$ orbital and has therefore no bubble structure, is also an adjoint candidate of ^{34}Si . These adjoint candidates can be used as a comparison to show clearly the contribution of s -orbital wave function into central nucleon density. The depletion factor of proton density in ^{34}Si was predicted about 40% in Ref. [5] with the occupancy of $2s_{1/2}$ orbital being around 0.08. Very recently, the very low occupancy of $2s_{1/2}$ orbital (about 0.17) in ^{34}Si has been detected experimentally by the one-proton removal technique [15] at zero temperature. This is the first experimental evidence to reinforce the existence of bubble structure in this nucleus.

It is well-known that the occupancies of levels upper Fermi surface, which are unoccupied at zero temperature, are not zero at finite temperature ($T \neq 0$) due to the temperature effect. They will increase with increasing T . Therefore, the occupancy of $2s_{1/2}$ orbital will also increase as T increases. This is expected to reduce the depletion of the central nucleon density leading to the disappearance of bubble structure when T is high enough. In the present paper, we employ three microscopic models to investigate the evolution of bubble structure in ^{34}Si nucleus at finite temperature, namely the finite temperature Skyrme-Hartree-Fock (FTHF), the Hartree-Fock plus finite temperature Bardeen-Cooper-Schrieffer theory (FTBCS) and the Hartree-Fock plus exact pairing at finite temperature (FTEP).

The density-dependent Skyrme forces, which are expected to produce better single-particle spectra than the density-independent ones [2], are employed to construct the nuclear mean-field.

2. Formalism

2.1. Finite temperature Hartree-Fock (FTHF)

To describe the nuclear system, the nuclear Hamiltonian is given as

$$\hat{H} = \hat{T} + \hat{V}, \quad (1)$$

where \hat{T} and \hat{V} being the nuclear kinetic energy and potentials, respectively. The potential \hat{V} can be expressed in terms of the two-body and three-body forces by using the Skyrme-type interaction [16]

$$V_{skyrme} = \sum_{i<j} v_{ij}^{(2)} + \sum_{i<j<k} v_{ijk}^{(3)}, \quad (2)$$

where $v_{ij}^{(2)}$ and $v_{ijk}^{(3)}$ are two and three body potentials, respectively. The three-body interactions are often approximated via the two-body ones using the nuclear density $\rho = \rho_p + \rho_n$ with ρ_p and ρ_n being the proton and neutron densities, respectively [17]. The Skyrme interaction is then written as

$$\begin{aligned} V_{skyrme} = & t_0(1+x_0P^\sigma)\delta(\vec{r}_1-\vec{r}_2) + \\ & + \frac{1}{2}t_1(1+x_1P^\sigma)\left[\delta(\vec{r}_1-\vec{r}_2)\vec{k}^2 + \vec{k}'^2\delta(\vec{r}_1-\vec{r}_2)\right] \\ & + t_2(1+x_2P^\sigma)\vec{k}'\delta(\vec{r}_1-\vec{r}_2)\vec{k} \\ & + iW_0(\vec{\sigma}_1+\vec{\sigma}_2)\vec{k}\times\delta(\vec{r}_1-\vec{r}_2)\vec{k} \\ & + \frac{1}{6}t_3(1+x_3P^\sigma)\delta(\vec{r})\rho^\alpha\left(\frac{\vec{r}_1+\vec{r}_2}{2}\right), \end{aligned} \quad (3)$$

where $\vec{k} = \frac{1}{2}(\vec{\nabla}_1 - \vec{\nabla}_2)$, \vec{k}' is the conjugate of \vec{k} and P^σ is the spin exchange operator with $\vec{\sigma}$ being the Pauli matrices. The function $\delta(\vec{r})$ is delta function with $\vec{r} = (\vec{r}_1 - \vec{r}_2)$. The parameters and ($i=0, 1, 2$ and 3) are the strength interaction parameters of the Skyrme force, which are adjusted to reproduce the experimental ground

state properties [18]. The Skyrme Hartree-Fock equations is written in spherical symmetry as [19, 20]

$$\left[-\nabla \frac{\hbar^2}{2m^*(\vec{r})} \nabla + U(\vec{r}) + U_{coul}(\vec{r}) + \frac{1}{j} W(\vec{r})(\nabla \times \sigma) \right] \varphi_j(\vec{r}) = \epsilon_j \varphi_j(\vec{r}), \quad (4)$$

where U, U_{coul} and W are the Skyrme, Coulomb and spin-orbit potentials, respectively. $m^*(\vec{r})$ is the effective mass. Equation (4) can be solved by an iterative process. The single-particle wave function φ_j , single-particle energy ϵ_j , binding energy and density quantities can be obtained by solving the HF equation (4) using the currents and densities. In particular, we refer to the form of these quantities in Ref. [21]:

$$\rho_q(r) = \sum_{n,l,j} f_j \frac{2j+1}{4\pi} \varphi_j(r)^2, \quad (5)$$

$$\begin{aligned} \tau_q(r) = & \sum_{n,l,j} f_j \frac{2j+1}{4\pi} \left[(\partial_r \varphi_j(r))^2 + \right. \\ & \left. + \frac{l(l+1)}{r^2} \varphi_j(r)^2 \right], \end{aligned} \quad (6)$$

$$\begin{aligned} J_q(r) = & \sum_{n,l,j} f_j \frac{2j+1}{4\pi} \left[j(j+1) - \right. \\ & \left. - l(l+1) - \frac{3}{4} \right] \frac{2}{r} \varphi_j(r)^2, \end{aligned} \quad (7)$$

where $\rho_q(r)$ is the nucleon density, $\tau_q(r)$ is the kinetic density, and $J_q(r)$ is the spin-orbit density. Notation q here denotes neutron or proton. The term f_j denotes the single-particle occupation number, which correspond to each j th level. At $T=0$, the HF solutions show that the levels below the Fermi surface ($\epsilon_j < \epsilon_F$) are fully occupied, and those above it ($\epsilon_j > \epsilon_F$) are empty. This leads the values of f_j , which correspond to the levels below (above) Fermi surface, always equal to 1 (0). At $T \neq 0$, the solutions of HF equation are treated in the grand

canonical ensemble(GCE), resulting the values of the single-particle occupation number follow the rule of the Fermi-Dirac distribution as

$$f_j = \frac{1}{e^{(\epsilon_j - \lambda)/T} + 1}, \quad (8)$$

where λ is the nuclear chemical potential, which is obtained from solving the particle number equation N with the degeneracies Ω_j for proton or neutron number, separately. The particle number equation is defined as

$$N = 2 \sum_j \Omega_j f_j, \quad \Omega_j = j+1/2. \quad (9)$$

Because of the distribution of f_j at $T \neq 0$ the obtained single-particle spectra consist of the single-particle levels below and above the chemical potential λ , whose values are obtained by discretizing the continuum [22]. This set of Eqs. (4)-(8) forms the finite temperature Hartree-Fock (FTHF) equations. The single-particle wave function φ_j , single-particle energies ϵ_j , and occupation number f_j , which depend on T , are obtained by solving these equations.

2.2. Pairing effect in hot nuclei

Pairing plays an important role in nuclear physics, especially the neutron-rich nuclei where the nuclear properties as the single-particle occupancies, single-particle spectra, nuclear level density, nuclear binding energy, and nucleon separation energy are affected by this effect [18, 19]. At $T = 0$, this effect is often described by employing the BCS [23, 24] theory or using the exact eigenvalues (EP). The latter is obtained by diagonalizing the pairing Hamiltonian, directly [25]. With increasing T , the pairing effect is quenched by temperature effect which breaks the nucleon pairs [26]. The methods using BCS and EP at finite temperature are presented below.

2.2.1. Finite temperature BCS theory (FTBCS)

The nuclear Hamiltonian include pairing which is constructed by employing BCS theory in atomic physics [19, 23, 24], is given as

$$H = \sum_j \epsilon_j a_{jm}^+ a_{jm} - G \sum_j a_{jm}^+ a_{j\bar{m}}^+ a_{j\bar{m}} a_{jm}, \quad (10)$$

where a_{jm} and a_{jm}^+ is the creation and annihilation operators of a nucleon which stays on j th level with projections $\pm m$ correspond to the single-particle energy ϵ_j and its degeneracies Ω_j . The symbol \sim denotes the time-reversal operator $\tilde{a}_{j\bar{m}} = (-1)^{j-m} a_{j-m}$. The pairing Hamiltonian (10) describes the pairing interaction between neutrons or protons via a monopole-pairing force with a constant pairing strength G . By applying the variational principle and Bogoliubov's transformation to minimize the expectation value of average Hamiltonian $\bar{H} = H - \lambda \hat{N}$ within the grand canonical ensemble (GCE), where $\hat{N} = \sum_j a_{jm}^+ a_{jm}$ is the particle number operator and λ is the chemical potential. In short, we refer to the results of this transformation process in Ref. [27] as a set of FTBCS equations for pairing gap Δ and particle number N :

$$\begin{cases} \Delta = G \sum_j \Omega_j u_j v_j (1 - 2n_j), \\ N = 2 \sum_j \Omega_j [n_j u_j^2 + (1 - n_j) v_j^2], \end{cases} \quad (11)$$

where u_j and v_j are the Bogoliubov's transformation coefficients, which are expressed as

$$u_j = \sqrt{\frac{1}{2} \left[1 + \frac{\epsilon_j - \lambda}{E_j} \right]}, \quad v_j = \sqrt{\frac{1}{2} \left[1 - \frac{\epsilon_j - \lambda}{E_j} \right]}, \quad (12)$$

with E_j and n_j are the quasi-particle energy and the quasi-particle occupation number, respectively. They are defined as

$$E_j = \sqrt{(\epsilon_j - \lambda)^2 + \Delta^2}, \quad (13)$$

$$n_j = \frac{1}{e^{E_j \beta} + 1}, \quad (14)$$

within the FTBCS, the single-particle occupation numbers f_j which contribute in the HF densities (5)-(7), are expressed in terms of the Bogoliubov coefficients and quasiparticle occupation numbers as

$$f_j = n_j u_j^2 + (1 - n_j) v_j^2. \quad (15)$$

It is well-known that the major deficiency of the FTBCS theory is the violation of the particle number. The quantity \hat{N} , which is added to the pairing Hamiltonian to conserve the particle number, is only the average value. With increasing T , the FTBCS pairing gap collapses at a critical temperature $T_c \sim 0.57\Delta(T=0)$ and the pairing effect is quenched at this temperature. However, some approximations beyond the FTBCS have indicated that the pairing gap at $T > T_c$ does not vanish [26]. Instead, it monotonically decreases with increasing T .

2.2.2. Exact pairing at finite temperature (FTEP)

Another access to pairing effect is to solve it exactly. This method, which is called exact pairing (EP), presents a new way to diagonalize directly the pairing Hamiltonian (10) using quasi-spin algebras $SU(2)$ [25]. The direct diagonalization of the pairing Hamiltonian allows us to obtain all the exact eigenvalues E_s and single-particle occupation number $f_j^{(s)}$ at $T=0$ and at different total seniority S , which is the total number of unpaired particles. Using these exact eigenvalues, one can construct the exact partition function within the canonical ensemble at $T \neq 0$ as [26]

$$Z(T) = \sum_S 2^S e^{-E_s/T}. \quad (16)$$

All of the thermodynamic quantities such as free energy F , total energy E , entropy S , heat

capacity C , and pairing gap Δ can be calculated by using this partition function, namely

$$F = -T \ln Z, \quad S = -\frac{\partial F}{\partial T}, \quad (17)$$

$$E = F + TS, \quad C = \frac{\partial E}{\partial T} \quad (18)$$

$$\Delta = \sqrt{-GE_{pair}}, \quad (19)$$

$$E_{pair} = E - \sum_j (2\epsilon_j - Gf_j) f_j,$$

where the exact single-particle occupation number f_j at $T \neq 0$ is given as

$$f_j = \frac{1}{Z} \sum_S 2^S f_j^{(s)} e^{-E_s/T}. \quad (20)$$

Within this FTEP method, the particle number always conserves exactly not only at zero temperature but also at finite temperature. The exact pairing gap decreases with increasing T but does not collapse at $T = T_c$ as the FTBCS pairing gap.

3. Results and discussions

The numerical calculations within the FTBF, FTBCS and FTEP are undertaken for ^{34}Si to study its bubble structure which is predicted to be dominant at $T=0$. The Skyrme interactions are tested within the HFEP using full center-of-mass correction for ^{34}Si at $T=0$. The pairing strength G is adjusted to reproduce the experimental binding energy.

Methods	FTBF*	FTBCS*	FTEP*	FTEP*	HFB[29]	RMF[5]	SM[5]
Skyrme forces	MSk3	MSk3	MSk3	BSk14	BSk14	NL3	
F	24%	19%	19%	14%	15%	37%	41%

Table 1. The values (%) of depletion factor F obtained within different methods at $T=0$. The asterisk (*) denotes the methods using in the present work.

Because ^{34}Si has a neutron closed shell ($N=20$) which prevents any correlation; the pairing effect within the FTBCS and FTEP is treated only for proton using the single-particle energies obtained from HF equations. In addition, due to the limitation on the size of the

matrix to be diagonalized, which is not required in the FTBF and FTBCS, the FTEP is carried out using a truncated spectrum, which consists of the single-particle levels around the Fermi surface. For ^{34}Si , seven proton levels are used, namely $1d_{5/2}$, $2s_{1/2}$, $1d_{3/2}$, $1f_{7/2}$, $2p_{3/2}$, $1f_{5/2}$ and $2p_{1/2}$. In this

space, the first level locates below the Fermi surface and the rest are above it. The remaining inner core including eight protons is a magic core which does not contribute to pairing correlation. The independent particle model (IPM), in which the single-particle occupation numbers obey the Fermi-Dirac distribution as Eqs. (8), is used for the levels outside the truncated levels. The occupation numbers obtained from Eqs. (8), (15), and (20) are used as input for density quantities in Eqs. (5), (6), and (7). To be consistent, the above single-particle configuration, is also used for the FTBCS calculations. Recently, the occupancy of $2s_{1/2}$ orbital in ^{34}Si at $T = 0$ has been measured in Ref. [15], whose value is found to be 0.17 ± 0.03 , which corresponds to the occupation number $f_{2s_{1/2}} = 0.085 \pm 0.015$. This very low occupancy of $2s_{1/2}$ orbital causes the depletion of proton density at its center in this nucleus. Therefore, the value of $f_{2s_{1/2}}$ in the interval $[0.07, 0.1]$ is an important quantity and should be used as a criterion to choose the appropriate Skyrme interaction using for the FTEP calculation.

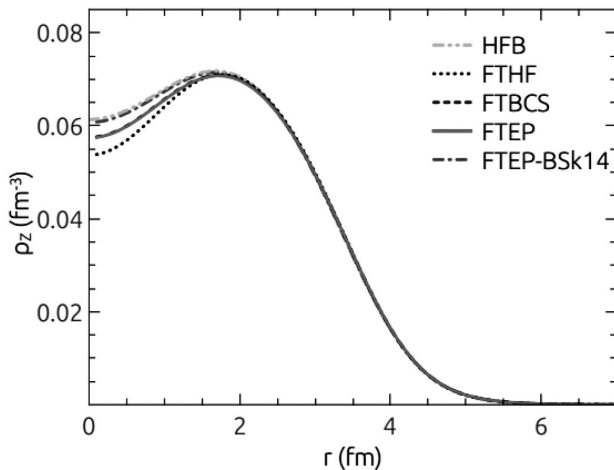


Figure 1. Proton density ρ_z for ^{34}Si obtained within the FTHF, FTBCS, FTEP and HFB at $T = 0$.

By adjusting G to reproduce the experimental binding energy per nucleon $\text{BE}/A = -8.336$ MeV, the FTEP calculation using the MSk3 Skyrme interaction [28] at $T = 0$ also reproduces the experimental value of $2s_{1/2}$ occupation number ($f_{2s_{1/2}} = 0.09$). The obtained value of pairing strength

G is then 0.55 MeV and it is kept uncharged with T . The same value of $f_{2s_{1/2}}$ is reproduced within the FTBCS calculation using the same MSk3 interaction. By doing so, the obtained pairing gaps within the FTBCS and FTEP at $T = 0$ are 0.85 and 1.34 MeV, respectively. By reproducing well the experimental binding energy, we are also able to reproduce the experimental two-proton separation energy $S_{2p} = B(N; Z) - B(N; Z - 2) = 33.7$ MeV, with $B(N; Z)$ being the binding energy of a nucleus with N neutrons and Z protons. The BSk14 interaction is also used in order to compare the results obtained within the present approaches with those obtained within the Hartree-Fock-Bogolyubov (HFB) using the same interaction [29].

To evaluate the depletion of the central nucleon density, one defines the depletion factor, whose expression is

$$F = \frac{\rho_{max} - \rho_{cent}}{\rho_{max}}, \quad (21)$$

where ρ_{max} and ρ_{cent} are the nucleon maximum density and central density ($r = 0$), respectively. The values of depletion factor F obtained within the FTHF, FTBCS, and HFEP at $T = 0$ in comparison with those obtained within other approaches such as HFB [29], relativistic mean field (RMF) [5], and shell model (SM) [5] are presented in Table 1. The proton densities obtained within the FTHF, FTBCS, FTEP (by using the Skyrme MSk3) and FTEP-BSk14 (by using the Skyrme BSk14) at $T = 0$ are also shown in Fig. 1. The FTBCS and FTEP calculations with MSk3 interaction produce the depletion factor $F = 19\%$, whereas the FTHF one (without pairing) shows $F = 24\%$. The depletion factors obtained within the FTEP and HFB [29] using BSk14 ($F \sim 15\%$) are smaller than the FTEP prediction using MSk3. This comparison indicates that the pairing effect, employed in the HFB in Ref. [29], is stronger than that treated within our calculations for ^{34}Si , a doubly magic nucleus. This result implies that for this nucleus, the MSk3 interaction is more

suitable than the BSk14 one and therefore it will be used for further investigation within the present study. Our predictions also indicate that the pairing correlation in a doubly magic nucleus ^{34}Si should be small but can not be ignored as

mentioned in Ref. [5]. In the latter, the depletion factor F is found to be around 40% with $f_{2s_{1/2}} \sim 0.08$ (see e.g., Tables II and IV in Ref. [5]) instead of the experimental value of 0.09 used in our FTBCS and FTEP calculations.

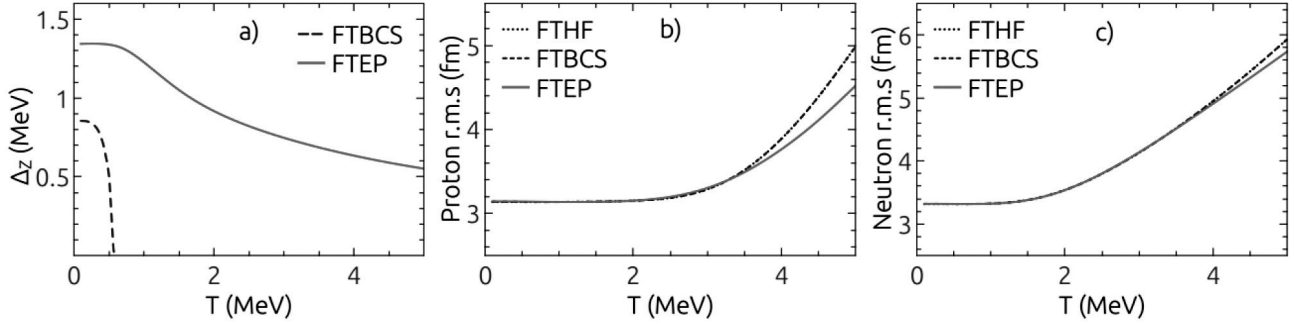


Figure 2. The proton pairing gaps (a), root-mean square radii of protons (b), and neutrons (c) in ^{34}Si obtained within the FTHF, FTBCS, and FTEP.

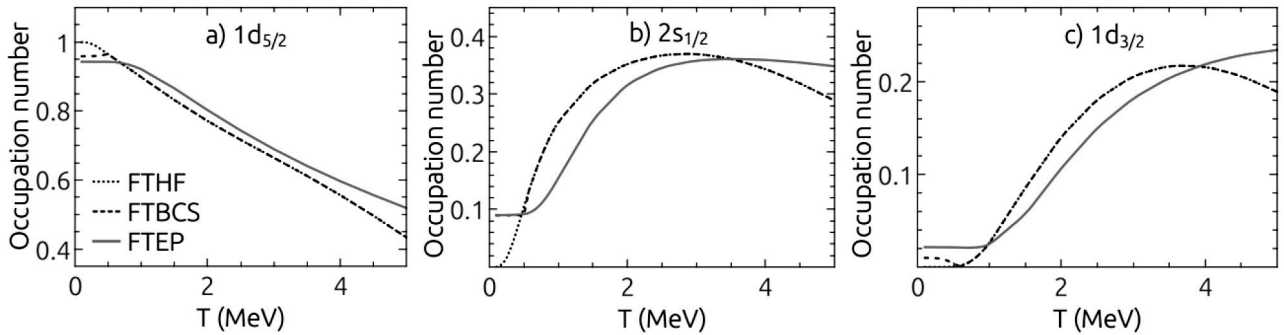


Figure 3. The single-particle occupation numbers of $1d_{5/2}$ (a), $2s_{1/2}$ (b), and $1d_{3/2}$ (c) proton levels in ^{34}Si obtained within the FTHF, FTBCS, and FTEP.

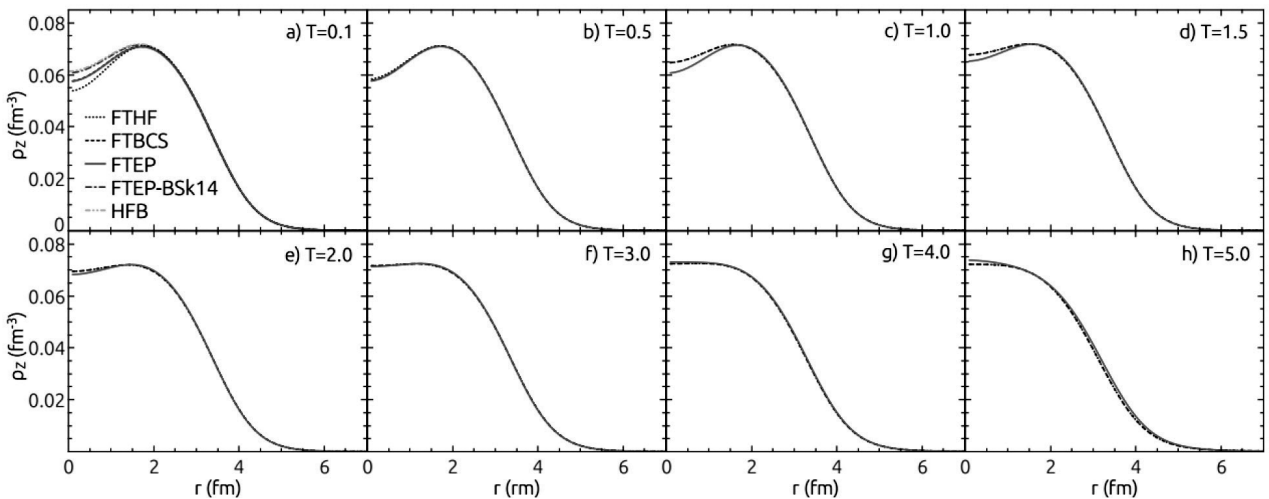


Figure 4. The proton densities of ^{34}Si at several temperatures obtained within the FTHF, FTBCS, and FTEP.

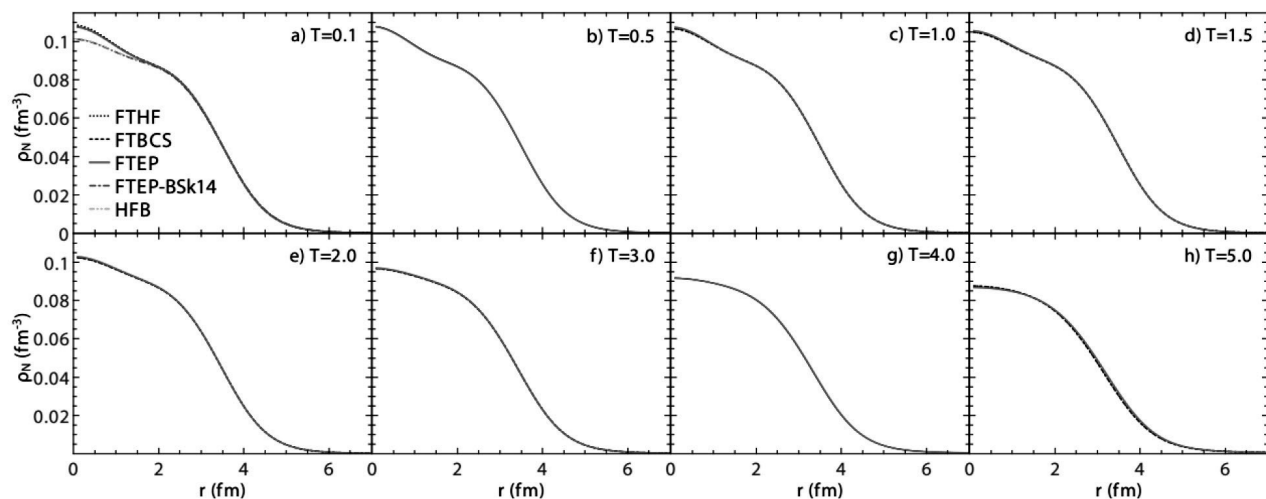


Figure 5. The same as Fig. 3 but for neutron densities in ^{34}Si .

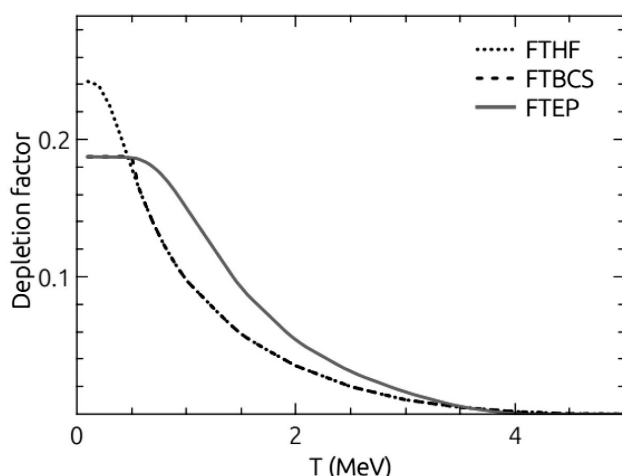


Figure 6. The depletion factor for the proton density of ^{34}Si obtained within the FTHF, FTBCS, and FTEP.

Figure 2(a) shows the pairing gaps as functions of T obtained within the FTBCS and FTEP calculations using the MSk3 interaction. With increasing T , the FTBCS pairing gap collapses at $T_c \sim 0.57$ MeV and the pairing effect is quenched starting from this temperature. At $T > T_c$, the FTBCS results coincide with the FTHF ones as their occupation numbers are exactly the same [see e.g., Eq. (8)]. The pairing gap obtained within the FTEP is always finite in the whole temperature region from 0 to 5 MeV as shown in Fig. 2(a). Furthermore, this non-vanishing pairing gap within the FTEP at high T makes the proton root-mean-square radius (rms) slowing down its increase with T at $T > 2$ MeV as shown in Fig. 2(b). Because of the absence of the neutron pairing in

this neutron closed-shell nucleus, the neutron rms predicted within three methods are nearly the same as seen in Fig. 2(c). A slight difference between the neutron rms obtained within the FTBCS (FTHF) and FTEP at $T > 2$ MeV comes from the difference between the FTBCS (FTHF) and FTEP proton pairings, which affect not only the proton but also the neutron parts of the HF potential and wave functions. Both of proton and neutron rms increase with increasing T . This result agrees with that predicted in Refs. [30, 31].

The single-particle occupation numbers obtained within the FTHF, FTBCS, and FTEP at $T > 0$ are shown in Fig. 3 for three levels around the Fermi surface, namely $1d_{5/2}$, $2s_{1/2}$, and $1d_{3/2}$ levels. It is well-known that the occupied (unoccupied) levels decrease (increase) their occupancies with increasing T . Within the FTHF, the occupation number of the level below Fermi surface ($1d_{5/2}$) decreases from 1 to 0.43, whereas those of the two levels above it increase from 0 to 0.29 ($2s_{1/2}$) and 0.19 ($1d_{3/2}$) when T increases from 0 to 5 MeV. At $T < T_c$, the occupation numbers obtained within the FTBCS and FTEP are different from that obtained within the FTHF because of the existence of the pairing gap. The FTBCS and FTEP occupation numbers are also different because of the difference of their pairing gaps [see Fig. 2(a)]. At $T > T_c$, the FTBCS gap is

queched whereas the FTEP gap is still finite until $T \approx 5$ MeV. Therefore, the occupation numbers of the levels below (above) the Fermi surface obtained within the FTEP decrease (increase) slower than those obtained within the FTHF and FTBCS (see Fig. 3).

To investigate the evolution of bubble structure in ^{34}Si at $T > 0$, its proton densities ρ_Z obtained within the FTHF, FTBCS, and FTEP are presented in Fig. 4. The proton bubble can be clearly observed in the central density at $T = 0$. The bubble structure predicted by the FTBCS and FTEP, which include pairing, is less pronounced than the FTHF prediction which does not take into account the pairing correlation. With increasing T , the bubble structure becomes shallower and disappears at a given $T = T_F$ above which the bubble structure completely vanishes as seen in Fig. 4. The gradual disappearance of proton bubble structure seen in Fig. 4 can be explained by the increase in the occupancy of $2s_{1/2}$ level at $T > 0$ as presented in Fig. 2(b). When T increases from 0.1 to 2 MeV, due to the presence of exact pairing the variation of the FTEP central proton density occurs slower than the FTBCS one. However, at $T > 2$ MeV, the presence of the FTEP pairing gap leads to the disappearance of bubble structure at $T_F^{FTEP} = 4$ MeV. This critical temperature is lower than the FTBCS value $T_F^{FTBCS} = 4.5$ MeV, which coincides with the FTHF one at $T > T_C$ as can be seen in Fig. 6. Combining with the results presented in Fig. 3(b), one can easily find that the proton bubble of ^{34}Si nucleus completely disappear when the occupation number $f_{2s_{1/2}}$ reaches a value of about 0.35. This result also indicates that the pairing effect in this doubly magic nucleus is not strong enough to cause a significant difference between the FTBCS and FTEP predictions. Figure 5 shows the neutron densities obtained within three methods. For the neutron, its $2s_{1/2}$ orbital is always fully occupied. Therefore, the

central neutron density is built up by the fully contribution of $2s_{1/2}$ wave function, leading to the inexistence of the neutron bubble structure. No significant differences are seen in the neutron densities obtained within three methods because all of them do not include the neutron pairing in this case as the neutron number is magic.

4. Conclusions

The bubble structure of ^{34}Si , which is caused by the very low occupancy of the $2s_{1/2}$ orbital, has been studied with three microscopic methods, namely the finite-temperature Hartree-Fock (FTHF), the finite-temperature BCS theory (FTBCS), and the exact solutions of the pairing Hamiltonian at finite temperature (FTEP). By using the Skyrme MSk3 interaction, our calculations within the FTEP reproduce well the binding energies and two-proton separation energies of this ^{34}Si nucleus. By reproducing also the occupancy of $2s_{1/2}$ level, whose experimental value has been recently reported at $T = 0$, the depletion of proton bubble predicted within the FTBCS and FTEP is found to be about 19%, whereas it is about 24% with the FTHF calculation, which does not treat the pairing correlation. With increasing T , the proton bubble becomes less pronounced and completely disappears when temperature reaches a critical value $T_F \sim 4.5$ MeV within the FTBCS and $T_F \sim 4$ MeV within the FTEP. At $T \geq T_F$, the occupation number of $2s_{1/2}$ level is found to be equal or higher than 0.35. In general, a stronger pairing is seen in our calculations as compared to those predicted in Ref. [5]. Exact thermal pairing also makes the central proton density in ^{34}Si less sensitive to the change of T from 0 to 2 MeV.

The present work is funded by the National Foundation for Science and Technology Development (NAFOSTED) of Vietnam under the Grant No. 103.04-2017.69.

References

- [1] H. A. Wilson, A spherical shell nuclear model, *Phys. Rev.* **69** (1946) 538.
- [2] X. Campi, D. W. L. Sprung, Possible bubble nuclei ^{36}Ar and ^{200}Hg , *Phys. Lett. B* **46** (1973) 291–295.
- [3] C. Y. Wong, Toroidal and spherical bubble nuclei, *Ann. Phys.* **77** (1973) 279–353.
- [4] E. Khan, M. Grasso, J. Margueron, N. V. Giai, Detecting bubbles in exotic nuclei, *Nucl. Phys. A* **800** (2008) 37–46.
- [5] M. Grasso *et al*, Nuclear “bubble” structure in ^{34}Si , *Phys. Rev. C* **79** (2009) 034318.
- [6] J. M. Yao, S. Baroni, M. Bender, P. H. Heenen, Beyond-mean-field study of the possible “bubble” structure of ^{34}Si , *Phys. Rev. C* **86** (2012) 014310.
- [7] J. M. Yao, H. Mei, Z. P. Li, Does a proton “bubble” structure exist in the low-lying states of ^{34}Si ?, *Phys. Lett. B* **723** (2013) 459–463.
- [8] K. Dietrich, K. Pomorski, On the shell structure of nuclear bubbles, *Nucl. Phys. A* **627** (1997) 175–221.
- [9] M. Bender, K. Rutz, P. G. Reinhard, J. A. Maruhn, W. Greiner, Shell structure of superheavy nuclei in self-consistent mean-field models, *Phys. Rev. C* **60** (1999) 034304.
- [10] J. Decharge, J. F. Berger, M. Girod, K. Dietrich, Bubbles and semi-bubbles as a new kind of superheavy nuclei, *Nucl. Phys. A* **716** (2003) 55–86.
- [11] J. C. Pei, F. R. Xu, P. D. Stevenson, Density distributions of superheavy nuclei, *Phys. Rev. C* **71** (2005) 034302.
- [12] J. M. Cavedon *et al*, Is the shell-model concept relevant for the nuclear interior?, *Phys. Rev. Lett.* **49** (1982) 978–981.
- [13] V. R. Pandharipande *et al*, Independent particle motion and correlations in fermion systems, *Rev. Mod. Phys.* **69** (1997) 981–992.
- [14] M. Grasso *et al*, Bubbles in exotic nuclei, *Int. J. Mod. Phys. E* **18** (2009) 2009.
- [15] A. Mutschler *et al*, A proton density bubble in the doubly magic ^{34}Si nucleus, *Nature* **13** (2017) 152–156.
- [16] T. H. R. Skyrme, The effective nuclear potential, *Nucl. Phys.* **9** (1958) 615–634.
- [17] D. Vautherin, D. M. Brink, Hartree-Fock calculations with Skyrme’s interaction. I. Spherical nuclei, *Phys. Rev. C* **5** (1972) 626–647.
- [18] L. Tan Phuc, N. Quang Hung, Mean-field description of nuclear ground-state properties, *Journal of Science and Technology, Duy Tan University* **3(22)** (2017) 34–40.
- [19] P. Ring, P. Schuck, *The nuclear many-body problems* (Springer-1980).
- [20] E. Yuksel, E. Khan, K. Bozkurt, G. Colo, Effect of temperature on the effective mass and the neutron skin of nuclei, *Eur. Phys. J. A* **50** (2014) 160.
- [21] P. Ring, P. Schuck, *Computational nuclear physics 1* (Springer-1990).
- [22] G. Colò *et al*, Self-consistent RPA calculations with Skyrme-type interactions: The `skyrme_rpa` program, *Comput. Phys. Commun.* **184** (2013) 142–161.
- [23] J. Bardeen, L. N. Cooper, J. R. Schrieffer, Microscopic theory of superconductivity, *Phys. Rev.* **106** (1957) 162–164.
- [24] J. Bardeen, L. N. Cooper, J. R. Schrieffer, Theory of superconductivity, *Phys. Rev.* **108** (1957) 1175–1204.
- [25] A. Volya, B. A. Brown, V. Zelevinsky, Exact solution of the nuclear pairing problem, *Phys. Lett. B* **509** (2001) 37–42.
- [26] N. Quang Hung, N. Dinh Dang, Exact and approximate ensemble treatments of thermal pairing in a multilevel model, *Phys. Rev. C* **79** (2009) 054328.
- [27] N. Quang Hung, N. Dinh Dang, Pairing in hot rotating nuclei, *Phys. Rev. C* **78** (2008) 064315.
- [28] F. Tondeur, S. Goriely, J. M. Pearson, M. Onsi, Towards a hartree-fock mass formula, *Phys. Rev. C* **62** (2000) 024308.
- [29] <https://www-nds.iaea.org/RIPL-3/>
- [30] P. Bonche, S. Levit, D. Vautherin, Statistical properties and stability of hot nuclei, *Nucl. Phys. A* **436** (1985) 265–293.
- [31] A. N. Antonov, D. N. Kadrev, M. K. Gaidarov, P. Sarriguren, E. M. de Guerra, Temperature dependence of the symmetry energy and neutron skins in Ni, Sn, and Pb isotopic chains, *Phys. Rev. C* **95** (2017) 024314.

Thermoluminescence Property of Eu^{3+} doped $\text{Sr}_3\text{B}_2\text{O}_6$ Phosphors Prepare by Combustion Method

Tính chất nhiệt phát quang của $\text{Sr}_3\text{B}_2\text{O}_6$ pha tạp Eu^{3+} chế tạo bằng phương pháp nổ

Ho Van Tuyen^a, Nguyen Thi Thai An^a, Le Van Khoa Bao^b, Nguyen Ha Vi^c

^a*Institute of Research and Development, Duy Tan University, Vietnam
Viện Nghiên cứu và Phát triển Công nghệ cao, Đại học Duy Tân, Việt Nam*

^b*Department of Scientific Management, Duy Tan University, Vietnam
Phòng Quản lý Khoa học, Đại học Duy Tân, Việt Nam*

^c*The Faculty of Natural Sciences, Duy Tan University, Vietnam
Khoa Khoa học Tự nhiên, Đại học Duy Tân, Việt Nam*

(Ngày nhận bài: 26/02/2018, ngày phản biện xong: 12/03/2018, ngày chấp nhận đăng: 20/03/2018)

Abstract

This work illuminates the effects of Eu^{3+} concentrations on thermoluminescence (TL) behavior of $\text{Sr}_3\text{B}_2\text{O}_6:\text{Eu}^{3+}$ phosphor prepared by using the combustion method. The structural properties were estimated by X-ray diffraction (XRD). The XRD result indicates that the synthesized samples have a rhombohedral phase and the particle's average size was found to be 37 nm. TL glow curve of $\text{Sr}_3\text{B}_2\text{O}_6:\text{Eu}^{3+}$ phosphor, which was irradiated by β -ray, was recorded at a heating rate of $2^\circ\text{C}/\text{s}$. The activation energy, order of kinetic and frequency factor were evaluated through TL glow curve using a peak shape method of R. Chen. The result shows that the activation energy of trap locating around 271°C was affected by Eu^{3+} concentrations.

Keywords: $\text{Sr}_3\text{B}_2\text{O}_6$, thermoluminescence, Eu^{3+}

Tóm tắt

Bài báo này trình bày ảnh hưởng của nồng độ Eu^{3+} đến tính chất nhiệt phát quang của vật liệu $\text{Sr}_3\text{B}_2\text{O}_6:\text{Eu}^{3+}$ được tổng hợp bằng phương pháp nổ. Đặc trưng cấu trúc được phân tích bằng nhiễu xạ tia X (XRD). Kết quả XRD chỉ ra các mẫu đã chế tạo có pha cấu trúc rhombohedral và kích thước hạt trung bình vào khoảng 37 nm. Đường cong nhiệt phát quang tích phân của $\text{Sr}_3\text{B}_2\text{O}_6:\text{Eu}^{3+}$ sau khi chiếu xạ bằng tia β được ghi lại với tốc độ gia nhiệt $2^\circ\text{C}/\text{s}$. Năng lượng kích hoạt, bậc động học và hệ số tần số đã được xác định từ đường cong nhiệt phát quang tích phân bằng cách sử dụng phương pháp phân tích dạng đỉnh của R. Chen. Kết quả cho thấy giá trị năng lượng ứng với bẫy ở gần 271°C chịu ảnh hưởng bởi nồng độ Eu^{3+} pha tạp.

Từ khóa: $\text{Sr}_3\text{B}_2\text{O}_6$, nhiệt phát quang, Eu^{3+}

INTRODUCTION

Rare earth (RE) elements doped luminescence materials have researched and applied in several decades and they have become important materials in light technology, information display and solid-state laser medium [1-4]. Particularly

in last decade, the phosphors which based on borate matrices have attracted more researchers due to their advantages, such as: low prepared temperature, easy change in components of phosphor and cheap raw materials [2, 5]. The optical properties of $\text{Sr}_3\text{B}_2\text{O}_6$ phosphor doped Eu

have been researched and published from 2007 to presents [4, 6-13]. In this period, our research group has contributed some literature focusing on several optical properties of Eu^{3+} doped $\text{Sr}_3\text{B}_2\text{O}_6$ at room temperature, such as: structural information around Eu^{3+} ion, Eu^{3+} concentration-dependence of photoluminescence intensity and the energy transfer between Tb^{3+} and Eu^{3+} [14, 15]. However, there is little literature that mentions to thermoluminescence (TL) property of $\text{Sr}_3\text{B}_2\text{O}_6:\text{Eu}^{3+}$ phosphor. It is known that TL spectra provide the information of intrinsic defects in materials. In addition, TL is a widely used method for detecting the dose of various energetic rays such as X-, β - or γ -rays [16].

In this work, we present an experimental study of thermoluminescence property of $\text{Sr}_3\text{B}_2\text{O}_6:\text{Eu}^{3+}$ and the effect of Eu^{3+} concentration on it.

EXPERIMENTAL

$\text{Sr}_3\text{B}_2\text{O}_6$ phosphors doped with various Eu^{3+} concentrations (1 mol.%, 3 mol.%, 5 mol.% and 7 mol.%) were prepared by combustion method. Raw materials include $\text{Sr}(\text{NO}_3)_2$ (Merck), $\text{Eu}(\text{NO}_3)_3$ (Sigma), H_3BO_3 acid (AR) and urea (Sigma). The used urea amount was calculated properly to supply enough fuel for the combustion process. The amount of ingredients was mixed and heated at 70 °C in 2 hours by a magnetic stirrer to form a white gel. In next step, the gel was combusted at 600 °C for 5 minutes then the temperature was decreased to room temperature in order to obtain a white powder sample.

Phase structure of the prepared samples was determined by X-ray diffraction (XRD) pattern using a Bruker D8-advance X-ray diffractometer. A beta-source of ^{90}Sr was used for irradiating the samples. Thermoluminescence characteristics were evaluated by glow curves using Harshaw 3500 TLD reader.

RESULTS AND DISCUSSIONS

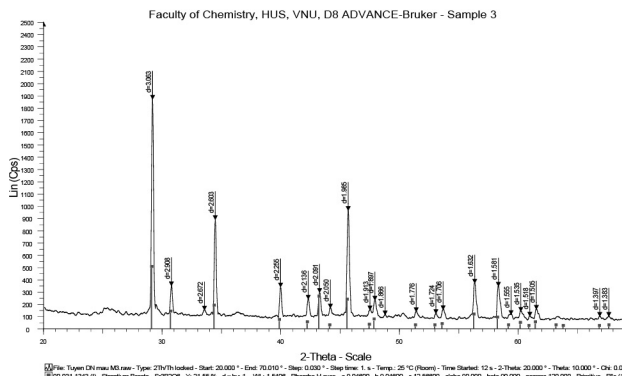


Figure 1. XRD pattern of $\text{Sr}_3\text{B}_2\text{O}_6:\text{Eu}^{3+}$ (3 mol.%) sample

Fig.1 presents the XRD pattern of the prepared sample $\text{Sr}_3\text{B}_2\text{O}_6:\text{Eu}^{3+}$ (3 mol.%). The diffraction peaks of the XRD pattern can be assigned for the rhombohedral phase, which is well fitted with the standard data of $\text{Sr}_3\text{B}_2\text{O}_6$ (JCPDS PDF: 31-1343). The absence of any other phases shows that the pure $\text{Sr}_3\text{B}_2\text{O}_6$ sample can be obtained by using combustion method. The average particle size was calculated using Sherrer's formula [17].

$$d = \frac{0.9\lambda}{\beta \cdot \cos\theta} \quad (1)$$

where, $\lambda = 0.154$ nm is the X-ray wavelength, β is the full-width at half maximum (FWHM) intensity (in radian), θ is the diffraction angle (in degrees), d is the average size of the particle. The value d of the prepared samples is around 37 nm.

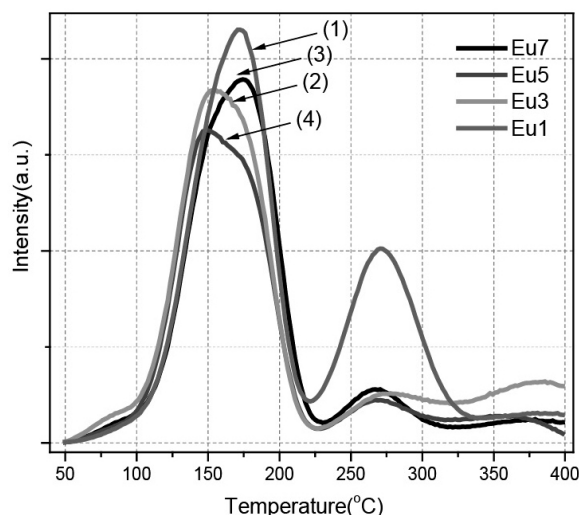


Figure 2. Glow curve of $\text{Sr}_3\text{B}_2\text{O}_6:\text{Eu}^{3+}$ phosphors with various Eu^{3+} concentrations

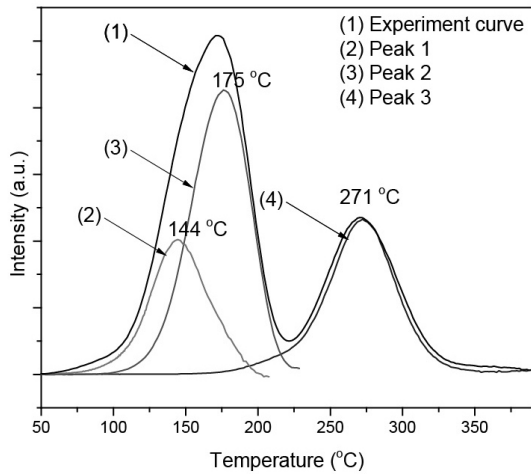


Figure 3. TL peaks of Sr₃B₂O₆:Eu³⁺ (1 mol.%) with thermal cleaning technique

After an irradiation under 3 Gy β-ray, the prepared samples were measured TL glow curve. All samples were kept the same at 2 mg and the heating rate was constant of 2 °C/s for the TL measuring. Fig.2 shows the glow curves of the samples with various Eu³⁺ concentrations. TL glow curves have the same shape and they include three peaks: One peak at high temperature around 271 °C and two overlapped peaks in the range from 100 °C to 200 °C. In order to separate these peaks, a thermal cleaning technique was used. The result for Sr₃B₂O₆:Eu³⁺ (1 mol%) after using the thermal cleaning method is shown in Fig.3. Indeed, the glow curve comprises three peaks which locate at 144 °C, 175°C, and 271 °C.

Activation energy (E_a) and frequency factor (s) of TL peaks were determined by peak sharp method of R. Chen [18]. This method based on a symmetrical property of peak which the parameters include the full width of the peak at its half-height ($\omega = T_2 - T_1$), its high-temperature half-width ($\delta = T_2 - T_m$) and its low-temperature half-width ($\tau = T_m - T_1$). The symmetry factor (μ_g) is defined by the following equation [18]:

$$\mu_g = \delta/\omega = (T_2 - T_m)/(T_2 - T_1) \quad (2)$$

For Sr₃B₂O₆:Eu³⁺ samples, the symmetry factors are close to 0.52 which shows they belong to the second-order kinetic. The activation energy

can be evaluated by using the general formula:

$$E_a = c_\gamma(k.T_m/\gamma) - b_\gamma(2k.T_m) \quad (3)$$

where, γ stands for τ , δ , and ω . k is the Boltzmann constant. The values of c_γ and b_γ for second-order kinetic are listed in Table 1, which were provided from ref. [18, 19]. The frequency factor (s) can be determined by inserting E_a and the known values b (2 for second-order kinetics), β (heating rate 2 °C/s) into formula [16]:

$$\frac{\beta E}{kT_m^2} = s \left[1 + (b-1) \frac{2kT_m}{E} \right] \exp \left(-\frac{E}{kT_m} \right) \quad (4)$$

The activation energy and the frequency factor for all samples calculated from equations (3) and (4) are listed in Table 2. The results of all are shown in Fig.4. It shows that the energies of peak 1 and peak 2 are little different with various Eu³⁺ concentrations, whereas the energy of peak 3 increases with the increasing of Eu³⁺ concentration. This suggested that the dopant Eu³⁺ concentration affects the deep trap in the Sr₃B₂O₆ material.

Table 1. Values of c_γ , b_γ depending on τ , δ or ω

	τ	δ	ω
c_γ	1.81	1.71	3.54
b_γ	2.0	0	1.0

Table 2. Values of activation energy (E_a) and frequency factor (s)

Sample (mol% Eu ³⁺)	Peak number	T _{max} (°C)	Activated Energy (eV)			Frequency factor (s)
			Peak1	Peak 2	Peak 3	
1	Peak 1	144	1.08			1.83x10 ¹²
	Peak 2	175		1.13		7.34x10 ¹¹
	Peak 3	271			1.52	3.73x10 ¹³
3	Peak 1	144	1.02			3.15x10 ¹¹
	Peak 2	179		1.21		4.08x10 ¹²
	Peak 3	279			1.50	4.78x10 ¹²
5	Peak 1	143	1.08			2.69x10 ¹²
	Peak 2	179		1.24		9.09x10 ¹²
	Peak 3	268			1.76	4.00x10 ¹⁵
7	Peak 1	144	1.07			1.24x10 ¹²
	Peak 2	174		1.14		1.17x10 ¹²
	Peak 3	269			1.93	1.46x10 ¹⁷

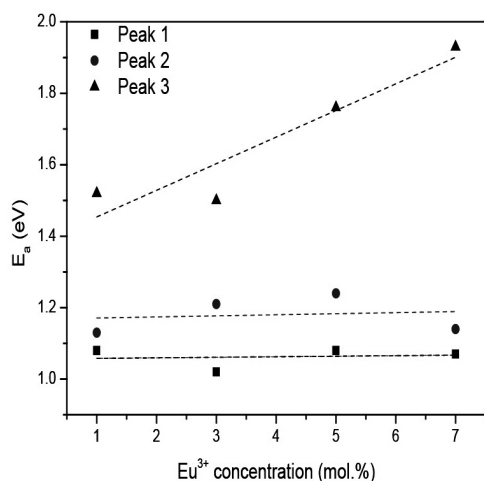


Figure 4. The relationship between the activation energy and Eu^{3+} concentrations

CONCLUSIONS

The analysis from glow curves of the synthesized samples indicates that all $\text{Sr}_3\text{B}_2\text{O}_6$ samples with various Eu^{3+} concentration have three traps in the host material. The maximum position of peaks seems not change. However, the activation energy of peak 3 (around 271°C) increases with the increasing of Eu^{3+} concentrations.

References

- [1] S. Liu, G. Zhao, H. Ying, J. Wang, G. Han, Eu/Dy ions co-doped white light luminescence zinc-aluminoborosilicate glasses for white LED, *Optical Materials*, 31 (2008) 47-50.
- [2] S. Ekamparam, K.C. Patil, M. Maaza, Synthesis of lamp phosphors: facile combustion approach, *Journal of Alloys and Compounds*, 393 (2005) 81-92.
- [3] Z.C. Wu, J.X. Shi, J. Wang, H. Wu, Q. Su, M.L. Gong, Synthesis and luminescent properties of $\text{SrAl}_2\text{O}_4:\text{Eu}^{2+}$ green-emitting phosphor for white LEDs, *Materials Letters*, 60 (2006) 3499-3501.
- [4] C.-K. Chang, T.-M. Chen, $\text{Sr}_3\text{B}_2\text{O}_6:\text{Ce}^{3+},\text{Eu}^{2+}$: A potential single-phased white-emitting borate phosphor for ultraviolet light-emitting diodes, *Applied Physics Letters*, 91 (2007) 081902.
- [5] Z.-C. Wu, P. Wang, J. Liu, C. Li, W.-H. Zhou, S.-P. Kuang, Improved photoluminescence properties of a new green $\text{SrB}_2\text{O}_4:\text{Tb}^{3+}$ phosphor by charge compensation, *Materials Research Bulletin*, 47 (2012) 3413-3416.
- [6] W.-S. Song, Y.-S. Kim, H. Yang, Yellow-emitting phosphor of $\text{Sr}_3\text{B}_2\text{O}_6:\text{Eu}^{2+}$ for application to white light-emitting diodes, *Materials Chemistry and Physics*, 117 (2009) 500-503.
- [7] S. Hoon Jung, D. Seok Kang, D. Young Jeon, Effect of substitution of nitrogen ions to red-emitting $\text{Sr}_3\text{B}_2\text{O}_{6-3/2x}\text{N}_x:\text{Eu}^{2+}$ oxy-nitride phosphor for the application to white LED, *Journal of Crystal Growth*, 326 (2011) 116-119.
- [8] Y. Xue, X. Xu, L. Hu, Y. Fan, X. Li, J. Li, Z. Mo, C. Tang, Synthesis and photoluminescence characteristics of $(\text{Sr}, \text{Ca})_3\text{B}_2\text{O}_6:\text{Eu}$ for application in white light-emitting diodes, *Journal of Luminescence*, 131 (2011) 2016-2020.
- [9] X. Li, C. Liu, L. Guan, W. Wei, Z. Yang, Q. Guo, G. Fu, An ideal blue $\text{Sr}_3\text{B}_2\text{O}_6:\text{Ce}^{3+}$ phosphor prepared by sol-combustion method, *Materials Letters*, 87 (2012) 121-123.
- [10] Neharika, V. Kumar, J. Sharma, V.K. Singh, O.M. Ntwaeaborwa, H.C. Swart, Surface and spectral studies of green emitting $\text{Sr}_3\text{B}_2\text{O}_6:\text{Tb}^{3+}$ phosphor, *Journal of Electron Spectroscopy and Related Phenomena*, 206 (2016) 52-57.
- [11] H. Liu, Z. Guo, Ce^{3+} and Dy^{3+} doped $\text{Sr}_3\text{B}_2\text{O}_6$: Solid state synthesis and tunable luminescence, *Journal of Luminescence*, 187 (2017) 181-185.
- [12] S. Khursheed, V. Kumar, V.K. Singh, J. Sharma, H.C. Swart, Optical properties of $\text{Sr}_3\text{B}_2\text{O}_6:\text{Dy}^{3+}$ /PMMA polymer nanocomposites, *Physica B: Condensed Matter*, (2017).
- [13] K.-W. Chae, T.-R. Park, C. Cheon, II, J.S. Kim, Persistent luminescence of RE^{3+} co-doped $\text{Sr}_3\text{B}_2\text{O}_6:\text{Eu}^{2+}$ yellow phosphors (RE = Nd, Gd, Dy), *Journal of Luminescence*, 194 (2018) 649-655.
- [14] H.V. Tuyen, N.M. Son, V.X. Quang, Structural behavior and Judd-Ofelt intensity parameter of $\text{Sr}_3\text{B}_2\text{O}_6:\text{Eu}^{3+}$ phosphor, *International Journal of Modern Physics B*, 29 (2015) 1550235.
- [15] H.V. Tuyen, M.S. Nguyen, Luminescence properties and energy transfer of $\text{Tb}^{3+}-\text{Eu}^{3+}$ co-doped $\text{Sr}_3\text{B}_2\text{O}_6$ phosphors, *International Journal of Modern Physics B*, 31 (2017) 1750128.
- [16] L. Liu, Y. Zhang, J. Hao, C. Li, Q. Tang, C. Zhang, Q. Su, Thermoluminescence characteristics of terbium-doped $\text{Ba}_2\text{Ca}(\text{BO}_3)_2$ phosphor, *physica status solidi (a)*, 202 (2005) 2800-2806.
- [17] S. Som, M. Chowdhury, S.K. Sharma, Band gap and trapping parameters of color tunable $\text{Yb}^{3+}/\text{Er}^{3+}$ codoped Y_2O_3 upconversion phosphor synthesized by combustion route, *Journal of Materials Science*, 49 (2013) 858-867.
- [18] R. Chen, Glow curves with general order kinetics, *Journal of The Electrochemical Society*, 116 (1969) 1254-1259.
- [19] S.W.S. McKeever, *Thermoluminescence of Solid*, Cambridge University Press, Cambridge, 1985.

An experiment on using agar layer as the confining medium for the laser-induced shock process

Thí nghiệm sử dụng agar làm môi trường giới hạn trong quá trình shock gây nên bởi tia laser

Nguyen Thi Phuong Thao

*Viện Nghiên cứu và Phát triển Công nghệ cao, Đại học Duy Tân, 03 Quang Trung, Đà Nẵng, Việt Nam
Institute of Research and Development, Duy Tan University, 03 Quang Trung, Da Nang, Vietnam
(Ngày nhận bài: 22/01/2018, ngày phản biện xong: 30/01/2018, ngày chấp nhận đăng: 20/03/2018)*

Abstract

This paper presents an experiment on using a thin agar laser-induced shock process. The laser pulse was 1064 nm, FWHM 13 ns, operated at the pulse energy of 40 mJ. The findings show that the laser-induced shock under an agar layer represents all the typical dynamical features of a shock process induced in liquid-confining regime. Our empirical finding also proves, for the first time, the ability of a thin agar layer in improving the laser-induced stress wave to the same level of laser ablation in water.

Keywords: Laser-induced shock process, photoelasticity imaging technique, confining medium.

Tóm tắt

Trong bài báo này, chúng tôi trình bày thí nghiệm nghiên cứu sử dụng một lớp agar làm môi trường giới hạn trong kỹ thuật shock gây nên bởi xung laser. Chúng tôi sử dụng xung laser có bước sóng 1064 nm, độ rộng xung 13 ns, năng lượng 40 mJ. Kết quả thực nghiệm cho thấy quá trình shock gây nên bởi tia laser trong môi trường agar thể hiện đầy đủ các đặc điểm động học điển hình của quá trình shock gây nên bởi tia laser trong môi trường nước. Kết quả thực nghiệm của chúng tôi cũng chứng minh rằng việc phủ một lớp mỏng agar trên bề mặt vật liệu cho phép làm tăng cường độ sóng ứng suất tương đương với việc ngâm vật mẫu trong môi trường nước.

Từ khóa: Quá trình shock gây nên bởi tia laser, kỹ thuật chụp ảnh quang đàn hồi, môi trường giới hạn.

1. Introduction

When focusing an intense, short laser pulse onto a solid surface, the laser ablation is induced to form a high pressure plasma, which drives a shock wave into the surrounding environment during its expansion. In laser-induced shock technology, a confining medium is applied to restrain the plasma expansion thus induces a much stronger shock in

comparison to ablation in normal atmospheric conditions [1-7]. Normally, a transparent liquid like water is used as the confining medium. The advantages of using liquid are cheap, easy to apply, help removing the ablated material and reduce heat during the ablating process. However, to achieve the maximum stress, the water layer must be thicker than a certain thickness to be able to

confine all the induced plasma [1]. Moreover, the thickness of water layer must be kept uniform to avoid the effect of changing the focal position [2]. To maintain that requirement, the sample should be totally immersed under water, a condition that is difficult to apply in industrial treatment process.

In this experiment, we propose a new method to provide a confining medium for laser induced shock process: using agar to provide a transparent, uniform layer in the solid form. The purpose of this experiment is to investigate the ability of agar layer in enhancing the laser-induced stress wave, in comparison to water. The dynamical behavior of the shock process induced when using an agar layer as the confining medium is observed by photoelasticity imaging technique and being discussed in details.

2. Experimental method

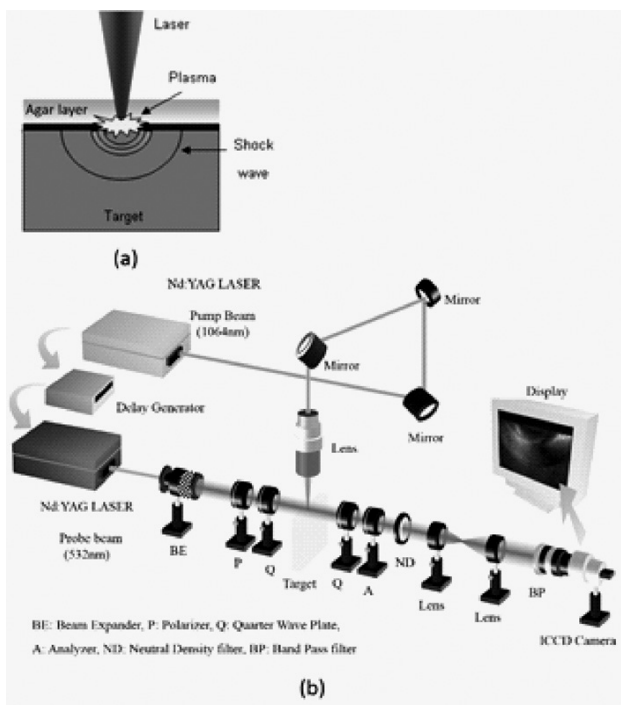


Figure 1: Configuration of the experiment. (a) Laser induced ablation under an agar layer. (b) Photoelasticity imaging technique.

We applied the high-speed photoelasticity imaging technique to investigate the ablation process and semi-quantitatively compare the

strength of laser-induced stress wave. The experiment system has been described elsewhere [1-4] and only a brief description is reported here. The shock process was induced by focusing a single pulse (1064 nm, FWHM 13ns) onto a sample surface with spot diameter approximate 300 μm . The samples are epoxy-resin block of 25x8x20 mm³. For ablation in water, the samples were immersed in static water, with the upper surface was located 5 mm under the water-air interface. In the experiment to investigate the performance of agar layer as a confining medium, we casted an 6 mm agar (0.2%) layer on top of the sample surface (Figure 1(a)).

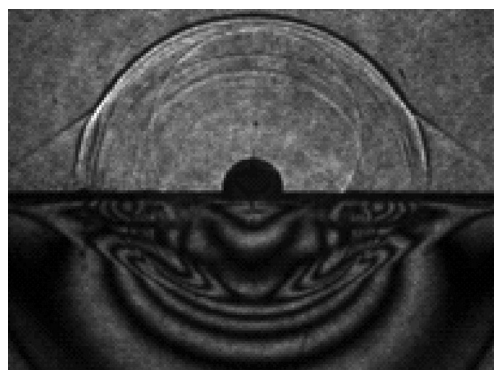
The imaging system was based on a kind of pump and probe imaging system with a photoelastic polariscope added to provide photoelastic images. The delay time was defined as the interval between the pump and probe pulse and was controlled by a Stanford research system DG Digital Delay/Pulse Generator (Figure 1(b)).

3. Results and discussion

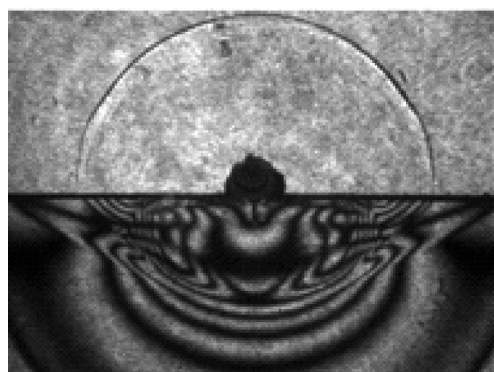
Figure 2 (a) shows the photoelastic images of laser-induced shock process under the 6mm agar layer, captured at 1500 ns delay time. The dark line dividing the image by half is the sample surface. The upper half of the image is agar medium and the lower half is the epoxy resin. The image reveals that the ablation induced under the agar layer represents all the typical features of an ablation induced in the liquid-confining regime. In the agar medium, we can observe the shock wave and the V-shaped wave. The dark semi-circle on top of the sample surface is the image of the cavitation bubble. The V-shaped wave makes an angle of 34.5 degrees against the sample surface. This angle is similar to what we observed in under-water ablation [1,3]. This similarity can be explained by that the heat from the initial plasma melted the surrounding area to the liquid form (99.8 % water) thus the propagation of shock

waves, headwave and the developing of cavitation bubble is the same as in water. Since the heat from laser ablation is very local, the rest of the agar layer remained untouched during the ablation process. When the ablation ended, the melted agar re-solidified. We observed no detachment between the sample and the agar layer during and after the shock process.

In the epoxy-resin medium, we can observe black-and-white fringes which represent the strength of laser-induced stress wave. Compared to the image of laser-induced ablation in water at the same ablating condition, we can see that the number of photoelastic fringes is the same for the two cases. This result demonstrated that the stress wave induced when using a thin agar layer as confining medium is equal to that induced in under-water ablation.



(a)



(b)

Figure 2. (a) Ablation under a thin agar layer. (b) Ablation under water. Pulse energy was 40 mJ. Sample surfaces were not covered with black pain. The images were taken at 1500 ns.

In the context of laser-induced shock process, water is normally used as the confining medium. Although water is cheap and easy to apply, it has a major disadvantage that it is difficult to maintain a uniform layer thickness over the sample surface, especially for the curved surface. Since the confining layer thickness has a significant effect on the ablation process, we propose that a method to apply a uniform confining medium on the treating surfaces is required. With this experiment, we prove the ability of an agar layer as a confining medium for laser-induced ablation. Using agar, we can cast a uniform layer at any thickness onto a surface. It will serve as the confining medium during the laser treatment and can be removed easily by heat. We propose that using agar instead of water as confining medium for laser ablation process will improve the efficiency of laser shock peening process if being applied in industrial scale.

Our experiment is, however, only the first example to demonstrate the ability of an agar layer as a confining medium for laser-induced shock process. We suggest that deeper experiments should be carried out to further investigate the dynamical aspect of the ablation under the agar layer, including but not limited to the developing of cavitation bubble, the motion of ablated material, the effect of layer thickness, and the effect of physical properties of the agar layer on the ablation process.

4. Conclusion

In this experiment, we investigated the laser-induced ablation under an agar layer in comparison to that induced under water. We demonstrated, for the first time, the ability of agar layer as a confining medium for laser-induced shock process. The ablation under the agar layer represented all the typical features of a laser-induced ablation in the liquid confining regime. The stress wave induced when using a thin agar layer as confining medium is equal to that induced in underwater ablation. We

thus propose the future application of an agar layer in the industrial laser-induced surface treatment technology.

Acknowledgment

The results presented in this paper were based on the experiments performed at Department of Mechanical Engineering, Nagaoka University of Technology, Japan. I would like to express the great appreciation to Prof. Yoshiro Ito and Dr. Tanabe Rie for their valuable support and advice during the experiment. Special thanks to Dr. Nguyen Thi Phuong Anh, Department of Bioengineering, Nagaoka University of Technology for her help in preparing the agar layer.

References

- [1] T. T. P. Nguyen, R. Tanabe, and Y. Ito. Laser-induced shock process in under-liquid regime studied by time-resolved photoelasticity imaging technique. *Appl. Phys. Lett.*, 102:124103–1, 2013.
- [2] T. T. P. Nguyen, R. Tanabe, and Y. Ito. Influences of focusing conditions on dynamics of laser ablation at a solid-liquid interface. *Appl. Phys. Express*, 6:122701, 2013.
- [3] T. T. P. Nguyen, R. Tanabe, and Y. Ito. Effects of absorptive coating on the dynamics of underwater laser-induced shock process. *Appl. Phys. A*, 116:1109, 2014.
- [4] T. T. P. Nguyen, R. Tanabe, and Y. Ito. Dynamical visualization of laser-induced shock phenomena in liquid. *The Review of Laser Engineering*, 6:448, 2014.
- [5] L. Martí-López, R. Ocaña, J. A. Porro, M. Morales, and J. L. Ocaña. Optical observation of shock waves and cavitation bubbles in high intensity laser-induced shock processes. *Appl. Optics*, 48:3671, 2009.
- [6] L. Martí-Lopez, R. Ocaña, E. Pineiro, and A. Asensio. Laser peening induced shock waves and cavitation bubbles in water studied by optical schlieren visualization. *Physics procedia*, 12:442, 2001.
- [7] A. Nath and A. Khare. Effect of focusing conditions on laser-induced shock waves at titanium-water interface. *Appl. Opt.*, 50:3275, 2011.

Soil Slope Stability Evaluation Using a Fuzzy Instance-Based Classifier with Flower Pollination Algorithm

Đánh giá sự ổn định của mái dốc bằng phương pháp phân loại mờ và thuật toán tối ưu hóa

Hoang Nhat Duc*, Tran Xuan Linh

*Viện Nghiên Cứu Và Phát Triển Công Nghệ Cao, Đại Học Duy Tân, Việt Nam
Institute of Research and Development, Duy Tan University*

(Ngày nhận bài: 01/03/2018, ngày phản biện xong: 02/03/2018, ngày chấp nhận đăng: 20/03/2018)

Abstract

This research proposes a new hybrid soft computing solution based on the Fuzzy k -Nearest Neighbor algorithm (FKNN) and the Flower Pollination Algorithm (FPA) for predicting soil slope stability. The FKNN is an instance-based learning method for pattern recognition; in addition, the FPA - a recently developed metaheuristic - is deployed to optimize the FKNN's model selection process. A dataset that contains 168 real cases of slope evaluation, collected in various locations, is used to construct and verify the proposed hybrid method. Experimental results show that new approach has achieved a roughly 11% improvement in terms of prediction accuracy compared to other state-of-the-art methods.

Key words: Slope Stability Evaluation; Fuzzy Instance-Based Learning; Flower Pollination Algorithm

Tóm tắt

Nghiên cứu này đề xuất một giải pháp thông minh dựa trên thuật toán phân loại mờ Fuzzy k -Nearest Neighbour (FKNN) và thuật toán tối ưu hóa dựa trên quá trình thụ phấn cho hoa (FPA) để dự đoán sự ổn định của mái dốc. FKNN là một phương pháp học máy dựa trên độ tương tự của các điểm dữ liệu để nhận dạng mẫu. Ngoài ra, FPA - một công cụ tối ưu hóa mới được phát triển gần đây - được triển khai nhằm tối ưu hóa quá trình lựa chọn mô hình của FKNN. Một bộ dữ liệu chứa 168 trường hợp đánh giá độ dốc, được thu thập để xây dựng và xác minh phương pháp được đề xuất. Kết quả thực nghiệm cho thấy phương pháp mới đã đạt được cải thiện khoảng 11% về độ chính xác về dự đoán so với một số phương pháp khác.

Từ khóa: Đánh giá độ ổn định mái dốc; Học máy dựa trên thuật toán mờ; Thuật toán tối ưu hóa

1. Introduction

The population expansion and economic development in many countries around the world lead to the construction of road networks and residential areas in the hilly or mountainous regions [1-3]. Accordingly, many man-made facilities are susceptible to be damaged by soil slope collapses. Slope collapses can bring about

disastrous consequences [4]. Such disastrous events are responsible for considerable damages of public/ private property, disruption of traffic, and losses of human lives [5, 6].

As a consequence, slope stability analyses are necessary to prevent and mitigate the damages caused by slope failure [7]. Better tools for slope assessment are of practical need in civil

engineering. The slope analysis can be used for identifying collapse-prone areas. Based on that, financial resources can be appropriately allocated to construct the retaining structures or can establish evacuation plans effectively [8].

Currently, analytical methods and soft computing are commonly employed for slope stability analysis [9]. The analytical methods are based on the slope displacement models; one can analyze the slope stability by identifying of the most dangerous sliding surface and computing the factor of safety [10]. The analytical methods require input parameters for every calculation point of the investigated area and they are only appropriate for evaluating slope stability in small areas [11]. Recently, soft computing has been shown to provide feasible and effective tools for slope assessment. Soft computing based models for slope evaluation are generally constructed by combining supervised learning techniques and historical databases [12-14]. Using such models, the slope stability prediction can be equivalently stated as a classification task in which prediction outputs are either “stable” or “unstable”.

Lu and Rosenbaum [4], Zhou and Chen [15], Jiang [16], Das et al. [17], and Wang et al. [18] utilized the Artificial Neural Network (ANN) to forecast the slope stability. Zhao et al. [19] utilized the Relevance Vector Machine (RVM) to explore the nonlinear relationship between slope stability and its influence factors. Prediction models of slope assessment employing the Support Vector Machine (SVM) were developed by Li and Wang [20], Li and Dong [21], and Cheng and Hoang [22].

The Evolutionary Polynomial Regression [9] and the Least Squares Support Vector Machine [23] have been employed to model the mapping function between the input pattern and the factor of safety of slopes against failure. Cheng and Hoang [2] construct a probabilistic slope assessment

model based on Bayesian Framework. Yan and Li [24] established a method for predicting the stability of open pit slope based on the Bayes Discriminant Analysis (BDA). A swarm-optimized fuzzy instance based classifier has been proposed for predicting slope collapses in mountain roads [25]. These researches conclude that soft computing can provide a viable tool to establish a structured representation of the slope system, which allows the prediction of the slope stability.

Due to the complex and multi-factorial interactions between factors that affect slope stability, the task of slope assessment remains a significant challenge for civil engineers. This research investigates a hybrid soft computing framework to construct a novel soil slope evaluation model. In this hybrid framework, the Fuzzy k -Nearest Neighbor algorithm (FKNN) [26], a flexible and effective pattern recognition method, is employed to generalize the classification boundary that separate the input pattern into distinctive two classes: ‘stable’ and ‘unstable’. Furthermore, to determine the FKNN’s hyper-parameters, the Flower Pollination Algorithm (FPA) [27], a recently developed nature-inspired metaheuristic, is employed. The remaining part of this paper is organized as follows. The second section of this paper presents the research methodology. The framework of the proposed model is described in the third section, followed by the experimental results. Conclusions of this study are stated in the final section.

2. Research Methodology

2.1 Historical dataset of soil slope stability

A database consisting of 168 data samples, collected from previous studies [4, 15, 20, 24, 28], are employed to establish and verify the new slope assessment method. Based on previous researches, 6 influencing factors, including unit

weight (kN/m^3), soil cohesion (kPa), internal friction angle ($^\circ$), slope angle ($^\circ$), slope height (m), and pore pressure ratio, are employed to characterize an earth slope (see Fig. 1).

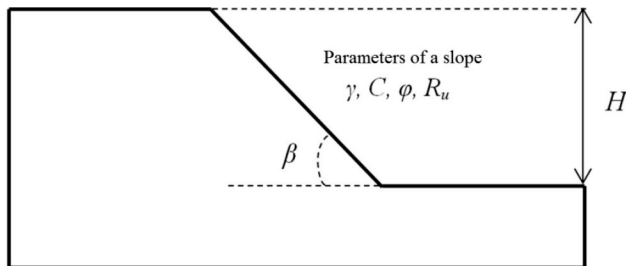


Fig. 1 Illustration of a soil slope

Table 1 provides the information of the influencing factors and their statistical descriptions. The several data samples are shown minimum values of the factor, respectively.

Table 1. Influencing Factors

Factors	Notation	Definition	Max	Average	Std.	Min
X_1	γ	Unit weight (kN/m^3)	31.30	21.76	4.13	12.00
X_2	C	Soil cohesion (kPa)	300.00	34.12	45.82	0.00
X_3	ϕ	Internal friction angle ($^\circ$)	45.00	28.72	10.58	0.00
X_4	β	Slope angle ($^\circ$)	59.00	36.10	10.22	16.00
X_5	H	Slope height (m)	511.00	104.19	132.68	3.60
X_6	R_u	Pore pressure ratio	45.00	0.48	3.45	0.00

Table 2. The Historical Cases

Case No.	X_1	X_2	X_3	X_4	X_5	X_6	Y
<i>Sah et al., (1994)</i>							
1	18.68	26.34	15	35	8.23	0	0
2	16.5	11.49	0	30	3.66	0	0
3	18.84	14.36	25	20	30.5	0	1
4	18.84	57.46	20	20	30.5	0	1
5	28.44	29.42	35	35	100	0	1
...
164	25	46	35	46	393	0.25	1
165	16.5	11.49	0	30	3.66	0	0
166	25	120	45	53	120	0	1
167	19.06	11.75	28	35	21	0.11	0
168	18.84	14.36	25	20.3	50	45	0

in Table 2 where the output of $Y = 1$ indicates a stable slope and the output of $Y = 0$ represents an unstable slope. In the current database, there are 84 stable slopes and 84 unstable slopes. To prevent the situation in which inputs with greater magnitudes dominate those with smaller magnitudes, the influencing factors have been normalized into a $[0, 1]$ range using the following formula:

$$X_n = \frac{X_o - X_{min}}{X_{max} - X_{min}} \quad (1)$$

where X_n is the normalized data. X_o is the original data. X_{max} and X_{min} denote the maximum and

2.2 The Fuzzy k -Nearest Neighbor algorithm (FKNN)

The FKNN [26] belongs to the class of instance-based learning. This algorithm employs the all the collected dataset to establish its memory. The FKNN assigns class memberships to a data sample based on the characteristic of its input vector. Furthermore, the membership values provide a level of assurance to accompany the resultant classification [25, 29, 30]. The algorithm also assigns fuzzy memberships as a function of the data sample's distance from its k nearest neighbors and those neighbors' memberships in the possible classes. Due to such features, competitive prediction performance of the FKNN has been demonstrated in various studies [25, 31, 32]. This section of the article describes the concept of the FKNN in detail.

The first step of the FKNN is to compute the fuzzy partition matrix $U = [u_{ij}]$ from the memory which stores a set of n training sample vectors $[x_1, \dots, x_n]$. Herein, j is denoted as the sample index ($j = 1, 2, \dots, n$), where n is the number of training samples. And, the variable i represents the class index ($i = 1, 2, \dots, C$), where C is the number of classes. For each training case x , we identify its k nearest neighbors by calculating Euclidean distances. The membership degree of the data sample x_j in the class i is given as follows:

$$u_{ij}(x) = u_i(x_j) = \begin{cases} 0.51 + (n_i/k) \times 0.49, & \text{if } c(x_j) = i \\ (n_i/k) \times 0.49, & \text{if } c(x_j) \neq i \end{cases} \quad (2)$$

where n_i denotes the number of neighbors found which belong to the class i and $c(x_j)$ is the class label of the data sample x_j . It is noted that u_{ij} is an element of the C -by- n matrix U . Moreover, it is also worth noticing that the purpose of Eq. (1) is to assign higher fuzzy membership grades to the training samples that stay away from the decision boundary and lower fuzzy memberships grade to the patterns that stay in the vicinity of the classification

boundary (Keller et al., 1985). The reason is that the information supplied by the samples in the region close to the decision surface is more uncertain than that provided by other samples.

Because u_{ij} is a fuzzy membership grade of the sample x_j in the class i , u_{ij} must satisfy the following properties:

$$u_{ij} \in [0,1] \quad (3)$$

$$\sum_{i=1}^C u_{ij} = 1 \quad (4)$$

$$0 < \sum_{j=1}^n u_{ij} < n \quad (5)$$

The second step assigns fuzzy memberships of the unknown sample x to different classes according to the following equation:

$$u_i(x) = \frac{\sum_{j=1}^k u_{ij} (1 / \|x - x_j\|^{2/(m-1)})}{\sum_{j=1}^k (1 / \|x - x_j\|^{2/(m-1)})} \quad (6)$$

where $i = 1, 2, \dots, C$, and $j = 1, 2, \dots, k$. It is noted that j represents the j^{th} sample vector among the k nearest neighbors of x . C denotes the number of classes; k is the neighboring size. The fuzzy strength m reflects how heavily the distance is weighted when computing each neighbor's contribution to the membership value. $\|x - x_j\|$ is the Euclidean distance between x and its j^{th} nearest neighbor x_j . u_{ij} represents the membership degree of the sample vector x_j in the class i and is computed in the first step of the algorithm (as shown in Eq. 1).

2.3 The Flower Pollenation Algorithm (FPA)

The FPA [33] is a metaheuristic that has the inspiration from the characteristics of the flower pollination process. In the natural world, pollination is the process by which pollen is transported from the male section (anther) to the female section (stigma) of the plant. Typically, there are two means of pollination: biotic and

abiotic [34]. The first means of pollination is often achieved by the assistance of pollinators such as insects, birds, and other animals. The second means of pollination does not involve pollinators; instead of that, wind and water flow are employed to deliver pollen.

In addition, pollination can be categorized into two major forms: self-pollination and cross-pollination [35]. In cross-pollination, pollen of a flower is transferred to a flower of a different plant. Meanwhile, the second form of pollination is the process of transferring pollen from one flower to another flower of the same plant. It is noted that in biotic and cross-pollination, pollen can be transported to distant areas since pollinators such as bees and birds can travel long distances.

```

Generate an initial population of  $N$  flowers randomly
Evaluate population fitness
Identify the best solution  $x_{best}$  in the current population
Define the switch probability  $p$ 
Define the maximum iteration  $T_{max}$ 
For  $t = 1$  to  $T_{max}$ 
  For  $i = 1$  to  $N$ 
     $r \sim U(0,1)$  //  $r$  is a uniform random number
    If  $r < p$ 
      Generate  $L \sim Levy$ 
      Perform global pollination:  $x_i^{trial} = x_i^t + L \cdot (x_i^t - x_{best}^t)$ 
    else
      Perform local pollination:  $x_i^{trial} = x_i^t + \epsilon \cdot (x_i^t - x_j^t)$ 
    End if
    If  $f(x_i^{trial}) < f(x_i^t)$ 
       $x_i^t = x_i^{trial}$ 
      If  $f(x_i^t) < f(x_{best}^t)$ 
         $x_{best}^t = x_i^t$ 
      End if
    End if
  End For
End For
Return  $x_{best}$ 

```

Fig. 2 The Flower Pollination Algorithm (FPA)

Inspired from such features of the pollination process, the FPA is formulated as an optimization algorithm in which biotic and cross-pollinations act as global search, abiotic and self-pollinations are utilized as local search (see **Fig. 2**) [33]. Compared to other nature-inspired algorithms, the FPA possesses a promising capability of global search [27, 36-38]. In the FPA, a solution

x in the search space represents a flower. For the purpose of locating the optimal solution, pollination, in either global or local forms, is considered to be successful if the pollen from the solution x_i is transferred to the solution x_j with a better fitness. Because the moving patterns of bees and birds can have Levy flight [35, 39] behavior with fly distance steps following a Levy distribution, the global search of the algorithm may benefit from Levy flights. Furthermore, the local and global pollinations can be controlled by a switch probability p . Experimentally, Yang [33] recommended that p can be set as 0.8.

The Levy flight-based global pollination can be mathematically stated as follows:

$$x_i^{trial} = x_i^t + L \times (x_i^t - x_{best}^t) \quad (7)$$

where x_i^t and x_i^{trial} are solution vector x_i at iteration t and a trial solution, respectively. x_{best}^t denotes the current best solution. The parameter L dictates the length of pollen traveling distance. Herein, the Levy flight is employed to mimic flying patterns of pollinators. L is a random variable drawn from a Levy distribution.

The local pollination as a means of local search can be expressed as follows:

$$x_i^{trial} = x_i^t + \epsilon (x_i^t - x_j^t) \quad (8)$$

where x_i^t and x_j^t are pollens produced by different flowers of the same plant species. $\epsilon \in [0, 1]$ is a random number generated from a uniform distribution.

3. The proposed Fuzzy Instance-Based Classifier with Flower Pollination Algorithm (FIBC-FPA) for slope stability assessment

This section describes the model concept of the proposed slope stability assessment approach, named as FIBC-FPA, in detail. The model (see **Fig. 3**) is constructed by a combination of the FKNN and the FPA algorithms. The FIBC-FPA employs the FKNN to generalize the classification boundary that separates an input vector into two

classes: ‘Stable’ and ‘Unstable’. Additionally, the FIBC-FPA employs the FPA to properly determine the values of the FKNN’s hyper-parameters: the neighboring size (k) and the fuzzy strength (m).

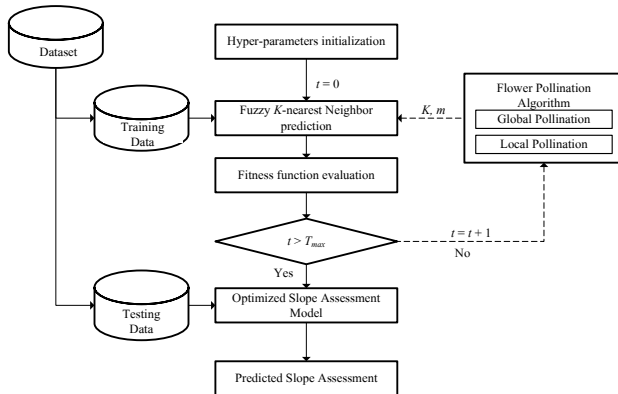


Fig. 3 The proposed Fuzzy Instance-Based Classifier with Flower Pollination Algorithm (FIBC-FPA) for slope stability assessment

3.1 The Dataset

As described earlier, the dataset used in this research includes 168 real cases of soil slope stability collected in various regions. It is noted that within the dataset, the numbers of stable ($Y = 1$) and unstable slopes ($Y = 0$) are both 84 samples. The dataset is randomly divided into two sets: the training set (used to establish the model memory) and the testing set (used to verify the model performance). It is noticed that the training and the testing sets occupy 90% and 10% of the whole dataset.

3.2 Fuzzy k -Nearest Neighbor Prediction

Before the FKNN can carry out prediction tasks, the model tuning parameters (k and m) are randomly generated within their ranges of lower and upper boundaries. On the basis of experiment, the lower and upper boundaries of the neighboring size (k) are 1 and 30, respectively. Meanwhile, the lower and upper boundaries of the fuzzy strength (m) are 1.0001 and 10. After the two hyper-parameters have been specified, the FKNN algorithm can assign fuzzy memberships of an input sample to two classes (‘stable’ and ‘unstable’). Thus, for each input pattern x , there are two outputs, $u_1(x)$ and

$u_2(x)$, representing membership degrees of the input sample x within the two aforementioned classes. Since the FKNN produces fuzzy memberships of an input pattern in the two classes, a step of defuzzification is needed to convert fuzzy outputs to crisp outputs $Y(x)$ as follows:

$$Y(x) = \arg \max_{i=1}^2 (u_i(x)) \quad (9)$$

3.3 The Flower Pollination Algorithm

The FPA optimizer is integrated with the FKNN to optimize the classification algorithm’s model selection process. Iteratively, the FPA carries out the global and local pollination phases to guide the population of flowers to better solutions. By evaluating the fitness of each individual, the algorithm discards inferior combinations of m and k , and allows high quality combinations of these parameters to be passed on the next iterations.

3.4 Fitness Function Evaluation

At this step, the training data set is separated into five mutually exclusive subsets. One subset is in turn used as a validating set; meanwhile, the other subsets are used for building up the FKNN’s memory. To evaluate the model’s fitness, the following objective function is used:

$$F_{fitness} = \frac{1}{\sum_{k=1}^5 CAR_k} \quad (10)$$

where CAR_k denotes the classification accuracy rate of the validating set at the k^{th} run. The classification accuracy rate is simply computed as the number of correct classifications divided by the number of all data instances within a data set.

3.5 Optimized Slope Assessment Model

The optimization process of the FPA will terminate when the maximum number of generation is achieved. When the searching process terminates, the most desirable set of hyper-parameters has been identified. The proposed FIBC-FPA is ready to predict new input patterns.

4. Experimental Results and Comparison

As mentioned earlier, 90% of the dataset is used for constructing the prediction model; 10% of the dataset is reserved for the model testing process. The slope conditions of testing data points are unknown for the prediction model. Thus, the testing samples have the role of new slope evaluation tasks which need to be assessed and such reserved samples can be used to verify the constructed model. In fact, since the FIBC-FPA is an instance-based classifier, the training process of the model is not required. The model simply stores all of the training samples in its memory.

Furthermore, to alleviate the randomness in selecting testing samples, the whole dataset (containing 168 cases) is randomly divided into ten mutually exclusive data folds. Each fold in turn serves as testing samples; and the performance of the prediction model can be evaluated via average results of the ten folds. This process is the ten-fold cross validation which is commonly used for verifying model performance [29, 40]. Because all of the subsamples are mutually exclusive, this approach can estimate how accurately the proposed slope assessment model performs in the real world circumstance.

Table 3. The confusion matrices of the FIBC-FPA’s prediction results

Fold 1		Predicted		Fold 6		Predicted	
		Stable	Unstable			Stable	Unstable
Actual	Stable	8	1	Actual	Stable	8	2
	Unstable	0	6		Unstable	0	7
Fold 2		Predicted		Fold 7		Predicted	
		Stable	Unstable			Stable	Unstable
Actual	Stable	7	1	Actual	Stable	7	2
	Unstable	1	8		Unstable	0	8
Fold 3		Predicted		Fold 8		Predicted	
		Stable	Unstable			Stable	Unstable
Actual	Stable	8	1	Actual	Stable	8	1
	Unstable	2	6		Unstable	0	8
Fold 4		Predicted		Fold 9		Predicted	
		Stable	Unstable			Stable	Unstable
Actual	Stable	8	1	Actual	Stable	8	0
	Unstable	1	7		Unstable	1	8
Fold 5		Predicted		Fold 10		Predicted	
		Stable	Unstable			Stable	Unstable
Actual	Stable	6	0	Actual	Stable	7	0
	Unstable	2	9		Unstable	0	10

Table 4. The FIBC-FPA's prediction results

Fold	1	2	3	4	5	6	7	8	9	10	Average
Training											
AUC	0.99	0.99	0.99	0.99	1.00	1.00	0.99	0.99	0.99	0.99	0.99
CAR	99.35	99.34	99.34	99.34	100.00	100.00	99.34	99.34	99.34	99.34	99.47
Testing											
AUC	0.94	0.88	0.82	0.88	0.91	0.90	0.89	0.94	0.94	1.00	0.91
CAR	93.33	88.24	82.35	88.24	88.24	88.24	88.24	94.12	94.12	100.00	90.51

The confusion matrices of the FIBC-FPA's prediction results are shown in **Table 3**. The detail result of the proposed model obtained from the ten-fold cross validation process is provided in **Table 4**. In **Table 4**, the Area Under the Curve (AUC) and the Classification Accuracy Rate (CAR) are employed to quantify the model performance. It is worth noticing that an AUC is a portion of the area of the unit squares, its value will always be between 0.0 and 1.0 [41, 42]. It is worth noticing that higher the AUC value better is the model prediction performance. The CAR is calculated as the ratio of correctly classified cases over the total number of classified cases.

Table 5. Result Comparison

Models	BDA	RMV	ANN	SVC	FIBC-FPA
<i>Training</i>					
CAR	75.07	80.23	87.03	95.97	99.47
AUC	0.75	0.80	0.87	0.96	0.99
<i>Testing</i>					
CAR	75.06	76.24	78.67	79.25	90.51
AUC	0.75	0.76	0.79	0.79	0.91

Additionally, to benchmark the capability of the proposed FIBC-FPA, its performance is compared to results obtained from the other state-of-the-art approach including: the Support Vector Classifier (SVC) [43], the Artificial Neural Network (ANN) [44], the Relevance Vector Machine (RMV) [45], and the Bayes Discriminant Analysis (BDA) [46]. The result comparison is provided in **Table 5**. Observed from the **Table 5**, the average AUC values of the

BDA, RVM, ANN, SVC, and the proposed FIBC-FPA algorithms for the testing cases are 0.75, 0.6, 0.79, 0.79, and 0.91, respectively. In addition, the average CAR of these prediction models for the testing cases are 75.06%, 76.24%, 78.67%, 79.25%, and 90.51%. From the experiment, it can be seen that the newly proposed method has achieved a roughly 11% in terms of classification accuracy. These facts convincingly prove that the new approach is a very promising tool to assist civil engineers in slope assessment.

5. Conclusion

This study contributes to the body of knowledge by introducing a novel approach for soil slope assessment. The proposed FIBC-FPA is established by hybridization of the FKNN, FPA and a dataset consisting of 168 actual cases of slope conditions. The FIBC-FPA employs the FKNN as a classifier to predict the stable/unstable condition of a soil slope when the input information of the slope is available. Furthermore, the FPA is utilized to optimize the FKNN's model selection process.

Since the FIBC-FPA is an instance-based learning model, its prediction process can be easily comprehended by practical engineers; this is contrasted to the black box learning approach used in the SVC, RMV, and ANN algorithms. Moreover, the proposed model can operate independently and change its structure adaptively according to updating information; this enhances the applicability of the model because the

geotechnical engineers can use it without domain knowledge in soft computing.

To verify the performance of the FIBC-FPA, the BDA, RVM, ANN, and SVC algorithms are employed as benchmark approaches. The experimental result has shown that the new hybrid soft computing method is capable of delivering the most accurate slope prediction result. Accordingly, the proposed FIBC-FPA deems best suited to tackle the problem of interest. The future direction of the current research is to apply the FIBC-FPA to solve other problems in the civil engineering domains and experiment novel modification to enhance the model prediction accuracy.

References

- [1] D. Tien Bui, B. Pradhan, I. Revhaug, D.B. Nguyen, H.V. Pham, Q.N. Bui, A novel hybrid evidential belief function-based fuzzy logic model in spatial prediction of rainfall-induced shallow landslides in the Lang Son city area (Vietnam), *Geomat. Nat. Haz. Risk*, 6 (2013) 243-271.
- [2] M.-Y. Cheng, N.-D. Hoang, Slope Collapse Prediction Using Bayesian Framework with K-Nearest Neighbor Density Estimation: Case Study in Taiwan, *J. Comput. Civ. Eng.*, 30 (2016) 04014116.
- [3] N.-D. Hoang, D. Tien Bui, GIS-Based Landslide Spatial Modeling Using Batch-Training Back-propagation Artificial Neural Network: A Study of Model Parameters, in: D. Tien Bui, A. Ngoc Do, H.-B. Bui, N.-D. Hoang (Eds.) *Advances and Applications in Geospatial Technology and Earth Resources: Proceedings of the International Conference on Geo-Spatial Technologies and Earth Resources 2017*, Springer International Publishing, Cham, 2018, pp. 239-254.
- [4] P. Lu, M.S. Rosenbaum, Artificial Neural Networks and Grey Systems for the Prediction of Slope Stability, *Nat. Hazards*, 30 (2003) 383-398.
- [5] J. Ching, H.-J. Liao, J.-Y. Lee, Predicting rainfall-induced landslide potential along a mountain road in Taiwan, *Geotechnique*, 61 (2011) 153-166.
- [6] S. Yang, C. Shen, C. Huang, C. Lee, C. Cheng, C. Chen, Prediction of Mountain Road Closure Due to Rainfall-Induced Landslides, *Journal of Performance of Constructed Facilities*, 26 (2012) 197-202.
- [7] A. Manouchehrian, J. Gholamnejad, M. Sharifzadeh, Development of a model for analysis of slope stability for circular mode failure using genetic algorithm, *Environ. Earth Sci.*, 71 (2014) 1267-1277.
- [8] T.-V. Tran, Slope Stability Assessment of Man Made Slopes A Case Study In Yen Bai, Master Thesis, University Of Twente, The Netherlands, (2011).
- [9] A. Ahangar-Asr, A. Faramarzi, A.A. Javadi, A new approach for prediction of the stability of soil and rock slopes, *Eng. Computation*, 27 (2010) 878 - 893.
- [10] R. Baker, Sufficient conditions for existence of physically significant solutions in limiting equilibrium slope stability analysis, *Int. J. Solids. Struct*, 40 (2003) 3717-3735.
- [11] Y. Song, J. Gong, S. Gao, D. Wang, T. Cui, Y. Li, B. Wei, Susceptibility assessment of earthquake-induced landslides using Bayesian network: A case study in Beichuan, China, *Comput. Geosci.*, 42 (2012) 189-199.
- [12] S.-C. Chen, C.-C. Chang, H.-C. Chan, L.-M. Huang, L.-L. Lin, Modeling Typhoon Event-Induced Landslides Using GIS-Based Logistic Regression: A Case Study of Alishan Forestry Railway, Taiwan, *Math. Probl. Eng.*, 2013 (2013) 9.
- [13] H.-H. Tran, N.-D. Hoang, An Artificial Intelligence Approach for Groutability Estimation Based on Autotuning Support Vector Machine, *Journal of Construction Engineering*, Article ID 109184, 2014 (2014) 1-9.
- [14] D. Tien Bui, A.T. Tran, H. Klempe, B. Pradhan, I. Revhaug, Spatial prediction models for shallow landslide hazards: a comparative assessment of the efficacy of support vector machines, artificial neural networks, kernel logistic regression, and logistic model tree, *Landslides*, (2015) 1-18.
- [15] K.-p. Zhou, Z.-Q. Chen, Stability Prediction of Tailing Dam Slope Based on Neural Network Pattern Recognition, In *Proc. of the Second International Conference on Environmental and Computer Science ICECS '09*, 28-30 Dec. 2009 , Dubai, the United Arab Emirates, (2009) 380-383.
- [16] J.-P. Jiang, BP neural networks for Prediction of the factor of safety of slope stability, In *Proc. of the International Conference on Computing, Control and Industrial Engineering (CCIE)*, 20-21 Aug. 2011 , Wuhan, China, (2011).
- [17] S.K. Das, R.i. Biswal, N. Sivakugan, B. Das, Classification of slopes and prediction of factor of safety using differential evolution neural networks, *Environ. Earth Sci.*, 64 (2011) 201-210.
- [18] H.B. Wang, W.Y. Xu, R.C. Xu, Slope stability evaluation using Back Propagation Neural Networks, *Eng. Geol.*, 80 (2005) 302-315.
- [19] H. Zhao, S. Yin, Z. Ru, Relevance vector machine applied to slope stability analysis, *Int. J. Numer. Anal.*

- Meth. Geomech., 36 (2012) 643–652.
- [20] J. Li, F. Wang, Study on the Forecasting Models of Slope Stability under Data Mining, in: In Proc. of the Earth and Space 2012: : Engineering, Science, Construction, and Operations in Challenging Environments, Honolulu, Hawaii, United States, ASCE, 2010, pp. 765-776.
- [21] J. Li, M. Dong, Method to Predict Slope Safety Factor Using SVM, in: In Proc. of the Earth and Space 2012: Engineering, Science, Construction, and Operations in Challenging Environments, Pasadena, California, United States, ASCE, 2012, pp. 888-899.
- [22] M.-Y. Cheng, N.-D. Hoang, Typhoon-induced slope collapse assessment using a novel bee colony optimized support vector classifier, *Nat. Hazards*, 78 (2015) 1961-1978.
- [23] P. Samui, D.P. Kothari, Utilization of a least square support vector machine (LSSVM) for slope stability analysis, *Sci. Iran.*, 18 (2011) 53-58.
- [24] X. Yan, X. Li, Bayes discriminant analysis method for predicting the stability of open pit slope, In Proc. of the International Conference on Electric Technology and Civil Engineering (ICETCE), 22-24 April 2011, Lushan, China, (2011) 147-150.
- [25] M.-Y. Cheng, N.-D. Hoang, A Swarm-Optimized Fuzzy Instance-based Learning approach for predicting slope collapses in mountain roads, *Knowl.-Based Syst.*, 76 (2015) 256–263.
- [26] J.M. Keller, M.R. Gray, J.A. Given, A Fuzzy K-Nearest Neighbor Algorithm, *IEEE T. Syst. Man Cy.*, 15 (1985) 580-585.
- [27] X.-S. Yang, M. Karamanoglu, X. He, Flower pollination algorithm: A novel approach for multiobjective optimization, *Eng. Optimiz.*, 46 (2013) 1222-1237.
- [28] N.K. Sah, P.R. Sheorey, L.N. Upadhyaya, Maximum likelihood estimation of slope stability, *International Journal of Rock Mechanics and Mining Sciences & Geomechanics Abstracts*, 31 (1994) 47-53.
- [29] M. Cheng, N. Hoang, Groutability Estimation of Grouting Processes with Microfine Cements Using an Evolutionary Instance-Based Learning Approach, *J. Comput. Civ. Eng.*, ASCE, 28 (2014) 04014014.
- [30] D. Tien Bui, Q.P. Nguyen, N.-D. Hoang, H. Klempe, A novel fuzzy K-nearest neighbor inference model with differential evolution for spatial prediction of rainfall-induced shallow landslides in a tropical hilly area using GIS, *Landslides*, (2016) 1-17.
- [31] H. Chen, J. Lu, Q. Li, C. Lou, D. Pan, Z. Yu, A New Evolutionary Fuzzy Instance-Based Learning Approach: Application for Detection of Parkinson's Disease, *Advances in Swarm and Computational Intelligence*, 9141 (2015) 42-50.
- [32] Z. Yang, C. Liu, P. Huang, J. Qian, Membership-Degree Preserving Discriminant Analysis with Applications to Face Recognition, *Computational and Mathematical Methods in Medicine*, 2013 (2013) 7.
- [33] X.-S. Yang, Flower Pollination Algorithm for Global Optimization, in: J. Durand-Lose, N. Jonoska (Eds.) *Unconventional Computation and Natural Computation*, Springer Berlin Heidelberg, 2012, pp. 240-249.
- [34] B.J. Glover, *Understanding Flowers and Flowering: An Integrated Approach*, Oxford University Press, (2007).
- [35] X.-S. Yang, *Nature-Inspired Optimization Algorithms*, 2014.
- [36] S. Łukasik, P. Kowalski, Study of Flower Pollination Algorithm for Continuous Optimization, in: P. Angelov, K.T. Atanassov, L. Doukowska, M. Hadjiski, V. Jotsov, J. Kacprzyk, N. Kasabov, S. Sotirov, E. Szmidi, S. Zadrożny (Eds.) *Intelligent Systems'2014*, Springer International Publishing, 2015, pp. 451-459.
- [37] D. Chakraborty, S. Saha, O. Dutta, DE-FPA: A hybrid differential evolution-flower pollination algorithm for function minimization, In Proc. of the International Conference on High Performance Computing and Applications (ICHPCA), 22-24 Dec. 2014, Bhubaneswar, India, (2014) 1-6.
- [38] R. Wang, Y. Zhou, Flower Pollination Algorithm with Dimension by Dimension Improvement, *Math. Probl. Eng.*, 2014 (2014) 9.
- [39] Y. Celik, E. Ulker, An Improved Marriage in Honey Bees Optimization Algorithm for Single Objective Unconstrained Optimization, *The Scientific World Journal*, 2013 (2013) 11.
- [40] P. Zhang, Model Selection Via Multifold Cross Validation, *The Annals of Statistics*, 21 (1993) 299-313.
- [41] T. Fawcett, An introduction to ROC analysis, *Pattern Recognition Letters*, 27 (2006) 861-874.
- [42] M. Cheng, N. Hoang, Evaluating Contractor Financial Status Using a Hybrid Fuzzy Instance Based Classifier: Case Study in the Construction Industry, *IEEE Trans. Eng. Manag.*, 62 (2015) 184 - 192
- [43] V.N. Vapnik, *Statistical Learning Theory*, John Wiley & Sons, Inc., Printed in the United States of America, (1998).
- [44] C. Bishop, *Neural Networks For Pattern Recognition*, Clarendon Press, Oxford, (1995).
- [45] M.E. Tipping Sparse bayesian learning and the relevance vector machine, *J. Mach. Learn. Res.*, 1 (2001) 211-244
- [46] W.J. Krzanowski, *Principles of Multivariate Analysis: A User's Perspective*, Oxford University Press, New York, (1988).

Introduction to Differential Privacy and Its Applications

Giới thiệu Differential Privacy và ứng dụng

Nguyen Huu Hiep

Viện Nghiên cứu Phát triển Công nghệ cao, Đại học Duy Tân, Đà Nẵng, Việt Nam

Institute of Research and Development, Duy Tan University, Da Nang, Vietnam

(Ngày nhận bài: 20/12/2017, ngày phản biện xong: 16/01/2018, ngày chấp nhận đăng: 20/03/2018)

Abstract

We introduce the concept of Differential Privacy which provides us a guarantee that no matter what the adversary knows about you via auxiliary information sources, your participation in a given dataset will not be affected (this is what “differential” means). This concept has brought about significant results over the past ten years. In this article, we briefly describe the origins of the definitions of differential privacy and its main mechanisms then comes a short list of important applications using differential privacy. We hope that the study attracts a wider interest for this beautiful privacy concept and invites further research for applications in statistical analysis.

Keywords: Differential privacy, Laplace mechanism, Exponential mechanism, Data analysis.

Tóm tắt

Trong bài báo này chúng tôi giới thiệu về Differential Privacy (Tính riêng tư sai phân), một định nghĩa về tính riêng tư đảm bảo rằng: bất kể kẻ tấn công biết những thông tin bên ngoài, việc bạn có mặt hay không trong một tập dữ liệu sẽ không bị ảnh hưởng (đó cũng là ý nghĩa của từ “differential” trong tên gọi). Khái niệm này đã đưa đến rất nhiều kết quả quan trọng trong hơn mười năm qua. Ở đây chúng tôi mô tả ngắn gọn nguồn gốc khái niệm và các cơ chế thường dùng trong differential privacy. Chúng tôi hy vọng bài giới thiệu này sẽ giúp khái niệm được phổ cập hơn và thu hút những nghiên cứu mới, đặc biệt là các ứng dụng phân tích thống kê.

Từ khóa: Tính riêng tư sai phân, Cơ chế Laplace, Cơ chế hàm mũ, Phân tích dữ liệu.

I. INTRODUCTION

Nowadays, data is produced and collected at a phenomenal rate. Analysis of huge data sources brings unprecedented benefits but also threatens the privacy of people. We usually encounter a paradox of learning nothing about an individual while learning useful information about a population. Syntactic processing paradigms like the suppression of identifying fields were eventually proven unsuccessful, as confirmed in past privacy breaches, by simply joining

a de-identified table with publicly available databases. Therefore, the need increases for a robust, meaningful, and mathematically rigorous definition of privacy, together with a computationally rich class of algorithms that satisfy this definition. Differential Privacy (DP) [12] is such a definition.

Previous ad hoc privacy models like k-anonymity [31], l-diversity [23], and t-closeness [20] formalize the intuition of “privacy by blending yourself into a crowd” to hinder re-

identification attacks. In k -anonymity, quasi-identifier fields are suppressed or generalized, so that each record is indistinguishable from at least $k - 1$ other records. Record linkage attacks are avoided, but not attribute linkage attacks, which are prevented in l -diversity. The concept of earth mover's distance employed by t -closeness deals with probabilistic attacks, focusing on how the attacker would change his probabilistic trust in the sensitive information of a victim after accessing the published data. Common limitations of these approaches include ad hoc assumptions on auxiliary information, heavy information loss, and suboptimality. An excellent survey on different privacy preserving data publishing (PPDP) was presented by Fung et al. [13].

Differential privacy is a formal privacy model initially developed for use on tabular data to offer strong privacy guarantees without depending on an adversary's background knowledge, computational power or subsequent behavior. Because absolute privacy is impossible (see [9] and [12, Section 1.1]), differential privacy as an instance of relative privacy proves to be useful with many successful applications in data analysis tasks. It is also found to have tight relations to other fields such as cryptography, statistics, complexity, combinatorics, mechanism design and optimization.

In this paper, we review the concept of differential privacy as well as its key properties and mechanisms (Section II). Then we illustrate the usefulness of differential privacy via a few statistical applications (Section III). Finally, Section IV concludes the paper with further discussion.

II. DEFINITIONS AND MECHANISMS

The underlying principle of differential privacy is that given two databases D and D' such that $D' = D \cup \{x\}$, i.e. D and D' differ only by a

single item, the probability distributions on the results of D and D' under differential privacy will be "essentially the same". More formally,

Definition 2.1: A randomized algorithm A is (ϵ, δ) -differentially private ((ϵ, δ) -DP) if for any two neighboring datasets D and D' , and for any output $O \in \text{Range}(A)$,

$$\Pr[A(D) \in O] \leq e^\epsilon \Pr[A(D') \in O] + \delta \quad (1)$$

If $\delta = 0$, we have the definition of ϵ -DP which is proved stricter than (ϵ, δ) -DP in [8], i.e. the (ϵ, δ) -DP requires less distortion than ϵ -DP.

Bear in mind that, as a relative privacy, differential privacy merely ensures that one's participation in a dataset will not be disclosed. It is very likely that conclusions drawn from the dataset may reflect statistical information about an individual. For example, given a dataset of 100 individuals, 80 of them have a certain property P . Noisy answers to the queries of the dataset size and the numbers of users having the property P are, for example, 101.3 and 78.6 respectively. From these noisy counts, an analyst (as well as an attacker) can estimate that any user has the property P with probability of 77.6%, very close to the true statistics 80%. However, this is a statistical information over the whole population, not related to the participation of any individual to the dataset as guaranteed by differential privacy.

A. Properties

Composability is a nice property of differential privacy which is not satisfied by other syntactic privacy models such as k -anonymity, l -diversity or t -closeness.

Theorem 2.1: (Sequential and parallel compositions [25])

Let each A_i provide ϵ_i -DP. A sequence of A_i (D) over the dataset D provides $\sum_{i=1}^n \epsilon_i$ -DP. Let each A_i provide ϵ_i -DP.

Let $\{D_i\}$ be arbitrary disjoint subsets of the dataset D . The sequence of A_i (D_i) provides $\max \epsilon_i$ -DP.

These composition properties allow many complex differentially private algorithms to break down to composable steps in which Laplace and exponential mechanisms play the role of building blocks. Most of the cases, the proof of ϵ -DP for a given algorithm is obtained automatically. The remaining task of algorithm designers is to reduce the variance of randomized outputs for better utility. To our knowledge, none of the previous privacy concepts like k -anonymity, l -diversity or t -closeness and their variants possesses these composition properties.

B. Mechanisms

Laplacemechanism [11] and *Exponential mechanism* [25] are two standard techniques in differential privacy. The latter is a generalization of the former.

Laplace mechanism is based on the concept of *global sensitivity* of a function f which is defined as $\Delta f = \max_{D, D'} \|f(D) - f(D')\|_1$ where the maximum is taken over all pairs of neighboring D, D' . Given a function f and a privacy budget ϵ , the noise is drawn from a Laplace distribution $Lap(\lambda) = p(x|\lambda) = 1/2\lambda e^{-|x|/\lambda}$ where $\lambda = \Delta f/\epsilon$.

Theorem 2.2: (Laplace mechanism [11]) For any function $f: D \rightarrow \mathbb{R}^d$, the mechanism A

$$A(D) = f(D) + \left\langle Lap_1\left(\frac{\Delta f}{\epsilon}\right), \dots, Lap_d\left(\frac{\Delta f}{\epsilon}\right) \right\rangle \quad (2)$$

satisfies ϵ -DP.

Note that Laplace noise has zero mean and variance $2\lambda^2$. So larger values of ϵ mean lower noise variance, the noisy outputs is then closer to the ground-truth, hence better utility and lower privacy level.

Geometric mechanism [14] is a discrete variant of Laplace mechanism with integral output range Z and random noise Δ generated from a two-sided geometric distribution $Geom(\alpha)$: $Pr[\Delta = \delta | \alpha] = \frac{1-\alpha}{1+\alpha} \alpha^{|\delta|}$. To satisfy ϵ -DP, we set $\alpha = \exp(-\epsilon)$.

For non-numeric data, the exponential

mechanism is a better choice. Its main idea is based on sampling an output O from the output space O using a score function u . This function assigns exponentially greater probabilities to outputs of higher scores.

Theorem 2.3: (Exponential mechanism [24]) Given a score function $u: (D \times O) \rightarrow \mathbb{R}$, for a dataset $D \in D$, the mechanism A that samples an output O with probability proportional to $\exp(\epsilon \cdot u(D, O))$ satisfies $2\epsilon \Delta u$ -DP.

When the queries are monotonic, i.e. changing from D to D' , all queries change in the same direction, the privacy bound is strengthened to $\epsilon \Delta u$ -DP.

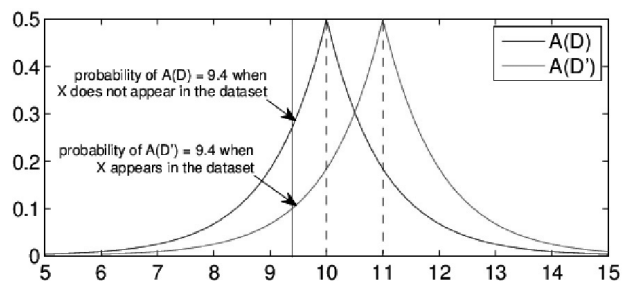


Fig.1. Illustration of differential privacy.

Fig. 1 shows an example of differential privacy via Laplace mechanism. Assuming that a counting query on dataset D returns 10 if user X does not appear in it and returns 11 otherwise (i.e. the case of dataset D'). If true results are returned, the participation of X is revealed by a simple difference attack. To hide this sensitive information, randomized results would be preferred. Assuming that $\epsilon = 1$, the randomized result via Laplace mechanism will be $A(D) = 10 + Lap(1)$ because the global sensitivity Δf is 1 for this example. Similarly, $A(D') = 11 + Lap(1)$. The ratio between the probabilities of $A(D)$ and $A(D')$ at any possible values (e.g. 9.4 as in Fig. 1) is bounded in $[e^{-1}, e]$.

To achieve (ϵ, δ) -DP, we can use Gaussian noise with L_1 -sensitivity replaced by L_2 -sensitivity $\Delta f = \max_{D, D'} \|f(D) - f(D')\|_2$. Zero-mean Gaussian noise

has the pdf $\frac{1}{\sigma\sqrt{2\pi}}\exp\left(-\frac{x^2}{2\sigma^2}\right)$

Theorem 2.4: (Gaussian mechanism [10]) For any function $f: D \rightarrow \mathbb{R}^d$, the mechanism

$$A(D) = f(D) + \langle N_1(0, \sigma), \dots, N_d(0, \sigma) \rangle \quad (3)$$

satisfies (ϵ, δ) -DP if $\sigma = \sqrt{2 \ln(2/\delta)} / \epsilon \times \Delta f$ and $N_i(0, \sigma^2)$ are i.i.d Gaussian random variables.

C. Interactive vs. Non-interactive Settings

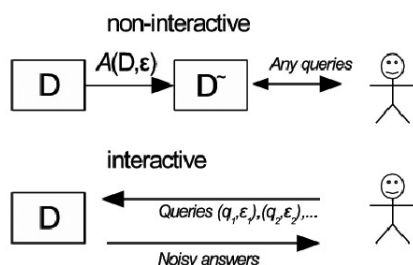


Fig.2. Interactive vs. Non-interactive settings

There are two common settings for releasing data differential privacy: *interactive* versus *non-interactive* as illustrated in Fig. 2. In non-interactive setting, given a privacy budget ϵ , the data curator publishes a noisy dataset and shuts down D . The users can perform any mining operations on D . In interactive settings, the users are allowed to submit a number of queries (q_i, ϵ_i) where q_i is the query over D and ϵ_i is the budget of q_i such that $\sum_i \epsilon_i \leq \epsilon$. It means after a query, the privacy budget is reduced and when it reaches zero, no more queries are allowed.

III. STATISTICAL APPLICATIONS

In this section, we review typical applications of differential privacy in data analysis tasks on tabular, graph and location data.

A. Tabular Data

Tabular data represents a collection of items in a multidimensional space (each dimension is an attribute). Simple statistical operators like *counting* and *summing* can be used as building blocks in a wide range of learning tasks [3] over tabular data. We review below two types of

counting problems and the well-known k-means that can be converted to ϵ -DP versions.

1) *Histogram and contingency table publication:* A histogram is typically defined over a specific domain as a partition of data points into disjoint bins. Two widely used types of histogram are unattributed (semantic meaning of each bin is irrelevant to the analysis, the histogram can be viewed as a multiset of counts) and attributed (keeping the semantic meaning of each bin).

Contingency table is a table of counts over set of attributes. These counts are called marginals and their release has the goal of revealing correlations between many different sets of attributes. Barak et al. [2] applied Laplace mechanism on the Fourier coefficients of dataset vector (after being cast from high-dimensional space, indexed by attribute tuples), and then employ linear programming to create non-negative synthetic contingency tables. An improvement for sparse data is sketched in [7], with a short-cut approach using sampling and filtering techniques. Geometric noise is added to fulfill ϵ -DP.

Example 3.1: Assuming a tabular dataset in three dimension (Table I) with domains $\text{Dom}(A) = \{a1, a2\}$, $\text{Dom}(B) = \{b1, b2, b3\}$, $\text{Dom}(C) = \{c1, c2\}$, the ground-truth histogram of attribute A is $h(a1) = 4$, $h(a2) = 2$. Similarly, the ground-truth contingency table of attribute set $\{A, B\}$ is shown on the right. To obtain a noisy histogram satisfying ϵ -DP over attribute A , we may add geometric noise (Section II-B) to the ground-truth histogram. One such noisy output may be $h = [3, 6]$.

TABLE I. A TABULAR DATASET AND A CONTINGENCY TABLE

	A	B	C
1	a1	b1	c1
2	a1	b3	c1
3	a1	b1	c2
4	a2	b1	c2
5	a2	b1	c2
6	a1	b1	c1

	b1	b2	b3
a1	3	0	1
a2	2	0	0

Hay et al. [17] pointed out that consistency-constrained inference, if used as a post-processing step, is able to boost the accuracy of histogram queries, for both unattributed and universal histograms. The application of [17] to estimate the degree distribution of private networks is demonstrated in [16].

Range count queries are optimized by wavelet transform in Privelet technique [35]. Privelet adds polylogarithmic noise to the transformed data. One-dimensional ordinal (resp. nominal) data goes with Haar (resp. nominal) wavelet while multidimensional data needs standard decompositions to apply onedimensional transform along each dimension in turn.

2) *Linear counting queries*: Li et al. [18] generalize two approaches in [17] and [35] by *matrix mechanism*, an algorithm answering a workload W of linear counting queries. Their idea is to use another set of queries (called query strategy) A as query proxy to the database. Noisy answers on the query strategy are then used to derive answers for the workload. By doing so, they hope to exploit noise distribution correlation to increase accuracy.

Definition 3.1: (Linear query) A linear query is a length- n row vector $\mathbf{q} = [q_1 \dots q_n]$ with each $q_i \in \mathbb{R}$. The answer to a linear query \mathbf{q} on \mathbf{x} is the vector product $\mathbf{q}\mathbf{x} = q_1x_1 + \dots + q_nx_n$.

If \mathbf{Q} is an $m \times n$ query, the query answer for \mathbf{Q} is a length m column vector of query results, which can be computed as the product $\mathbf{Q}\mathbf{x}$.

Example 3.2: Given the dataset in Table I, the full domain is of size $2 \times 3 \times 2 = 12$. The counting vector \mathbf{x} would be $[2 \ 1 \ 0 \ 0 \ 1 \ 0 \ 0 \ 2 \ 0 \ 0 \ 0 \ 0]$ because the number of occurrences of tuple $\{a1, b1, c1\}$ is 2 and so on. To get the number of tuples containing $a1$, we need the linear query $q(a1) = [1 \ 1 \ 1 \ 1 \ 1 \ 1 \ 0 \ 0 \ 0 \ 0 \ 0 \ 0]$. Similarly, to get the histogram of attribute A as in Example 3.1, we need the following query

$$\begin{bmatrix} 111111000000 \\ 000000111111 \end{bmatrix}$$

In [18], a semidefinite program with rank constraint is formulated with complexity $O(n^8)$ and some approximations are developed. The distinct novelty of [18] is to point out that some mechanisms in [17] and [35] are special cases of matrix mechanism. Eigen-Design [19] is an efficient implementation with complexity of $O(n^4)$. It uses singular value decomposition (SVD) lower bound to reduce the search space for matrix A from full space $\mathbb{R}^{n \times n}$ to linear space spanned by eigenvectors of $W^T W$.

The full-rank limitation of [18] is emphasized in [36]. Yuan et al. then proposed the low-rank mechanism (LRM) to reach the theoretical lower bound proven in [15]. The workload matrix is decomposed and its constraint is relaxed. The results show LRM's outperformance over [35] and [17] in most of query scenarios.

3) *K-means*: We use the k-means problem [3], [21] to illustrate the usage of Laplace mechanism as building blocks. Given a d dimensional dataset $D = \{x_1, \dots, x_N\}$, k-means tries to find K centroids $\{o_1, \dots, o_K\}$ so that the Normalized Intra-Cluster Variance (NICV) is minimized

$$NICV = \frac{1}{N} \sum_{j=1}^N \left\| x_j - o_{k, k = \arg \min_k |x_j - o_k|^2} \right\|^2 \quad (4)$$

It means that with a fixed set of K points $\{o_1, \dots, o_K\}$, each data point x_j is assigned to the nearest o_k and NICV is the average distance. The standard k-means starts by selecting K points as the initial centroids. The algorithm then tries to improve these centroids iteratively until no improvement can be made. In each iteration, one first partitions the data points into K clusters, with each point assigned to the nearest centroid. Then, one updates each centroid to be the center of the data points in the cluster.

Assuming that all data points are normalized to the hyper-rectangle $[0, 1]^d$, an ϵ -DP version of

k-means is as in Algorithm 1 (see [3]). Noise is injected into the computation in Lines 5 and 7. The computations in these two lines consume a privacy budget of $\varepsilon/T(d+1)$ and $\varepsilon d/T(d+1)$ respectively. Therefore in each iteration, we need a privacy budget of $\varepsilon/T(d+1) + \varepsilon d/T(d+1) = \varepsilon/T$. After T such iterations, DP-Lloyd uses up all the budget ε . Note that Line 4 partitions the dataset into K disjoint subsets, so the parallel composition (Theorem 2.1) applies.

Algorithm 1 DP-Lloyd

Input: X : dataset with N data points in \mathbb{R}^d . K : number of clusters. T : number of iterations. ε : privacy budget.

Output: K noisy means

1: initialize a set of random K means
 $O^{(0)} = \{\tilde{\delta}_1^{(0)}, \dots, \tilde{\delta}_K^{(0)}\}$

2: **for** $t = 1 \rightarrow T$ **do**

3: **for** $k = 1 \rightarrow K$ **do**

4: $O_k = \{x_j \mid j = \arg \min_j \|x_j - \tilde{\delta}_k^{(t)}\|^2\}$

5: $n_k = |O_k| + \text{Lap}(T(d+1)/\varepsilon)$

6: $s_k = \sum_{x_j \in O_k} x_j$

7: $s_k = s_k + \langle \text{Lap}_1(T(d+1)/d\varepsilon), \dots, \text{Lap}_d(T(d+1)/d\varepsilon) \rangle$

8: $\tilde{\delta}_k^{(t)} = s_k/n_k$

9: **return** $\{\tilde{\delta}_1^{(T)}, \dots, \tilde{\delta}_K^{(T)}\}$

B. Graph Data

1) Graph Structure and Statistics Publication:

Although tabular data is very popular, many problems would be better represented in graph form which composes of nodes standing for entities and edges characterizing the relationships among the entities. In Fig. 3, a simple graph of 6 nodes and 7 edges is displayed. Several privacy problems for graph data are: graph structure publication, graph statistics publication, graph

private computation and so on. In the context of graph, two neighboring datasets D and D' are replaced by two neighboring graphs G and G'

If G and G' differ in only one edge, we have the concept of *edge differential privacy*.

If G and G' differ in only one node and its adjacent edges, we have the concept of *node differential privacy*. Node differential privacy is much harder to achieve than edge differential privacy.

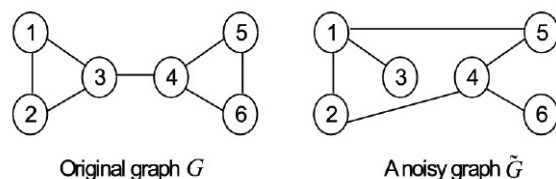


Fig.3. A simple graph whose structure should be protected

Recent work on edge/node differential privacy is surveyed in [29]. Given a simple graph in Fig. 3 (left), a possible noisy graph is shown on the right. We can represent the two graphs in the form of adjacency matrix as follows.

$$A(G) = \begin{bmatrix} 0 & 1 & 1 & 0 & 0 & 0 \\ 1 & 0 & 1 & 0 & 0 & 0 \\ 1 & 1 & 0 & 1 & 0 & 0 \\ 0 & 0 & 1 & 0 & 1 & 1 \\ 0 & 0 & 0 & 1 & 0 & 1 \\ 0 & 0 & 0 & 1 & 1 & 0 \end{bmatrix} \quad A(\tilde{G}) = \begin{bmatrix} 0 & 1 & 1 & 0 & 1 & 0 \\ 1 & 0 & 0 & 1 & 0 & 0 \\ 1 & 0 & 0 & 0 & 0 & 0 \\ 0 & 1 & 0 & 0 & 1 & 1 \\ 1 & 0 & 0 & 1 & 0 & 0 \\ 0 & 0 & 0 & 1 & 0 & 0 \end{bmatrix}$$

The problem of graph publication under edge differential privacy comprises two main techniques: direct publication and model-based publication. Direct publication means that the output graph is constructed by directly adding noise to each edge, followed by a post-processing step. TmF [29] and EdgeFlip [27] belong to this category. The other technique, model-based publication, relies on an intermediary structure to extract some crucial statistics from the original graph. The noise is added to the statistics in a differentially private manner. Finally, sample output graphs are regenerated from these noisy statistics. This category includes 1K-series,

2K-series [30], [32], Kronecker graph model [26], graph spectral analysis [33], DER [6], HRGMMC [34] and ERGM (Exponential Random Graph Model) [22].

2) *Community Detection*: For private computations on graph that satisfy differential privacy, we select the community detection problem [28]. It is quite related to ϵ -DP K-means (Section III-A3) but is much harder and the algorithms by Nguyen et al. [28] address only the case of edge differential privacy. The objective of ϵ -DP community detection is to find a clustering of nodes C such that the modularity $Q(G,C)$ is maximized. Modularity is a quality measure for network clustering. It is based on the idea that a random graph is not expected to have a modular structure, so the possible existence of clusters is revealed by the comparison between the actual density of edges in a subgraph and the density one would expect to have in the subgraph if the nodes of the graph were connected randomly (the null model). The modularity Q is defined as

$$Q = \sum_{c=1}^{n_c} \left[\frac{l_c}{m} - \left(\frac{d_c}{2m} \right)^2 \right] \quad (5)$$

where m is the number of edges in G , n_c is the number of clusters, l_c is the total number of edges joining nodes of community c and d_c is the sum of the degrees of the nodes of c . Fig. 4 demonstrates the two clusterings of nodes C_1 and C_2 with different modularity scores.

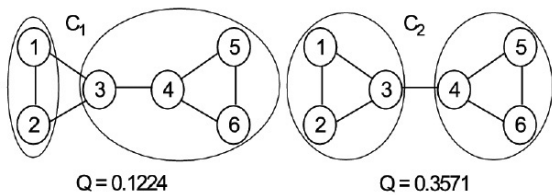


Fig. 4. Community detection

In [28], Nguyen et al. propose two schemes: LouvainDP which runs Louvain algorithm on a noisy supergraph and ModDivisive uses exponential mechanism (Theorem 2.3) with the modularity Q as the score.

C. Location Data

In the context of location privacy, user exact location will be replaced by a noisy location with a requirement that the closer the noisy location is from the exact location, the stronger the privacy is asked for. Differential privacy concept can be extended from Formula (1) in which D, D' and O are locations.

Geo-indistinguishability [1] is such an extension. Let x, x' be any locations and y is any output, we should have

$$\Pr(y | x') \leq e^{\epsilon d(x,x')} \Pr(y | x)$$

Also, Laplace mechanism can be extended to count for Euclidean distance on the plane. The 2D noise is sampled from the following distribution [1]

$$D_\epsilon(x_0)(x) = \frac{\epsilon^2}{2\pi} e^{-\epsilon d(x_0,x)}$$

where $x_0 \in \mathbb{R}^2$ is the exact location and $\epsilon^2/2\pi$ is the normalization factor. Fig. 5 shows an example of $D_\epsilon(x_0)(x)$.

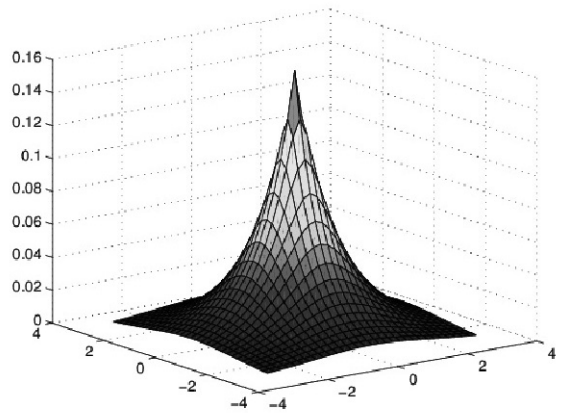


Fig. 5. $D_\epsilon(x_0)(x)$ with $\epsilon = 1$ at $x_0 = (0, 0)$

In [4], Bordenabe et al. consider the geo-indistinguishability approach to location privacy, and the trade-off with respect to utility. They construct a mechanism that minimizes the service quality loss, using linear programming techniques. Another application of geo-indistinguishability appears in [5] in which the authors propose a

novel elastic distinguishability metric that warps the geometrical distance, capturing the different degrees of density of each area.

IV. CONCLUSION

We have presented a gentle introduction to Differential Privacy, a mathematically rigorous definition of privacy with a variety of applications in statistical data analysis. Apart from simple definition, differential privacy also possesses several important properties such as composition which makes privacy proof automatic in most cases. This beautiful privacy concept still attracts a vibrant community searching for new techniques and extensions. We hope to see new theoretical results and applications in upcoming years.

REFERENCES

- [1] M. E. Andrés, N. E. Bordenabe, K. Chatzikokolakis, and C. Palamidessi. Geo-indistinguishability: Differential privacy for location-based systems. In Proceedings of the 2013 ACM SIGSAC conference on Computer & communications security, pages 901–914. ACM, 2013.
- [2] B. Barak, K. Chaudhuri, C. Dwork, S. Kale, F. McSherry, and K. Talwar. Privacy, accuracy, and consistency too: a holistic solution to contingency table release. In PODS, pages 273–282. ACM, 2007.
- [3] A. Blum, C. Dwork, F. McSherry, and K. Nissim. Practical privacy: the sulq framework. In PODS, pages 128–138. ACM, 2005.
- [4] N. E. Bordenabe, K. Chatzikokolakis, and C. Palamidessi. Optimal geoindistinguishable mechanisms for location privacy. In Proceedings of the 2014 ACM SIGSAC Conference on Computer and Communications Security, pages 251–262. ACM, 2014.
- [5] K. Chatzikokolakis, C. Palamidessi, and M. Stronati. Constructing elastic distinguishability metrics for location privacy. Proceedings on Privacy Enhancing Technologies, 2015(2):156–170, 2015.
- [6] R. Chen, B. C. Fung, P. S. Yu, and B. C. Desai. Correlated network data publication via differential privacy. VLDB Journal, 23(4):653–676, 2014.
- [7] G. Cormode, C. Procopiuc, D. Srivastava, and T. T. Tran. Differentially private summaries for sparse data. In ICDT, pages 299–311. ACM, 2012.
- [8] A. De. Lower bounds in differential privacy. In Theory of Cryptography, pages 321–338. Springer, 2012.
- [9] I. Dinur and K. Nissim. Revealing information while preserving privacy. In PODS, pages 202–210. ACM, 2003.
- [10] C. Dwork, K. Kenthapadi, F. McSherry, I. Mironov, and M. Naor. Our data, ourselves: Privacy via distributed noise generation. Advances in Cryptology-EUROCRYPT 2006, pages 486–503, 2006.
- [11] C. Dwork, F. McSherry, K. Nissim, and A. Smith. Calibrating noise to sensitivity in private data analysis. Theory of Cryptography, pages 265–284, 2006.
- [12] C. Dwork and A. Roth. The algorithmic foundations of differential privacy. Foundations and Trends in Theoretical Computer Science, 9(3-4):211–407, 2014.
- [13] B. Fung, K. Wang, R. Chen, and P. S. Yu. Privacy-preserving data publishing: A survey of recent developments. ACM Computing Surveys (CSUR), 42(4):14, 2010.
- [14] A. Ghosh, T. Roughgarden, and M. Sundararajan. Universally utility maximizing privacy mechanisms. SIAM Journal on Computing, 41(6):1673–1693, 2012.
- [15] M. Hardt and K. Talwar. On the geometry of differential privacy. In STOC, pages 705–714. ACM, 2010.
- [16] M. Hay, C. Li, G. Miklau, and D. Jensen. Accurate estimation of the degree distribution of private networks. In ICDM, pages 169–178. IEEE, 2009.
- [17] M. Hay, V. Rastogi, G. Miklau, and D. Suci. Boosting the accuracy of differentially private histograms through consistency. Proceedings of the VLDB Endowment, 3(1-2):1021–1032, 2010.
- [18] C. Li, M. Hay, V. Rastogi, G. Miklau, and A. McGregor. Optimizing linear counting queries under differential privacy. In PODS, pages 123–134. ACM, 2010.
- [19] C. Li and G. Miklau. An adaptive mechanism for accurate query answering under differential privacy. Proceedings of the VLDB Endowment, 5(6):514–525, 2012.
- [20] N. Li, T. Li, and S. Venkatasubramanian. t-closeness: beyond k-anonymity and l-diversity. In ICDE, pages 106–115. IEEE, 2007.
- [21] S. Lloyd. Least squares quantization in pcm. IEEE transactions on information theory, 28(2):129–137, 1982.
- [22] W. Lu and G. Miklau. Exponential random graph estimation under differential privacy. In Proceedings of the 20th ACM SIGKDD international conference

- on Knowledge discovery and data mining, pages 921–930. ACM, 2014.
- [23] A. Machanavajjhala, D. Kifer, J. Gehrke, and M. Venkatasubramanian. Diversity: Privacy beyond k-anonymity. *ACM Transactions on Knowledge Discovery from Data (TKDD)*, 1(1):3, 2007.
- [24] F. McSherry and K. Talwar. Mechanism design via differential privacy. In *FOCS*, pages 94–103. IEEE, 2007.
- [25] F. D. McSherry. Privacy integrated queries: an extensible platform for privacy-preserving data analysis. In *SIGMOD*, pages 19–30. ACM, 2009.
- [26] D. Mir and R. N. Wright. A differentially private estimator for the stochastic kronecker graph model. In *Proceedings of the 2012 Joint EDBT/ICDT Workshops*, pages 167–176. ACM, 2012.
- [27] Y. Mülle, C. Clifton, and K. Böhm. Privacy-integrated graph clustering through differential privacy. In *PAIS 2015*, 2015.
- [28] H. H. Nguyen, A. Imine, and M. Rusinowitch. Detecting communities under differential privacy. In *Proceedings of the 2016 ACM on Workshop on Privacy in the Electronic Society*, pages 83–93. ACM, 2016.
- [29] H. H. Nguyen, A. Imine, and M. Rusinowitch. Network structure release under differential privacy. *Transactions on Data Privacy*, 9(3):26, 2016.
- [30] A. Sala, X. Zhao, C. Wilson, H. Zheng, and B. Y. Zhao. Sharing graphs using differentially private graph models. In *IMC*, pages 81–98. ACM, 2011.
- [31] L. Sweeney. k-anonymity: A model for protecting privacy. *International Journal of Uncertainty, Fuzziness and Knowledge-Based Systems*, 10(05):557–570, 2002.
- [32] Y. Wang and X. Wu. Preserving differential privacy in degree-correlation based graph generation. *TDP*, 6(2):127, 2013.
- [33] Y. Wang, X. Wu, and L. Wu. Differential privacy preserving spectral graph analysis. In *PAKDD*. Springer, 2013.
- [34] Q. Xiao, R. Chen, and K.-L. Tan. Differentially private network data release via structural inference. In *KDD*, pages 911–920. ACM, 2014.
- [35] X. Xiao, G. Wang, and J. Gehrke. Differential privacy via wavelet transforms. *Knowledge and Data Engineering, IEEE Transactions on*, 23(8):1200–1214, 2011.
- [36] G. Yuan, Z. Zhang, M. Winslett, X. Xiao, Y. Yang, and Z. Hao. Lowrank mechanism: optimizing batch queries under differential privacy. *Proceedings of the VLDB Endowment*, 5(11):1352–1363, 2012.

A Passivity Approach to Proportional Controller Design for dynamic systems

Thiết kế bộ điều khiển tỉ lệ dựa trên thụ động cho hệ thống động

Hoang Ngoc Ha^a, Le Phuong Quyen^b

^aTrung tâm công nghệ Thông tin và Truyền thông, Viện Nghiên cứu và Phát triển công nghệ cao Đại học Duy Tân, Việt Nam
Center of Information Technology & Communication, Institute of Research & Development, Duy Tan University, Viet Nam

^bKhoa Điện - Điện Tử, Đại học Duy Tân, Việt Nam
Faculty of Electrical & Electronics Engineering, Duy Tan, University, Viet Nam

Abstract

This study concerns dynamical systems whose dynamics are affine in the control input. Such dynamics are considered to be written into a canonical form, namely the passive port-Hamiltonian representation in order to explore further some structural properties usable for the control design (such as interconnection and damping matrices, bounded Hamiltonian storage function and proportional feedback controller design). The case of a mass-spring-damper system is used to illustrate the approach. Besides, numerical simulations are included in both the open loop and closed loop.

Keywords: Port-Hamiltonian representation, modeling, dynamical systems, passivity, proportional controller.

Tóm tắt

Báo cáo này liên quan đến các hệ thống mà động lực là *affine* theo đầu vào điều khiển. Động lực của hệ được xem xét để viết lại trong một dạng chính tắc, gọi là biểu diễn Hamilton thụ động, nhằm khảo sát rõ hơn các đặc tính cấu trúc và thiết kế điều khiển (như ma trận kết nối/ giảm chấn, hàm trữ năng bị chặn và thiết kế bộ điều khiển tỉ lệ). Hệ khối lượng lò xo giảm sóc được sử dụng để minh họa phương pháp. Mô phỏng số được thực hiện trong vòng hở và vòng kín.

Từ khóa: Biểu diễn Hamilton, mô hình hóa, hệ động lực, thụ động, bộ điều khiển tỉ lệ.

1. Introduction

This paper deals with the port-based modeling of general nonlinear dynamical systems Khalil (2002); Ortega et al. (1998); Van der Schaft (2017); Brogliato et al. (2007) whose dynamics are described by a set of Ordinary Differential Equations (ODEs) and affine in the input u as follows:

$$\dot{x} = f(x) + g(x)u; x(t = 0) = x_{ini} \quad (1)$$

where $x = x(t)$ is the state vector in the operating region $D \in \mathbb{R}^n$, $f(x) \in \mathbb{R}^n$ expresses the smooth (nonlinear) function with respect to the vector field x . The input-state map and the control input are represented by $g(x) \in \mathbb{R}^{n \times m}$ and $u \in \mathbb{R}^m$, respectively. It is worth noting that many industrial applications occurred in electrical systems, electromechanical systems or biochemical systems, etc. belong to this kind of systems Maschke et al. (2000); Van derSchaft (2000);

* The material in this paper was partially presented at the 4th Conference on Electrical, Electronics, communications and Automation (EECA), October 28, 2017, Duy Tân University, Đà Nẵng, Việt Nam.

Ortega *et al.* (2001, 2002); Antonelli and Astolfi (2003); Favache and Dochain (2010); Ramírez *et al.* (2013); Guay and Hudon (2016).

In addition to the Bond graph modeling Couenne *et al.* (2006); Eberard *et al.* (2007); Vu *et al.* (2016), the port-based modeling Maschke *et al.* (2000); Van der Schaft (2000) leads to extension of the so-called port- Hamiltonian (pH) systems. It is always important to transfer the (original) dynamics of the systems to the port-Hamiltonian representation prior to developing state feedback laws for control Ortega *et al.* (2002, 2008); Ortega and Borja (2014); Sira-Ramírez and Angulo-Núñez (1997); Sira-Ramírez (1998). In other words, once a canonical form (i.e., expressed by the pH model Maschke *et al.* (2000); Van der Schaft (2000); Ortega *et al.* (2001)) of the system dynamics is *a priori* derived, then the passivity-based control strategy or interconnection and damping assignment passivity-based control (IDA-PBC) and other extensions (such as the energy shaping control or tracking-error-based control) can be advantageously applied to show stabilization properties. The proportional feedback law design and control scenarios proposed for the simulations are main contributions of this work.

This paper is organized as follows. Section 2 gives a brief overview of the pH representation of (affine) nonlinear dynamical systems. Section 3 is devoted to the modelling and control design of a mass-spring-damper system in the pH framework. Some further discussions are given in Section 4. Section 5 ends the paper with some concluding remarks.

Notations: The following notations are considered throughout the paper:

- \mathbb{R} is the the set of real number.
- T is the matrix transpose operator.
- m and n ($m \leq n$) are the positive integers.
- x_{init} is the initial value of the state vector.

2. The Passive Port-hamiltonian Representation of Affine Dynamical Systems

Assume that if the function $f(x)$ verifies the so-called separability condition Guay and Hudon (2016); Dörfler *et al.* (2009); Ramírez *et al.* (2009); Favache *et al.* (2011); Hudon *et al.* (2015); Hoang *et al.* (2017), that is, $f(x)$ can be decomposed and expressed as the product of some (interconnection and damping) structure matrices and the gradient of a potential function with respect to the state variables, i.e., the co-state variables :

$$f(x) = [J(x) - R(x)] \frac{\partial H(x)}{\partial x} \quad (2)$$

where $J(x)$ and $R(x)$ are the $n \times n$ skew-symmetric inter-connection matrix (i.e., $J(x) = -J^T(x)$) and the $n \times n$ symmetric damping matrix (i.e. $R(x) = R^T(x)$), respectively while $H(x): \mathbb{R}^n \rightarrow \mathbb{R}$ represents the Hamiltonian storage function of the system (possibly related to the total energy of the system). Furthermore, if the damping matrix $R(x)$ is positive semi-definite,

$$R(x) \geq 0 \quad (3)$$

Then, the original dynamics described by (1) is said to be apH representation with dissipation Maschke *et al.* (2000); Van der Schaft (2000); Ortega *et al.* (2001). Equation (1) is then rewritten as follows:

$$\begin{cases} \dot{x} = [J(x) - R(x)] \frac{\partial H(x)}{\partial x} + g(x)u \\ y = g(x)^T \frac{\partial H(x)}{\partial x} \end{cases} \quad (4)$$

where y is the output.

It can be clearly seen for the pH models defined by (3) (4) that the time derivative of the Hamiltonian storage function $H(x)$ satisfies the energy balance equation Ortega *et al.* (2001) below:

$$\frac{dH(x)}{dt} = - \left[\frac{\partial H(x)}{\partial x} \right]^T R(x) \frac{\partial H(x)}{\partial x} + u^T y \quad (5)$$

Thanks to (3), (5) becomes:

$$\underbrace{\frac{dH(x)}{dt}}_{\text{stored power}} \leq \underbrace{u^T y}_{\text{sup plied power}} \quad (6)$$

From a physical point of view, inequality in (6) implies that the total amount of energy supplied from external source is always greater than the increase in the energy stored in the system. Also, equality in (6) holds only if the damping matrix $R(x)$, that is strongly related to the dissipation term, is equal to 0. Hence, the pH system (4) is said to be passive with input u and output y corresponding to the Hamiltonian storage function $H(x)$ Van der Schaft (2017); Bao and Lee (2007). This is one of advantageous features of the pH representation and has been applied for the control design, even for the stabilization of infinite dimensional systems (see e.g., Alonso and Ydstie (2001); Hoang and Phan (2016)).

We shall not elaborate any further on the pH representation here (for example, the concepts related to the cyclopassive/ passive property or Dirac structure, etc.) and refer the reader to Maschke *et al.* (2000); Van der Schaft (2000); Ortega *et al.* (2002); Dörfler *et al.* (2009); Hoang *et al.* (2017) for more information.

3. The Mass-spring-damper System Case Study

To illustrate the concepts proposed in Section 2, we illustrate our main points with a simple case study, that is the mass-spring-damper system. Originally, the port Hamiltonian representation has been first considered for electrical or mechanical systems as seen in the literature (see e.g., (Ortega *et al.* (1998); Van der Schaft (2000); Batlle (2005))).

Drag system of a car traveling over a bumpy road can be modeled as a mass-spring-damper system as shown in Figure 1 Batlle (2005).

The following equation is derived using Newton's secondlaw McCall (2010)¹:

$$M \frac{d^2 z(t)}{dt^2} = F - kz(t) - c \frac{dz(t)}{dt} \quad (7)$$

where :

- M is the mass of the body;
- F is the external force;
- k is the stiffness constant of the (linear) spring;
- c is the damping constant.

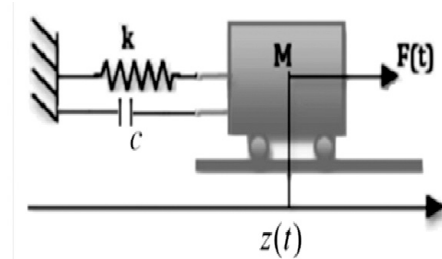


Figure 1: A mass-spring-damper system.

Let x be the vector consisting of the movement $z(t)$ and the momentum of the body $M \frac{dz(t)}{dt}$, i.e.

$$x = (x_1, x_2)^T \equiv \left(z(t), M \frac{dz(t)}{dt} \right)^T, \quad (7) \text{ can be}$$

rewritten as follows:

$$\begin{pmatrix} \frac{dx_1}{dt} \\ \frac{dx_2}{dt} \end{pmatrix} = \begin{pmatrix} 0 & 1 \\ -1 & -c \end{pmatrix} \begin{pmatrix} x_1 \\ x_2 \end{pmatrix} + \begin{pmatrix} 0 \\ 1 \end{pmatrix} F \quad (8)$$

The system dynamics (8) leads to a pH representation (4)with:

$$J(x) = \begin{pmatrix} 0 & 1 \\ -1 & 0 \end{pmatrix} \quad (9)$$

$$R(x) = \begin{pmatrix} 0 & 0 \\ 0 & c \end{pmatrix} \quad (10)$$

$$g(x) = \begin{pmatrix} 0 \\ 1 \end{pmatrix}, u = F \quad (11)$$

$$y = \frac{x_2}{M} \equiv \frac{dz(t)}{dt} \quad (\text{the velocity}) \quad (12)$$

¹This belongs to the so-called (generalized) Euler-Lagrange equations of classical mechanics Ortega *et al.* (1998); Van der Schaft (2000).

and,
$$H(x) = \frac{1}{2} kx_1^2 + \frac{1}{2} \frac{x_2^2}{M} \quad (13)$$

In this case, the Hamiltonian storage function $H(x)$ (13) is equal to the total energy of the system, (i.e., it characterizes the amount of the elastic potential energy of the spring and the kinetic energy of the body, respectively). It therefore has the unit of energy. The damping matrix $R(x)$ (10) is symmetric and positive semi-definite.

Remark 1. As an analogy between mechanical and electrical systems Firestone (1933), it is worth noting that a second order ordinary differential equation of the series RLC circuit operated under a voltage source $V(t)$ can be written as follows:

$$L \frac{d^2 i(t)}{dt^2} + R \frac{di(t)}{dt} + \frac{1}{C} i(t) = \frac{dV(t)}{dt}$$

where $i(t)$ is the electric current. This is clearly equivalent to (7) in some sense.

For the sake of illustration, a geometric shape of the Hamiltonian storage function $H(x)$ (13) is shown in Figure 2.

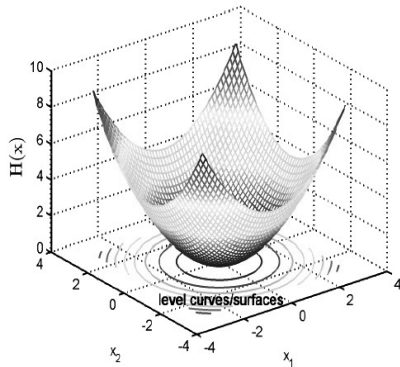


Figure 2: The Hamiltonian storage function $H(x) = \alpha_1 x_1^2 + \alpha_2 x_2^2$ with $\alpha_1 = \alpha_2 = \frac{1}{2}$

4. Some Further Discussions

4.1 The proportional controller design

Let us state the following proposition.

Proposition 1. Under a zero state detectability condition and the boundedness from below of the Hamiltonian storage function $H(x)$ by 0, it follows that an explicit proportional static output

feedback law of the form,

$$u = -Ky \quad (14)$$

with $K = K^T > 0$ so-called damping injection gain, renders the controlled pH system dissipative and therefore asymptotically stabilized at the (singular) equilibrium x^* .

Proof. From (6)(14), one obtains:

$$\frac{dH(x)}{dt} \leq y^T Ky < 0$$

The proof follows immediately by invoking La Salle's invariance principle Khalil (2002); Brogliato et al. (2007); Ortega et al. (2002). A complete version of the proof can be found in Hoang and Phan (2016).

Remark 2. The convergence speed of the controlled system goes faster by increasing the controller gain K . Better performance of the controller can be proposed with the gain K derived from the Ziegler-Nichols tuning method.

Remark 3. Interestingly, the proportional feedback law u (14) can be considered in Figure 3 as control by simple interconnection where the controller here is so that

$$y_c = C(u_c) = Ku_c \quad (15)$$

It can be checked easily that

$$u_c(t)^T y_c(t) + u(t)^T y(t) = 0, \forall t \quad (16)$$

since $U_c(t) = y(t)$ and $u(t) = -Y_c(t)$. The interconnection is therefore power continuous Ortega et al. (1998); Van der Schaft (2017); Battle (2005).

Note also that the feedback law (14) may make the overall system worse when the Hamiltonian storage function $H(x)$ (or also, the power) at any equilibrium except the trivial one x^* is nonzero Ortega et al. (2001). The situation is similar to that of the so-called dissipation obstacle Ortega et al. (2002).

4.2 Numerical simulations

The simulations are carried out for the mass-springdamper system using MATLAB & SIMULINK.

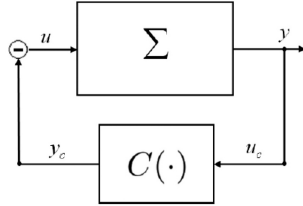


Figure 3: A standard negative feedback interconnection structure where Σ and $C(\cdot)$ are the plant and the controller, respectively.

The open loop SIMULINK model designed for the simulations is given in Figure A1 of Appendix with $k = 0.25$ (N/m), $c = 0.5$ (N/(s.m)) and $M = 6.25$ (kg) (see also Longoria (2014))². The input force of the system is a unit step, *i.e.*, $u(t) = S(t)$ where $S(t)$ is the unit stepfunction.

The initial conditions are chosen to be $x_1(t = 0) = x_{1,init} = 3$ and $x_2(t = 0) = x_{2,init} = 0$. Figure 4 shows the time evolutions of the states of the system and the storage function. It is shown that the storage function is bounded from below by a positive scalar. In other words, it is not equal to 0 since the states x_1 and/or x_2 converge to the nonzero values at steady state (*i.e.*, $x_{1,ss} = \frac{F}{k}$ and $x_{2,ss} = 0$).

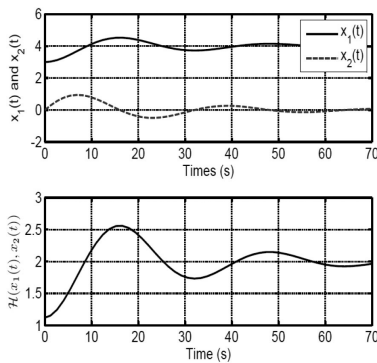


Figure 4: The states and storage function *w.r.t.* time.

Now, we propose to stabilize the system at the natural equilibrium $x^* = (x_1^*, x_2^*)^T = (0, 0)^T$. The control situation is that the system is operating

² It can be shown that the damping factor $\zeta := \frac{1}{2} \frac{c}{\sqrt{kM}}$ equals 0.2. The open loop system is therefore underdamped.

normally with the unit step input, at time $t = t_1 > 0$, the unit step input is switched off and the proportional feedback law (14) is applied. The explicit expression of the manipulated input is then expressed as follows:

$$u(t) = (S(t) - S(t - t_1)) - K \frac{x_2}{M}(t - t_1) \quad (17)$$

where equations (14) and (12) have been used. The closedloop SIMULINK model with the proportional feedback law is given in Figure A2 of Appendix with $K = 2$ and $t_1 = 30$ (s).

Figure 5 shows that the controlled Hamiltonian storage function with the proportional feedback law (17) converges to 0 as $t \rightarrow +\infty$. As consequence, the global asymptotic convergence of the controlled states x to x^* is guaranteed as seen in Figure 6. Furthermore, the manipulated input $u(17)$ is physically admissible in terms of amplitude and dynamics.

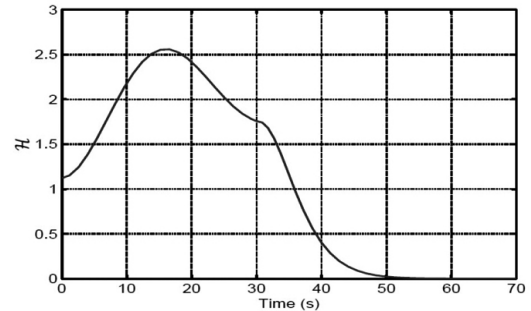


Figure 5: The controlled Hamiltonian storage function with the proportional feedback law.

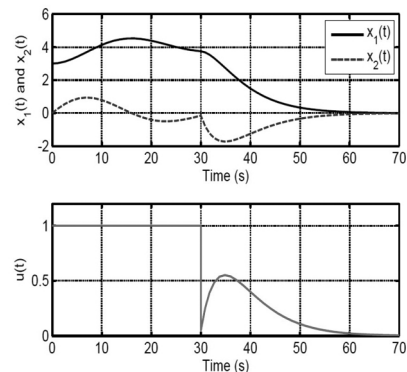


Figure 6: The controlled states and manipulated input *w.r.t.* time with the proportional feedback law.

5. Conclusion

In this work, a port-based modeling of mass-

spring-damper systems is reintroduced and leads to the so-called port-Hamiltonian representation. In this presentation, some structural properties such as interconnection and damping matrices and Hamiltonian storage function are explicitly shown. Interestingly, those terms have clear physical meaning. The feedback design and control scenarios proposed for the simulations are main contributions of the paper.

As the pH model is of great interest, it remains now to extend this structure to biochemical reaction systems or multi-physics systems (see, e.g. *Dörfler et al. (2009)*).

References

- [1] H.K. Khalil, *Nonlinear systems*. Prentice Hall, Upper Saddle River, 3rd edition, 2002.
- [2] R. Ortega, J.A. Loria Perez, P.J. Nicklasson, and H. Sira-Ramirez, *Passivity-based control of Euler-Lagrange systems: Mechanical, electrical and electromechanical applications*. Springer London, 1st edition, 1998.
- [3] A. Van der Schaft, *L_2 -gain and passivity techniques in nonlinear control*. Springer, 3rd edition, 2017.
- [4] B. Brogliato, R. Lozano, B. Maschke, and O. Egeland, *Dissipative system analysis and control - Theory and applications*. Springer-Verlag London, second edition, 2007.
- [5] B. Maschke, R. Ortega, and A. Van der Schaft, "Energybased Lyapunov functions for forced Hamiltonian systems with dissipation," *IEEE Transactions on Automatic Control*, 45(8), pp. 1498-1502, 2000.
- [6] A. Van der Schaft, "Port-controlled Hamiltonian systems: Towards a theory for control and design of nonlinear physical systems," *SICE journal*, 39(2), pp. 91-98, 2000.
- [7] R. Ortega, A. Van der Schaft, I. Mareels, and B. Maschke, "Putting energy back in control," *IEEE Control Syst. Mag.*, 21(2), pp. 18-33, 2001.
- [8] R. Ortega, A. Van der Schaft, B. Maschke, and G. Escobar, "Interconnection and damping assignment passivity based control of port-controlled Hamiltonian systems," *Automatica*, 38(4), pp. 585-596, 2002.
- [9] R. Antonelli, and A. Astolfi, "Continuous stirred tank reactors: easy to stabilise?" *Automatica*, 39(10), pp.1817-1827, 2003.
- [10] A. Favache, and D. Dochain, "Power-shaping control of reaction systems: The CSTR case," *Automatica*, 46(11), pp. 1877-1883, 2010.
- [11] H. Ramirez, B. Maschke, and D. Sbarbaro, "Irreversible port-Hamiltonian systems: A general formulation of irreversible processes with application to the CSTR," *Chemical Engineering Science*, 89, pp. 223-234, 2013.
- [12] M. Guay, and N. Hudon, "Stabilization of nonlinear systems via potential-based realization," *IEEE Transactions on Automatic Control*, 61(4), pp. 1075-1080, 2016.
- [13] F. Couenne, C. Jallut, B. Maschke, P. Breedveld, and M. Tayakout, "Bond graph modelling for chemical reactors," *Mathematical and Computer Modelling of Dynamical Systems*, 12(2-3), pp. 159-174, 2006.
- [14] D. Eberard, B. Maschke, and A. Van der Schaft, "An extension of Hamiltonian systems to the thermodynamic phase space: Towards a geometry of nonreversible processes," *Reports on Mathematical Physics*, 60(2), pp.175-198, 2007.
- [15] N.M.T. Vu, L. Lefèvre, and B. Maschke, "A structured control model for the thermo-magneto-hydrodynamics of plasmas in tokamaks," *Mathematical and Computer Modelling of Dynamical Systems*, 22(3), pp. 181-206, 2016.
- [16] R. Ortega, A. Van der Schaft, F. Castanos, and A. Astolfi, "Control by interconnection and standard passivity based control of port-Hamiltonian systems," *IEEE Transactions on Automatic Control*, 53(11), pp. 2527-2542, 2008.
- [17] R. Ortega, and L.P. Borja, "New results on control by interconnection and energy-balancing passivity-based control of port-Hamiltonian systems," *In Proc. The 53rd IEEE Conference on Decision and Control (CDC)*, Los Angeles, CA, USA, 2014, pp. 2346-2351.
- [18] H. Sira-Ramirez, and I. Angulo-Núñez, "Passivity-based control of nonlinear chemical processes," *International Journal of Control*, 68(5), pp. 971-996, 1997.
- [19] H. Sira-Ramirez, "A general canonical form for feedback passivity of nonlinear systems," *International Journal of Control*, 71(5), 891-905, 1998.
- [20] F. Dörfler, J.K. Johnsen, and F. Allgöwer, "An introduction to interconnection and damping assignment passivity-based control in process engineering," *Journal of Process Control*, 19(9), pp. 1413-1426, 2009.
- [21] H. Ramirez, D. Sbarbaro, and R. Ortega, "On the control of non-linear processes: An IDA-PBC approach," *Journal of Process Control*, 19(3), pp. 405-414, 2009.
- [22] A. Favache, D. Dochain, and J.J. Winkin, "Power-shaping control: Writing the system dynamics into the Brayton-Moser form," *Systems & Control Letters*, 60(8), pp. 618-624, 2011.
- [23] N. Hudon, H. Hoang, J.P. Gacia-Sandoval, and D.

- Dochain, “Towards a potential-based analysis of reacting systems,” *IFAC-PapersOnLine*, 48(13), pp. 141-143, 2015.
- [24] H. Hoang, D. Dochain, F. Couenne, and Y. Le Gorrec, “Dissipative pseudo-Hamiltonian realization of chemical systems using irreversible thermodynamics,” *Mathematical and Computer Modelling of Dynamical Systems*, 23(2), pp. 135-155, 2017.
- [25] J. Bao, and P.L. Lee, *Advances in Industrial Control: Process control - The passive systems approach*. Springer-Verlag London, first edition, 2007.
- [26] A.A. Alonso, and B.E. Ydstie, “Stabilization of distributed systems using irreversible thermodynamics,” *Automatica*, 37(11), pp. 1739-1755, 2001.
- [27] N.H. Hoang, and D.T. Phan, “Nonlinear control of temperature profile of unstable heat conduction systems: A port-Hamiltonian approach,” *Journal of Computer Science and Cybernetics*, 32(1), pp. 61-74, 2016.
- [28] C. Batlle, “Passive control theory I and II,” *II EURON/ GEOPLEX Summer School on Modeling and Control of Complex Dynamical Systems*, July 18-22, 2005, Bertinoro, Italy.
- [29] M.W. McCall, *Classical mechanics: From Newton to Einstein - A modern introduction*. Wiley, 2nd edition, 2010. ISBN: 9780470715741
- [30] F.A. Firestone, “A new analogy between mechanical and electrical systems,” *The Journal of the Acoustical Society of America*, 4(3), pp. 249-267, 1933.
- [31] R.G. Longoria, “Modeling and experimentation: Mass spring-damper system dynamics,” *Department of Mechanical Engineering, The University of Texas at Austin*, July 20, 2014.

A. APPENDIX

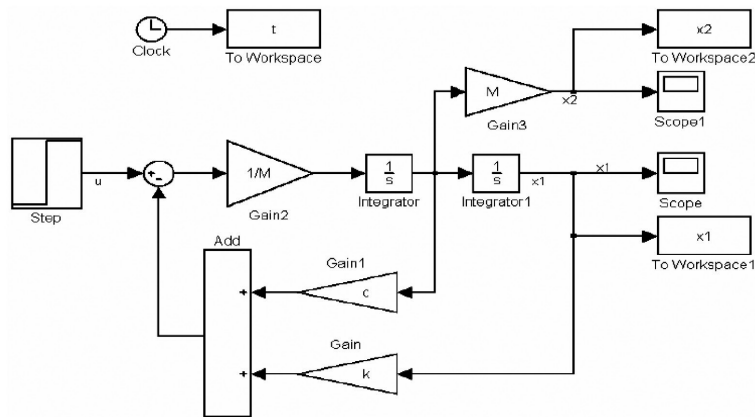


Figure A1. The open Loop SIMULINK Model

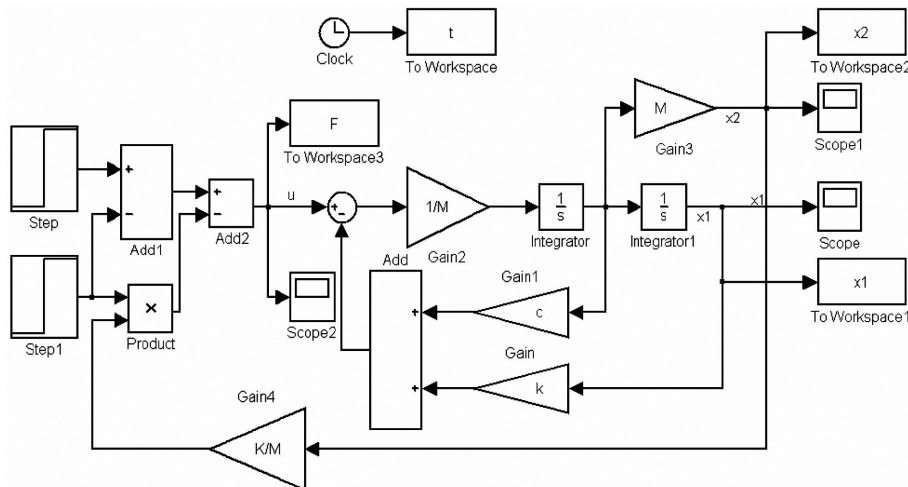


Figure A2. The closed loop SIMULINK model with the proportional feedback law.

A Computational Study of Antioxidant Potential of Diterpenoid Amides in the Extract of the Leaves of *Erythrophleum fordii*

Nghiên cứu tiềm năng chống oxi hóa của các hợp chất Diterpenoid Amides trong chiết xuất từ lá của cây Lim xanh bằng phương pháp Hóa tính toán

Truc Xuyen Nguyen Phan,^a Thi Hau Nguyen,^b Mai Thi Hai Anh,^c Thi Chinh Ngo,^d Duy Quang Dao^{d,*}

¹Faculty of Environment and Chemical Engineering, Duy Tan University, Vietnam

Khoa Môi trường và Công nghệ hóa, Đại học Duy Tân, Việt Nam

²Department of Pharmacy, Duy Tan University, Vietnam

Khoa Dược, Đại học Duy Tân, Việt Nam

³Faculty of Forestry Agriculture, Tay Nguyen University, Vietnam

Khoa Nông Lâm nghiệp, Đại học Tây Nguyên, 567 Lê Duẩn, Việt Nam

⁴Institute of Research and Development, Duy Tan University, Vietnam

Viện Nghiên cứu và Phát triển, Đại học Duy Tân, Việt Nam

(Ngày nhận bài: 21/11/2017, ngày phản biện xong: 10/01/2018, ngày chấp nhận đăng: 20/03/2018)

Abstract

Antioxidant properties of 4 diterpenoid amide derivatives (3HDTA, 3ADTA, 3TDTA, 6HDCA) have been investigated via hydrogen atom transfer (HAT), single electron transfer-proton transfer (SET-PT) and sequential proton loss electron transfer (SPLET) mechanisms using density functional theory (DFT) methods. The characterizing thermodynamic parameters such as C–H bond dissociation enthalpy (BDE), ionization energy (IE), electron affinity (EA) and proton affinity (PA) have been calculated for the gas phase at the B3LYP/6-311G(d,p) model chemistry. The results show that the antioxidant capacity follows decreasing trend: 3TDTA > 6HDCA > 3HDTA > 3ADTA. H-atoms at C nearby π -bond play an important role in the antioxidant ability of diterpenoid amides via HAT mechanism (i.e. C7). 3HDTA is considered the most antioxidant potential with the BDE (C-H) values at C7 atom is 70.52 kcal/mol. Moreover, via the SETPT mechanism 6HDCA is the most potential with IE and EA value are 9.37 eV and 0.990eV, respectively. Via SPLET mechanism, 3TDTA and 6HDCA show higher antioxidant capacity with PA value are 324.27 and 338.22 kcal/mol, singly.

Keywords: Erythrophleum fordii, diterpenoid amide; antioxidant; HAT; SET-PT; SPLET, DFT.

Tóm tắt

Tính chất chống oxi hóa của bốn dẫn xuất diterpenoid amide (3HDTA, 3ADTA, 3TDTA, 6HDCA) đã được khảo sát bằng lý thuyết phiếm hàm mật độ (DFT) thông qua các cơ chế chuyển nguyên tử H (HAT), chuyển đơn điện tử-chuyển proton (SET-PT) và mất proton chuyển điện tử liên tiếp (SPLET). Các thông số nhiệt động học đặc trưng như năng lượng phân ly liên kết C-H (BDE), năng lượng ion hóa (IE), ái lực điện tử (EA) và ái lực proton (PA) đã được tính toán trong pha khí ở mức lý thuyết B3LYP/6-311G(d,p). Kết quả chỉ ra rằng khả năng chống oxi hóa giảm theo chiều hướng 3TDTA > 6HDCA > 3HDTA > 3ADTA. Các nguyên tử H tại nguyên tử C gắn liền kết π (i.e. C7) đóng vai trò quan trọng trong khả năng chống oxi hóa của các hợp chất diterpenoid amides theo cơ chế HAT. Hợp chất 3HDTA được xem như là chất chống oxi

hóa tiềm năng nhất với giá trị BDE(C-H) tại nguyên tử C7 bằng 70.52 kcal/mol. Ngoài ra, theo cơ chế SETPT, hợp chất 6HDCA tỏ ra là chất chống oxi hóa tiềm năng nhất với giá trị IE và EA lần lượt bằng 9.37 và 0.990eV. Theo cơ chế SPLET, hợp chất 3TDTA và 6HDCA có khả năng chống oxi hóa cao hơn với giá trị PA lần lượt bằng 324.27 và 338.22 kcal/mol.

Từ khóa: Erythrophleum fordii, diterpenoid amide; chất chống oxi hóa; HAT; SET-PT; SPLET, DFT.

1. Introduction

Erythrophleum fordii (Leguminosae) is a large tree species that is widely distributed in China, Taiwan and Vietnam. It is a medicinal and least toxic plant. It is used as a medicine for invigoration and promotion of blood circulation¹. Recently, Du *et al*² have reported phytochemical investigation from the leaves of *Erythrophleum fordii* resulted in the isolation of 13 compounds². The isolation, structural elucidation and biotesting of three novel cassaine diterpenoid–diterpenoid amide dimers, seven new cassaine diterpenoid amides, erythrophlesins and 3 beta-hydroxynorery throsuamid from the leaves of *E. fordii* were performed². Among them, diterpenoid amides represent as ones of the most massive components with significantly selective cytotoxic activities ($IC_{50} < 10 \mu M$) against cancer cells. Manh-Hung T.*et al*³ reported a phytochemical investigation into the bark of *Erythrophleum fordii*. This experiment isolated and characterized four new compounds, two new cassaine diterpenoids (erythrofordin T and U) and two new cassaine diterpenoid amines (erythroformine A and B), as well as nine known compounds. The results in this *in vitro* study suggest that cassaine diterpenoid amines had potential application in the treatment of human lung. In fact, cassaine diterpene amines showed potent cytotoxic activity against all non-small cell lung cancer cell lines less than $6 \mu M$ ³. Insight into the possible antioxidant mechanisms of these interesting compounds may allow explaining their interesting medicinal activities.

Thus, in this work, the antioxidant capacities of four selected diterpenoid amides identified in the leaves of *Erythrophleum fordii* including 3 β -Hydroxydinorerythrosuamide (**3HDTA**), 3 β -Acetoxydinorerythrosuamide (**3ADTA**),

3 β -Tigloyloxydinorerythrosuamide (**3TDTA**) and 6 α -Hydroxydinorcassamide (**6HDCA**) (Figure 1) were evaluated. Three common mechanisms, namely the hydrogen atom transfer (HAT), single electron transfer (SET) mechanisms and sequential proton loss electron transfer (SPLET) were taken into account. The characterizing thermodynamic parameters including bond dissociation enthalpy (BDE), vertical ionization energy (IE), affinity electrons (EA) and the proton affinity (PA) were calculated for the gas phase using density-functional theory (DFT) at B3LYP/6-311G(d,p) model chemistry.

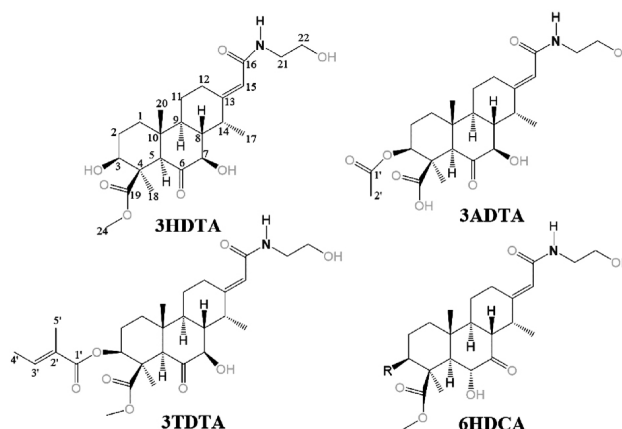


Figure 1: Chemical structures and numbering atomic sites of four studied diterpenoid amides.

2. Theoretical and Computational Methods

The geometry optimization and the vibrational frequency calculation of each compound and the related radicals, cationic and anionic radicals were calculated using B3LYP/6-311G(d,p) methods. All calculations were performed using the Gaussian 09 Revision E.01 suite of program⁴.

Three common antioxidant mechanisms are represented as follows:

- Hydrogen atom transfer (HAT)



- Single electron transfer (SET)



- Sequential proton loss electron transfer (SPL-ET)



The BDE, IE, EA and PA values were determined from total enthalpies of the individual species in the gasphase, as follows:

$$\text{BDE}(\text{ArO-H}) = \text{H}(\text{ArO}^\bullet) + \text{H}(\text{H}^\bullet) - \text{H}(\text{ArOH})$$

$$\text{IE} = \text{H}(\text{AH}^{+\bullet}) - \text{H}(\text{AH})$$

$$\text{EA} = \text{H}(\text{AH}^{\bullet-}) - \text{H}(\text{AH})$$

$$\text{PA} = \text{H}(\text{A}^-) + \text{H}(\text{H}^+) - \text{H}(\text{AH})$$

Where H is the enthalpy of different species at 298.15 K and 1.0 atm. The enthalpies were estimated from the given expression: $H(T) = E_0 + \text{ZPE} + H_{\text{trans}} + H_{\text{rot}} + H_{\text{vib}} + RT$. The H_{trans} , H_{rot} , and H_{vib} are the translational, rotational, and vibrational contributions to the enthalpy, respectively. E_0 is the total energy at 0 K and ZPE is the zero-point vibrational energy.

3. Results and Discussion

3.1. Optimized structure and molecular properties

Figure 2 shows the optimized geometry of four diterpenoid amides. It can be observed in Figure 2 that molecular structures are stabilized by forming several hydrogen bonds with different oxy atoms with high electron density. For example, the length of hydrogen bonds recognizing in 3HDTA (Figure 2-A) varies from 1.86 to 1.99 Å, while the hydrogen bond length changes from 1.85 to 2.04 Å for 3ADTA (Figure 2-B), 1.86 to 2.04 Å for 3TDTA (Figure 2-C) and 1.86 to 1.93 Å for 6HDCA (Figure 2-D).

The HOMO and LUMO structures show that diterpenoid amide moiety plays as electron donating as well as accepting center of the

compounds. The HOMO and LUMO of four studied compounds are present in Figure 3. It is observed that HOMO structures are found that C=C, C=O bonds and oxygen, nitrogen with high electron densities (i.e. red color parts) than the other parts of the molecule. In the cases of 3HDTA, HOMO orbital has high electron density at C13=C15, C16-N... Moreover, LUMO orbital displays at substituent of cyclohexane rings such as: C12-C13, C16-N, C17-H, C13=C15, C16-O... (Figure 3-A).

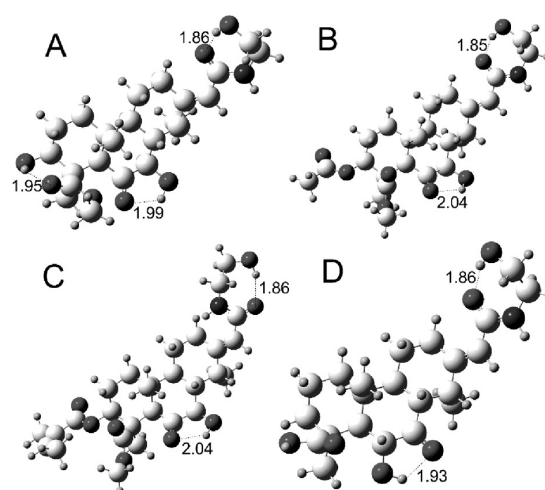


Figure 2: Optimized structures of the diterpenoid amides: (A) 3HDTA, (B) 3ADTA, (C) 3TDTA and (D) 6HDCA at the B3LYP/6-311G(d,p) level of theory.

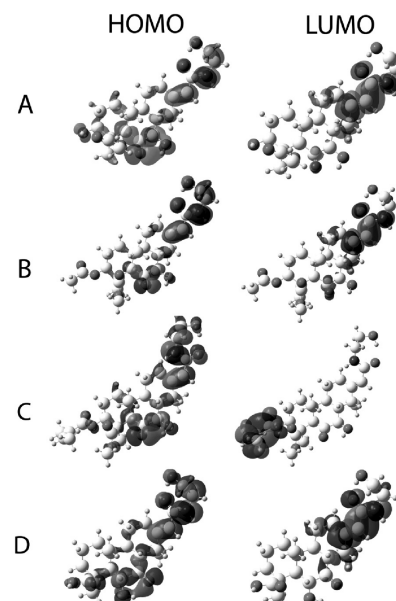


Figure 3: HOMO and LUMO distributions of four diterpenoid amides: (A) 3HDTA, (B) 3ADTA, (C) 3TDTA and (D) 6HDCA.

3.2. The antioxidant capacity of diterpenoid amides

3.2.1. The H atom transfer (HAT) mechanism

In this study, the BDEs(C-H) corresponding to the weakest C-H bond of each diterpenoid amides in the gas phase are computed at B3LYP/6-311G(d,p) level of theory (Table 1).

As a result, the highest H atom donating ability of the studied compounds follows decreasing trend: 3TDTA > 3HDTA ≈ 6HDCA > 3ADTA. The lowest BDE(C-H) value is determined at C7-H position. The lowest BDE (C-H) of 3TDTA, 3HDTA, 6HDCA and 3ADTA are equal to 69.44, 70.52, 70.86 and 72.96 kcal/mol, respectively. The H-donating capacity at C7 is easier than the other C-H bonds because C6=O bond nearby C7 that makes this bond to dissociate easily. In comparison with BDE of phenol (89.4 kcal/mol)⁵ and α -terpinene (74.4 kcal/mol)⁶, these four compounds are the potential antioxidants via HAT mechanism.

3.2.2. The single electron transfer followed by proton transfer (SET-PT) mechanism

The ionization energy (IE) and electron affinity (EA) are important parameters of the antioxidants

characterizing the single electron transfer (SET) mechanism. IE value is corresponding to the electron donating capacity. The electron affinity (EA) represents the amount of energy released when an electron is added to a neutral molecule in the gaseous state to form a negative ion. The lower IE value is, the easier electron transfer is, while the higher EA value is the easier electron acceptor is.

Hence, vertical IE and EA of diterpenoid amide compounds are systematically computed using the semi-empirical PM6 method. The results are reported in Table 2. IE values fluctuate from 9.37 (6HDCA) to 9.59 eV (3ADTA). In comparison with IE of phenol (8.49 eV), α -pinene (8.07 eV), limonene (8.3 eV)⁷, the ones of these four diterpenoid amides are all higher. It means that the electron transfer is not favored in this case. In contrast, the four compounds have high EA values which follows the trend: 6HDCA (0.990 eV) > 3HDTA (0.979 eV) > 3ADTA (0.934 eV) > 3TDTA (0.714 eV). This illustrates that studied four diterpenoid amides may have the high antioxidant capacity via electron accepting capacity from free radicals.

Table 1: Calculated the BDE(C-H)s for diterpenoid amides in the gas phase by B3LYP/6-311G(d,p) model chemistry

Compounds	C-H bond positions	BDE(i), kcal/mol	Δ BDE*, kcal/mol	PA (kcal/mol)
3HDTA	C21-H	88.47	0.93	344.92
	C22-H	88.87	0.53	
	C14-H	78.92	10.48	
	C7-H	70.52	18.88	
3ADTA	C22-H	88.88	0.52	346.61
	C7-H	72.96	16.44	
3TDTA	C7-H	69.44	19.96	324.27
6HDCA	C22-H	89.02	0.38	338.22
	C6-H	70.86	18.54	

* Δ BDE = |BDE(O-H)phenol - BDE(C-H)|, (BDE(O-H)phenol = 89.4 kcal/mol⁵)

Table 2: Vertical ionization energy (IE), electron affinity (EA) calculated by PM6

Compounds	IE (eV)	EA (eV)
3HDTA	9.53	0.979
3ADTA	9.59	0.934
3TDTA	9.58	0.714
6HDCA	9.37	0.990

3.2.3. The sequential proton loss electron transfer (SPLET) mechanism

In the first step of the SPLET mechanism, diterpenoid amides donate a proton to free radicals that is characterized by proton affinity (PA) values. The easier proton donating capacity corresponds to lower PA value. The lower PA is described for higher antioxidant capacity via this mechanism. PA values of each diterpenoid amide calculated at B3LYP/6-311G(d,p) method are reported in Table 1.

As can be seen in Table 1, the calculated PA values of four compounds increase from 324.27 kcal/mol (for 3TDTA) to 346.61 kcal/mol (for 3ADTA). Thus, the antioxidant capacity follows decreasing trend: 3TDTA > 6HDCA > 3HDTA > 3ADTA corresponding to PA values of 324.27, 338.22, 344.92 and 344.92 kcal/mol, respectively. It means that 3TDTA may be the most potential antioxidant via this mechanism.

4. Conclusions

In this study, the antioxidant capacity of 4 diterpenoid amide compounds extracted from the leaves of *Erythrophleum fordii* has been studied via HAT, SET and SPLET mechanisms. Semi-empirical PM6 and B3LYP/6-311G(d,p) DFT methods were used to calculate various

thermodynamic parameters including BDE, IE, EA and PA. The obtained results show that 3HDTA, 3ADTA, 3TDTA and 6HDCA represent as potential antioxidants via HAT mechanism. The easiest C–H breaking bond is usually found at the C7 atom located nearby π bonds. The SET mechanism demonstrates that 6HDCA is considered the most antioxidant potential with EA value of 0.99 eV. Via SPLET mechanism, 3TDTA and 6HDCA are high antioxidant capacity with PA value of 324.27 and 338.22 kcal/mol, singly.

Acknowledgements

This research is funded by Vietnam National Foundation for Science and Technology Development (NAFOSTED) under grant number 104.06-2015.09.

References

1. F. Yu, N. Li, and S.-S. Yu, A new diterpenoid glucopyranoside from *Erythrophleum fordii*. *J.Asian Nat. Prod. Res.* **2005**, 7, 19–24,
2. D. Du et al., Cytotoxic cassaine diterpenoid-diterpenoid amide dimers and diterpenoid amides from the leaves of *Erythrophleum fordii*. *Phytochemistry* **2010**, 71(14–15), 1749–1755,
3. Manh Tuan Ha et al., Cytotoxic and apoptosis-inducing activities against human lung cancer cell lines of cassaine diterpenoids from the bark of *Erythrophleum fordii*. *Bioorganic & Medicinal Chemistry Letters*, 2017,**13**, 2946-2952.,
4. Frisch M. J., et al. Gaussian 09, Revision E.01, Gaussian, Inc., Wallingford CT, 2013.
5. Yu-Ran L, Bond dissociation energies in organic compound. CRC Press LLC, 2003.
6. T. C. Ngo, D. Q. Dao, N. M. Thong, and P. C. Nam, Insight into the antioxidant properties of non-phenolic terpenoids contained in essential oils extracted from the buds of *Cleistocalyx operculatus*: a DFT study. *RSC Adv.* **2016**, 6 (37), 30824–30834.
7. NIST Webbook, <http://webbook.nist.gov/chemistry/2017>

Physical Layer Secrecy of 5G Non-Orthogonal Multiple Access in Uplink Networks

Bảo mật lớp vật lý trong mạng 5G sử dụng cơ chế đa truy cập phi trực giao NOMA ở đường truyền lên

Nguyen Van Long, Ha Duc Binh, Tran Duc Dung

Khoa Sau Đại học, Đại học Duy Tân, Việt Nam

Faculty of Graduate School, Duy Tan University, Vietnam

Khoa Điện - Điện tử, Đại học Duy Tân, Việt Nam

Faculty of Electrical & Electronics Engineering, Duy Tan University, Vietnam

(Ngày nhận bài: 17/01/2018, ngày phản biện xong: 28/02/2018, ngày chấp nhận đăng: 20/03/2018)

Abstract

In this paper, the secrecy performance of non-orthogonal multiple access (NOMA) in uplink networks is studied. The NOMA system consists of one base station, one legitimate user pair and one eavesdropper. In this considered system, two users transmit the messages to base station. Meanwhile, the eavesdropper tries to extract these users' messages without attack. In order to evaluate the secrecy performance of this system, the exact closed-form expressions of secrecy outage probability of two users are derived by using statistical characteristics of signal-to-noise ratio (SNR) and signal-to-interference-plus-noise ratio (SINR). Moreover, in order to gain insight into this system, we investigate the performance of this considered system according to key parameters, such as transmitted power and distances. Finally, the correctness of the analytical results is confirmed by Monte-Carlo simulation.

Từ khóa: đa truy cập phi trực giao; NOMA; 5G; bảo mật lớp vật lý; dung lượng bảo mật.

Tóm tắt

Trong bài báo này, chúng tôi tiến hành nghiên cứu khả năng bảo mật lớp vật lý của mạng di động 5G sử dụng kỹ thuật đa truy cập phi trực giao (Non-Orthogonal Multiple Access - NOMA) cho đường truyền lên. Mô hình mạng được xem xét trong bài báo này gồm 1 trạm cơ sở, 1 cặp người sử dụng hợp pháp và 1 máy nghe lén. Trong hệ thống này, người dùng truyền thông tin đến trạm cơ sở, trong khi đó máy nghe lén tìm cách trích thông tin có ích của cặp người dùng mà không chủ động tấn công. Chúng tôi tìm ra các biểu thức dạng tường minh biểu diễn xác suất tồn tại dung lượng bảo mật để đánh giá khả năng bảo mật của hệ thống thông qua việc sử dụng đặc tính thống kê của tỉ số tín hiệu trên nhiễu (SNR) và tỉ số tín hiệu trên can nhiễu và nhiễu (SINR). Ngoài ra, để hiểu sâu sắc hành vi của hệ thống này, chúng tôi khảo sát hiệu năng của hệ thống theo các tham số quan trọng như công suất phát và khoảng cách. Cuối cùng, tính đúng đắn của kết quả phân tích được xác nhận bằng phương pháp mô phỏng Monte-Carlo.

Keywords: non-orthogonal multiple access; physical layer security; secrecy outage probability; uplink.

I. Introduction

Information security is an important issue in information exchange, especially in the

information-based society in which wireless communication technology plays a vital role. Due to the broadcast nature of wireless

communication, the information transmission between transceivers is vulnerable by wiretappers and unfortunately, it is difficult to detect. Physical layer security (PLS) is one of novel solutions that recently proposed to achieve secure transmission by exploiting the dynamic characteristics of the wireless transmission channels [1,2]. Meanwhile, the future 5G networks are required to support the demand of the fast growing number of wireless devices for low latency, low-cost and diversified services at higher quality and a thousand-time faster data rate compared to 4G networks. Recently, non-orthogonal multiple access (NOMA) technique has emerged as one of the most prominent candidates in meeting these requirements [3–5]. The research results show that NOMA technology can improve significantly the spectral efficiency as it takes advantage of the power domain to serve multiple users at the same time/frequency/code. In addition, compared with conventional multiple access, NOMA offers better than user fairness since even users with weak channel state information (CSI) can be served at a timely manner [3,6].

Naturally, the PLS concept can be considered to apply to NOMA system to improve the secrecy ability of 5G communication networks. However, the employment of successive interference cancellation (SIC) at receivers in NOMA networks, which introduces an unique interference status at the receivers, makes the secrecy performance analysis of the PLS of NOMA different from that of conventional multiple access technique. Recently, there are some works focusing on the PLS of NOMA networks [7–9]. The work in [7] investigated the PLS of simple NOMA model of downlink large-scale networks through the secrecy outage probability. In this model, stochastic geometry approaches were used to model the locations of NOMA users and eavesdroppers. In [8], the authors studied the PLS in a single-input single-

output (SISO) NOMA system for downlink, in which each legitimate user has its own predefined QoS requirement. The optimal power allocation policy was proposed to maximize the secrecy sum rate in closed-form expressions. To enhance the PLS performance of NOMA, multiple antennas and protected zone were introduced in the downlink system model of [9]. In the multiple-antenna scenario, artificial noise is generated at the base station that can improve the security of a beamforming-aided system. Unlike the above works, in this work we consider the PLS of uplink NOMA communication system. Our paper provides the following contributions: (i) The closed-form expressions of secrecy outage probability for two users are derived; (ii) Investigating the behavior of the considered system in different key parameters, such as transmitted power and distances. The rest of this paper is organized as follows. The system model is presented in Section II. Secrecy performance of the considered system is analyzed in Section III. The numerical results are shown in Section IV. Finally, Section V draws the conclusion of our paper.

II. SYSTEM MODEL

An uplink NOMA system is depicted as Fig. 1. Two mobile users denoted as $U_i, i = \{1,2\}$ intend to transmit information to base station BS in the presence of an eavesdropper E. We assume that all transceivers are single-antenna devices and operate in a half-duplex mode. The overall system transmission bandwidth is assumed to be one Hertz. Without loss of generality, assume that all the channel gains between BS and users follow the order of $|h_1|^2 \leq |h_2|^2$, where $|h_1|^2$ and $|h_2|^2$ are denoted as the channel gains of the 1st user and the 2st to BS links, respectively [10]. We also assume that the channel gains are constant during transmission block time T and we have the channel state information (CSI) of all links. Moreover, all wireless links are assumed to

undergo frequency non-selective Rayleigh block fading and additive white Gaussian noise (AWGN) with zero mean and variance N_0 . We denote d_1, d_2, d'_1, d'_2 as the Euclidean distances of to BS and E, respectively and σ denote the path-loss exponent of all links.

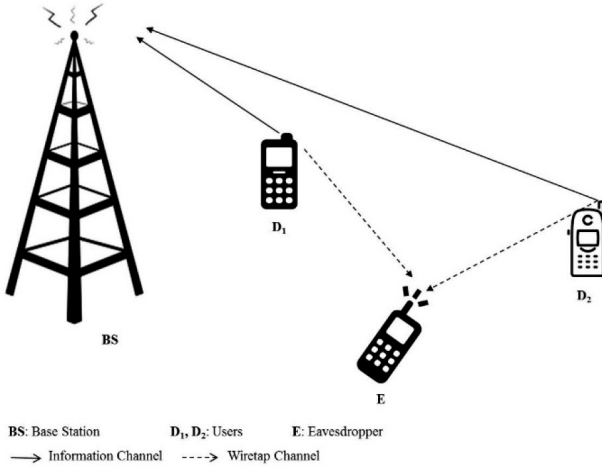


Fig.1. NOMA uplink system model with an eavesdropper

During block time T , two legitimate users transmit the message signal s_i ($i = \{1,2\}$) to base station with transmitted power P_i . The received signal at BS is expressed as

$$y = \frac{\sqrt{P_1}h_1}{\sqrt{d_1^\sigma}} s_1 + \frac{\sqrt{P_2}h_2}{\sqrt{d_2^\sigma}} s_2 + n_0, \quad (1)$$

where n_0 denotes the receiver Gaussian noise, In NOMA, s_1 and s_2 are transmitted by using the same frequency and the same time and the interfer to each other. In the uplink, the BS receiver applies successive interference cancellation (SIC) to decode the near user U_1 signal first by treating the far user U_2 signal as Gaussian interference [11]. After the receiver correctly decodes s_1 , it can subtract the s_1 from combined received signal y and finally decode s_2 . Therefore, the instantaneous SINR at BS to detect s_1 transmitted from U_1 can be written as

$$\text{SINR}_1 = X_1 = \frac{P_1|h_1|^2/d_1^\sigma}{P_2|h_2|^2/d_2^\sigma + N_0} = \frac{\gamma_{01}\gamma_1}{\gamma_{02}\gamma_2 + 1}, \quad (2)$$

and the received SNR at BS to detect s_2 is expressed as

$$\text{SNR}_2 = X_2 = \frac{P_2|h_2|^2/d_2^\sigma}{N_0} = \gamma_{02}\gamma_2, \quad (3)$$

where $\gamma_{01} = \frac{P_1}{N_0}$, $\gamma_{02} = \frac{P_2}{N_0}$, $\gamma_1 = \frac{|h_1|^2}{d_1^{\sigma_1}}$, $\gamma_2 = \frac{|h_2|^2}{d_2^{\sigma_2}}$.

Meanwhile, the eavesdropper tries to detect s_1 from U_1 without attack, therefore the received signal at E is expressed as

$$z = \frac{\sqrt{P_1}h'_1}{\sqrt{d_1'^{\sigma_1}}} s_1 + \frac{\sqrt{P_2}h'_2}{\sqrt{d_2'^{\sigma_2}}} s_2 + n_0, \quad (4)$$

where h'_1 and h'_2 are the channel coefficients of the link from U_1 and U_2 to E, respectively.

Assuming that eavesdropper do not apply SIC, the instantaneous SINRs at E to detect s_1 separately from U_1 are given by

$$\text{SINR}'_1 = Z_1 = \frac{P_1|h'_1|^2/d_1'^{\sigma_1}}{P_2|h'_2|^2/d_2'^{\sigma_2} + N_0} = \frac{\gamma_{01}\gamma'_1}{\gamma_{02}\gamma'_2 + 1}, \quad (5)$$

$$\text{SNR}'_2 = Z_2 = \frac{P_2|h'_2|^2/d_2'^{\sigma_2}}{P_1|h'_1|^2/d_1'^{\sigma_1} + N_0} = \frac{\gamma_{02}\gamma'_2}{\gamma_{01}\gamma'_1 + 1}, \quad (6)$$

where $\gamma'_1 = \frac{|h'_1|^2}{d_1'^{\sigma_1}}$, $\gamma'_2 = \frac{|h'_2|^2}{d_2'^{\sigma_2}}$.

The probability density function (PDF) and the cumulative distribution function (CDF) of random variable V are respectively expressed as

$$f_V(x) = \lambda e^{-\lambda x}, \quad (7)$$

$$F_V(x) = 1 - e^{-\lambda x}, \quad (8)$$

where $v \in \{\gamma_i, \gamma'_i\}$, $\lambda \in \left\{ \lambda_i = \frac{d_i^\sigma}{E(|h_i|^2)}, \lambda'_i = \frac{d_i'^{\sigma}}{E(|h'_i|^2)} \right\}$, $i = \{1,2\}$ and $E(\cdot)$ is expectation operator.

From (2), (7) and (8) we obtain the CDF and PDF of X_1 as follows

$$\begin{aligned} F_{X_1}(x) &= \Pr(X_1 < x) = \Pr\left(\frac{\gamma_{01}\gamma_1}{\gamma_{02}\gamma_2 + 1} < x\right) \\ &= \Pr\left(\gamma_1 < \frac{x(\gamma_{02}\gamma_2 + 1)}{\gamma_{01}}\right) \\ &= \int_0^\infty F_{\gamma_1}\left(\frac{x(\gamma_{02}\gamma_2 + 1)}{\gamma_{01}}\right) f_{(\gamma_2)} d\gamma_2 \\ &= 1 - \frac{\lambda_2\gamma_{01}}{\lambda_1\gamma_{02}x + \lambda_2\gamma_{01}} e^{-\frac{\lambda_1 x}{\gamma_{01}}}, \end{aligned} \quad (9)$$

$$f_{X_1(x)} = \frac{\lambda_1 \lambda_2 \gamma_{01} \gamma_{02}}{(\lambda_1 \gamma_{02} x + \lambda_2 \gamma_{01})^2} e^{-\frac{\lambda_1 x}{\gamma_{01}}} + \frac{\lambda_1 \lambda_2}{(\lambda_1 \gamma_{02} x + \lambda_2 \gamma_{01})} e^{-\frac{\lambda_1 x}{\gamma_{01}}}. \quad (10)$$

From (3), (7) and (8) we obtain the CDF and PDF of X_2 as follows

$$F_{X_2(x)} = 1 - e^{-\frac{\lambda_2 x}{\gamma_{02}}}, \quad (11)$$

$$f_{X_2(x)} = \frac{\lambda_2}{\gamma_{02}} e^{-\frac{\lambda_2 x}{\gamma_{02}}}. \quad (12)$$

Similarly, from (5), (6), (7) and (8) we obtain the CDF and PDF of Z_1 and Z_2 as follows

$$F_{Z_1(x)} = 1 - \frac{\lambda'_2 \gamma_{01}}{\lambda'_1 \gamma_{02} x + \lambda_2 \gamma_{01}} e^{-\frac{\lambda'_1 x}{\gamma_{01}}}, \quad (13)$$

$$f_{Z_1(x)} = \frac{\lambda'_1 \lambda'_2 \gamma_{01} \gamma_{02}}{(\lambda'_1 \gamma_{02} x + \lambda_2 \gamma_{01})^2} e^{-\frac{\lambda'_1 x}{\gamma_{01}}} + \frac{\lambda'_1 \lambda'_2}{(\lambda'_1 \gamma_{02} x + \lambda_2 \gamma_{01})} e^{-\frac{\lambda'_1 x}{\gamma_{01}}}, \quad (14)$$

$$F_{Z_2(x)} = 1 - \frac{\lambda'_1 \gamma_{02}}{\lambda'_2 \gamma_{01} x + \lambda_1 \gamma_{02}} e^{-\frac{\lambda'_2 x}{\gamma_{02}}}, \quad (15)$$

$$f_{Z_2(x)} = \frac{\lambda'_1 \lambda'_2 \gamma_{01} \gamma_{02}}{(\lambda'_2 \gamma_{01} x + \lambda_1 \gamma_{02})^2} e^{-\frac{\lambda'_2 x}{\gamma_{02}}} + \frac{\lambda'_1 \lambda'_2}{(\lambda'_2 \gamma_{01} x + \lambda_1 \gamma_{02})} e^{-\frac{\lambda'_2 x}{\gamma_{02}}}. \quad (16)$$

III. SECRECY PERFORMANCE ANALYSIS

3.1 Preliminaries

The instantaneous secrecy capacity is given by [12]

$$C_S = \max\{0, C_M - C_W\} = \max\left\{0, \log_2 \frac{1 + \gamma_M}{1 + \gamma_W}\right\} \quad (17)$$

where $C_M = \log_2[1 + \gamma_M]$ and $C_W = \log_2[1 + \gamma_W]$ trong đó, λ_M và λ_W represent SNRs of the legitimate and illegitimate links, respectively.

3.2 Secrecy Outage Probability

In this subsection, we analyze secrecy outage probability (Pout). Secrecy outage probability is also an important performance metric that is generally used to characterize the secrecy performance of a wireless communication system. It is defined as the probability that the instantaneous secrecy capacity

falls below a predetermined secrecy rate threshold $R > 0$, given by $P_{out} = \Pr(C_S < R)$. In this considered system, the eavesdropper only tries to hear the message of U_i ($1 \leq i \leq 2$), therefore the secrecy outage probabilities of U_i is expressed as

$$P_{out}^{U_i} = \Pr(C_S^{U_i} < R) = \Pr\left(\log_2 \frac{1 + X_i}{1 + Z_i} < R\right) \quad (18)$$

The derivation of $P_{out}^{U_1}$ and $P_{out}^{U_2}$ are analyzed through Theorem 1 and 2, respectively, as follows.

Theorem 1 Under Rayleigh fading, the closed-form expression of secrecy outage probability for U_1 is given by

$$P_{out}^{U_1} = 1 - uA_1 \left[qe^{aq} Ei(-aq) + \frac{1}{a} \right] + (uB_1 + vA_2)e^{aq} Ei(-aq) + (uC_1 + vB_2)e^{bq} Ei(-bq) \quad (19)$$

where

$$a = \frac{\lambda'_2 \gamma_{01}}{\lambda'_1 \gamma_{02}}, b = \frac{2^R - 1}{2^R} + \frac{\lambda_2 \gamma_{01}}{\lambda_1 \gamma_{02} 2^R},$$

$$A_1 = \frac{1}{b - a}, B_1 = \frac{-1}{(b - a)^2}, C_1 = \frac{1}{(b - a)^2},$$

$$A_2 = \frac{1}{(b - a)}, B_2 = \frac{1}{(a - b)}, q = \frac{\lambda_1 2^R}{\gamma_{01}} + \frac{\lambda'_1}{\gamma_{01}}, u = \frac{\lambda_2 \lambda'_2 \gamma_{01}^2}{\lambda_1 \lambda'_1 \gamma_{02}^2 2^R} e^{-\frac{\lambda_1 (2^R - 1)}{\gamma_{01}}},$$

$$v = \frac{\lambda_2 \lambda'_2 \gamma_{01}^2}{\lambda_1 \gamma_{02}^2 2^R} e^{-\frac{\lambda_1 (2^R - 1)}{\gamma_{01}}} \text{ and } Ei(.) \text{ is the exponential}$$

integral function [13].

Proof. See (21) in Appendix.

Theorem 2 Under Rayleigh fading, the closed-form expression of secrecy outage probability for U_2 is expressed as

$$P_{out}^{U_2} = 1 + \frac{\lambda'_1}{\gamma_{01}} e^{cp - \frac{\lambda_2 (2^R - 1)}{\gamma_{02}}} Ei(-cp) - cpe^{cp - \frac{\lambda_2 (2^R - 1)}{\gamma_{02}}} Ei(-cp) - e^{-\frac{\lambda_2 (2^R - 1)}{\gamma_{02}}}, \quad (20)$$

Proof. See (22) in Appendix.

IV. NUMERICAL RESULTS AND DISCUSSION

In this section, we provide the numerical examples in terms of secrecy outage probability to validate the secrecy performance of the uplink NOMA network.

Fig. 2 depicts the variation of the secrecy outage probability of near user $U_1(P_{out}^{U_1})$ with respect to $U_1 \rightarrow BS$ distance (d_1) for different values of average transmit SNR of $U_1(\gamma_{01})$. It can be seen from Fig. 2 that $P_{out}^{U_1}$ decreases when d_1 scales down and γ_{01} scales up. In other words, the better secrecy performance of U_1 is obtained in case that d_1 decreases and γ_{01} increases. The variation of average transmit SNR of far user $U_2(\gamma_{02})$ also impacts on secrecy performance of U_1 , as indicated in Fig. 3. In particular, Fig. 3 shows that secrecy performance of U_1 upgrades ($P_{out}^{U_1}$ decreases) with the decreases in γ_{02} because the reduction of interference in $SINR_1$ leads to the increase in channel capacity of $U_1 \rightarrow BS$ legitimate link.

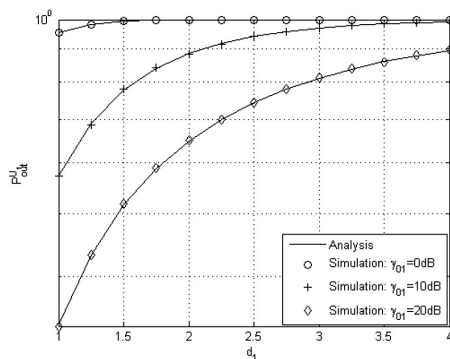


Fig.2. Secrecy outage probability for U1 vs distance and transmit power of U1

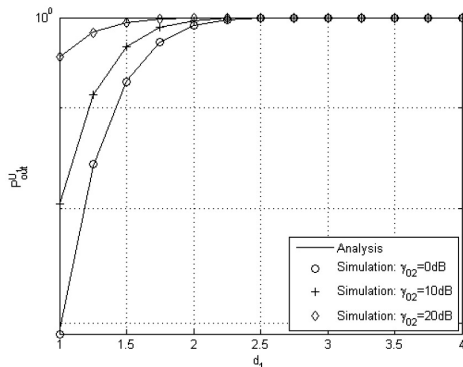


Fig.3. Secrecy outage probability for U1 vs distance and transmit power of U2

Fig. 4 depicts the effect of $U_1 \rightarrow E$ distance (d'_1) on $P_{out}^{U_1}$. As can be seen from this figure that the larger d'_1 is, the lower $P_{out}^{U_1}$ is obtained (i.e., the secrecy performance of U_1 is better) due to the higher effect of path loss phenomenon on illegitimate channel ($U_1 \rightarrow BS$ link).

Fig. 5 and Fig. 6 describe the variation of the secrecy outage probability of $U_2(P_{out}^{U_2})$ with respect to $U_2 \rightarrow BS$ distance (d_2) for different values γ_{02} and γ_{01} respectively. From these figures, we can see that the secrecy performance of U_2 upgrades ($P_{out}^{U_2}$ decreases) according to the increases in γ_{01} and γ_{02} or the decreases d_2 .

Fig. 7 depicts the the secrecy outage probability of U_1 in different distance values of $U_1 \rightarrow BS$ and distance values of $U_2 \rightarrow BS$. From this figure, we can see that the secrecy outage probability increase when the distance values of $U_1 \rightarrow BS$ increase or the distance values of $U_2 \rightarrow BS$ decreases.

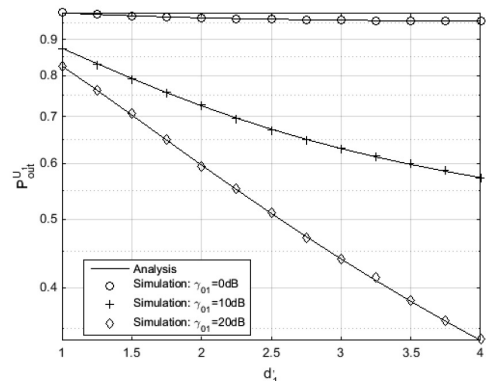


Fig.4. Secrecy outage probability for U1 vs distance d0 1 and transmit power of U1

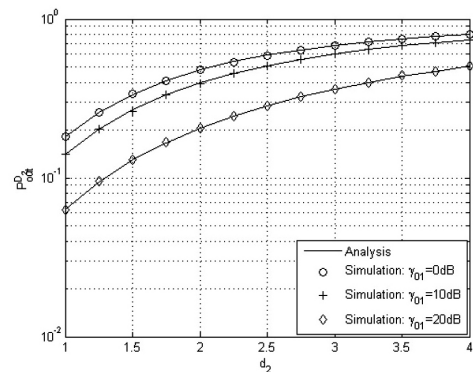


Fig.5. Secrecy outage probability for U2 vs distance and transmit power of U1

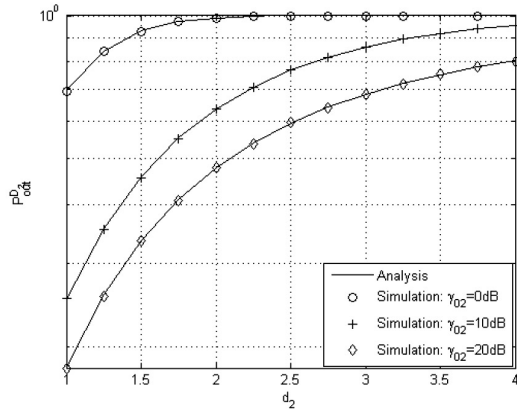


Fig.6. Secrecy outage probability for U2 vs distance and transmit power of U2

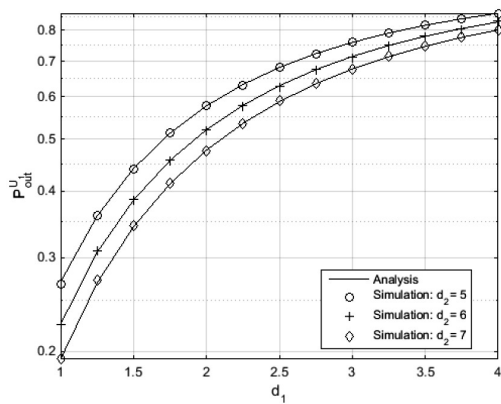


Fig.7. Secrecy outage probability for U1 vs distance of far user U2 and base station

Particularly, thefore mentioned results are confirmed by the excellent matching between analysis and simulation results, as observed from five figures

V. CONCLUSION

In this paper, the secrecy performance of uplink NOMA network has been studied. To evaluate the performance of this system, the closed-form expressions of secrecy outage probability of two users have been derived. Based on these expressions, the impact of some system parameters on the secrecy performance of the considered systems has investigated. The numerical results show that the secrecy performance of this system can be improved by increasing the transmit power of near user or decreasing the distance between users and base station.

Appendix

In this section, we provide the detailed calculation of P_{out}^{U1} and P_{out}^{U2} , as depicted in (21) and (22) in the top of this page, respectively.

$$\begin{aligned}
 P_{out}^{U1} &= \Pr(X_1 < 2^R(1 + Z_1) - 1) \\
 &= \int_0^\infty f_1(x)F_{x_1}(2^R(1 + x) - 1)dx \\
 &= 1 - u \int_0^\infty \frac{e^{-qx}}{(x+a)^2(x+b)}dx \\
 &\quad - v \int_0^\infty \frac{e^{-qx}}{(x+a)(x+b)}dx \\
 &= 1 - u \left[\int_0^\infty \frac{A_1 e^{-qx}}{(x+a)^2}dx \right. \\
 &\quad \left. + \int_0^\infty \frac{B_1 e^{-qx}}{(x+a)}dx \right. \\
 &\quad \left. + \int_0^\infty \frac{C_1 e^{-qx}}{(x+b)}dx \right] \\
 &\quad - v \left[\int_0^\infty \frac{A_2 e^{-qx}}{(x+a)}dx + \int_0^\infty \frac{B_2 e^{-qx}}{(x+b)}dx \right] \\
 &= 1 - u \left\{ A_1 \left[qe^{aq} Ei(-aq) + \frac{1}{a} \right] \right. \\
 &\quad \left. - B_1 e^{aq} Ei(-aq) \right. \\
 &\quad \left. - C_1 e^{bq} Ei(-bq) \right\} \\
 &\quad + v[A_2 e^{aq} Ei(-aq) + B_2 e^{bq} Ei(-bq)]. \tag{21}
 \end{aligned}$$

$$\begin{aligned}
 P_{out}^{U2} &= \Pr(X_2 < 2^R(1 + Z_2) - 1) \\
 &= \int_0^\infty f_{z_2}(x)F_{x_2}(2^R(1 + x) - 1)dx \\
 &= \int_0^\infty \left[\frac{\lambda'_1 \lambda'_2 \gamma_{01} \gamma_{02} e^{-\frac{\lambda'_2 x}{\gamma_{02}}}}{(\lambda'_2 \gamma_{01} x + \lambda'_1 \gamma_{02})^2} \right. \\
 &\quad \left. + \frac{\lambda'_1 \lambda'_2 e^{-\frac{\lambda'_2 x}{\gamma_{02}}}}{(\lambda_2 \gamma_{01} x + \lambda_1 \gamma_{02})} \right] \left[1 - e^{-\frac{\lambda_2 [e^{R(1+x)} - 1]}{\gamma_{02}}} \right] dx \\
 &= 1 + \frac{\lambda'_1}{\gamma_{01}} e^{cp - \frac{\lambda_2(2^R - 1)}{\gamma_{02}}} Ei(-cp) \\
 &\quad - cpe^{cp - \frac{\lambda_2(2^R - 1)}{\gamma_{02}}} Ei(-cp) \\
 &\quad - e^{-\frac{\lambda_2(2^R - 1)}{\gamma_{02}}} \tag{22}
 \end{aligned}$$

References

- [1] M. Bloch, J. Barros, M. R. Rodrigues, and S. W. McLaughlin, "Wireless information-theoretic security," *IEEE Trans. Inf. Tech.*, vol. 54(6), pp. 2515–2534, 2008.
- [2] D.B.Ha, T.T.Vu, T.T.Duy, and V.N.Q.Bao, "Secure cognitive reactive decode-and-forward relay networks: With and without eavesdropper," *Wireless Personal Communications (WPC)*, vol. 85, no. 4, pp. 2619–2641, 2015.
- [3] L. Dai, B. Wang, Y. Yuan, S. Han, C.-L. I, and Z. Wang, "Non-orthogonal multiple access for 5G: Solutions, challenges, opportunities, and future research trends," *IEEE Communications Magazine*, vol. 53(9), pp. 74–81, 2015.
- [4] T. Nakamura, A. Benjebbour, Y. Kishiyama, S. Suyama, and T. Imai, "5G radio access: Requirements, concept, experimental trials," *IEICE Trans. Commun.*, vol. E98-B(8), pp. 1397–1406, 2015.
- [5] K. Higuchi and Y. Kishiyama, "Non-orthogonal multiple access using intra-beam superposition coding and successive interference cancellation for cellular MIMO downlink," *IEICE Trans. Commun.*, vol. E98-B(9), pp. 1888–1895, 2015.
- [6] J. Men and J. Ge, "Performance analysis of non-orthogonal multiple access in downlink cooperative network," *IET Commun.*, vol. 9(18), pp. 2267–2273, 2015.
- [7] Z. Qin, Y. Liu, Z. Ding, Y. Gao, and M. Elkashlan, "Physical layer security for 5g non-orthogonal multiple access in large-scale networks," in *IEEE ICC 2016 Wireless Communications Symposium*, May 2016.
- [8] Y. Zhang, H.-M. Wang, Q. Yang, and Z. Ding, "Secrecy sum rate maximization in non-orthogonal multiple access," *IEEE Commun. Lett.*, vol. 20, no. 5, pp. 930–933, May 2016.
- [9] Y. Liu, Z. Qin, M. Elkashlan, Y. Gao, and L. Hanzo, "Enhancing the physical layer security of non-orthogonal multiple access in large-scale networks," *IEEE Transaction on Wireless Communications*, vol. 16, no. 163, pp. 1656–1672, Mar. 2017.
- [10] Y. Liu, Z. Ding, M. Elkashlan, and H. V. Poor, "Cooperative non-orthogonal multiple access with simultaneous wireless information and power transfer," [Online] <http://arxiv.org/abs/1511.02833>, 2015.
- [11] K. Higuchi and A. Benjebbour, "Non-orthogonal multiple access (NOMA) with successive interference cancellation for future radio access," *IEICE Trans. Commun.*, vol. E98-B(3), pp. 403–414, 2015.
- [12] D.-B. Ha, T. Q. Duong, D.-D. Tran, H.-J. Zepernick, and T. T. Vu, "Physical layer secrecy performance over Rayleigh/Rician fading channels," in *The 2014 International Conference on Advanced Technologies for Communications (ATC'14)*, Hanoi, Vietnam, Oct. 15-17, 2014, pp. 113–118.
- [13] Fig.4. Secrecy outage probability for U1 vs distance $d_0 = 1$ and transmit power of U1. Gradshteyn and I. Ryzhik, *Table of Integrals, Series, and Products*, D. Zwillinger, Ed. Elsevier Academic Press, 2007.

An Investigation of Space Vector Modulation Methods for Matrix Converters

Khảo Sát Phương Pháp Điều Chế Vector Không Gian Cho Bộ Biến Tần Ma Trận

Nguyen Huu Nhan

*Viện Nghiên Cứu và Phát Triển Công Nghệ Cao, Trường Đại học Duy Tân, Việt Nam
Institute of Research and Development, Duy Tan University, Vietnam*

(Ngày nhận bài: 29/01/2018, ngày phản biện xong: 12/03/2018, ngày chấp nhận đăng: 20/03/2018)

Tóm tắt

Bài báo này trình bày khảo sát các phương pháp điều chế vector không gian cho bộ biến tần ma trận. Có hai phương pháp điều chế vector không gian phổ biến để điều khiển bộ biến tần ma trận. Phương pháp thứ nhất sử dụng hai điện áp đầu vào lớn để điều chế điện áp đầu ra và đạt được tỉ số điều chế cực đại 0.866. Ở phương pháp thứ hai, hai điện áp đầu vào nhỏ được sử dụng để điều khiển bộ biến tần ma trận, do đó tỉ số điều chế bị giới hạn từ 0 đến 0.5. Tuy vậy phương pháp điều chế thứ hai cho ra chất lượng điện áp tốt hơn phương pháp thứ nhất. Các kết quả mô phỏng đã kiểm chứng được rằng tổng độ méo dạng sóng hài ở phương pháp điều chế vector không gian thứ hai thấp hơn ở phương pháp thứ nhất.

Từ khóa: Bộ biến tần ma trận, bộ biến tần ac-ac, phương pháp điều chế vector không gian.

Abstract

This paper presents an investigation of space vector modulation (SVM) methods for matrix converters (MCs). There are two common SVM methods for the MC drive. The first method uses two higher instantaneous values of input voltages to generate the output voltage and gives the maximum voltage transfer ratio of 0.866. In the second method, two lower instantaneous values of input voltages are selected to drive the MC, so the voltage transfer ratio is limited from 0 to 0.5. However, the second modulation method gives a better performance than the first one. Simulation results confirm that the second SVM method shows lower total harmonic distortion (THD) of line-to-line output voltage than that of the first SVM method.

Keywords: Matrix converter, ac-ac power converter, space vector modulation method.

I. INTRODUCTION

Matrix converter (MC) is a direct ac-ac power converter which consists of 9 bi-directional switches that allow any output phase to be connected to any input phase. It has several advantages such as the lack of dc-link capacitor, sinusoidal input and output current waveforms and unity input power factor [1]. With the

safe commutation, MC is reliable to apply for industrial applications.

Several modulation methods for MCs with different characteristics have been developed and are introduced in [2] and [3]. Among them, the space vector modulation (SVM) is currently considered as the most popular technique since it provides a clear comprehension of the modulation

process and relatively simple algorithm [4]–[6].

The SVM methods presented in [6], [7] are very popular to control the MC. These methods are based on the instantaneous space vector representation of input/output voltages and currents. There are two ways to select the input voltage space vectors to generate the output voltage space vector. Firstly, two higher instantaneous values of input voltages are chosen to generate the output voltage. Secondly, two lower instantaneous values of line-to-line input voltage will be used.

This paper presents an investigation and a comparison of two SVM methods for MCs. The paper also focuses on how to make the symmetrical switching pattern and reduce the switching loss.

II. Principles of Matrix Converter

A common 3x3 MC configuration is shown in Fig. 1. It consists 9 bidirectional switches which have 3 types: diode bridge, common emitter, and common collector bi-directional switch. In order to reduce the switching loss and isolated power supplies for the gate drive board, the common collector bidirectional switch should be used. A passive LC input filter is required to lower the high order harmonics of the input current. To damp the oscillations that result from the MC hard switching, it is necessary to include a resistor in the filter. This resistor may be connected in series or in parallel with the filter inductor or in parallel with the capacitor.

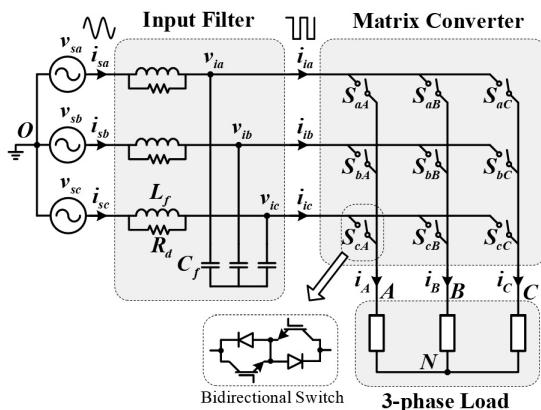


Fig. 1. A common three-phase to three-phase MC configuration

III. SVM Methods for MCs

In a balanced operation, the instantaneous source voltages are as follows:

$$\mathbf{v}_s = \begin{bmatrix} v_{sa} \\ v_{sb} \\ v_{sc} \end{bmatrix} = V_s \begin{bmatrix} \cos(\omega_i t) \\ \cos(\omega_i t - 2\pi/3) \\ \cos(\omega_i t + 2\pi/3) \end{bmatrix} \quad (1)$$

where V_s and ω_i are the amplitude and the angular frequency of the source voltage, respectively.

With the relevant symbols shown in Fig. 1, the space vectors of input/output voltages and currents are defined, respectively, by the following equations:

$$\vec{v}_i = 2(v_{ia} + v_{ib}e^{j2\pi/3} + v_{ic}e^{j4\pi/3})/3 = V_i e^{j\alpha_i} \quad (2)$$

$$\vec{v}_o = 2(v_A + v_Be^{j2\pi/3} + v_Ce^{j4\pi/3})/3 = V_o e^{j\alpha_o} \quad (3)$$

$$\vec{i}_i = 2(i_{ia} + i_{ib}e^{j2\pi/3} + i_{ic}e^{j4\pi/3})/3 = I_i e^{j\beta_i} \quad (4)$$

$$\vec{i}_o = 2(i_A + i_Be^{j2\pi/3} + i_Ce^{j4\pi/3})/3 = I_o e^{j\beta_o} \quad (5)$$

Hereafter, any space vector will be referred to simply as a vector.

Basically, there are 27 possible switching configurations (SCs) to satisfy the two main rules in an MC: i) the input phases should never be short-circuited, and ii) the output phases should not be unconnected. These SCs are listed in Table I and categorized into three groups:

1) Group I consists of 18 active vectors that produce the output-voltage and input-current vectors with fixed directions and time-varying amplitudes.

2) Group II consists of 3 zero vectors that determine the zero-output voltage and input-current vectors.

3) Group III consists of 6 rotating vectors; because the output-voltage and input-current vectors have time-varying directions, they are rarely used in SVM strategies.

In principle, the conventional SVM methods are based on the selection of four suitable active vectors in Group I to synthesize the reference

output voltage vector under the unity input power factor constraint [3], [6]. The zero SCs are applied to complete the sampling period T_s .

For example, both \vec{v}_o and \vec{i}_i are lying in sector 1 ($k_v = 1, k_i = 1$, where k_v and k_i are the output voltage sector and the input current sector,

respectively) as shown in Fig. 2. The desired output voltage vector \vec{v}_o can be synthesized from two vectors \vec{v}_o' and \vec{v}_o'' . The \vec{v}_o' and \vec{v}_o'' components can be synthesized using two of six possible SCs $\pm 1, \pm 2, \pm 3$, and $\pm 7, \pm 8, \pm 9$, respectively.

Table I: Possible switching configurations in the MC

Switching Configurations		Output Voltage		Input Current		
		No	A B C	V_o	α_o	I_i
Group I	+1	a b b	$2v_{ab}/3$	0	$2i_A/\sqrt{3}$	$-\pi/6$
	-1	b a a	$-2v_{ab}/3$	0	$-2i_A/\sqrt{3}$	$-\pi/6$
	+2	b c c	$2v_{bc}/3$	0	$2i_A/\sqrt{3}$	$\pi/2$
	-2	c b b	$-2v_{bc}/3$	0	$-2i_A/\sqrt{3}$	$\pi/2$
	+3	c a a	$2v_{ca}/3$	0	$2i_A/\sqrt{3}$	$7\pi/6$
	-3	a c c	$-2v_{ca}/3$	0	$-2i_A/\sqrt{3}$	$7\pi/6$
	+4	b a b	$2v_{ab}/3$	$2\pi/3$	$2i_B/\sqrt{3}$	$-\pi/6$
	-4	a b a	$-2v_{ab}/3$	$2\pi/3$	$-2i_B/\sqrt{3}$	$-\pi/6$
	+5	c b c	$2v_{bc}/3$	$2\pi/3$	$2i_B/\sqrt{3}$	$\pi/2$
	-5	b c b	$-2v_{bc}/3$	$2\pi/3$	$-2i_B/\sqrt{3}$	$\pi/2$
	+6	a c a	$2v_{ca}/3$	$2\pi/3$	$2i_B/\sqrt{3}$	$7\pi/6$
	-6	c a c	$-2v_{ca}/3$	$2\pi/3$	$-2i_B/\sqrt{3}$	$7\pi/6$
	+7	b b a	$2v_{ab}/3$	$4\pi/3$	$2i_C/\sqrt{3}$	$-\pi/6$
	-7	a a b	$-2v_{ab}/3$	$4\pi/3$	$-2i_C/\sqrt{3}$	$-\pi/6$
	+8	c c b	$2v_{bc}/3$	$4\pi/3$	$2i_C/\sqrt{3}$	$\pi/2$
-8	b b c	$-2v_{bc}/3$	$4\pi/3$	$-2i_C/\sqrt{3}$	$\pi/2$	
+9	a a c	$2v_{ca}/3$	$4\pi/3$	$2i_C/\sqrt{3}$	$7\pi/6$	
-9	c c a	$-2v_{ca}/3$	$4\pi/3$	$-2i_C/\sqrt{3}$	$7\pi/6$	
Group II	0 _a	a a a	0	x	0	x
	0 _b	b b b	0	x	0	x
	0 _c	c c c	0	x	0	x
Group III	r ₁	a b c	x	x	x	x
	r ₂	a c b	x	x	x	x
	r ₃	b c a	x	x	x	x
	r ₄	b a c	x	x	x	x
	r ₅	c a b	x	x	x	x
	r ₆	c b a	x	x	x	x

A. SVM Method 1

Input current sector in SVM method 1 is defined as Fig. 2(b). In this case, SCs $\pm 1, \pm 4, \pm 7$ and $\pm 3, \pm 6, \pm 9$ are used to generate an input current vector in sector 1. In order to maximize the amplitude of output voltage, two higher input voltage magnitude are selected to drive the MC.

When the input current vector \vec{i}_i is in sector 1, two higher input line-to-line voltages are v_{ab} and v_{ac} . From these analyses, four SCs $+1, -3, -7$, and $+9$ are selected for the case of $k_v = 1, k_i = 1$.

With a similar procedure, the selected SCs for all combinations of the output voltage and the input current sectors are summarized in Table II.

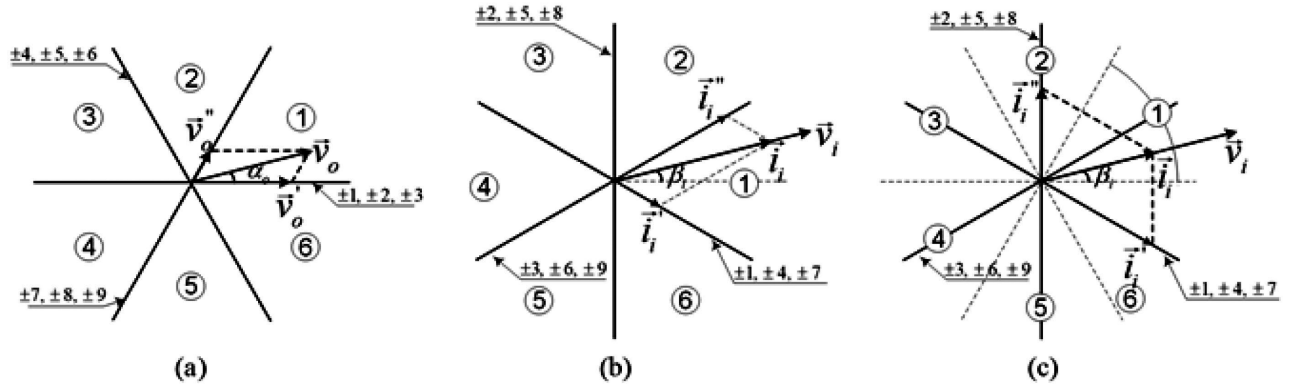


Fig. 2. (a) Output voltage vector. (b) Input current vector for the SVM method 1. (c) Input current vector for the SVM method 2.

Table II: Selected SCS for each combination of output voltage and input current sectors in the SVM method 1

		Input Current Vector Sector																											
		1				2				3				4				5				6							
Output Voltage Vector Sector	1	-7	+9	+1	-3	+9	-8	-3	+2	-8	+7	+2	-1	+7	-9	-1	+3	-9	+8	+3	-2	+8	-7	-2	+1				
	2	+4	-6	-7	+9	-6	+5	+9	-8	+5	-4	-8	+7	-4	+6	+7	-9	+6	-5	-9	+8	-5	+4	+8	-7				
	3	-1	+3	+4	-6	+3	-2	-6	+5	-2	+1	+5	-4	+1	-3	-4	+6	-3	+2	+6	-5	+2	-1	-5	+4				
	4	+7	-9	-1	+3	-9	+8	+3	-2	+8	-7	-2	+1	-7	+9	+1	-3	+9	-8	-3	+2	-8	+7	+2	-1				
	5	-4	+6	+7	-9	+6	-5	-9	+8	-5	+4	+8	-7	+4	-6	-7	+9	-6	+5	+9	-8	+5	-4	-8	+7				
	6	+1	-3	-4	+6	-3	+2	+6	-5	+2	-1	-5	+4	-1	+3	+4	-6	+3	-2	-6	+5	-2	+1	+5	-4				
Duty cycles		d ₁	d ₂	d ₃	d ₄	d ₁	d ₂	d ₃	d ₄	d ₁	d ₂	d ₃	d ₄	d ₁	d ₂	d ₃	d ₄	d ₁	d ₂	d ₃	d ₄	d ₁	d ₂	d ₃	d ₄	d ₁	d ₂	d ₃	d ₄

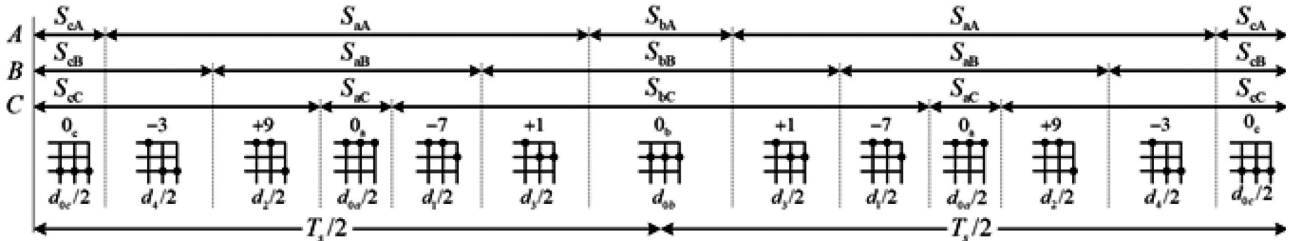


Fig. 3. Switching pattern for output voltage sector 1 and input current sector 1 of the SVM method 1.

The duty ratios of SCs -7 (d_1) and $+9$ (d_2) should satisfy the following relationship:

$$\frac{2}{3}v_{ab}d_1 + \frac{2}{3}v_{ac}d_2 = v_o'' = \frac{2}{\sqrt{3}}V_o \sin \alpha_o. \quad (6)$$

Because the magnitude of input currents is independent of the phase angle of output current, so:

$$\frac{d_1}{\sin(\pi/6 - \beta_i)} = \frac{d_2}{\sin(\pi/6 + \beta_i)}. \quad (7)$$

From (6) and (7), the duty ratios for SCs -7 and $+9$ are respectively as follows:

$$d_1 = \frac{2q \sin \tilde{\alpha}_o \sin(\pi/6 - \tilde{\beta}_i)}{\sqrt{3} \cos \delta_i} \quad (8)$$

$$d_2 = \frac{2q \sin \tilde{\alpha}_o \sin(\pi/6 + \tilde{\beta}_i)}{\sqrt{3} \cos \delta_i} \quad (9)$$

where $q = V_o/V_i$ is the voltage transfer ratio, $\delta_i = \alpha_i - \beta_i$ is the input current displacement angle, and $\tilde{\alpha}_o$ and $\tilde{\beta}_i$ are defined as:

$$\tilde{\alpha}_o = \alpha_o - (k_v - 1) \times \pi/3 \quad (10)$$

$$\tilde{\beta}_i = \beta_i - (k_i - 1) \times \pi/3. \quad (11)$$

By similar analysis, the duty ratios for SCs $+1$ and -3 are respectively as follows:

$$d_3 = \frac{2q \sin(\pi/3 - \tilde{\alpha}_o) \sin(\pi/6 - \tilde{\beta}_i)}{\sqrt{3} \cos \delta_i} \quad (12)$$

$$d_4 = \frac{2q \sin(\pi/3 - \tilde{\alpha}_o) \sin(\pi/6 + \tilde{\beta}_i)}{\sqrt{3} \cos \delta_i} \quad (13)$$

Zero SCs are required to complete the sampling period with the duty cycle:

$$d_0 = 1 - \frac{2q \cos(\tilde{\alpha}_o - \pi/6) \cos \tilde{\beta}_i}{\sqrt{3} \cos \delta_i} \quad (14)$$

$$0 \leq d_n \leq 1; \quad n = 0, \dots, 4. \quad (15)$$

Fig. 3 shows the switching pattern corresponding to the case of $k_v = 1, k_i = 1$.

All duty cycles in the SVM method 1 must satisfy the following constraints:

This leads to the well-known restriction of the voltage transfer ratio in the MC:

$$q \leq \frac{\sqrt{3}}{2} \cos \delta_i. \quad (16)$$

Table III: Selected SCS for each combination of output voltage and input current sectors in the SVM method 2

		Input Current Vector Sector																							
		1				2				3				4				5				6			
Output Voltage Vector Sector	1	-7	-8	+1	+2	+9	+7	-3	-1	-8	-9	+2	+3	+7	+8	-1	-2	-9	-7	+3	+1	+8	+9	-2	-3
	2	+4	+5	-7	-8	-6	-4	+9	+7	+5	+6	-8	-9	-4	-5	+7	+8	+6	+4	-9	-7	-5	-6	+8	+9
	3	-1	-2	+4	+5	+3	+1	-6	-4	-2	-3	+5	+6	+1	+2	-4	-5	-3	-1	+6	+4	+2	+3	-5	-6
	4	+7	+8	-1	-2	-9	-7	+3	+1	+8	+9	-2	-3	-7	-8	+1	+2	+9	+7	-3	-1	-8	-9	+2	+3
	5	-4	-5	+7	+8	+6	+4	-9	-7	-5	-6	+8	+9	+4	+5	-7	-8	-6	-4	+9	+7	+5	+6	-8	-9
	6	+1	+2	-4	-5	-3	-1	+6	+4	+2	+3	-5	-6	-1	-2	+4	+5	+3	+1	-6	-4	-2	-3	+5	+6
Duty cycles		d_1	d_2	d_3	d_4	d_1	d_2	d_3	d_4	d_1	d_2	d_3	d_4	d_1	d_2	d_3	d_4	d_1	d_2	d_3	d_4	d_1	d_2	d_3	d_4

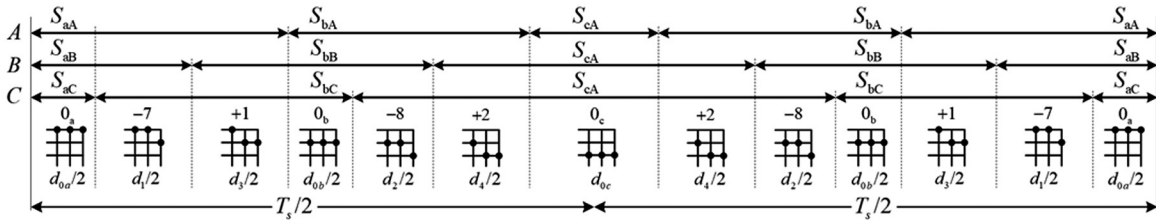


Fig. 4. Switching pattern for input voltage sector 1 and output voltage sector 1 of the SVM method 2.

B. SVM method 2

To reduce the output current ripple, the voltage difference between the output-voltage reference and the modulated output-voltage vectors should be minimized [8]. When the voltage transfer ratio is low, the highest active vectors are excluded because they are far from the reference-voltage vector. Therefore, two lower instantaneous values of input voltages are used to synthesize the reference output voltage.

The input current sector is redefined as shown in Fig. 2(c). Considering again the case of $k_v = 1, k_i = 1$, two lower voltage magnitude vectors are v_{ab} and v_{bc} . From Table I, states +1, +2, -7, -8 will be selected. Using a similar analysis, the selected SCs are summarized in Table III for any combination of input voltage and output voltage sectors.

Similar to the SVM method 1, the duty ratios for SCs -7, -8, +1, +2 and zero SCs are respectively as follows:

$$d_1 = \frac{2q \sin \tilde{\alpha}_o \sin(\pi/2 - \tilde{\beta}_i)}{\sqrt{3} \cos \delta_i} \quad (17)$$

$$d_2 = \frac{2q \sin \tilde{\alpha}_o \sin(\pi/6 + \tilde{\beta}_i)}{\sqrt{3} \cos \delta_i} \quad (18)$$

$$d_3 = \frac{2q \sin(\pi/3 - \tilde{\alpha}_o) \sin(\pi/2 - \tilde{\beta}_i)}{\sqrt{3} \cos \delta_i} \quad (19)$$

$$d_4 = \frac{2q \sin(\pi/3 - \tilde{\alpha}_o) \sin(\pi/6 + \tilde{\beta}_i)}{\sqrt{3} \cos \delta_i} \quad (20)$$

$$d_0 = 1 - 2q \frac{\cos(\tilde{\alpha}_o - \pi/6) \cdot \cos(\tilde{\beta}_i - \pi/6)}{\cos \delta_i} \quad (21)$$

Fig. 4 shows the switching pattern corresponding to the case of $k_v = 1, k_i = 1$.

All duty cycles must be non-negative and lower than or equal to unity. Therefore, the limit of the voltage transfer ratio in the SVM method 2 is:

$$q \leq \frac{1}{2} \cos \delta_i. \quad (22)$$

From (22), the output-to-input voltage ratio is limited from 0 to 0.5. Thus, the SVM method

2 is suitable for applications with low voltage transfer ratios.

C. Total Harmonic Distortion

Total harmonic distortion (THD) of the line-to-line output voltage is useful to evaluate the system performance. The THD is calculated by:

$$THD = \frac{\sqrt{\sum_{n=2}^{\infty} U_{(n)}^2}}{U_{(1)}} = \frac{\sqrt{U_{RMS}^2 - U_{(1)}^2}}{U_{(1)}} \quad (23)$$

where $U_{(1)}$ is the amplitude of the fundamental voltage component, $U_{(n)}$ is the amplitude of the n -th harmonic.

IV. Simulation Results

Table IV: Simulation parameters

Power supply	Input filter	Output load
$V_z = 100 \text{ V}$	$L_f = 1.4 \text{ mH}$	$R = 20 \text{ } \Omega$
$f_i = 60 \text{ Hz}$	$C_f = 22 \text{ } \mu\text{F}$	$L = 12 \text{ mH}$
	$R_d = 20 \text{ } \Omega$	$f_o = 50 \text{ Hz}$

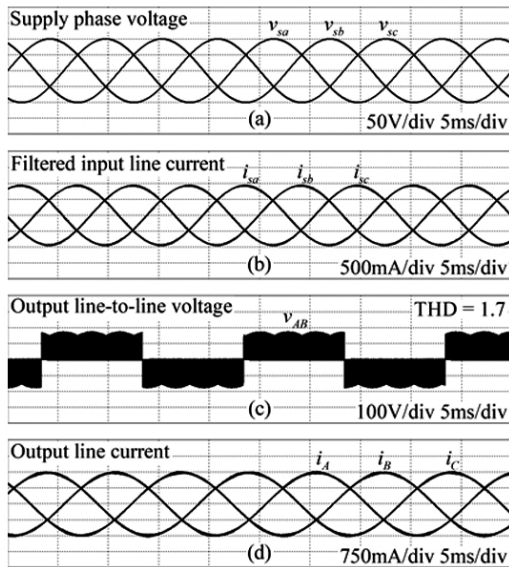


Fig. 5. (a) Supply phase voltage. (b) Filtered input current. (c) Output line-to-line voltage. (d) Output line current at $f_o = 50 \text{ Hz}$, $q = 0.3$ with the SVM method 1

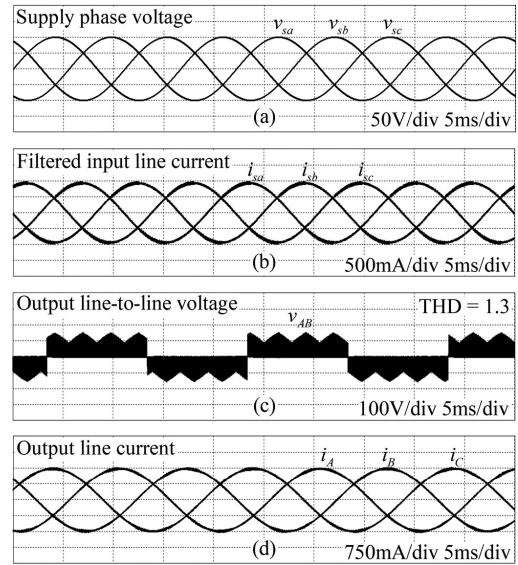


Fig. 6. (a) Supply phase voltage. (b) Filtered input current. (c) Output line-to-line voltage. (d) Output line current at $f_o = 50 \text{ Hz}$, $q = 0.3$ with the SVM method 2.

Numerical simulations were carried out using Psim 9.0 software to evaluate the performance of two SMV methods. The simulation parameters are shown in Table IV. The switching frequency of the SVM methods is 10 kHz, corresponding to the switching period of 100 μs .

Figs. 5 and 6 show the simulation results of the input/output waveforms with the SVM method 1 and SVM method 2, respectively, at $f_o = 50 \text{ Hz}$, $q = 0.4$. As can be seen, the SVM method 2 shows the same quality for the input current compared with the SVM method 1. Figs. 5(c) and 6(c) show the output voltage-waveform characteristics for the SVM methods 1 and 2, respectively. From a total harmonic distortion (THD) analysis, the output-voltage performance of the SVM method 2 was improved through a reduction of the THD from the 1.7 of the SVM method 1 to the 1.3 of the SVM method 2.

Fig. 7 shows a comparison between two SVM methods in terms of output voltage THD versus voltage transfer ratio. As can be seen, the THD with the SVM method 2 is lower than that with the SVM method 1, therefore it can be said that the SVM method 2 achieves a better performance at

low voltage transfer ratio, i.e., $q \leq 0.5$. This result is in good agreement with the theoretical analysis.

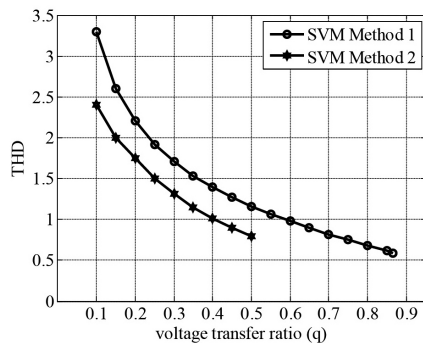


Fig. 7. Comparison between two SVM methods in terms of output voltage THD versus voltage transfer ratio.

Fig. 8 shows the THD comparison of the input current between two SVM methods. Because the far input current vectors from the reference one are used in the SVM method 2, the harmonic content of the input current is increased. As a result, the input current THD of the SVM method 2 becomes higher (around 260%) than that of the SVM method 1 at a voltage transfer ratio of 0.5.

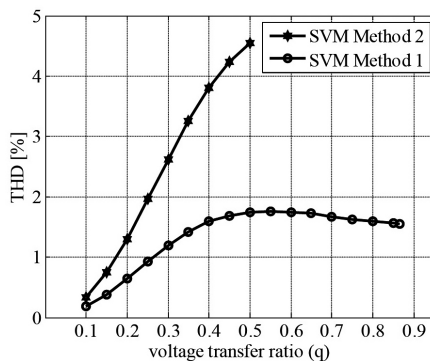


Fig. 8. Comparison between two SVM methods in terms of input current THD versus voltage transfer ratio.

V. Conclusion

This paper presents an investigation of two SVM methods for MCs. The two SVM methods use two higher or two lower instantaneous input voltages to generate the output voltage. With the SVM method 1, the voltage transfer ratio can reach $\sqrt{3}/2 = 0.886$ while voltage transfer ratio in the SVM method 2 is limited from 0 to 0.5. The SVM method 2 can give a better output performance with a lower output voltage THD

and a worse input performance with a higher input current THD. The two SVM methods can be combined for the entire modulation index to utilize the power usage of MC.

Acknowledgement

This work was carried out during my Ph.D. study at the University of Ulsan, South Korea. I would like to acknowledge the support provided by Professor Hong-Hee Lee, Director of Network-based Automation Research Center (NARC), the University of Ulsan, South Korea during the research of this work.

References

- [1] P. W. Wheeler, J. Rodríguez, J. C. Clare, L. Empringham, and A. Weinstein, "Matrix converters: A technology review," *IEEE Trans. Ind. Electron.*, vol. 49, no. 2, pp. 276–288, Apr. 2002.
- [2] J. Rodriguez, M. Rivera, J. W. Kolar, and Patrick W. Wheeler, "A review of control and modulation methods for matrix converters," *IEEE Trans. Ind. Electron.*, vol. 59, no. 1, pp. 58–70, Jan. 2012.
- [3] D. Casadei, G. Serra, A. Tani, and L. Zarri, "Matrix converter modulation strategies: A new general approach based on space vector representation of switch state," *IEEE Trans. Ind. Electron.*, vol. 49, no. 2, pp. 370–381, Apr. 2002.
- [4] A. Arias, L. Empringham, G. M. Asher, P. W. Wheeler, M. Bland, M. Apap, M. Sumner, and J. C. Clare, "Elimination of waveform distortions in matrix converters using a new dual compensation method," *IEEE Trans. Ind. Electron.*, vol. 54, no. 4, pp. 2079–2087, Aug. 2007.
- [5] J V. Padhee, A. K. Sahoo, N. Mohan, "Modulation techniques for enhanced reduction in common-mode voltage and output voltage distortion in indirect MCs," *IEEE Trans. Power Electron.*, vol. 32, no. 11, pp. 8655–8670, Aug. 2017.
- [6] H. M. Nguyen, H. H. Lee, and T. W. Chun, "Input power factor compensation algorithms using a new Direct-SVM method for Matrix Converter," *IEEE Trans. Ind. Electron.*, vol. 58, no. 1, pp. 232–243, Jan. 2011.
- [7] H. H. Lee, and H. M. Nguyen, "An effective direct-SVM method for matrix converters operating with low-voltage transfer ratio," *IEEE Trans. Power Electron.*, vol. 28, no. 2, pp. 920–929, Feb. 2013.
- [8] S. Kim, Y.-D. Yoon, and S.-K. Sul, "Pulsewidth modulation method of matrix converter for reducing output current ripple," *IEEE Trans. Power Electron.*, vol. 20, no. 6, pp. 1372–1378, Nov. 2005.

THỂ LỆ VIẾT VÀ GỬI BÀI

1. Bài nhận đăng là các công trình mới có ý nghĩa khoa học và thực tiễn trong các lĩnh vực khoa học và công nghệ, chưa công bố ở bất kỳ tạp chí nào.

2. Một số lưu ý về hình thức và bố cục của bài báo

2.1. Hình thức của bài báo

- Bài viết được soạn thảo bằng các phần mềm soạn thảo văn bản MS Word, không quá 10 trang giấy khổ A4. Hình ảnh trong bài viết rõ ràng, theo định dạng PNG, JPG hoặc WMF. Tên hình vẽ đặt ở phía dưới, tên bảng biểu đặt ở phía trên, hình và bảng được đánh số thứ tự.

2.2. Bố cục của bài báo

- Phần tiêu đề: chứa các thông tin sau:

- Tiêu đề bài báo: bằng tiếng Việt và tiếng Anh, súc tích, đầy đủ thông tin.
- Tên các tác giả: ghi đầy đủ theo thứ tự họ, chữ lót và tên. Phía trên tên tác giả liên lạc (corresponding author) được đánh dấu *.
- Cơ quan công tác: cung cấp địa chỉ thuận lợi cho việc liên hệ.
- Địa chỉ e-mail: địa chỉ e-mail (nếu có) của các tác giả có tên trong bài báo.

- Phần tóm tắt: bằng tiếng Việt và tiếng Anh giới thiệu một cách ngắn gọn về mục đích nghiên cứu và kết quả đạt được của bài báo.

- Phần nội dung: đầy đủ các mục: a. Đặt vấn đề (nêu rõ mục đích, đối tượng nghiên cứu, tính thời sự của vấn đề); b. Giải quyết vấn đề (phương pháp nghiên cứu, phương tiện sử dụng khi nghiên cứu, nội dung nghiên cứu đã thực hiện); c. Kết quả nghiên cứu và thảo luận; d. Kết luận.

- Phần tài liệu tham khảo: chỉ nêu các tài liệu trích dẫn đã được liệt kê, sắp thứ tự bằng số chứa trong các ngoặc vuông, định dạng như sau:

- Đối với sách, luận án, báo cáo: số thứ tự, họ và tên tác giả hoặc tên cơ quan ban hành, tên sách (luận án, báo cáo), nhà xuất bản, nơi xuất bản, năm xuất bản.
- Đối với bài báo: số thứ tự, họ và tên tác giả, tên bài báo, tên tạp chí, tập, số, năm xuất bản, số trang.

3. Địa chỉ gửi bài: Tạp chí Khoa học và Công nghệ Đại học Duy Tân, 03 Quang Trung, Đà Nẵng; ĐT: 0236.3827111- 413; Fax: 0236.3650443; Email: tapchikhcn@duytan.edu.vn.

Lưu ý:

- Ban biên tập chỉ nhận những bài đã được chuẩn bị theo đúng các qui định trên. Nếu bài không được đăng, tòa soạn sẽ không trả lại bản thảo.

Giấy phép hoạt động báo chí in số 1245/GP-BTTTT ngày 05/08/2011

In tại Công ty CP In và Dịch vụ Đà Nẵng, 420 Lê Duẩn, TP Đà Nẵng

Số lượng 150 bản; Khổ 21 × 28,5 cm

In xong và nộp lưu chiểu ngày: 05/04/2018